

DISS. ETH NO. 25176

**Hydropower potential and
reservoir sedimentation in
the periglacial environment
under climate change**

A thesis submitted to attain the degree of
DOCTOR OF SCIENCES of ETH ZURICH
(Dr. sc. ETH Zurich)

presented by
Daniel Ehrbar
MSc ETH Civil Eng

born on 31 August 1986

citizen of
Urnäsch AR

accepted on the recommendation of

PROF. DR. ROBERT M. BOES

PROF. DR. FLAVIO S. ANSELMETTI

DR. DAVID F. VETSCH

DR. LUKAS SCHMOCKER

2018

Preface

Hydropower is the most important source of renewable energy in Switzerland and constitutes the backbone of the Swiss electricity generation portfolio. Many reservoirs are located in the periglacial environment, i.e. in catchment areas with a glacierized share of at least 30%. Climate change and the changeover to a new energy system will challenge the existing infrastructure. The retreat of many glaciers in Switzerland and worldwide may have significant impacts on water resources but also provides opportunities such as new sites for reservoir dams. New natural proglacial lakes have recently started forming at the terminus of a number of Swiss glaciers. These reservoirs partly form naturally at rock rims after glacier retreat, and partly need a man-made dam. However, melting glaciers tend to increase the sediment availability, so that the sedimentation of downstream reservoirs becomes more acute. For their sustainable use, it is imperative to consider sedimentation and to plan and implement counter-measures.

The overarching goal of this research was a better understanding of the effect of climate change on reservoir sedimentation and its effects on hydropower in the periglacial environment. The study was divided into three distinct parts, namely a systematic investigation of the hydropower potential in Swiss periglacial catchments, a field investigation of sediment fluxes into and inside periglacial reservoirs, and the investigation of long-term sedimentation processes and patterns in such reservoirs using a numerical model.

Based on current glacier runoff projections of the VAW glaciology group, Dr. Ehrbar has analyzed the hydropower potential in Swiss periglacial catchments. He developed a framework based on an evaluation matrix with 16 economical, environmental and social criteria for the consistent rating of all feasible sites. Suitable reservoir sites for new potential HPPs were selected and cross-compared by applying the evaluation matrix. New HPPs at the best-rated seven sites could in theory meet the *Swiss Energy Strategy* goals for 2035 in terms of an additional annual hydropower production of 1.1 TWh/a relative to 2016. The results are strongly linked to Swiss boundary conditions, but the methodology itself is generally applicable for all glaciers worldwide, as the required input data are available.

To better understand sedimentation processes and patterns like delta formation and sedimentation of fines from homopycnal, i.e. non-stratified flows, Dr. Ehrbar conducted field campaigns in three periglacial reservoirs. For the first

time, the combination of water sample analysis, LISST, and ADCP was applied systematically and successfully in periglacial reservoirs to gain profound insights into the sediment fluxes into and inside the reservoirs based on measured particle size distributions (PSD), suspended sediment concentrations (SSC) and flow velocities. Usually, ca. 80–100% of the suspended sediments in the reservoirs were found to be in the range of silt and clay, while sand portions were less than 10%. The median particle diameter is typically between 6 and 60 μm , while maximum grain diameters found in suspension were 200 μm . There was no evidence of significant changes of PSD and SSC on the horizontal plane within the reservoirs. Sediment-laden inflowing river water may lead to turbidity currents, but these hyperpycnal, i.e. stratified flows were restricted close to the inflow zones for the given reservoirs. In most parts of the reservoirs, homopycnal conditions were dominant.

To assess the long-term reservoir sedimentation under climate change Dr. Ehrbar further developed a 1D numerical model, enabling simulations of both the delta formation of coarse sediments and the lake-wide sedimentation from homopycnal flows. The model was used to assess the effects and significance of varying boundary conditions like inflow, SSC, PSD or reservoir operation. It was demonstrated that future reservoir operation and PSD are as important as future runoff evolution. Based on these findings, implications on future reservoir operation under climate change are discussed herein.

This research project is part of the National Research Programme NRP 70 “Energy Turnaround” of the Swiss National Science Foundation (SNSF). My sincere thanks go to SNSF (grant number 407040153927) for its financial support. The field work at *Gebidem* reservoir was technically supported by *Electra-Massa AG / Alpiq* and *HYDRO Exploitation SA*, who also provided bathymetry measurements as well as lake level and discharge records. The support of the operators *Forces Motrices de Mauvoisin / Azpo (Lac de Mauvoisin)* and *Ofima / Kraftwerk Aegina AG (Gries reservoir)* for enabling the field investigations at their reservoirs is greatly appreciated. Dr. Michael Döring from ZHAW Zurich University of Applied Sciences supported the ADCP measurements and gave valuable inputs on data processing, and Dr. Michael Plötze from the Institute for Geotechnical Engineering of ETH Zurich gave Dr. Ehrbar access to the geotechnical laboratory for sample analysis; I express my gratitude to both of them. Last but not least, the co-reviews of Prof. Dr. Flavio Anselmetti, Institute of Geological Sciences, University of Bern, and of Dr. Lukas Schmocker and Dr. David Vetsch, both VAW, are gratefully acknowledged.

Zürich, September 2018

Prof. Dr. Robert M. Boes

Acknowledgements

This doctoral thesis was written at the Laboratory of Hydraulics, Hydrology and Glaciology (VAW) at ETH Zurich. The project was funded by the Swiss National Science Foundation (SNSF), Project No. 153927. It is under the umbrella of the Swiss Competence Center for Energy Research – Supply of Electricity (SCCER–SoE). I would like to express my sincere gratitude to all who supported this PhD thesis:

First of all, I would like to thank my supervisor, Prof. Dr. Robert M. Boes, for giving me the opportunity to write a PhD thesis at VAW. It was a great experience; I appreciated the diversity of the research topics and methods in combination with the close proximity to practical questions, as well as the freedom to set priorities on my own. I would also like to thank my co-supervisors, Dr. Lukas Schmocker and Dr. David F. Vetsch, for advising me throughout, assisting during field measurements, improving the methodological set-up and finally editing and publishing the work.

I would like to thank our partners, above all Dr. Michael Döring (ZHAW Zurich University of Applied Sciences), who supported the field measurements and ADCP analysis. Gérald Bourban (*HYDRO Exploitation*), Marco Cortesi (*Alpiq*), Guido Köppel (*KW Aegina*), Riccardo Radogna (*Ofima*) and Johan Savioz (*Azpo*) who provided boats for the field measurements and made records of inflow, lake level and bathymetry data available, are gratefully acknowledged.

I appreciate the support from my colleagues at VAW very much: The close cooperation with Ian Delaney and countless discussions with Dr. Marius Bühlmann and Dr. Christopher Paschmann were invaluable and improved this work immensely; Dr. David Felix was a great help during the preparation of the LISST measurements. Furthermore, Prof. Dr. Martin Funk and Dr. Andreas Bauder who provided a lot of data and answered glaciological questions; Yvo Weidmann who helped processing geodata; Dr. Davide Vanzo who supported the further development of the software BASEMENT; and Eva Gerke and Stephan Kammerer who assisted using BASEMENT and QGIS and were always open to discussing research questions, methods and tools.

I would like to thank Dr. Ralf Herzog and Dr. Michael Plötze (both IGT Institute for Geotechnical Engineering, ETH Zurich) for providing access to analytical instruments in the laboratory as well as offering space in the climate chamber for sample storage. Urs Grob (Laboratory for Solid State Physics, ETH

Zurich) elucidated the physical principles behind the sophisticated measuring techniques, which allowed me to take a critical look at the field measurements and thereby improved the quality of the data analysis.

Last, but not least, I am very grateful for the constant encouragement I received from outside ETH from my family and friends; above all, from my fiancée Luzia.

Schwerzenbach, August 2018

Daniel Ehrbar

Abstract

Climate change has a manifold impact on hydropower in the periglacial environment. It offers perspectives for new hydropower plants (HPPs), but it will challenge existing HPPs by changing boundary conditions or endangering them by natural hazards (such as thawing permafrost). New HPPs will be possible when suitable reservoir locations become ice-free, what is in line with the *Swiss Energy Strategy 2050* that demands for additional electricity production from hydropower to manage the energy turnaround. Existing HPPs will benefit from additional meltwater on the short- to mid-term and thereby contribute to an increase of production, but they may have to cope with additional or disturbed sediment input and corresponding reservoir sedimentation.

There are 1576 glaciers in the Swiss Alps and 62 were identified as potentially suitable for new periglacial HPPs. An evaluation matrix was applied to rate these sites, and the most promising seven sites at *Aletsch Glacier*, *Gorner Glacier*, *Grindelwald Glacier*, *Hüfi Glacier*, *Rhône Glacier*, *Roseg Glacier*, and *Trift Glacier* were subjected to a preliminary design study. A total installed capacity of 400 MW and a total annual electricity production of 1100 GWh was estimated, which would cover the additional demand imposed by the *Swiss Energy Strategy 2050* for the year 2035.

Reservoir sedimentation is determined by sediment fluxes into and inside the reservoir. Suspended sediment transport was investigated *in situ* for three periglacial reservoirs: *Lac de Mauvoisin*, *Griessee*, and *Gebidem*, all of them located in the Swiss Canton of Valais. Particle size distributions (PSD), suspended sediment concentrations, and flow velocities were measured by means of a systematic combination of water sample analysis, laser in-situ scattering and transmissometry, and acoustic Doppler current profiler. Apart from quantitative data, it was found that homopycnal (non-stratified) conditions are dominant on reservoir scale and on the long-term.

A numerical 1D model was developed to simulate reservoir sedimentation processes. It masters challenges typically found in periglacial reservoirs, such as flow transitions (hydraulic jumps), highly unsteady boundary conditions, large range of PSD, bed and suspended load transport, strongly varying geometries, and long time periods. The model was verified for *Gebidem* reservoir, where Gilbert-type delta formation of coarse sediments as well as sedimentation from homopycnal flows were successfully captured. In subsequent scenario computations,

main links between climate change scenarios, reservoir characteristics, boundary conditions and sedimentation processes were analysed. Furthermore, the model was applied to the potential future reservoir at *Gorner Glacier*. Although sedimentation mainly affects dead storage, the importance of long-term deposition patterns—not only sedimentation volumes inside the reservoir—regarding sustainable and safe use of reservoirs could be demonstrated. The numerical model has a wide-ranging prediction potential; therefore, it can be applied to plan future reservoirs and optimize existing reservoirs to unfold the maximum sustainable hydropower potential.

Kurzfassung

Der Klimawandel hat vielfältige Auswirkungen auf die Wasserkraft im periglazialen Umfeld. Einerseits ergeben sich Chancen für neue Wasserkraftanlagen, andererseits werden bestehende Anlagen mit neuen Herausforderungen konfrontiert, wie z.B. sich ändernde Randbedingungen oder neue Naturgefahren (z.B. auftauender Permafrost). Zwei Entwicklungen begünstigen neue Wasserkraftanlagen, nämlich erstens der Gletscherrückzug, welcher attraktive Standorte für Speicherseen freigibt, und zweitens die Schweizer *Energiestrategie 2050*, welche einen Ausbau der Wasserkraft fordert, um die Energiewende zu bewältigen. Bestehende Anlagen profitieren kurz- bis mittelfristig von höheren Zuflüssen, welche zu einer Produktionssteigerung führen können, doch sie müssen auch mit veränderten Sedimenteinträgen und damit verbundener Stauraumverlandung rechnen.

Von 1576 Gletschern in den Schweizer Alpen sind 62 grundsätzlich geeignet für neue Wasserkraftanlagen. Mit einer Bewertungsmatrix wurden die einzelnen Standorte miteinander verglichen und die am besten bewerteten sieben Standorte *Aletschgletscher*, *Gornergletscher*, *Gründelwaldgletscher*, *Hüfigletscher*, *Rhonegletscher*, *Roseggletscher* und *Triftgletscher* einer Machbarkeitsstudie unterworfen. Die gesamte installierte Leistung beläuft sich auf ca. 400 MW und die jährliche Energieproduktion auf 1100 GWh, was das Defizit decken würde, welches aufgrund der *Energiestrategie 2050* für 2035 anvisiert wird.

Stauraumverlandung ist eine Funktion des Sedimenttransports in den, innerhalb und aus dem Stausee. Der Schwebstofftransport in den drei periglazialen Stauseen *Lac de Mauvoisin*, *Griessee* und *Gebidem* im Schweizer Kanton Wallis wurde mit einer systematischen Kombination aus Wasserproben-Analyse, Laser in-situ scattering and transmissometry (LISST) und acoustic Doppler current profiler (ADCP) untersucht. Dabei wurden Korngrößenverteilungen, Schwebstoffkonzentrationen und Fliessgeschwindigkeiten gemessen. Neben quantitativen Daten wurde festgestellt, dass grossräumig und langfristig homopycnale Verhältnisse, d.h. nicht-geschichtete Strömungen, dominant sind.

Mit dieser Datengrundlage konnte ein numerisches 1D Modell entwickelt werden, welches die Stauraumverlandung abbilden kann. Das Modell bewältigt typische Herausforderungen wie Fliesswechsel (Wechselsprung), instationäre Randbedingungen, breite Korngrößenverteilungen, kombinierter Geschiebe- und Schwebstofftransport, variable Geometrien und lange Simulationszeiträume,

welche bei periglazialen Stauseen beachtet werden müssen. Das Modell wurde am Beispiel *Gebidem* verifiziert, wo sowohl Deltabildung als auch homopycnale Ablagerungen auftreten. In nachfolgenden Szenariorechnungen wurden bedeutende Zusammenhänge zwischen Klimawandel, Eigenschaften des Stausees, Randbedingungen und Sedimenttransportprozessen analysiert. Zudem wurde das Modell für einen potentiellen zukünftigen Stausee am *Gornergletscher* angewendet. Obwohl die Verlandung hauptsächlich den Totraum eines Stausees betrifft, sind die langfristigen Ablagerungsmuster – und nicht nur die absoluten Ablagerungsvolumina – von grosser Bedeutung, um die nachhaltige Nutzung des Stausees sicherzustellen. Das numerische Modell hat eine hohe Prognosequalität und kann eingesetzt werden, um zukünftige Anlagen zu planen und existierende Anlagen zu optimieren, damit die periglaziale Wasserkraft ihr volles Potential entfalten kann.

Contents

Preface	i
Acknowledgements	iii
Abstract	v
Kurzfassung	vii
Contents	ix
List of Figures	xiii
List of Tables	xv
1 Introduction	1
1.1 Motivation	1
1.2 Objectives	3
1.3 Outline	5
2 Literature review	7
2.1 Climate change	7
2.1.1 Climate change on a global scale	7
2.1.2 Climate change in Switzerland	8
2.1.3 Impacts on Swiss glaciers	9
2.1.4 Perspectives for Swiss periglacial hydropower	11
2.2 Reservoir sedimentation	15
2.2.1 Periglacial sediment yield	15
2.2.2 Sediment transport in reservoirs	19
2.2.3 Reservoir sedimentation problems	21
2.2.4 Reservoir sedimentation in Switzerland	22
2.2.5 Delta formation	27
2.2.6 Sedimentation from homopycnal flows	28

2.2.7	Turbidity currents	29
2.3	Suspended sediment and flow velocity measurement techniques	33
2.3.1	Secchi disk	35
2.3.2	Water sample analysis (Niskin bottle sampler)	36
2.3.3	Laser in-situ scattering and transmissometry (LISST)	36
2.3.4	Acoustic Doppler current profiler (ADCP)	43
2.3.5	Comparison of measuring techniques	54
2.4	Mathematical and numerical reservoir sedimentation models	55
2.4.1	Delta formation	55
2.4.2	Turbidity currents	58
2.4.3	Reservoir-scale sediment transport models	64
3	Swiss periglacial hydropower potential	69
3.1	Introduction	69
3.1.1	Swiss Energy Strategy 2050	69
3.1.2	Previous studies	70
3.2	Methods	72
3.2.1	Site selection	72
3.2.2	Site rating criteria	73
3.2.3	Evaluation matrix	79
3.3	Results	79
3.3.1	Best-rated potential HPPs	79
3.3.2	Technical potential	86
3.3.3	Feasibility	87
3.4	Discussion	87
3.4.1	Upgrade projects	87
3.4.2	Uncertainties	88
3.4.3	Challenges	88
3.4.4	Reservoir sedimentation	91
3.4.5	Layout of the HPP schemes	92
3.4.6	Comparison with previous studies	93
3.5	Conclusions	95
4	Field measurements	99
4.1	Introduction	99
4.2	Methods	100
4.2.1	Prototypes	100
4.2.2	Measurement techniques	105
4.2.3	Field measurements	108
4.3	Results	109
4.3.1	Secchi disk measurements	109

4.3.2	Water sample analysis	109
4.3.3	LISST measurements	109
4.3.4	ADCP measurements	126
4.4	Discussion	135
4.4.1	Secchi disk measurements	135
4.4.2	Water sample analysis	135
4.4.3	LISST measurements	137
4.4.4	ADCP measurements	139
4.5	Conclusions	142
4.5.1	Summary	142
4.5.2	Main findings	143
5	Numerical modelling	147
5.1	Introduction	147
5.2	Scope of application	147
5.3	Mathematical and numerical model	149
5.3.1	Introduction	149
5.3.2	Governing flow equations	149
5.3.3	Governing sediment transport equations	152
5.4	Model verification	158
5.4.1	Test case selection	158
5.4.2	Test case set-up	158
5.4.3	Calibration	161
5.4.4	Validation	165
5.5	Scenario simulations	170
5.5.1	Sensitivity of boundary conditions at Gebidem	170
5.5.2	Potential future reservoir at Gerner Glacier	171
5.6	Discussion	177
5.6.1	Numerical and mathematical model	177
5.6.2	Governing processes	179
5.6.3	Boundary conditions	180
5.7	Conclusions	181
6	Conclusions	187
6.1	Summary	187
6.2	Recommendations for future research	189
	Nomenclature	191
	Bibliography	195
	Curriculum vitae	231

List of Figures

1	<i>Undre Triftchessel</i> and <i>Trift Glacier</i> in 2004 and 2014	2
2	Historical and projected future radiative forcings for scenarios . . .	9
3	Sketch of a Gilbert-type delta and a plunging turbidity current . .	20
4	Infill times of selected Swiss alpine reservoirs	23
5	Delta evolution in <i>Gebidem</i> from 2014 to 2015	25
6	Sedimentation patterns in reservoirs	30
7	Secchi disk and Niskin bottle sampler	36
8	Laser in-situ scattering and transmissometry <i>100X Type C</i>	38
9	Principles of LISST measurements	39
10	Absorption coefficients for electromagnetic waves in water	40
11	Principles of acoustic Doppler current profiler measurements . . .	44
12	Simplified attenuation values of sound in water	46
13	Comparison of different measuring techniques	56
14	Layouts of HPPs <i>Aletsch</i> , <i>Gorner</i> , <i>Grindelwald</i> and <i>Rhône Glacier</i>	83
15	Layouts of HPPs <i>Hüfi</i> and <i>Roseg Glacier</i>	85
16	Sketch of the eastern part of the <i>Grande Dixence</i> scheme	90
17	<i>Lac de Mauvoisin</i> on 11/08/2015 near the inflow	101
18	Sedimentation pattern in empty <i>Griessee</i> on 02/07/2015	103
19	Catchment of <i>Gebidem</i> reservoir on 13/08/2016	104
20	PSD in <i>Lac de Mauvoisin</i> – water samples, 11/08/2015	110
21	PSD in <i>Griessee</i> – water samples, 18/08/2015	110
22	PSD in <i>Griessee</i> – water samples, 01/10/2015	111
23	PSD in <i>Griessee</i> – water samples, 08/08/2016	111
24	PSD in <i>Gebidem</i> – water samples, 06/10/2015	112
25	Location of LISST profiles in <i>Lac de Mauvoisin</i>	112
26	d_{50} in <i>Lac de Mauvoisin</i> – LISST, 11/08/2015	113
27	SSC in <i>Lac de Mauvoisin</i> – LISST, 11/08/2015	116
28	PSD ($h < 20m$) of <i>Lac de Mauvoisin</i> – LISST, 11/08/2015	117

29	PSD ($h > 20m$) of <i>Lac de Mauvoisin</i> – LISST, 11/08/2015	118
30	Location of LISST profiles in <i>Griessee</i>	119
31	Location of LISST profiles in <i>Gebidem</i>	119
32	d_{50} in <i>Griessee</i> – LISST, 18/08/2015	121
33	SSC in <i>Griessee</i> – LISST, 18/08/2015	122
34	PSD ($h < 20m$) of <i>Griessee</i> – LISST, 18/08/2015	123
35	d_{50} in <i>Griessee</i> – LISST, 08/08/2016	124
36	SSC in <i>Griessee</i> – LISST, 08/08/2016	125
37	PSD ($h < 20m$) of <i>Griessee</i> – LISST, 08/08/2016	127
38	d_{50} in <i>Gebidem</i> – LISST, 06/10/2015	128
39	SSC in <i>Gebidem</i> – LISST, 06/10/2015	129
40	PSD ($h < 20m$) of <i>Gebidem</i> – LISST, 06/10/2015	130
41	PSD ($h > 20m$) of <i>Gebidem</i> – LISST, 06/10/2015	131
42	Flow velocities in <i>Griessee</i> – ADCP, 18/08/2015	133
43	SNR in <i>Griessee</i> – ADCP, 18/08/2015	133
44	Flow velocities in <i>Griessee</i> – ADCP, 08/08/2016	134
45	SNR in <i>Griessee</i> – ADCP, 08/08/2016	134
46	Two-way-transmission losses according to Moore (2011)	141
47	Nomenclature in the numerical 1D model	150
48	Nomenclature for the <i>QUICKEST</i> scheme	156
49	Geometry of the cross sections of <i>Gebidem</i> reservoir	160
50	Sketch of the <i>Gebidem</i> test case	160
51	Composite PSD of the sediment discharge into <i>Gebidem</i>	162
52	Measured inflow into <i>Gebidem</i> reservoir and lake level in 2015	162
53	Results of <i>Gebidem</i> test case for the calibration	166
54	SSC in <i>Gebidem</i> in the calibration period	167
55	Measured inflow into <i>Gebidem</i> reservoir and lake level in 2014	167
56	Results of <i>Gebidem</i> test case for the validation	169
57	Daily-avg. inflow and monthly-avg. lake levels for <i>Gebidem</i>	172
58	Results of <i>Gebidem</i> calibration for monthly-averaged lake levels	173
59	Geometry of the cross sections of <i>Gorner Glacier</i> reservoir	175
60	Inflow and lake level of <i>Gorner Glacier</i> 2030–2039	175
61	Simulation results of <i>Gorner Glacier</i> reservoir	176
62	Long-term simulation results of <i>Gorner Glacier</i> reservoir	178
63	Links of periglacial reservoir sedimentation	185

List of Tables

1	Temperature and precipitation changes in Switzerland 2070–2100	10
2	Annual runoff changes from glacierized catchments in the Alps	12
3	Summer runoff changes from glacierized catchments in the Alps	12
4	Turbidity currents in Switzerland (with density excess)	33
5	Selected field applications of LISST technology	41
6	Selected field applications of ADCP technology	52
7	Evaluation matrix applied to rate potential HPPs	74
8	Best-scored potential future HPPs in the periglacial environment	80
9	Sedimentation volumes and infill times of the new HPPs	92
10	Potential future HPPs proposed in previous studies	94
11	Characteristics of investigated reservoirs	105
12	Secchi depths measured in three periglacial reservoirs	114
13	Summary of 15 water sample analyses from the inflowing rivers	115
14	Summary of 69 water sample analyses from the reservoirs	115
15	Discretisation of the composite PSD of <i>Gebidem</i>	164

1 Introduction

1.1 Motivation

At present, most economically feasible hydropower potential in Switzerland is being exploited. In future, due to the retreat of glaciers, new potential sites will develop in the so-called periglacial¹ environment of the Swiss Alps. The basin of *Undre Triftchessel* (Figure 1) outlines the scope of this thesis excellently. The *Trift Glacier* used to cover the whole basin, but it has been retreating since the Little Ice Age. In 1929, it had an ice volume of 1.9 km³ (Farinotti *et al.* 2012); in 2010, it was reduced to 1.2 km³. By 2100, it is likely that there will be no ice left. Climate change and the corresponding atmospheric warming are main drivers of glacier retreat (IPCC 2013). Their impacts on Swiss glacier have been studied by many researchers, for example, Huss *et al.* (2008b), Jouvett *et al.* (2011), Farinotti *et al.* (2012), Uhlmann *et al.* (2013), and others.

At the turn of the millennium, a natural lake with a volume of 16 hm³ started to form at *Undre Triftchessel*. Several new lakes are expected to form at the terminus of many alpine glaciers (Haeberli *et al.* 2013). This offers new perspectives for hydropower in the periglacial environment. Glacier meltdown will release additional water, which has been stored as ice and can now be used for energy production. At *Trift Glacier*, *Kraftwerke Oberhasli AG (KWO)* is planning to use this water for additional power production by means of a new reservoir. Climate change does not only affect glaciers, but the whole runoff regime because of changing precipitation patterns. Again, several studies addressed this question, for example, Westaway (2000), Schaeffli *et al.* (2007), SGHL & CHy (2011), and others. Both changing glacial meltwater and precipitation determine future runoff from glaciated catchment.

Figure 1 shows not only the remarkable retreat of *Trift Glacier* within ten years, but also the evolution of the proglacial area. The area in front of the glacier is not yet covered with vegetation; it is bare, unconsolidated ground that can easily be eroded (Geilhausen *et al.* 2013). The color of *Trift Lake* indicates the presence of suspended sediments in the water. They originate from erosion of hillslopes (supraglacial erosion), underneath the glacier (subglacial erosion), and

¹ the term “periglacial environment” will be used for catchments with a significant degree of glaciation, that is, more than 30%, following Hallet *et al.* (1996) (Section 2.2.1)



Figure 1: *Undre Triftchessel* and *Trift Glacier* on 30 June 2004 (left) and 3 July 2014 (right) [Images from VAW ETH Zürich]

glacier forefield (proglacial erosion) (Guillon 2016). The sediment input of these three different sources depends on various factors. Consequently, climate change affects both water discharge and sediment conveyance from the periglacial environment. This link has been identified and studied by several researchers, for example, Clifford *et al.* (1995), Stott and Mount (2007), Raymond Pralong *et al.* (2015), and others. Whereas additional water discharge may be a benefit for hydropower, additional sediment input would most likely have negative impacts on construction, operation and maintenance of hydropower schemes. For the time being, there is no general answer to the question whether climate change will lead to increased sediment discharge or not.

Especially reservoir sedimentation starts to attract attention. Auel and Boes (2012) showed that, on a global scale, net reservoir volume is currently decreasing, because the sedimentation rate is growing faster than new storage is installed. Schleiss *et al.* (2010) estimated that 80% of Asia's storage volume will be lost due to reservoir sedimentation by 2035. In Switzerland, sedimentation rates are not as distinct. Nevertheless, changing sedimentation patterns that are likely linked to climate change have been observed in some reservoirs.

Hydropower potential and reservoir sedimentation in the periglacial environment under climate change are the subject of this research project. It is integrated into the National Research Programme 70 “Energy Turnaround”², which has been launched against the backdrop of the Swiss *Energy Strategy 2050*. Climate change will be an important driver in the changeover to a new energy system. Firstly, new hydropower potential in the periglacial will develop; secondly, storage of existing hydropower plants (HPPs) will be affected by reservoir sedimentation, which is closely linked to climate conditions. This project provides information for strategic decisions in the hydropower sector on the mid- to long-term, and it covers research for the further development of HPPs and existing infrastructure under changing conditions.

1.2 Objectives

In 2017, the annual electricity production from hydropower in Switzerland reached ca. 36.3 TWh. In 2035, the Swiss *Energy Strategy 2050* anticipates 37.4 TWh of annual electricity production. Therefore, a further annual potential of ca. 1.1 TWh needs to be exploited until then as an interim target. The long-term goal for 2050 amounts to an annual production increase of up to some 3.16 TWh under optimized boundary conditions compared to the reference state on 1 January 2012 BFE (2012). As the latter amounted to 35.8 TWh, the total annual production in 2050 would therefore be roughly 39.0 TWh in the best-case scenario of BFE (2012). Therefore, the first project phase aimed at identifying hydropower potential in the periglacial environment. Runoff volume projections are available for all Swiss glacier catchments for different climate change scenarios. Based on these data sets, potential future sites were identified, rated and compared against each other. Most promising sites were analysed further. Main research questions of the first phase “Swiss periglacial hydropower potential” were:

1. How can the periglacial hydropower potential be enhanced?
2. Which sites and schemes are suitable for future HPPs?
3. How many new HPPs would be needed to exploit the gap until 2035?
4. What are the main challenges at the individual sites and in general?
5. Which course of action should be pushed further?

² <http://www.nfp70.ch/en/Pages/Home.aspx>

Both future and existing reservoirs will be subject to reservoir sedimentation. Various problems are attributed to reservoir sedimentation, such as, decrease of volume and corresponding loss of storage for energy production, blockage of outlet structures, turbine abrasion or negative impacts on downstream morphology and ecology. Reservoir sedimentation is controlled by sediment fluxes into, inside, and out of the reservoir. Field data from measurements of particle size distribution (PSD) or suspended sediment concentration (SSC) is relatively sparse for periglacial reservoirs in the Swiss Alps. For the first time, sediment fluxes in periglacial reservoirs were studied with a systematic combination of water sample analysis, LISST and ADCP as well as Secchi disk measurements. Main research questions of the second phase “field measurements” were:

6. What are characteristic PSD and SSC in periglacial reservoirs?
7. Are there significant changes of PSD and SSC within a reservoir?
8. How large are differences of PSD and SSC between individual reservoirs?
9. What are the application ranges and limitations of LISST and ADCP?
10. Which are the governing transport processes in periglacial reservoirs?

The third project phase was dedicated to the numerical modelling of reservoir sedimentation. Emphasis was put on the long-term simulations on reservoir scale, so that a 1D model was set up. The numerical model must be able to capture two different sedimentation processes: the formation of a Gilbert-type delta with coarse grains (sand and gravel) and the sedimentation of fine grains (clay and silt) from homopycnal (non-stratified) flows. The main research questions of the third phase “numerical modelling” were:

11. Can delta formation be modelled with a depth-averaged 1D model?
12. Is it also possible to capture homopycnal sedimentation in this framework?
13. Which are governing parameters and processes of reservoir sedimentation?
14. Is the model generally applicable for arbitrary, highly unsteady boundary and initial conditions?
15. How does climate change affect reservoir sedimentation?

1.3 Outline

This thesis is divided into four major parts. In Chapter 2, a literature review is given. The vast amount of literature on climate change, measurement techniques and numerical modelling required a deliberate selection. Chapter 3 shows the hydropower potential in the periglacial environment of Switzerland. Best-suited sites are investigated more in detail and their electricity production is estimated. In Chapter 4, the field measurements are described. Results are shown and interpreted with regards to the numerical modelling. The field measurements have already been documented in (Ehrbar *et al.* 2017). In Chapter 5, the numerical modelling is documented. The calibration and validation of the prototype chosen for a proof of concept, as well as applications of the model regarding impacts of climate change on both existing and future reservoirs are shown. The conclusions of the whole project and an outlook on future research are given in Chapter 6.

2 Literature review

2.1 Climate change

2.1.1 Climate change on a global scale

Observations of climate change are reported in detail in IPCC (2013). Since 1880, the average global surface temperature has risen by 0.85 °C. Human influence is “extremely likely” to be the dominant cause of the observed warming. An obvious impact of atmospheric warming is the shrinking of glaciers. Global rates of ice loss are 275 Gt/a for glaciers, 215 Gt/a for the Greenland ice sheet and 147 Gt/a for the Antarctic ice sheet. Corresponding sea level rises are 0.76 mm/a (contribution from glaciers), 0.33 mm/a (contribution from Greenland ice sheet) and 0.27 mm/a (contribution from Antarctic ice sheet), which is 1.36 mm/a in total. Another important impact of atmospheric warming is the change in extreme weather and climate events that has been observed since about 1950. The number of cold days and nights has decreased, whereas the number of warm days and nights has increased. However, these impacts vary significantly on regional scales.

Different representative concentration pathways (RCP) allow predictions of the impacts of atmospheric warming. RCP are spatially resolved data sets of land use changes and emissions of air pollutants. They do not explicitly account for demographic and economic development, energy production and use, technology or other factors, but simply specify overall concentrations of greenhouse gases and corresponding anthropogenic emissions up to 2100. They are expressed in terms of radiative forcing³ in 2100 compared to 1750. The radiative forcing can have both anthropogenic and natural causes like, for example, volcanoes (Sigl *et al.* 2015). Large eruptions, like *Laki* in Iceland in 1783 or *Mount Tambora* in Indonesia in 1815, had huge impacts on radiative forcing and short-term climate, respectively (Figure 2). The eruption of *Mount Tambora* led to a drop in global mean temperature of 0.5–1 °C and was a major reason for the 1816 “year without a summer” in Switzerland (Rössler and Brönnimann 2018). Three main RCPs developed by IPCC (2013) are shown in Figure 2. RCP2.6 is a mitigation scenario, RCP4.5 is a stabilisation scenario and RCP8.5 is a non-intervention

³ radiative forcing is defined as the change in net downward heat flux at the tropopause

scenario. For RCP2.6, radiative forcing will peak at 2.6 W/m^2 around 2050 and later decline to 2.3 W/m^2 until 2100. For RCP4.5, radiative forcing will stabilize by 2100 at 4 W/m^2 ; for RCP8.5, radiative forcing does not peak by 2100 but increases further. Global mean surface temperature changes and global mean sea level rises can be attributed to these RCPs. They are usually compared to the “reference period” of 1986–2005, which is already affected by climate change; that is, global mean surface temperature has already changed by $0.61 \text{ }^\circ\text{C}$ between the “pre-industrial level” 1850–1900 and the “reference period” 1986–2005. Global mean surface temperature change at the end of the 21st century is likely⁴ $0.3\text{--}1.7 \text{ }^\circ\text{C}$ for RCP2.6, $1.1\text{--}2.6 \text{ }^\circ\text{C}$ for RCP4.5 and $2.6\text{--}4.8 \text{ }^\circ\text{C}$ for RCP8.5, compared to 1986–2005. Corresponding global mean sea level rises are $0.26\text{--}0.55 \text{ m}$, $0.32\text{--}0.63 \text{ m}$ and $0.45\text{--}0.82 \text{ m}$.

In the past, scenario SRES-A1B⁵ from IPCC (2007) was widely used. It is a non-intervention scenario that assumes that total radiative forcing will continue to increase until 2100, when it reaches a maximum of 6 W/m^2 . Relative to the average from 1850–1900, global mean surface temperature change is likely in the range $2.57\text{--}3.66 \text{ }^\circ\text{C}$. By the end of the 21st century, global glacier volume will likely decrease by 30–78% compared to the 1986–2005 reference period. Mean global sea level would rise $0.37\text{--}0.69 \text{ m}$ relative to 1986–2005. SRES-A1B and RCP2.6, RCP4.5 as well as RCP8.5 are shown in Figure 2.

Scenario RCP2.6 can be seen as the best case, whereas SRES-A1B and RCP8.5 are worst cases. All scenarios are feasible, given the current political situation, where mitigation measures are intensively discussed on a global level. RCP2.6 would require strong actions which seem not realistic for the time being.

2.1.2 Climate change in Switzerland

Since the end of the Little Ice Age (ca. 1864), average annual temperature in Switzerland has risen by more than $1.8 \text{ }^\circ\text{C}$. Due to this atmospheric warming, the glacier area was reduced from 1300 km^2 to 940 km^2 (-28%) between 1973 and 2010 (SCNAT 2016). For the SRES-A1B scenario, Swiss glaciers will cover only ca. 300 km^2 at the end of the century (SGHL & CHy 2011). Impacts of climate change in general were studied by CH2011 (2011). The non-intervention scenarios SRES-A2 and SRES-A1B as well as the climate stabilisation scenario RCP2.6 scenarios were applied to the three main geographical regions of Switzerland: north-east, west and south of the Alps. The highly complex climate of the central Alps was excluded in this study. The reference period of this study is 1980–2009. Increases of seasonal mean temperature for 2070–

⁴ in IPCC (2013), “likely” is attributed to a probability of 66–100%

⁵ SRES stands for Special Report on Emissions Scenarios

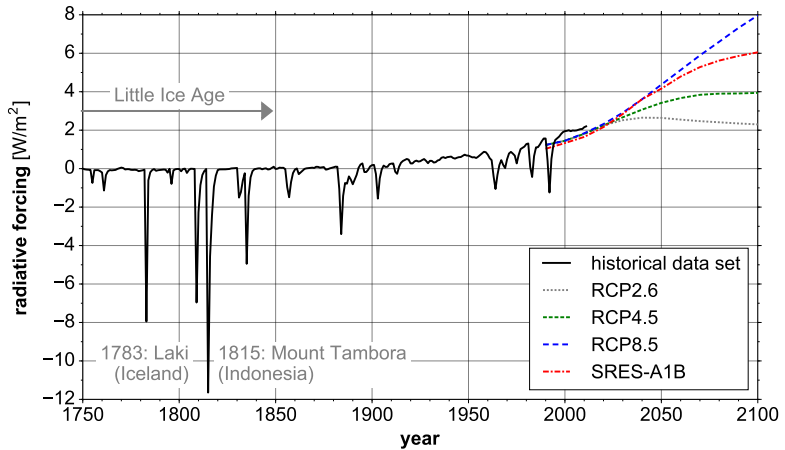


Figure 2: Historical and projected future radiative forcings for different climate change scenarios according to IPCC (2013)

2099 are 3.2–4.8 °C for SRES-A2, 2.7–4.1 °C for SRES-A1B and 1.2–1.8 °C for RCP2.6. Seasonal precipitation changes in 2070–2099 are expected in the range of –28 to +23% (SRES-A2), –24 to +20% (SRES-A1B) and –10 to +8% (RCP2.6). Uncertainties are in the range of 1 °C (temperature) and 15% (precipitation), respectively. Table 1 shows the predicted changes in SRES-A1B scenario for each season: winter (December–February), spring (March–May), summer (June–August) and autumn (September–November).

2.1.3 Impacts on Swiss glaciers

BAFU (2012) examined the impacts of climate change on glaciers, snow, runoff and water temperature in general. SRES-A1B scenario was used. Glacier volume loss will be 60–80% until the end of the century compared to the present. Snow melt proportion of runoff out of Switzerland will decline from 40% in 1980–2009 to 25% in 2085. Summer precipitation will decrease by 20% compared to 1980–2009 (as predicted by CH2011 (2011) as well), but it will increase in the rest of the year. Salzmann *et al.* (2012) applied a RCP2.6-like scenario to 101 glaciers in the Swiss Alps, which limits global warming to 2 °C compared to 1970. They found that glacier-based hydrological runoff in 2100 will be reduced by 65–70% relative to present.

Table 1: Projected future temperature and precipitation changes in Switzerland in 2070–2099 for SRES-A1B scenario with reference to 1980–2009 (CH2011 2011)

region	temperature change [°C]				precipitation change [%]			
	winter	spring	summer	autumn	winter	spring	summer	autumn
north-east	3.12	2.77	3.74	3.16	2.9	5.8	−18.4	−0.1
west	3.10	2.71	3.83	3.18	4.4	0.9	−23.6	−3.2
south	3.28	3.13	4.14	3.27	19.5	−8.6	−23.2	−3.2

VAW (2011) and Farinotti *et al.* (2012) examined runoff from nine high-alpine catchments (*Aletsch*, *Morteratsch*, *Silvretta*, *Gorner*, *Mattmark*, *Rhône*, *Trift*, *Findelen* and *Gries*) in detail. They used scenarios with an atmospheric warming of 2.2–5.2 °C. Annual precipitation is expected to decrease by about 5% in south-Alpine catchments, but it will remain constant in inner-Alpine regions. They recognized a general pattern, valid in all catchments: in a first phase, annual discharge increases, followed by a second phase, where annual discharge decreases. The transition from glacial and glacio-nival regimes to nival regimes depends on (i) the degree of catchment glaciation; (ii) total ice volume present today; and (iii) distribution of glacier ice with altitude. Maximum daily discharge is 4.4 days earlier each decade. Maximum annual discharge occurs before 2050 in all catchments. Yearly precipitation and annual runoff correlate for catchments with glaciation of less than 40%; above, there is no correlation. Huss *et al.* (2008a) examined four glaciers in the Swiss Alps (*Aletsch Glacier*, *Rhône Glacier*, *Gries Glacier* and *Silvretta Glacier*) and concluded that, although being situated relatively close to each other, large differences between neighbouring glaciers make individual studies on each glacier indispensable.

There is a large set of studies on glacier change in Switzerland. However, they are hardly comparable as the underlying model concepts and input data differ significantly, as stated by Pellicciotti *et al.* (2014). Huss *et al.* (2014) showed that even for the single catchment of *Findelen Glacier*, the runoff change can be positive or negative, depending on the climate change scenario and glacio-hydrological model. Gabbi *et al.* (2012) examined impacts of climate change on glaciers in the *Lac de Mauvoisin* catchment. They predicted a reduction of daily runoff and a shift of peak runoff from summer to spring. The evolution of *Aletsch Glacier* (with *Oberaletsch Glacier* and *Mittelaletsch Glacier* included) was examined for different climate change scenarios by Juvet *et al.* (2011). The largest glacier in the Alps will lose at least 70% of its ice volume for all scenarios

(e.g. 90% if a SRES-A1B scenario is applied). Huss *et al.* (2008b) examined *Zinal Glacier*, *Moming Glacier* and *Weisshorn Glacier*, using their own climate change scenarios, which allow to investigate glacier response more in detail. They came to the same conclusion as Farinotti *et al.* (2012): By the end of the century, runoff will significantly decrease in the summer months, whereas it will increase in autumn and particularly in spring. The runoff evolution of *Findelen Glacier* was investigated in detail by Uhlmann *et al.* (2013) and Huss *et al.* (2014).

2.1.4 Perspectives for Swiss periglacial hydropower

2.1.4.1 Water discharge

Farinotti *et al.* (2016) examined the runoff contribution of glaciers in the European Alps on macroscale catchments (*Rhône* at *Chancy*, *Inn* at *Innsbruck*, *Po* at *Pontelagoscuro* and *Rhine* at *Basel*). Today, even large low-lying rivers have a significant runoff-share from glaciated catchment: in the case of *Rhône* at *Chancy*, 53% of the runoff in the summer months originate from glaciers; on the annual average, the share is 15%. They computed runoff changes for the three climate change scenarios RCP2.6, RCP4.5 and RCP8.5. The results can be found in Tables 2 and 3. Today, the total annual runoff from glaciated catchments in the Swiss Alps is $5.28 \pm 0.48 \text{ km}^3$, of which $3.97 \pm 0.36 \text{ km}^3$ occur in summer (July–September). The confidence intervals refer to the 95% level. By the end of this century, annual runoff will decrease by 13–17% for all chosen scenarios compared to 1980–2009. Summer runoff will decrease even larger by 29–55%. The authors claimed that precipitation changes are significantly lower than the runoff changes induced by melting glaciers.

Addor *et al.* (2014) modelled discharge by the end of the 21st century for six mesoscale catchments (*Rhône* at *Brig*, *Vorderrhein* at *Ilanz*, *Verzasca* at *Lavertezzo*, *Emme* at *Wiler*, *Thur* at *Andelfingen* and *Venoge* at *Ecublens*). They applied the three emission scenarios SRES-A1B, RCP2.6 and SRES-A2. Three hydrological models and two post-processing methods were applied. Their main findings were:

1. Summer peak discharge will most likely be lower (“damping”);
2. Spring-summer peak discharge will likely occur earlier in the season (“shifting”);
3. Winter discharges will likely be higher (“flattening”).

These impacts are quite robust. They are significantly reduced if the stringent emission policy of RCP2.6 is applied.

Table 2: Projected changes in total annual runoff from glacierized catchments in the European Alps with reference to 1980–2009 for three different climate change scenarios; confidence intervals refer to the 95% level (Farinotti *et al.* 2016) (V_w is the change in absolute runoff volume; and ΔV_w is the relative change in runoff volume compared to 1980–2009)

period	RCP2.6		RCP4.5		RCP8.5	
	V_w [km ³]	ΔV_w [%]	V_w [km ³]	ΔV_w [%]	V_w [km ³]	ΔV_w [%]
2010–2039	+1.00±0.74	+18	+1.05±0.75	+19	+1.14±0.76	+21
2040–2069	-0.10±0.69	-1	+0.05±0.74	0	+0.32±0.80	+6
2070–2099	-0.74±0.62	-14	-0.73±0.67	-13	-0.93±0.89	-17

Table 3: Projected changes in summer runoff (July–September) from glacierized catchments in the European Alps with reference to 1980–2009 for three different climate change scenarios; confidence intervals refer to the 95% level (Farinotti *et al.* 2016) (V_w is the change in absolute runoff volume; and ΔV_w is the relative change in runoff volume compared to 1980–2009)

period	RCP2.6		RCP4.5		RCP8.5	
	V_w [km ³]	ΔV_w [%]	V_w [km ³]	ΔV_w [%]	V_w [km ³]	ΔV_w [%]
2010–2039	+0.55±0.56	+13	+0.61±0.58	+15	+0.60±0.59	+15
2040–2069	-0.61±0.53	-15	+0.64±0.58	+16	+0.62±0.63	+15
2070–2099	-1.16±0.48	-29	-1.48±0.53	-37	-2.21±0.71	-55

SGHL & CHy (2011) examined the impacts of climate change on Swiss hydropower for microscale catchments. Case studies for *Kraftwerke Oberhasli AG (KWO)*, *Kraftwerk Mattmark*, *Gougra SA*, *KW Prättigau*, *Speicherkraftwerk Löntsch* and *Speicherkraftwerk Göschenen* showed that there are large differences between individual HPPs. In general, there will be only minor changes in 2021–2050 with slightly decreasing energy production in southern and eastern Valais and increasing energy production in the central and eastern Swiss Alps. In 2070–2099, a production loss of 4–8% relative to the reference period (1980–2009)

in southern and eastern Valais is expected, with a band width of 0–20%. The runoff shift from summer to winter (reduced discharge in summer, increased discharge in winter) will positively affect energy production, because more water can be stored, thereby increasing production.

Westaway (2000) conducted a case study of *Grande Dixence*. An average temperature increase of 1.4 °C and an annual precipitation increase of 2.6% would lead to an annual inflow increase of 26%.

Schaeffli *et al.* (2007) examined *Lac de Mauvoisin* in another case study. By assuming a mean global warming of 2.6 °C, they computed a decrease of hydropower production of 36% in 2070–2099 compared to 1961–1990. The modification of the hydrological regime results in a production shift of about 7% from winter to summer. The authors assumed uncertainties in their prediction of hydropower production to be in the same order as the uncertainties regarding the global warming prediction itself. So far, there is no general answer to the question of how water discharge will evolve for every reservoir in Switzerland.

Although the scenarios applied by Schaeffli *et al.* (2007) and Westaway (2000) cannot be compared directly, these two investigations show that atmospheric warming might lead to significant changes in discharge which are depending on individual catchment characteristics.

2.1.4.2 Sediment discharge

Raymond Pralong *et al.* (2015) investigated the impacts of climate change scenario SRES-A1B on bed load transport and conveyance into Alpine reservoirs. In the time frame 2021–2050, 13 out of 64 streams will have reduced bed load transport, 9 will have increased bed load transport and 42 will hardly be affected. In the time frame of 2070–2099, 38 streams will have reduced bed load transport, 10 will have increased bed load transport and 16 will not show significant differences to the present level. The general trend is towards less bed load transport. As for water discharge, there will likely be a shift of seasonal sediment transport dynamics: maximum transport will take place from May–July instead of July–September. In October and November, bed load transport will increase compared to today. The study assumed that sediment availability is equal or larger than transport capacity of the corresponding stream. This was considered plausible, given that glacier retreat and permafrost melt will likely increase sediment availability. Kammerlander *et al.* (2017) found that average annual bed load transport rate correlates significantly with the size of the catchment and the degree of glaciation; the former correlation is linear, the latter exponential. They showed that transport efficiency changes significantly throughout the years; that is, transport efficiency is higher in dry years than in wet years.

In the ablation seasons of 2003 and 2004, Stott and Mount (2007) measured SSC in *Torrent du Glacier Noir* (French Alps). Mean daily air temperature was 1.2 °C higher in 2003 than in 2004, and mean daily discharge was 2.3 times higher. In the authors' view, measurements in 2003 can be regarded as an example of "future climate" with significantly warmer temperatures than present. Suspended sediment load was 3.1–4.1 times higher in 2003 than in 2004. The authors concluded that a significant increase of suspended sediment input into reservoirs is likely, if atmospheric warming continues. Costa *et al.* (2018b) demonstrated that climate-driven changes have strong impact on SSC in the *Rhône* catchment. The changes in SSC were not consistent with changes in discharge and transport capacity, thus it was not possible to conclude if sediment fluxes will increase or decrease in future.

Glacier retreat affects the forefield evolution. The area just in front of the glacier is usually not covered with vegetation. Therefore, bare, unconsolidated soil can easily be eroded. Glacier retreat will likely lead to a general increase in bare forefield area, until vegetation has caught up (Geilhausen *et al.* 2013). As sediment yield is sensitive to vegetation cover in the catchment (Morris *et al.* 2008), the whole catchment evolution has to be taken into account when assessing future sediment yield.

Geilhausen *et al.* (2013) examined the impact of a proglacial lake in front of *Obersulzbachkees* (*High Tauern*, Austria). Measurements showed that, in general, 88–95% of suspended sediments were trapped in the lake, so the downstream SSC was significantly reduced. Bed load was interrupted by the lake; thus, bed load transport downstream of the lake was decoupled from bed load upstream of the lake. Mean grain sizes were therefore reduced from 20–44.5 µm (inflow) to 6.24–6.4 µm (outflow). Geilhausen *et al.* (2013) claimed that a proglacial lake reduces connectivity between glacial sediment production and downstream sediment fluxes. They expected that formation of such lakes will continue and accelerate due to climate change.

2.2 Reservoir sedimentation

2.2.1 Periglacial sediment yield

2.2.1.1 Catchment denudation rates

Hallet *et al.* (1996) analysed denudation⁶ rates of more than 60 glacierized catchments. They found that sediment yield increases with glacial cover. A glacier-coverage of more than 30% led to sediment yields that were one order of magnitude higher than for glacier-free basins. In the Swiss Alps, denudation rates were in the range of 0.41–1.7 mm/a. On the global scale, denudation rates were in the range from 0.01 mm/a at *Kangerdlug Glacier* (Greenland) to 60 mm/a at *Margerie Glacier* (Alaska). Beyer Portner (1998) reported denudation rates in the Swiss Alps in the range from 0.044 mm/a at *Les Toules* to 2.11 mm/a at *Gebidem*. Bogen (1989) reported denudation rates of 0.4–8 mm/a for glaciers in Switzerland, Norway, Iceland and the USA. Erosion rates strongly depend on the catchment. Governing parameters are: (a) area without vegetation cover; (b) area with soils prone to erosion; and (c) mean precipitation in summer, as Beyer Portner (1998) showed. Bezingé (1987) reported that deposition volumes from suspended sediment transport in the *Grande Dixence* scheme correspond to denudation rates of 0.065–1.32 mm/a. According to Bezingé and Aeschlimann (1989), denudation rates in basins in *Val d'Hérens* (Switzerland) were 0.15–1 mm/a for catchments with a degree of glaciation from 20 to 70% and areas of 2 to 36 km².

Schlunegger and Hinderer (2003) examined denudation rates of 27 Swiss drainage basins. They found values between 0.091 mm/a and 0.801 mm/a, which are in the same order of magnitude as rock uplift. Annual sediment yield is the product of annual denudation rate and catchment area:

$$V_s = j F \quad (1)$$

where V_s is the annual sediment volume [m³]; j is the annual denudation rate [mm] (presented in Figure 6 of the mentioned reference); and F is the catchment area [km²]. If this approach was applied to the reservoirs in Section 2.2.4, then measured sedimentation volumes could be over- or underestimated by a factor of 15 compared to measured values.

A similar study was conducted by Wittmann *et al.* (2007): Denudation rates varied between 0.10±0.01 mm/a and 6.44±3.18 mm/a (uncertainty estimates include errors on scaling laws, grain size effects and shielding effects). Walling

⁶ Turowski and Cook (2017) define denudation as “the loss of mass from a landscape through both solids and solutes, which thus includes all erosion processes”; this definition is used here as well

and Webb (1996) emphasised that catchment denudation rates are linked to anthropogenic and environmental (climatic) impacts. This was confirmed recently by Stutenbecker *et al.* (2017): In the *Rhône* catchment, a mean annual denudation rate of 16 ± 3 MT was estimated, but only 2–6 MT were actually conveyed into *Lake Geneva*. Storage in reservoirs or floodplains and sediment mining were identified as sediment sinks. Apart from that, they showed that denudation rates may be overestimated in catchments with strong human impact and high inputs of glaciogenic sediments. Within the *Rhône* catchment, denudation rates between 0.34 ± 0.06 and 7.45 ± 2.04 mm/a (the uncertainty range corresponds to 1-sigma) were computed for individual sub-catchments. Syvitski (2003) found that human settlement effects are the driving factor on sediment flux, followed then by climate shifts.

2.2.1.2 Suspended sediment yield

Gurnell *et al.* (1996) analysed suspended sediment yield from 72 glacier basins. Annual total suspended sediment yield was found to be positively related ($R^2 = 0.893$) to annual total discharge:

$$V_s = \frac{V_w^{1.167}}{10^{1.462}} \frac{1}{\rho_s} \quad (2)$$

where V_s is the annual sediment volume [m^3]; V_w is the annual runoff volume [m^3]; and ρ_s is the sediment density [kg/m^3]. This statistical regression is dimensionally inconsistent. If Equation (2) was applied to the reservoirs presented in Section 2.2.4, then measured sedimentation volumes could be over- or underestimated by a factor of four compared to measured values.

Felix (2017), however, did not find such a correlation for the highly glaciated *Fiescher* catchment in the Swiss Alps for the years 2012–2014, including a 20-year flood with a maximum SSC of 50 g/l. Correlation between annual total suspended sediment yield per unit area [$\text{m}^3/(\text{km}\cdot\text{a})$] was weakly related ($R^2 = 0.442$) to discharge per unit area [mm/a]. Both parameters varied between two orders of magnitude. Clifford *et al.* (1995) measured SSC in the meltwater stream of *Arolla Glacier* in *Val d'Hérens* (Switzerland) in 1990. SSC varied between 28 and 17 511 mg/l in June and July. Stott and Mount (2007) did similar measurements in *Torrent du Glacier Noir* (Section 2.1.4.2). SSC varied between 28 and 9664 mg/l. Collins (1989) measured maximum sediment concentration in *Gornera* (Switzerland). In spring 1987, subglacial flood events lead to maximum SSC of up to 15 430 mg/l. Fenn and Gomez (1989) analysed 1440 water samples from the proglacial stream of *Tsijiore Nouve Glacier* in the *Pennine Alps* (Switzerland) and found median grain diameters d_{50} of 14.6 μm (average of all samples). Bezinge and Aeschlimann (1989) reported maximum

SSC of 15–20 g/l in meltwater streams of *Gorner Glacier* and *Tsijiore Nouve Glacier*. In the *Dranse* river in *Val de Bagnes* (Switzerland), maximum SSC was 36 g/l in 1909 and 40 g/l in *Haut-Rhône* in a storm-flood in 1987. Riihimaki *et al.* (2005) measured peak SSC of 11–13 g/l in the proglacial stream of *Bench Glacier* in the *Chugach Mountains* (Alaska).

2.2.1.3 Sediment origin

Sediment yield from glaciated catchments has different origins. Alley *et al.* (1997) claimed that subglacial sediment yield per unit area is much larger than sediment yield from slopes around the glacier. Guillon *et al.* (2015) distinguished three domains: supraglacial, subglacial and proglacial sediment yield. Sediment load in subglacial streams is either from subglacial erosion at the base of temperate⁷ glaciers or from supraglacial hillslope erosion, where sediments have been transferred from the surface to the base. Guillon (2016) measured denudation rates in the catchment of *Glacier des Bossons* in *Mont Blanc* massif (France): supraglacial erosion was 0.76 ± 0.34 mm/a, subglacial erosion (derived from measurements in two streams) was 0.38 ± 0.22 mm/a and 0.63 ± 0.37 mm/a, and proglacial erosion was 0.25 ± 0.20 mm/a. Subglacial channel network evolution and surface-to-base transfer of sediments governed subglacial sediment yield, whereas channel migration and extreme events were driving processes of proglacial sediment yield. Sediment delivery was buffered by storage and release mechanisms. Clifford *et al.* (1995) measured SSC in the meltwater stream of *Haut Glacier d’Arolla* in *Val d’Hérens* (Switzerland). Over short periods, concentration varied independently of the discharge. Sediment supply from bank erosion and bar destruction seemed to be the governing source of SSC. Delaney *et al.* (2017) found that more than 70% of the sediment deposited in a periglacial reservoir originate from the subglacial area (i.e. less than 30% originate from the proglacial area). Glacier forefields may have a huge amount of loose sediment, but it can only be removed by fluvial transport, which is usually limited to channels and erosion gullies. Therefore, only a small portion of the total available sediment can be accessed and transported.

2.2.1.4 Subglacial erosion

Riihimaki *et al.* (2005) claimed that subglacial bedrock erosion rates are often interfered with sediment evacuation rates by subglacial storage. Swift *et al.* (2005) showed that subglacial drainage plays an important role in subglacial sediment yield. Subglacial drainage and seasonal changes of its structure and

⁷ glacial erosion under cold ice can be neglected

hydraulics are essential for determining subglacial erosion, because both water and sediment cannot be flushed from the subglacial hydrologic system before a conduit network is established (Riihimäki *et al.* 2005). In general, distributed and channelized systems have to be distinguished. Distributed systems are macroporous water sheets and films, cavities or porous flows. They are typically found in winter and considered to have low capacities and low efficiency regarding sediment transport. Channelized systems are ice-walled conduits (“Röthlisberger channels” or “R-channels”) or rock-walled conduits (“Nye channels”). They are typically found in summer and considered to have high capacity and high efficiency regarding sediment transport. Field measurements in *Arolla Glacier* (Switzerland) showed that glacial erosional capacity and efficiency of subglacial sediment evacuation is strongly non-linear. Suspended sediment concentration (SSC) of inefficient subglacial drainage was found to be proportional to $Q_w^{1.3}$, while SSC of efficient subglacial drainage was found to be proportional to $Q_w^{2.2}$, where Q_w is the water discharge. These findings correspond with Müller and Förstner (1968), who stated that a general empirical relation holds for most rivers worldwide:

$$SSC = \xi_1 \cdot Q_w^{\xi_2} \quad (3)$$

where SSC is in [mg/l]; Q_w is the water discharge in [m^3/s]; and ξ_1 and ξ_2 are dimensionless calibration parameters [-]. The authors found ξ_1 in the range 0.004–80 000 and ξ_2 in the range 1.1–2.5. Based on theoretical models, Alley *et al.* (1997) derived that SSC is proportional to Q_w^2 for channels with erodible banks or $Q_w^{4.5}$ for channels with non-erodible banks (e.g. “Röthlisberger channels”). In 1989, Gurnell (1995) analysed average SSC in the meltwater streams of *Arolla Glacier* and *Ferpècle Glacier* (Switzerland). Both glaciers are located next to each other in *Val d’Hérens* (Switzerland); the basins have similar size and orientation, but *Arolla Glacier* is believed to have a soft bed, whereas *Ferpècle Glacier* has a hard bed. Measurements were taken within a distance of 100 m from the glacier snout; that is, the sediments are mainly of subglacial origin. At *Arolla Glacier*, average suspended SSC increased from 390 mg/l in June to 1061 mg/l in July and 1628 mg/l in August. Contrary, at *Ferpècle Glacier*, suspended sediment concentration decreased from 320 mg/l in June to 254 mg/l in July and 154 mg/l in August.

2.2.1.5 Sediment availability and delivery

Gurnell (1995) compared sediment transport in the meltwater streams of *Arolla Glacier* and *Tsijiore Nouve Glacier* in *Val d’Hérens* (Switzerland). *Arolla Glacier* seemed to have a persistent sediment availability throughout the season, whereas *Tsijiore Nouve Glacier* was more productive early in the ablation

season. Timing of melt and access of meltwater to the sediment at different locations within the basin were assumed to be the governing factors of influence. White (2005) claimed that, worldwide and most of the time, sediment transport in rivers is limited by the amount of available sediment and not by transport capacity. Micheletti and Lane (2016) examined sediment export from two typical Alpine mountain watersheds. Glaciation of these catchments was 19 and 29%. Estimations of sediment transport capacity were orders of magnitude higher than the measured export. The authors concluded that sediment delivery determines sediment export and not transport capacity. There was evidence that erosion of morainic material and debris-flow events are driving processes for sediment delivery. Transport capacities are the upper limit of sediment conveyance. Connectivity of sediment source and transport medium determine the actual sediment yield. Topography plays a major role: depressions between sediment source (i.e. glacier tongue, forefield) and reservoir will significantly reduce sediment conveyance. Guillon (2016) supported this findings: if proglacial areas are not efficiently connected to the stream, then sediment load is determined by supra- and subglacial erosion. Stutenbecker *et al.* (2017) studied sediment transport in the *Rhône* basin: Sediment discharge calculated with denudation rates would be $16 \cdot 10^9$ kg/a, but measured values were as low as $2 \cdot 10^9$ kg/a. Hydropower and floodplain storage, sediment mining, and overestimated denudation rates due to anthropogenic impacts and high inputs of glaciogenic sediment from retreating glaciers were identified as potential reasons for this significant difference.

2.2.2 Sediment transport in reservoirs

Reservoir sedimentation in general has been investigated extensively. An overview is given by Morris and Fan (2010), for example. They identify three main processes of sediment transport in reservoirs:

1. transport of coarse particles as bed load along the topset delta deposits;
2. transport of fine particles in non-stratified (homopycnal) flows; and
3. transport of fine particles in stratified flows; for example, turbidity currents.

Delta deposits are divided into three zones: (a) topset, (b) foreset and (c) bottomset (Figure 3). On the topset, sediment particles with a high settling velocity are deposited. Therefore, the topset mainly consists of coarse sediments. The foreset has a steep slope and extends into the reservoir. The elevation of the transition zone from topset to foreset depends on reservoir operation and water surface elevation levels (Morris and Fan 2010). The bottomset consists of

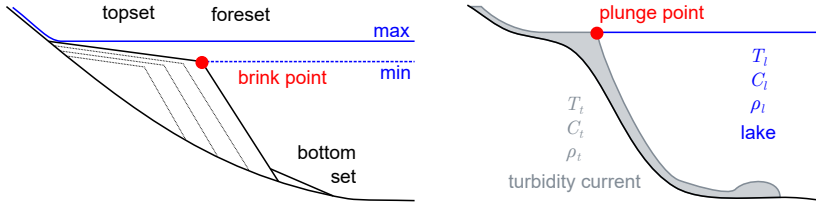


Figure 3: Sketch of a Gilbert-type delta (left) and a plunging turbidity current (right)

fine-grained sediments that were deposited by either stratified flows (such as turbidity currents) or non-stratified (homopycnal) flows.

Inflowing river water has usually a different density than the water of the lake or reservoir. If the lake is not stratified, either an overflow (lake water density is larger than inflow water density; hypopycnal flow) or an underflow (lake water density is smaller than inflow water density; hyperpycnal flow) can occur. If the lake is stratified, then an interflow might develop. In any case, the density difference must be distinct, so that stable stratified flows can develop. Turbidity currents are characterised by three criteria: (a) their density is larger than the density of the fluid above (this is often referred to as a “density excess”); (b) their higher density originates from suspended sediments; and (c) sediments are held in suspension by fluid turbulence⁸.

Brune (1953) defined the trap efficiency of a reservoir as the ratio of deposited sediments to total sediment input. Based on 44 records, he presented empirical relationships between “hydrologic size” and trap efficiency for different PSD. Hydrologic size is defined as the ratio of reservoir capacity to average annual inflow volume. These relations can be fitted closely with:

$$TE = \begin{cases} 0.95^{0.207 \log(CIR)} & \text{for fine-grained sediments} & (4a) \\ 0.97^{0.194 \log(CIR)} & \text{for medium-grained sediments} & (4b) \\ 0.99^{0.134 \log(CIR)} & \text{for coarse-grained sediments} & (4c) \end{cases}$$

where TE is the trap efficiency [-]; and CIR (“capacity-inflow ratio”) is the hydrologic size [-]. For a hydrologic size of 1.0, a trap efficiency of 95–99% is achieved, depending on the PSD. That means that the largest part of the sediments conveyed into the reservoir will be deposited. Many Swiss high-alpine

⁸ in debris flows or others, the sediments are dispersed by buoyancy, grain collisions etc. (Middleton 1993)

reservoirs are seasonal storages, so the reservoir size is comparable to the annual inflow rates.

2.2.3 Reservoir sedimentation problems

Reservoir sedimentation is a major issue in many reservoirs. Auel and Boes (2012) identified the following problems:

1. Reservoir volume decreases as it is being filled with sediment. The available amount of water is reduced along with the potential for energy production in case of hydropower reservoirs.
2. Several reservoirs provide retention volume for flood protection. Smaller storage capacities have a negative effect on flood protection projects because of decreased retention volume.
3. Once the sedimentation body reaches outlet structures, the operating safety of these facilities is endangered.
4. If the amount of wash load (sediments that are transported in suspension and never settle down in the reservoir) or of suspended load increases, hydro-abrasion at turbines is intensified and may result in efficiency loss.

Net reservoir capacity is decreasing worldwide because reservoir sedimentation increases faster than new reservoir capacity is installed (Auel and Boes 2012). Based on the analysis of 6399 reservoirs, Wisser *et al.* (2013) concluded that reservoir capacity has peaked in 2006 and declined since then. They claimed that reservoir lifetime and sustainability are often governed by sedimentation. According to Schleiss *et al.* (2010), 0.8% of worldwide active storage capacity are lost each year on average due to reservoir sedimentation. Especially reservoirs in Asia face severe sedimentation rates: in 2035, 80% of the active storage capacity in Asia will be lost. In Switzerland, average sedimentation rates are estimated to about 0.2% (Schleiss *et al.* 2010). Podolak and Doyle (2015) proposed that in many reservoirs the storage capacity loss cannot adequately be quantified and that it is different to the expected value used in the planning phase.

Despite the relatively low rate, sediment layers might grow 0.5–1 m each year at the deepest point of the reservoir, where bottom outlets are usually located. Within a few decades, serious problems may arise due to these deposited sediments. Furthermore, water intakes (which are typically located at higher elevations) may be affected by increasing SSC in the water.

Loss of net storage volume is directly linked with loss of energy production. Clogging of bottom outlets or water intakes is critical from a safety point of view. Both cases might require costly countermeasures. Schleiss *et al.* (2010)

estimated that worldwide replacement investments of 13–19 billion US-\$ are caused by reservoir sedimentation each year. This corresponds to $\frac{1}{3}$ of the annual operation and maintenance costs. Wisser *et al.* (2013) claimed that lifetime and sustainability of a reservoir are controlled by sedimentation and not by loss of integrity of the structure itself.

Finally, not only deposition of sediment has to be taken into account. Fine suspended sediments might not settle down and travel through the reservoir as wash load or suspended load. These sediments can cause problems once they enter the water intake: headrace tunnels or turbines can be significantly affected by hydro-abrasion due to fine particles. Reservoir sedimentation studies should therefore not only examine sedimentation processes, but also consider re-suspension and wash load.

2.2.4 Reservoir sedimentation in Switzerland

Impacts of reservoir sedimentation are different for each reservoir, as it has been illustrated with case studies in Morris and Fan (2010). Unfortunately, data for Swiss reservoirs in the periglacial environment are sparse. Several case studies are described below. The range of infill times is shown in Figure 4. The data are compared with catchment glaciation. It is expected that glaciation will decrease, but it is not yet known whether there will be a general trend of increasing or decreasing infill times.

2.2.4.1 Lac de Mauvoisin

Lac de Mauvoisin is a large reservoir situated in the *Pennine Alps*. Full supply level is at 1975 m a.s.l. First impounding took place in 1956. The reservoir has a volume of 204 hm³. It has a catchment area of 150 km², of which 42% are covered by glaciers. The average annual inflow is 265 hm³ (Gabbi *et al.* 2012). In 1985, the reservoir was flushed completely. Bezinge and Aeschlimann (1989) reported a deposition volume of 6 hm³. Photogrammetrical measurements showed a sedimentation volume of 9–10 hm³ (Schleiss *et al.* 1996). The annual sedimentation volume is 0.33 hm³, which equals 0.16% of the reservoir volume. The corresponding infill time is 618 years. Beyer Portner (1998) reported a higher infill time of 1072 years. Seiler and Thomann (2002) claimed that a large part of deposition was caused in the course of flood events (e.g. 1993 and 1994).

2.2.4.2 Griessee

Griessee is one of the reservoirs at highest elevation in Switzerland. Full supply level is at 2386.5 m a.s.l. First impounding took place in 1976. At that time, *Gries Glacier* occupied circa 0.3 hm³ of the reservoir. The reservoir has a

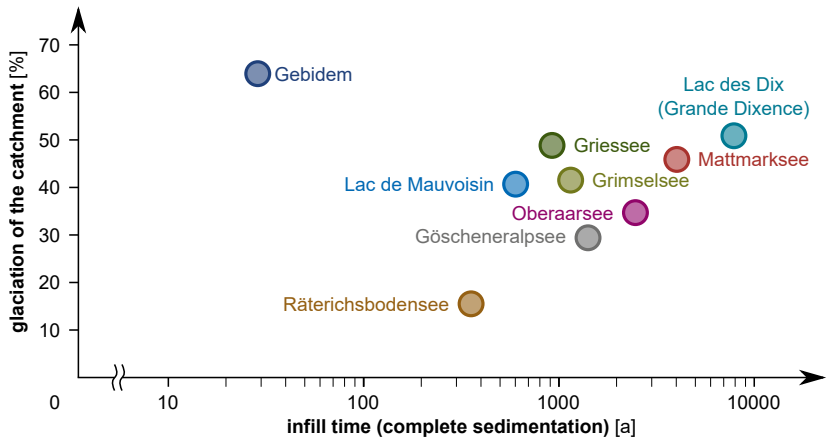


Figure 4: Infill times of selected Swiss alpine reservoirs [references are given in the text]

volume of 18.6 hm^3 . It has a catchment area of 10 km^2 , of which 48% are covered by glaciers. The average annual inflow is 20.7 hm^3 (Farinotti *et al.* 2012). Maintenance works in 2011 required closing the spherical valve of the penstock. Subsequent resetting of energy production failed due to blockage of the penstock by sediments. This is remarkable, because the hydraulic head was more than 400 m at the spherical valve in the power station. As a consequence, the water intake was heightened from 2335 to 2344 m a.s.l. and the minimum operating water level was heightened from 2340 to 2350 m a.s.l. The annual bottom outlet test will be combined with flushing of deposited sediments. According to Beck and Baron (2011, 2013, 2014), circa 0.79 hm^3 of sediment were deposited in the reservoir between 1976 and 2014. This equals roughly 4% of the reservoir volume or an average sedimentation rate of 0.11% per year. The corresponding infill time is 895 years.

2.2.4.3 Gebidem

Gebidem is a unique case regarding reservoir sedimentation in Switzerland. The reservoir is located downstream of *Aletsch Glacier*, the largest glacier in the Alps. Full supply level is at 1436.5 m a.s.l. First impounding took place in 1964. The reservoir has a volume of 9.2 hm^3 . It has a catchment area of 198 km^2 , of which 64% are covered by glaciers. The average annual inflow is 429 hm^3 (Meile *et al.* 2014), which is 47 times the reservoir volume. Giezendanner and Dawans (1981) reported annual sediment volumes of 0.5 hm^3 being conveyed into the reservoir. The corresponding infill time is 18 years. Rechsteiner (1996) reported

average deposition volumes of 0.335 hm^3 in the years 1991 and 1993–1996, which equals an infill time of 27 years. Meile *et al.* (2014) presented sediment volumes of $0.43\text{--}0.47 \text{ hm}^3$, which results in an infill time of 25–30 years. They stated that, since 2001, 10% of the sediments conveyed into *Gebidem* were discharged over the turbines and 90% were retained in the reservoir. Empirical trap efficiency according Brune (1953) (Equations 4a–4c) is 47–74%. Infill time would therefore be 20–25 years. To avoid complete reservoir sedimentation within only a few decades, yearly flushing operations are carried out. These are very efficient, as almost all sediment is evacuated during the flushing operations. These flushings last for 2–4 days and require roughly 3 hm^3 of water (Morris and Fan 2010). However, the problem of hydro-abrasion at the turbines cannot be solved with this countermeasure, because it is mainly due to wash load. Figure 5 shows the evolution of the delta in *Gebidem* within one year where no flushing operations were carried out.

2.2.4.4 Grimselsee

Grimselsee is the heart of the *Kraftwerke Oberhasli AG (KWO) Grimsel* scheme. Pumping operations link the reservoir with *Oberaarsee* upstream and *Räterichsbodensee* downstream. Full supply level is at 1909 m a.s.l. First impounding took place in 1929. The reservoir has a volume of 95 hm^3 . It has a catchment area of 77.2 km^2 , of which 44% are covered by glaciers. The average annual (natural) inflow is 215 hm^3 (Bonalumi *et al.* 2011). Anselmetti *et al.* (2007) reported an average annual sedimentation volume of 0.075 hm^3 . This is circa 0.08% of the reservoir volume. Therefore, infill time is 1270 years. According to Beyer Portner (1998), the infill time of *Grimselsee* is 1488 years.

2.2.4.5 Oberaarsee

Oberaarsee is situated 400 m above *Grimselsee*. Full supply level is at 2303 m a.s.l. First impounding took place in 1953. The reservoir has a volume of 57 hm^3 . It has a catchment area of 19.2 km^2 , of which 34% are covered by glaciers. The average annual (natural) inflow is 55 hm^3 (Bonalumi *et al.* 2011). According to Anselmetti *et al.* (2007), 0.022 hm^3 of sediment are deposited each year in *Oberaarsee*. This is 0.04% of the reservoir volume. Infill time is 2568 years.

2.2.4.6 Räterichsbodensee

Räterichsbodensee is located 140 m below *Grimselsee*. Full supply level is at 1767 m a.s.l. First impounding took place in 1950. The reservoir has a volume of 25 hm^3 . It has a direct catchment area of 18.6 km^2 , of which 14% are covered by glaciers. The average annual inflow is 129 hm^3 (Möller *et al.* 2011). Each

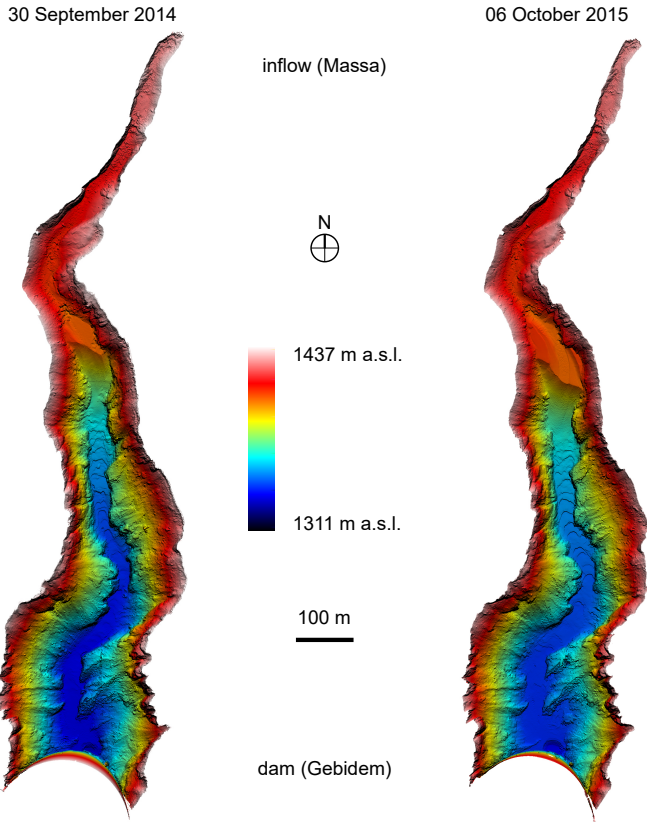


Figure 5: Delta evolution in *Gebidem* from 30 September 2014 to 06 October 2015: the topset slope is 1–5.5% (0.6–3°), the foreset slope is up to 67% (34°); mean bottom slope of the upstream Massa gorge is 5.5% [multi-beam echo-sounding data acquisition, post-processing and visualisation by G. Bourban / *HYDRO Exploitation*]

year, about 0.07 hm^3 of sediment are deposited in the reservoir (Anselmetti *et al.* 2007). This equals 0.3%. The infill time is 350 years, which is the fastest infill time in the *Grimsel* scheme. A different value of 1581 years was estimated by Beyer Portner (1998), but the analysis was carried out for the whole *KWO* system.

2.2.4.7 Göscheneralpsee

Göscheneralpsee is situated in the *Gotthard* region. Its total catchment is divided into a direct catchment of 42 km^2 and an indirect catchment of 53 km^2 from where water is transferred into the reservoir via tunnels. Full supply level is at 1792 m a.s.l. First impounding took place in 1957. The reservoir has a volume of 76 hm^3 . It has a total catchment area of 95 km^2 , of which 20% are covered by glaciers. The average annual inflow the total catchment is 202 hm^3 (Kobierska-Baffie 2014). According to Beyer Portner (1998), 1.5 hm^3 of sediment were deposited between 1957 and 1985. This is 0.07% of the reservoir volume each year. Infill time is 1392 years.

2.2.4.8 Lac des Dix (Grande Dixence)

Lac des Dix is the largest reservoir in Switzerland by volume. The dam, *Grande Dixence*, is 285 m high and still the world's tallest gravity dam (Boes and Hagemann 2015). Full supply level is at 2364 m a.s.l. First impounding took place in 1957. The reservoir has a volume of 400 hm^3 . 75 water intakes convey water from 35 glaciers into *Lac des Dix* (Grande Dixence 2010). This results in a total catchment area of 357 km^2 , of which circa 50% are covered by glaciers. The average annual inflow is 500 hm^3 . In Beyer Portner (1998), a deposition volume of $0.05 \text{ hm}^3/\text{a}$ is given. This is only 0.0125% of the reservoir volume each year. The corresponding infill time is 7996 years. The numerous water transfer tunnels make it impossible to link this number directly with catchment characteristics; It must be assumed that sediment connectivity is heavily distorted by the water transfer tunnels. Bezing (1987) reported deposition volumes of $0.05\text{--}0.06 \text{ hm}^3/\text{a}$ for years with a cool summer and $0.12\text{--}0.15 \text{ hm}^3/\text{a}$ for years with a warm summer; Bezing and Aeschlimann (1989) reported a deposition volume of 0.09 hm^3 for the summer 1975, an average year regarding hydrological conditions.

2.2.4.9 Mattmarksee

Mattmarksee is situated at the end of the *Saas Valley*. During its construction, on 30 August 1965, a huge ice avalanche with a volume of 2 hm^3 broke off from *Allalin Glacier* and buried the construction site. 88 people were killed. Glaciology subsequently became a fundamental research interest of VAW, which

finally led to the (re-)foundation of its glaciology group in 1979. The catchment is divided into a “natural” catchment of 37.1 km² and an “additional” catchment of 51.1 km² from where water is transferred into the reservoir. Full supply level is at 2197 m a.s.l. First impounding took place in 1969. The reservoir has a volume of 101 hm³. It has a total catchment area of 88.2 km², of which 45% are covered by glaciers (KWM 2003). The average annual inflow is estimated to be ca. 145 hm³, based on information provided by Farinotti *et al.* (2012). Beyer Portner (1998) estimates annual deposition volumes of 0.027 hm³. This corresponds to an annual sedimentation rate of 0.026%. The infill time is 3786 years.

2.2.5 Delta formation

When a river enters a lake or reservoir, a large part of its kinetic energy (or momentum) is dissipated. The flow velocity is reduced and a major part of the sediments carried by the river might be deposited, forming a delta (Bondurant 1975). These deposits usually have a triangular shape in the longitudinal view, hence the name according to the Greek capital letter “delta” (Figure 3). Gilbert (1890) described delta formation of coarse sediments: the topset starts where the maximum lake level meets the channel bottom. It consists of relatively coarse sediments that immediately start to settle when the river water enters the lake or reservoir. The foreset links the top- and the bottomset. It has a pronounced steep slope. The edge between top- and foreset is the brink point (Viparelli *et al.* 2012). The finer part of the sediments is transported in suspension beyond the delta face and then starts to settle down, forming the bottomset. The bottomset thickness diminishes outwards. Deltas formed by coarse sediment with a steep foreset are classified as Gilbert-type deltas. Figure 3 shows a sketch of a Gilbert-type delta.

Morris and Fan (2010) reported that topset slopes in U.S. reservoirs range from 20–100% of the stream slope. Strand and Pemberton (1987) stated that in the majority of reservoirs a topset slope of 1/2 of the channel slope can be supported based on statistical analysis. Another approach to determine topset slope would be using a bed load transport equation and computing the slope corresponding to zero transport, given the grain diameters observed. Gilbert (1890) supposed that the foreset angle is equal to the angle of repose. This was supported by Hunter (1985). According to Strand and Pemberton (1987), the observed foreset slopes are 6.5 times the topset slope on average. This mean value can be exceeded significantly, for example in *Lake Mead*, where the foreset slope was 100 times the topset slope. Therefore, these values allow merely an estimate of the delta dimensions. Saito (2011) examined delta front morphodynamics at *Kurobe River*, where the delta front changed its shape

seasonally: In winter, at low sediment supply, the delta was eroded due to wave interactions; in summer, at high sediment supply, it accumulated towards the sea.

Viparelli *et al.* (2012) classified Gilbert-type deltas as foreset-dominated deltas, because their evolution is governed by the growth of the foreset. Ferrer-Boix *et al.* (2015) attributed sediment transport in the three regions of the delta to different mechanisms. In the topset area, alluvial sediment transport is dominant. Bed load is deposited downstream of the brink point, in the upper part of the foreset. These aggradations periodically collapse and fall down the foreset. Thus, gravity-driven mechanisms govern the foreset area. This “avalanching” process (which might be interpreted as a cohesionless debris flow and debris falls) was described by Hunter (1985) for a sandy delta foreset and by Sohn *et al.* (1997) for a gravelly foreset. During the grain flow, “inverse grading” sediment sorting takes place: coarser grains are deposited near the toe, fine grains remain in proximity of the brink point (Hunter 1985; Bornhold and Prior 1990; Sohn *et al.* 1997; Viparelli *et al.* 2012). Bornhold and Prior (1990) reported a case where foreset evolution was not governed by slope failures, but mainly by river-based underflow processes. This foreset had a low inclination of less than 6.5° to the horizontal axis. In the bottomset area, settling of suspended sediments is the main deposition process. Deposits in this region may originate from turbidity currents as well.

2.2.6 Sedimentation from homopycnal flows

Wright (1977) claimed that homopycnal flows are most common whenever steep streams enter deep freshwater lakes. Homopycnal flows may also develop in situations where tidal mixing is sufficient to destroy vertical density gradients (Wright 1985). Homopycnal flows are characterised by fast mixing in all dimensions (Moore 1966). The sediments in suspension move by advection throughout the water column (Ashley 2002). So far, only little research has been done on homopycnal flows, as Chapron *et al.* (2007) stated.

Borland and Miller (1958) studied distribution of sediments in reservoirs. They did not account for transport processes explicitly, so their results can be used to predict homopycnal sedimentation. They distinguished between four different types of reservoirs (gorge, hill, flood plain-foothill and lake) and presented sediment distribution curves, which are shown in Figure 6. For gorge-type reservoirs, 85% of the sediments are deposited when the flow depth reaches half of the maximum reservoir depth; for lake-type reservoirs, only 20% of the sediments are deposited when the flow depth reaches half of the maximum reservoir depth. Thus, the former reservoir type tends to sedimentation near the inflow, whereas the latter tends to sedimentation close to the dam. Annandale

(1987) derived sediment distribution from stream power theory. The governing parameter is the gradient of the wetted perimeter in the main flow direction: if it tends towards zero, sediments will be deposited in the proximity of the dam; if it tends towards infinity, sediments will be deposited in the vicinity of the inflow. The former situation is encountered when small disturbances in a channel exist; the latter situation is found when a river flows into a large body of water. The corresponding sediment distributions are shown Figure 6. Rahmanian and Banihashemi (2011) developed this approach further, accounting for reservoir shapes, which may be important in small reservoirs (Michalec 2015).

2.2.7 Turbidity currents

2.2.7.1 Characteristics of turbidity currents

Turbidity currents are particle-laden, gravity-driven underflows (Meiburg and Kneller 2010). In general, the term is applied to flows of suspended sediment in water only, although it could be applied to flows in air (e.g. avalanches) as well (Middleton 1993). In reservoirs and lakes, they originate from density differences between inflowing river water and lake water. Gilbert (1890) was one of the first authors who suspected the existence of turbidity currents. Von Salis (1884) recognized that temperature differences may be one cause for density differences. Forel (1887/1888) showed that suspended sediments may be another cause. Both findings were confirmed with field measurements in the large pre-Alpine Swiss lakes *Lake Constance* and *Lake Geneva*, at the deltas of *Alpine Rhine* and *Rhône*, respectively. In periglacial lakes, suspended sediments are the driving force of turbidity currents, because density differences caused by temperature are orders of magnitude smaller (Menczel and Kostaschuk 2013). Fluid turbulence keeps particles in suspension. Turbidity currents exchange particles at the lower boundary by deposition or re-suspension and fluid at the upper boundary by entrainment or detrainment. Turbidity currents are believed to occur frequently and they are important to explain deposition patterns in reservoirs (Morris *et al.* 2008).

An extensive literature review on turbidity currents and a large set of measured data from both oceans and lakes is given in Talling *et al.* (2013). The following findings regarding turbidity currents in lakes were gained (SSC values in brackets are converted assuming a sediment density of 2650 kg/m³):

1. SSC in the inflow are usually 0.01–0.3% (0.265–7.95 g/l);
2. maximum SSC within the turbidity current are 0.001–0.07% (0.0265–1.855 g/l);

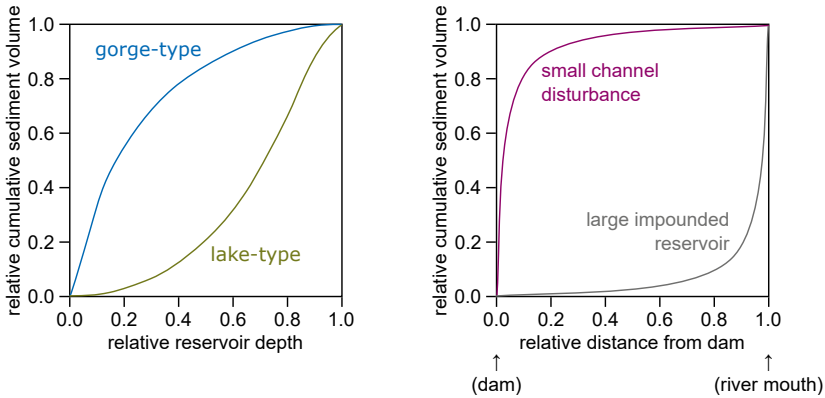


Figure 6: Sedimentation patterns for different types of reservoirs: Approach of Borland and Miller (1958) (left) and Annandale (1987) (right)

3. maximum velocities are usually 0.05–0.6 m/s, but might reach values of up to 1.2 m/s at steep slopes close to the shore;
4. thickness of the turbidity current is 3–16 m;
5. run out length is in the order of several kilometres; and
6. 60–99% of the transported sediments are in the range of clay and silt, and so are their deposits.

Oehy *et al.* (2000) identified five conditions for the evolution of turbidity currents:

1. high SSC in the inflowing river water;
2. large water depths at the river mouth;
3. low or zero flow velocity in the lake;
4. steep bottom slope at river mouth; and
5. channel-like bathymetry.

Two basic types can be distinguished: Type A turbidity currents originating from delta front slope failures and type B turbidity currents originating from plunging river water. Type A turbidity currents have hardly been monitored. Lambert and Giovanoli (1988) showed that they are rapid and capable to

transport large amounts of sediment. They are rare events. Nevertheless, slope failures and subaqueous debris-flows can be important depositional mechanisms (Saito *et al.* 2016). Different from the type B, they are not accompanied by an increase of water temperature at the measurement location. Type B turbidity currents are typically slow (velocities of some 10 cm/s) and very dilute (volume concentrations of less than 0.01%). As they often arise from river flood peaks, they last for several hours up to days and lead to an increase of water temperature at the measurement location, for example, an increase of 8.9 °C in *Lake Constance* in the 2005 flood event in *Alpine Rhine* (Mirbach and Lang 2016). In some cases, for example in *Lillooet Lake* (Menczel and Kostaschuk 2013), constant supply of glacial meltwater with heavy sediment loads leads to the formation of strong and persistent turbidity currents.

Density excess is the governing parameter of turbidity currents. It is defined as:

$$\delta = \rho_r - \rho_l \quad (5)$$

where δ is the density excess [kg/m³]; ρ_r is the density of the inflowing river (subscript *r*) water [kg/m³]; and ρ_l is the density of the lake (subscript *l*) water [kg/m³]. The density of sediment-laden water can be computed according to Chikita (2007):

$$\rho = \left(1 - \frac{SSC}{\rho_s}\right) \rho_w + SSC \quad (6)$$

where SSC is in [kg/m³]; ρ_s is the sediment grain density [kg/m³]; and ρ_w is the pure water density [kg/m³]. For atmospheric pressure, the equation of Tanaka *et al.* (2001) can be used to compute the density of pure water as a function of its temperature:

$$\rho_w = 999.97495 \pm 0.00084 \left(1 - \frac{(T_w - 3.983035 \pm 0.00067)^2 (T_w + 301.797)}{522\,528.9(T_w + 69.34881)}\right) \quad (7)$$

where T_w is the water temperature [°C].

2.2.7.2 Observations of underflows in Switzerland

The initiation of research on density currents was possibly at *Lake Constance*. Von Salis (1884) noticed that the delta of the *Alpine Rhine* did not grow as much as one could expect, given the heavy sediment loads of the *Alpine Rhine*. Depth measurements showed a lacustrine (erosion) gully, most likely formed by the *Alpine Rhine*. Combined with the observation of a plunge line (the

so-called “Rheinbrech”), he came to the conclusion that all these features are most likely caused by an underflow. He did not yet mention the influence of suspended sediments. 100 years later, Lambert (1982) proved existence of turbidity currents in the *Alpine Rhine* delta with field measurements. Eder *et al.* (2014) reported a turbidity current event that took place in August 2005 after a flood event of *Alpine Rhine* with a return period of ca. 100 years: the underflow had a temperature of 14 °C and travelled at 1.4 km/h more than 20 km into the lake. Mirbach and Lang (2016, 2017) presented measurements of the same event at two mooring sites. 8 km from the lakeshore (water depth of 140 m), a water temperature increase from 4.3 °C to 13.2 °C was observed; at the deepest point 30 km from the lakeshore (water depth of 250 m), a water temperature increase from 4 °C to 9 °C was observed.

Similar observations were reported by Forel (1887/1888) in *Lake Geneva* with a remarkably detailed set of field measurement data. He attributed gully formation at *Rhône* delta to the underflow of the cold, sediment-laden water of the *Rhône*. The subsequent study of Lambert and Giovanoli (1988) confirmed the existence of turbidity currents and provided measurement data. Ulmann *et al.* (2003) presented measurements at the *Versoix* delta (nearby *Geneva*), where sediment transport was linked to lake currents, not to turbidity currents.

Walensee is another lake where measurements of turbidity currents have been conducted. Lambert *et al.* (1976) examined turbidity currents in front of the river mouth of *Glärner Linth* in 1973. Subsequent field measurement in 1977 lead to similar results (Lambert 1979).

Turbidity currents in *Lake Lugano* were examined by de Cesare *et al.* (2006). Furthermore, there is evidence of underflows in *Lake Luzzone* (de Cesare *et al.* 2001), *Grimseelsee* (Bühler *et al.* 2004, 2005), *Lago Maggiore* (Ambrosetti *et al.* 2003) and *Griessee* (Bourban and Papilloud 2015). Sturm and Matter (1978) reported that high-density turbidity currents in *Lake Brienz* occur only once or twice per century, but they deposit layers of up to 1.5 m. Low density turbidity currents occur annually at flood discharges and lead to deposits in the range of centimetres. Müller and de Cesare (2009) described the venting of turbidity currents in *Mappragg* reservoir, where flood events with SSC of more than 30 g/l in the inflowing river water lead to turbidity currents with SSC of more than 8 g/l at the bottom outlet.

All reported turbidity current events have in common that inflowing river water had SSC in the range of a few grams per litre. Temperature differences act both as drivers (if lake water is warmer than inflowing river water) or restrainers (if lake water is colder than inflowing river water). Even a density excess of only a few g/l is enough to enable formation of a turbidity current. Available measurement data is summarised in Table 4.

Table 4: Examples of observed turbidity currents in Switzerland and corresponding density excess (SSC_r is the suspended sediment concentration in the river water; T_r is the temperature of the river water; T_l is the temperature of the lake water; and δ is the density excess computed with Equation (5) and assuming a sediment density of 2650 kg/m^3)

lake	author	SSC_r [g/l]	T_r [°C]	T_l [°C]	δ [g/l]
Lake Walensee	Lambert (1979)	6.0	10.4	17	4.6
Lake Constance	Lambert (1982)	5.0	8.5	5	3.0
Lake Geneva	Lambert and Giovanoli (1988)	2.6	10.5	6	1.3
Lake Lugano	de Cesare <i>et al.</i> (2006)	8.7	12.5	6	4.9

Forel (1887/1888) stated the *absence of turbidity currents* in *Lake Lucerne* at the *Reuss* delta and in *Lake Brienz* at the *Aare* delta. This was confirmed again by Lambert *et al.* (1976) and extended to *Lake Zurich*.

2.3 Suspended sediment and flow velocity measurement techniques

An overview over the numerous techniques for suspended sediment measurements is given in Wren *et al.* (2000). Techniques for continuous measurements, such as LISST or ADCP, are summarised in Rai and Kumar (2015). In this section, the four techniques used in the present study will be described more in detail:

- (a) Secchi disk
- (b) water sample analysis (Niskin bottle sampler)
- (c) Laser In-Situ Scattering and Transmissometry (LISST)
- (d) Acoustic Doppler Current Profiler (ADCP)

Secchi disk measurements (Section 2.3.1) are simple and straightforward. Measurement series of more than 100 years may be available, which is valuable for investigating long-term changes (i.e. changes due to climate change). They allow a rapid comparison between different water bodies. Secchi depths can be linked with SSC. They do not provide any information about PSD.

Water samples (Section 2.3.2) are the “standard” to calibrate other sampling techniques (Wren *et al.* 2000). Niskin bottle samplers allow isokinetic, streamlined sampling, which is essential for obtaining reliable data. The samples are analysed in the laboratory using the method that suits best to the sample properties and parameters of interest. Major disadvantages of bottle sampling are the poor temporal and spatial resolution due to the work-intensive and time-consuming data acquisition. Furthermore, bottle sampling is flow-intrusive.

Laser in-situ scattering and transmissometry (LISST) (Section 2.3.3) is a newly developed, sophisticated measurement technique. It provides the unique opportunity to measure both SSC and PSD independently. High temporal and spatial resolution can be achieved. Still it is an intrusive measurement technique. The range is limited and it is sensitive to ambient conditions, for example, the light field. More details are given in Felix (2017).

Acoustic Doppler current profiler (ADCP) (Section 2.3.4) is another measurement technique made possible by recent innovation. Designed to measure flow velocities, the acoustic backscatter data can be used to estimate SSC. It is a non-intrusive method, which allows highly specialised applications, for instance, in hazardous, high-energy flows such as turbidity currents (Xu 2011). It allows a high degree of spatial and temporal resolution as well. Depth ranges can be chosen between centimetres and several hundred metres by selecting an adequate frequency. Nevertheless, translation of the backscattered signal into SSC remains a major issue. Without any knowledge about the PSD, hardly any qualitative information of SSC can be gained. Variability of SSC in vertical direction is often larger than the resolution of the measurement technique. Noise floor of the instruments limit the application ranges.

For understanding of both LISST and ADCP, wave theory is needed. Optical or acoustical waves can be used for object detection, but it is crucial to keep in mind that the detectable object size depends on the wave length. Consider a toothpick in a lake: It will not affect the wave pattern, because its dimensions are magnitudes smaller than the wave length. In contrast, a heavy pier in the water will affect the wave pattern, because its dimensions are in the same order of magnitude as the wave length. Observations show that, in general, objects with equal or larger dimensions than the wave length can be detected. Small wave lengths are desirable to detect small particles, like suspended sediments. However, small wave lengths are subject to high absorption, so an optimum has to be found. In addition, signal processing is an important issue. Whereas low frequencies allow for detection of all wave characteristics (amplitude, wave length, distortions), waves of high frequencies cannot be fully resolved. At high frequencies, only intensities can be measured.

Absorption and attenuation are often used in the same context. Herein, absorption describes how matter takes up energy from a photon. Attenuation

describes the loss of intensity of a signal. It applies to optics or acoustics. Scattering can be interpreted as signal attenuation, because the signal in direction of propagation is “lost”. However, the lost energy is not necessarily transformed into matter.

2.3.1 Secchi disk

The Secchi disk is a very simple measurement device for turbidity (water transparency). It is a round white plate of 20 cm in diameter with holes. The device is shown in Figure 7. It is lowered down as far as the depth where it is no longer visible and moved up and down several times to get an average value of the depth of invisibility. This is the so-called Secchi depth. It can be assessed with an accuracy of ± 10 cm. Hutter *et al.* (2011) related Secchi depth and absorption coefficient of light in water based on empirical data:

$$\epsilon = 1.1z_{Secchi}^{-0.73} \quad (8)$$

where ϵ is the absorption coefficient of light in water [$1/m$]; and z_{Secchi} is the Secchi depth [m]. The *Beer-Lambert law* describes how light is absorbed as it penetrates into water:

$$I(h) = I_0e^{-\epsilon h} \quad (9)$$

where $I(h)$ is the light intensity at depth h [W/m^2]; I_0 is the light intensity at the water surface [W/m^2]; and h is the depth [m].

Lewis (1970) proposed to link Secchi depths directly with SSC by means of the following equation:

$$SSC = e^{\sqrt{64.36 - 14.02 \ln(100z_{Secchi})}} \quad (10)$$

where SSC is in [mg/l]. This regression relationship was derived from 296 water samples taken in the *Mackenzie delta* (*Northwest Territories, Canada*) with SSC ranging from 1 to 1156 mg/l . It can only be applied to Secchi depths lower than 0.986 m; at larger values, the radicand becomes negative.

Optical measurements (e.g. LISST) are influenced by ambient light. The influence of ambient light diminishes with increasing depth and decreasing Secchi depths. Hutter *et al.* (2011) reported Secchi depths of 19–21 m in *Lake Baikal*, a very clear and transparent lake, and 15 m in *Lake Constance*, a pre-Alpine lake. Andrews *et al.* (2011b) reported Secchi depths of 20–21 m in *Lake Tahoe*, again a lake with exceptionally clear water.

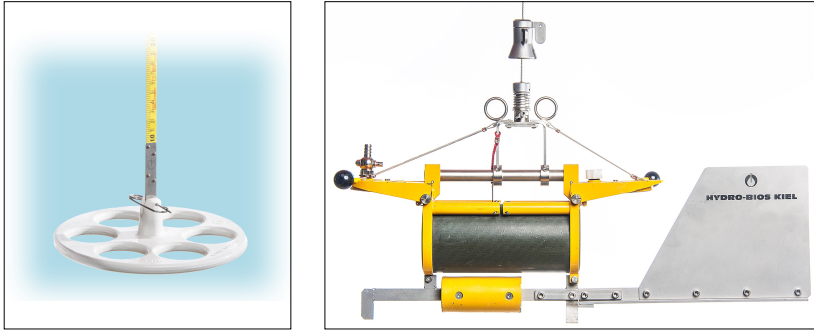


Figure 7: Secchi disk (left) and Niskin bottle sampler (right) [Images from VAW, ETH Zurich]

2.3.2 Water sample analysis (Niskin bottle sampler)

A typical Niskin bottle sampler is shown in Figure 7. It can be used to take water samples at different flow depths. Once lowered to the desired depth, a brass weight (the so-called “messenger”) is dropped down the cable of the bottle. The impact of the weight closes the caps and seals the water in the bottle. At large depths, the impact of the messenger is no longer strong enough to release the caps. Therefore, sampling depths are limited, depending on the weight of the messenger. The water samples can be analysed in a laboratory; for example, sediment concentration can be determined with a weighing procedure, PSD can be determined with laser diffraction and so forth (Felix 2017).

2.3.3 Laser in-situ scattering and transmissometry (LISST)

Laser diffraction has been applied for laboratory grain size analysis since the 1970s. Recent innovation made submersible and portable devices possible. For the time being, only *Sequoia Scientific, Inc.*⁹ provides devices suitable for field work. Their products are named laser in-situ scattering and transmissometry (LISST). A set of different instruments has been developed. The following sections focus mainly on *LISST-100X Type C*, which was applied in the present field measurements. The device is shown in Figure 8.

⁹ <http://www.sequoiasci.com>

2.3.3.1 Operating principles

LISST instruments are optical instruments. Some general information can be found, for instance, in Agrawal and Pottsmith (2000) or Agrawal *et al.* (2008). A principle setup is shown in Figure 9. A solid state laser diode emits visible red light at a wavelength of 670 nm with 1 mW. Due to the short cavity of the light, a collimating lens is needed. The laser beam enters the water sampling volume where it is being scattered because of particles present. This scattering can be described by *Mie scattering* theory, which is valid for small and spherical particles (Andrews *et al.* 2011b). Based on the *Fraunhofer diffraction* model, intensity of scattered light is directly proportional to particle size (Agrawal and Pottsmith 1994): The scattering angle and particle size are inversely proportional, so the scattering angle increases with decreasing particle size.

Behind a receiving lens, in the focal plane, an annular multi-ring photodiode detector senses the forward scattering. The 32 ring diameters increase logarithmically from the center with a ratio of 1.18 from 102 to 20 000 μm . Each ring diameter covers a so-called “size bin”. The rings cover angular ranges from 0.05 to 10°. A mathematical inversion allows a conversion from the multi-angle scattering distribution to a size distribution. This procedure identifies the size distribution that fits best the observed scattering. Two inversion methods are implemented so far: the spherical particle inversion and the randomly shaped particle inversion.

Laser light is not only scattered out of the beam, it is also being attenuated due to absorption in the medium. For particles larger than the wavelength, light removed from the beam is proportional to the (total) area of particles in the beam. The proportion of light transmitted through a turbid medium is therefore a measure for the area concentration. In addition to the scattering, also optical transmission is measured with a photodiode located behind a centered hole in the ring detector.

Electromagnetic absorption describes how much energy is taken up by matter. The transmission coefficient is a measure of how much energy is transmitted through the matter. Absorption in water is low for visible light, which is shown in Figure 10. Optical measurements in water are minimally affected by the water column if visible light is chosen. This is why LISST technique uses visible light, but in general it would not be limited to red light. According to *Rayleigh scattering* theory, the wavelength determines the size of detectable particles. From an optical point of view, particles in the order of 670 nm and larger could be detected by LISST, but signal processing procedures require slightly larger particles.

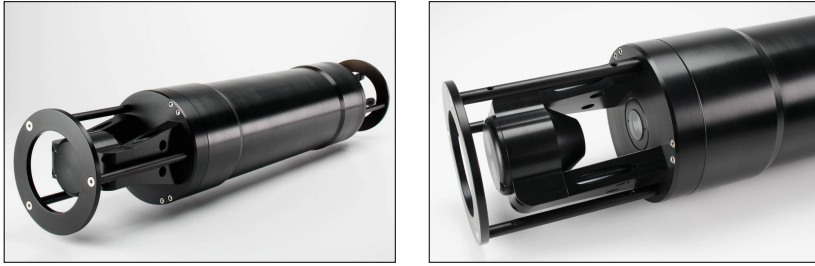


Figure 8: Laser in-situ scattering and transmissometry (LISST) 100X Type C (left) and detail of the instrument's head with laser and ring detectors (right) [Images from *Sequoia Scientific, Inc.*]

2.3.3.2 Limitations

The range of observable particles is determined by both detector size and chosen inversion method. For the spherical particle inversion method, particles in the range of 2.5–500 μm can be measured. For the randomly shaped particle inversion method, particles in the range of 1.9–381 μm can be measured. Out-of-range particles are added to the lowermost or uppermost size class, respectively (Lynch *et al.* 1994).

The lower bound of SSC is given by the noise floor of the instrument, which is in general less than 1 mg/l . The upper bound of SSC is usually in the order of 1 g/l . Higher concentrations lead to increased absorption, so that the received signal is too weak for reliable processing. A path reduction module (PRM) can be applied to decrease the sampling volume extent, which results in less absorption. Felix *et al.* (2013) achieved reliable measurements with a 90%-PRM in suspensions with concentrations of several g/l (angular silt) up to 25 g/l (rounded fine sand). Felix *et al.* (2018) proposed two practical empirical relations to estimate the upper limits of SSC as a function of d_{50} or the Sauter mean diameter and compared them to a relation provided by the manufacturer *Sequoia*.

Haun *et al.* (2015) suggest using LISST in a transmission range¹⁰ of 0.3–0.98. The application with regard to SSC depends on PSD as well, as it has been examined by Agrawal *et al.* (2008), for example. A small amount of particles or presence of a few relatively large particles can lead to errors due to small number

¹⁰ transmission is defined as the fraction of initial electromagnetic power that is transmitted through a sample volume

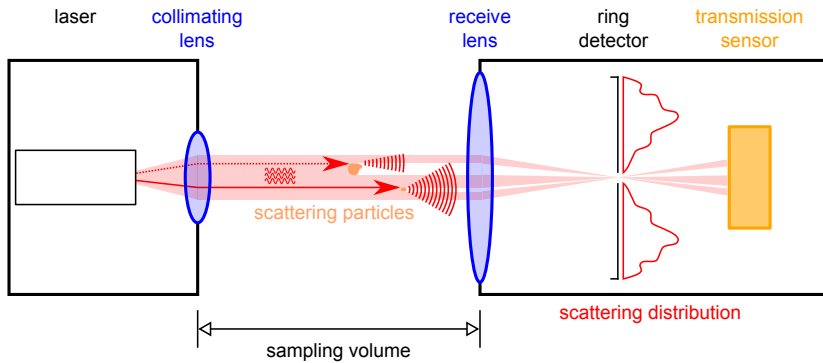


Figure 9: Principles of LISST measurements

statistics. High SSC will lead to multiple scattering, which is inconsistent with the forward model used in the inversion method (Lynch *et al.* 1994).

2.3.3.3 Application notes

Inspired by the laboratory particle sizers manufactured by *Malvern Instruments*, Bale and Morris (1987) developed the first submersible laser diffraction instrument. Their device was able to measure within a particle size range of 1.2–188 μm and a SSC range of 1–450 mg/l. They worked with two different focal lengths and five different path lengths. A first field application took place in 1985 in the *Tamar Estuary*. Additional information is given in Table 5. Application experiences of various field measurements applying laser diffraction units are given in the following.

Flocculation

Flocculation is a process where primary (dispersed) particles congregate to a larger particle. These flocs have different settling velocities and densities than the individual particles. The settling velocity of flocs is orders of magnitude larger than the settling velocity of individual particles, as Hodder and Gilbert (2007) or Guo and He (2011) reported. Hodder (2009) stated that small particles can settle as part of flocs, although they would remain in suspension as single particles. Flocculation can occur in rivers, estuaries and oceans, as Curran *et al.* (2007) or Guo and He (2011) showed. Hodder and Gilbert (2007) presumed that flocculation might be of major importance for settling processes in glacier-fed lakes. According to Fettweis (2008), uncertainties in the determination of size of both primary particles and flocs lead to standard deviations in settling velocities

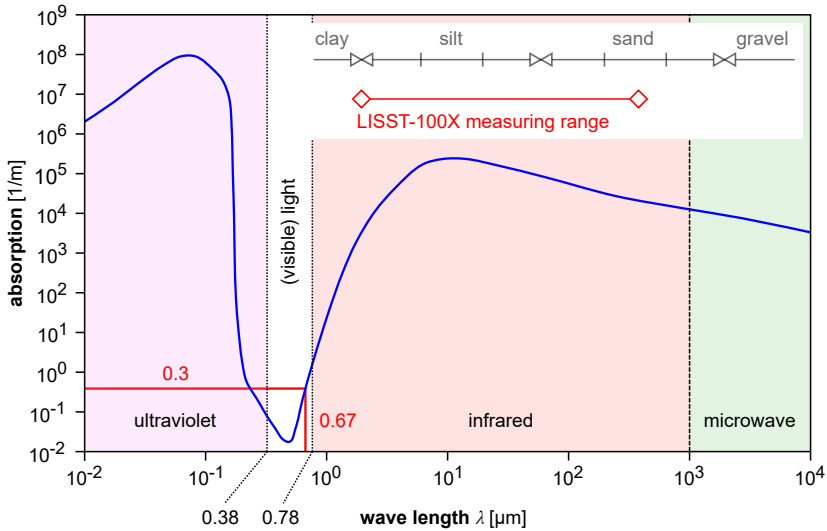


Figure 10: Simplified absorption coefficients for electromagnetic waves in water

of at least 100%. Flocs can amount to $1/3$ of suspended mass, as Curran *et al.* (2007) measured. Droppo and Ongley (1994) analysed flocs in six Canadian creeks and found that the proportion of flocs in terms of total particle number is generally less than 50%, but more than 99% of the total volume. Mikkelsen and Pejrup (2000) explained how flocculation processes alter the PSD from fine to coarse. Recent findings of Czuba *et al.* (2015) compared PSD of water samples with flocs and with dispersed flocs and concluded that they were very similar. This relativises the importance of flocculation which is commonly assumed. Droppo and Ongley (1992, 1994) measured floc sizes between 2 and 340 μm in six Canadian creeks with mean floc diameters d_m of 8.3–10.4 μm . Woodward *et al.* (2002) reported floc sizes in glacial meltwater streams of *Unteraar Glacier* (Switzerland) and *Batura and Passu Glaciers* (Pakistan) between 10 and 110 μm with d_m of 23–63 μm . Guo and He (2011) found floc sizes in the river *Yangtze* (China) between 22 and 182 μm and between 50 and 120 μm in the *Yangtze* estuary. In saltwater, larger flocs are expected than in freshwater (Droppo and Ongley 1992) because salinity is a governing factor of flocculation (Guo and He 2011). Felix *et al.* (2018) demonstrated that flocs and fouling affect largest size bins.

Table 5: Selected field applications of LISST technology (h is the depth; d_m is the mean particle diameter; d_{50} is the median particle diameter; and SSC is the suspended sediment concentration)

authors	location	h [m]	d_m or d_{50} [μm]	SSC [mg/l]
Bale and Morris (1987)	Tamar Estuary	–	$d_{50} = 25\text{--}70$	1–27.5
Lynch <i>et al.</i> (1994)	Pacific Ocean	89	$d_m = 15\text{--}30$	1–75
Mikkelsen and Pejrup (2000)	Øresund	9	$d_m = 41\text{--}109$	7–24
Hodder and Gilbert (2007)	Lillooet Lake	0–80	$d_{50} = 3\text{--}50$	20–220
Curran <i>et al.</i> (2007)	Gulf of Lions	26.5	$d_{50} = 5$	2–28
Williams <i>et al.</i> (2007)	Exe River	variable	$d_{50} = 50\text{--}330$	60–780
Fettweis (2008)	North Sea	5–32	$d_m = 1.1\text{--}7.2$	3.6–281
Guo and He (2011)	Yangtze River	–	$d_{50} = 4.4\text{--}11.4$	1.9–191

Conversion from volume concentration to mass concentration

Sediment density is used to convert from LISST’s volume concentration to mass concentration. Hubbart *et al.* (2014) showed that, although using densities of 2170, 1990 and 1760 kg/m³, differences of up to 60% between observed SSC from conventional water sample analysis and converted SSC from LISST measurements may arise. Felix *et al.* (2018) confirmed these findings, as SSC derived from LISST measurements (by multiplying LISST volume SSC with solid density of the particles) were on average 79% higher than SSC derived from gravimetric measurements (i.e. water sample analysis). Thus, it is problematic to convert from volume concentration to mass concentration. Sediment particles have a density of 2650 kg/m³ in general. If flocs are present, the density can be as low as 1600 kg/m³, 1530 kg/m³, 1370 kg/m³ or 1240 kg/m³, as shown in Curran *et al.* (2007), Felix *et al.* (2018), Sassi *et al.* (2012) or Czuba *et al.* (2015), respectively. As Czuba *et al.* (2015) pointed out, lower densities than 2650 kg/m³ cannot be explained by flocculation alone. Density can be reduced due to particle shape effects as well, as Felix *et al.* (2018) showed. A so-called “apparent density”, which is significantly lower than solid density of the particles, can be used to convert from volume to mass concentration.

Ambient light field

Ambient light is of major importance for LISST measurements, as Andrews *et al.* (2011b) demonstrated. By comparing measurements on the same water sample at night and day, the authors showed that the smallest size bins 1–8 (corresponding to particles below $\sim 7 \mu\text{m}$) were significantly affected by sunlight. As a consequence, impinging light was erroneously interpreted as fine particles. Andrews *et al.* (2011a) warned that light-contaminated results might hardly be identified because of their similarity to natural conditions.

Out-of-range particles

Out-of-range particles (i.e. particles outside measurable range) affect LISST measurements. Agrawal and Pottsmith (2000) expected that the scattered signal “leaks” into the nearest size bins. This was confirmed with measurements by Mikkelsen *et al.* (2005): particles larger than $500 \mu\text{m}$ scattered light to the innermost size bins 31 and 32, causing a “raising tail” in the PSD. Andrews *et al.* (2011b) concluded that, on the one hand, particles above the measurable range affect PSD only slightly, because they have their scattering peaks at angles less than the narrowest ring detector can detect. On the other hand, particles below the measurable range scatter across a wide range of angles and therefore affect the entire range of calculated PSD. Curran *et al.* (2007) came to the conclusion that, whenever out-of-range particles are present, the lowest and largest three size bins should be omitted. Williams *et al.* (2007) suggested to skip only the lowest or largest size bin.

Multiple scattering

Multiple scattering was examined both in laboratory and field studies by Agrawal and Pottsmith (2000). They concluded that multiple scattering effects appear at optical transmission of less than 30%. Based on laboratory investigations, Felix *et al.* (2013) showed that in cases of high SSC the lowest size bins are affected by multiple scattering. They sense too many particles, leading to wrong PSD. They recommended omitting the lowest three size bins in cases of high concentrations.

Other factors of influence

Haun *et al.* (2013) were able to capture turbulent fluctuations of SSC. They recommended time-averaging to obtain mean values. Haun *et al.* (2015) compared LISST measurements from stationary and moving mode operations: SSC differed up to 9%, d_{50} up to 19%. Czuba *et al.* (2015) emphasized the importance of the clean-water background. This null measurement is done to calibrate

the instrument. Any particles (e.g. sediment particles, air bubbles or others) lead to faulty clean-water backgrounds and disturb subsequent SSC and PSD measurements.

2.3.4 Acoustic Doppler current profiler (ADCP)

Animals like dolphins or bats use sound for communication and object detection. After the “Titanic” disaster in 1912, scientist started experiments on iceberg detection. Lewis Fry Richardson developed an iceberg detection system the same year by echo sounding in air. In 1913, Alexander Behm discovered the capabilities of echo sounding in water for naval applications. Although his system was not able to detect icebergs, it was suitable for depth measurements. In World War I, first attempts of SONAR (SOund NAVigation and Ranging) systems were made to detect enemy submarines. These were mainly passive devices; that is, they were just “listening”, but not emitting sound into the water. Nowadays, active sonars emit sound waves and listen to their echo. They are applied in many fields, such as vehicle location, fish finding, bathymetric mapping or echo sounding and cover a large frequency range from infrasonic to ultrasonic sound. ADCPs are primarily used to measure flow velocities (and discharge), but they can be used to assess various aspects of sediment transport, as Guerrero *et al.* (2013) or Latosinski *et al.* (2014) demonstrated. Xu (2011) advanced the view that ADCPs are “the most significant leap forward in flow measurement technology”.

2.3.4.1 Operating principles

The functionality of ADCP is described in detail in Fiedler (2008) or Moore (2011). Piezoelectric transducers inside the ADCP transmit and receive sound signals. An acoustic wave—usually at a non-audible frequency in the ultrasound regime—is released into the water. Backscatterers, such as solid particles, reflect the signal. Travelling time of the signal defines the distance between observer (ADCP) and target (backscatterer). If there is relative movement (i.e. a radial velocity component as shown in Figure 11) between observer and target, then the frequency of the echo will be modified according to the *Doppler effect*. This frequency shift allows to compute the relative speed between observer and target, given that the speed of the observer is known.

As distance increases, echo strength diminishes due to transmission losses and attenuation. Urick (1975) identified three types of major losses: (i) beam spreading; (ii) absorption by water; and (iii) absorption by sediment. If both losses by beam spreading and absorption by water are known, the remaining signal losses are due to absorption by particles. Consequently, echo strength is a measure for the amount of particles in the water. The return signal is

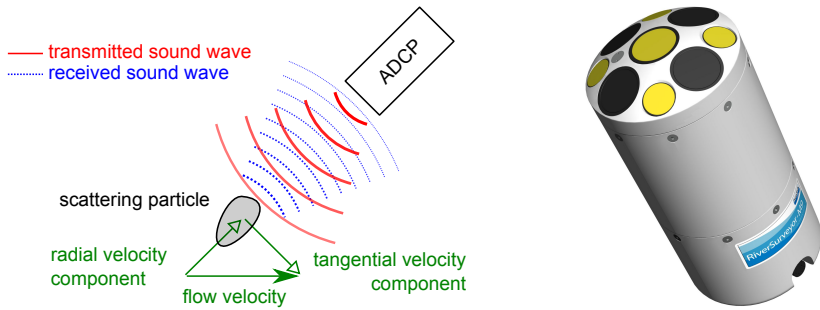


Figure 11: Principles of ADCP measurements (left) and *SonTek's RiverSurveyor M9* (right) [ADCP Image from *SonTek*]

converted into a digital signal and digitally processed with regard to the *Doppler shift*. Water temperature is measured in order to calculate the speed of sound in water. A compass measures heading of the observer, pitch and roll sensors correct movements of the observer. Basic operating principles are summarized in Figure 11.

2.3.4.2 Limitations

The depth range of ADCP is determined by frequency. Commercial devices cover ranges from a few meters (e.g. *Aquadopp Profiler* from *Nortek*¹¹ working at 2 MHz) up to more than 1000 meters (e.g. *Ocean Observer III* from *Teledyne RD Instruments*¹² working at 38 kHz).

Sound is attenuated when travelling through a medium and it is generally converted into heat. Attenuation of sound is much stronger in air than in water. Sound attenuation in water increases with frequency. With regards to echo sounding, large sampling ranges can be achieved with low frequency sound because of its weak attenuation. As low frequencies correspond to large wave lengths, the detectable object size increases proportionally. Echo sounding is therefore a trade-off between range and detectable object size. This is shown in Figure 12. *Kostaschuk et al.* (2005) presented minimum detectable particle diameters and peak sensitivities of different *SonTek* ADCPs. Peak sensitivity is reached when the particle circumference is equal to the wave length:

$$\pi d = \lambda = \frac{\sigma}{f} \tag{11}$$

¹¹ <http://www.nortek-as.com>

¹² <http://rdinstruments.com>

where d is the particle diameter [m]; λ is the wave length [m]; σ is the sound speed in water [m/s]; and f is the frequency of the ADCP [1/s].

Commercial ADCP devices provide Signal-to-Noise ratio (SNR) as an output. It is a by-product of the actual measurement and describes the level of (desired) signal to (undesired) background noise. The “signal” equals the magnitude of the acoustic wave reflected out of the water. Each ADCP measurement is disturbed by noise. Herein, “noise” includes electronic (thermal) noise, but also external effects like the sound of the boat machinery or wind. Ambient or man-made noise often occurs at lower frequencies than that of the ADCP and can be neglected (Deines 1999). Guerrero *et al.* (2012) identified air bubbles as the main source of noise. Returning signals with signal strength below noise level cannot be processed any more, as they cannot be distinguished from erroneous random noise measurements. The term “ratio” might be misleading at first glance, as *SonTek* devices deliver the quotient of signal and noise on the decibel scale where SNR is the difference of signal (in dB) and noise (in dB). SNR of 1 dB corresponds to a signal strength that is 10 times higher than the noise level.

2.3.4.3 Estimation of SSC from ADCP data

ADCP data can be used to estimate SSC. The most general procedure contains two steps:

1. correction of the received signal (SNR) for transmission losses
2. relation of the corrected signal (ABS) to SSC

Thus, the general procedure is SNR (Δ) \rightarrow ABS (Γ) \rightarrow SSC (C). Dwinovantyo *et al.* (2017) illustrated the process of signal correction and correlation to measured SSC values graphically and provided a complete set of equations for all tasks included. If the sampling volume is small and the sampling range is relatively short, then the first step might be skipped because of small transmission losses.

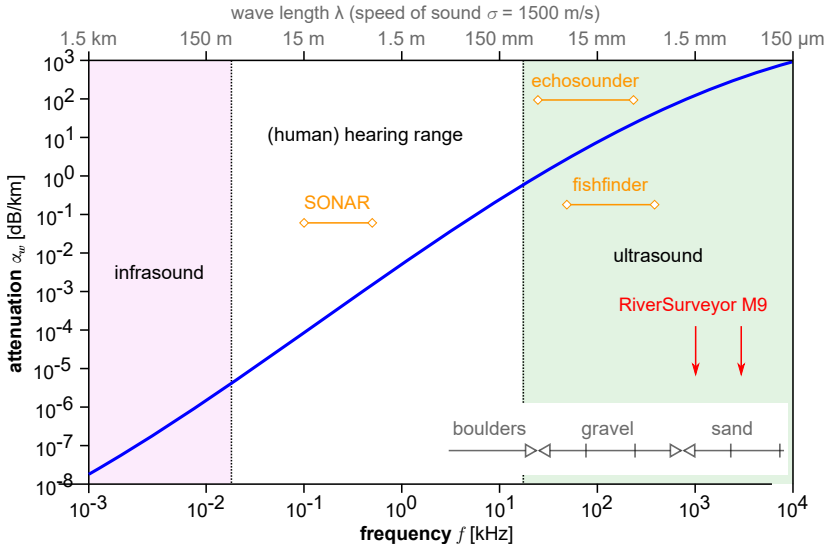


Figure 12: Simplified attenuation values of sound in water

Correction of the received signal for transmission losses

The SONAR equation is the very starting point for correcting ADCP signals for transmission losses. In Urlick (1975), a formulation for active SONARs is given in the following form¹³:

$$CS = SL - 2 \cdot TL + TS - (NL - DI) \quad (12)$$

where CS is the corrected signal [dB]; SL is the source level [dB]; TL is the transmission loss [dB]; TS is the target strength [dB]; NL is the noise level [dB]; and DI is the directivity index [dB]. The source level (SL) is the intensity of the signal sent out by the ADCP. The intensity of the signal is reduced with range. This is due to attenuation and beam spreading. Both effects are summarised as transmission losses (TL). Target strength (TS) is a measure of how good an object reflects the sound wave. It can be positive or negative. Noise level (NL) accounts for steady-state, isotropic sound which is not generated by the source itself. Noise background has to be distinguished clearly from reverberation background. Reverberation is sound reflected at the

¹³ since all terms are in decibels, addition and subtraction represents multiplication and division on linear (non-logarithmic) scales

water surface or at the bottom. Scattering by particulate matter would also be regarded as reverberation. It is an unwanted echo arising from the acoustic input. It decays with time, whereas noise is always present. Most acoustic sources focus the energy into a beam, which improves efficiency. Finally, the directivity index (DI) is the measure for this issue.

Deines (1999) tried to identify measurable quantities for the abstract terms in Equation (12). He proposed:

$$\Gamma = \xi + 20 \log_{10}(h) - 10 \log_{10}(l) - 10 \log_{10}(p) + 2\alpha h + K(E - N) \quad (13)$$

where Γ is the acoustic backscatter signal [dB]; ξ is a constant [-]; h is the depth (sampling range) [m]; l is the transmit pulse length [m]; p is the transmit power [W]; α is the attenuation coefficient of both water and sediment [dB/m]; K is the factor to convert counts into decibel (dB) [dB/counts]; E is the echo strength [counts]; and N is the received noise [counts]. It has to be noted that ADCP does not measure decibels, but counts. So the echo E and the noise N need to be converted into decibels via a factor K . For *SonTek* ADCPs, one count equals 0.43 dB (SonTek 2015, pers. comm.). Equation (13) is strongly linked to the output data of ADCPs manufactured by *RD Instruments*. Nevertheless, the basic structure of their equation can be maintained for other instruments as well. *SonTek* ADCPs provide SNR Δ as output. It can be related to the above equation via (SonTek 2015, pers. comm.):

$$\Delta = K(E - N) \quad (14)$$

Gostiaux and Van Haren (2010) broadened the application range of Equation (13). Implicitly, Deines (1999) assumed that the signal level is much larger than the noise level. This assumption can be skipped if the following equation is used:

$$10 \log_{10}(\Gamma) = \xi + 20 \log_{10}(h) - 10 \log_{10}(l) - 10 \log_{10}(p) + 2\alpha h + 10 \log_{10}(10^{0.1KE} - 10^{0.1KN}) \quad (15)$$

This equation is also valid when the echo level approaches the noise level.

Kim and Voulgaris (2003) simplified Equation (13). They combined the three terms

$10 \log_{10}(l)$, $10 \log_{10}(p)$ and N , because these can be regarded as instrument-specific constants. So these parameters can be added to the constant ξ_0 , which incorporates all parameters that cannot be measured independently. Furthermore, they directly linked the echo strength E to C by adding term ξ_1 from

Equation (18) into constant ξ from Equation (13) (see below) and using the theoretical value of 0.1 for ξ_2 in Equation (18):

$$20 \log_{10}(C) = \xi + 10 \log_{10}(h^2) + 2\alpha_w h + KE \quad (16)$$

where C is the suspended sediment volume concentration [-]; ξ is an instrument-specific constant [-]; and α_w is the attenuation of water [dB/m]. Their calibration lead to $\xi = -104.65$ and $K = 0.43$. Their equation would have a more general applicability, if they had used the overall attenuation coefficient α instead of the attenuation coefficient of water α_w . They explained that in their application field attenuation due to sediment was two orders of magnitude smaller than attenuation due to water, so it could be neglected.

A suitable formulation of the correction for SonTek ADCP data is given in Wood and Gartner (2010):

$$\Gamma = \Delta + 20 \log_{10}(h) + 2(\alpha_w + \alpha_s)h \quad (17)$$

where α_s is the attenuation of sediment [dB/m]. SNR (Δ) is directly given as an output. The range h is known and water attenuation α_w can be computed using various approaches provided in literature, such as Schulkin and Marsh (1962). The major problem is defining sediment attenuation α_s . If it cannot be neglected, then solutions provided by Topping *et al.* (2007) or Moore *et al.* (2012) can be used. The derivation of sediment attenuation value α_s is in general an iterative procedure. α_s is a function of SSC, which has an influence on SNR and therefore on ABS as well, and ABS itself has an influence on SSC.

Correlation of the corrected signal with SSC

An approach to link SNR and ABS was presented in Thevenot *et al.* (1992):

$$SSC = 10^{\xi_1 + \xi_2 \Gamma} \quad (18)$$

where SSC is in [mg/l]; ξ_1 and ξ_2 are calibration constants [-]; and Γ is the (corrected) acoustic backscatter signal [dB]. ξ_2 has a theoretical value of 0.1, but based on field measurements, the authors suggested to use $\xi_1 = 1.43$ and $\xi_2 = 0.042$. Alvarez and Jones (2002) followed this approach, but obtained $\xi_1 = 1.1186$ and $\xi_2 = 0.0245$ in their calibration. Calibration parameters ξ_1 and ξ_2 in Equation (18) include transmission losses, target strength, noise level and directivity index. Therefore, they need to be recalibrated if these parameters change. If measurement range, PSD or device change, the calibration parameters are most likely to change as well, as Gartner (2004) showed. Jay *et al.* (1999) calibrated the exponents for different regimes: in regimes with a high concentration of suspended sand, they obtained $\xi_1 = 1.7$, whereas in

regimes with low concentrations of silt, they obtained $\xi_1 = 17$. Coefficients of correlation were $R^2 = 0.86$ and $R^2 = 0.93$, respectively. The frequency of the ADCP had no significant effect on these parameters.

Wood and Teasdale (2013) used a slightly modified approach of Equation (18), namely:

$$SSC = 10^{\xi_1 \Gamma - \xi_2} \xi_3 \quad (19)$$

where SSC is in [mg/l]; ξ_1 , ξ_2 and ξ_3 are calibration coefficients which are dependent on both ADCP frequency and PSD [-]. In two field applications, coefficients of correlation (R^2) of 0.92 and 0.93 were achieved.

Hoitink and Hoekstra (2005) linked SSC and ABS (Γ) in the *Rayleigh scattering* regime, which is defined as:

$$0.5\omega r = \frac{\pi}{\lambda} d = \frac{\pi}{\sigma} f d \leq 1 \quad (20)$$

where ω is the wave number [1/m]. The authors proposed the following equation:

$$\Gamma = 10 \log_{10} \left(\frac{3\vartheta\omega^4}{\rho_s} \left[\frac{d}{2} \right]^3 SSC \right) \quad (21)$$

where ϑ is a material parameter [-]; and SSC is the suspended sediment concentration [g/l]. For a given ADCP frequency, Γ relates to d^3 , so bigger particles will have a disproportionate influence on backscattered signal.

Elçi *et al.* (2008) took PSD into account. They presented the relation which links SSC and SNR directly:

$$SSC = -13.8 + 0.8\Delta + 21.04 \frac{\alpha_w}{\alpha_{w,c}} + 4.52 \frac{d_{50}}{d_{50,b}} \psi \quad (22)$$

where SSC is in [mg/l]; $\alpha_{w,c}$ is the water absorption coefficient for calibration temperature [dB/m]; $d_{50,b}$ is the particle diameter corresponding to the predicted maximum sensitivity of the ADCP as given in Equation (11) [m]; and ψ is the coefficient of gradation of the PSD ($\psi = d_{30}^2 / (d_{60} d_{10})$) [-]. Equation (22) is valid for relatively low concentrations of less than 200 mg/l, so transmission losses due to absorption by sediment can be neglected. The authors do not explain how this approach can be used at larger depths, where transmission losses due to beam spreading become important.

Approach of Moore (2011)

SNR values need to be corrected for three types of transmission losses as shown in Equation (12). This can be done by applying Equation (17) on the SNR data. The attenuation of water α_w can be computed using the formula provided in Moore (2011):

$$\alpha_w = (55.9 - 2.37T + 0.0477T^2 - 0.000348T^3) \frac{f^2}{10^{15}} \quad (23)$$

where T is the water temperature [$^{\circ}\text{C}$]; and f is the ADCP frequency [Hz]. The attenuation of sediment α_s can be computed as:

$$\alpha_s = SSC (\zeta_{visc} + \zeta_{scat}) \quad (24)$$

where SSC is in [g/l]; ζ_{visc} is the viscous attenuation constant [m^2/kg]; and ζ_{scat} is the scattering attenuation constant [m^2/kg]. The viscous attenuation constant ζ_{visc} is computed with the following set of equations:

$$\eta_1 = \frac{\rho_s}{\rho_w} \quad (25a)$$

$$\eta_2 = \sqrt{\frac{\pi f}{\nu}} \quad (25b)$$

$$\eta_3 = \frac{1}{2} \left(1 + \frac{9}{\eta_2 d} \right) \quad (25c)$$

$$\eta_4 = \frac{9}{2\eta_2 d} \left(1 + \frac{2}{\eta_2 d} \right) \quad (25d)$$

$$\zeta_{visc} = \frac{\pi f (\eta_1 - 1)^2}{\sigma \rho_s} \left(\frac{\eta_4}{\eta_4^2 + (\eta_1 + \eta_3)^2} \right) \quad (25e)$$

The scattering attenuation constant ζ_{scat} is:

$$\zeta_{scat} = \frac{3}{2\rho_s d} \frac{0.29(0.5\omega d)^4}{0.95 + 1.28(0.5\omega d)^2 + 0.25(0.5\omega d)^4} \quad (26)$$

where ω is the wave number [1/m]. The term $0.5\omega d$ is defined in Equation (20). Both viscous attenuation and sediment attenuation depend on SSC and particle diameters. Therefore, it is an iterative procedure to convert ABS (Γ) to SSC. Information about PSD is needed, which can be obtained from water sample analysis or laser in-situ scattering and transmissometry (LISST), amongst others.

Approach of Moore et al. (2012)

ADCP provides cell data as point measurements at different depths. The above equations try to numeralise signal losses over the entire sampling range. The approach of Moore *et al.* (2012) looks at what happens between two point measurements. It compares received signal intensity P from depth ranges h_1 (upper point) and h_2 (lower point) and derives attenuation within this range:

$$\alpha = \left(P_2 - P_1 + 20 \log_{10} \left(\frac{h_2}{h_1} \right) \right) \frac{\ln(10)}{40(h_1 - h_2)} \quad (27)$$

where α is the attenuation between ranges h_1 and h_2 [dB/m]; P_1 and P_2 are the received signal intensities from depth ranges [dB]; and h_1 and h_2 are the depth ranges [m]. The received signal intensities are defined as:

$$P = 10 \log_{10} (10^{0.1KE} - 10^{0.1KN}) \quad (28)$$

The attenuation α is the sum of water attenuation (α_w) and sediment attenuation (α_s). Moore *et al.* (2012) suggested to use Equation (23) for calculating the attenuation of water. By subtracting water attenuation from each attenuation value, attenuation of the sediment in this range is obtained. If sediment size and concentration are homogeneous across the insonified volume, then concentration depends linearly on sediment attenuation. By calibration, the regression line can be found, as the authors presented for a case study in *Isère River*. Later, Moore *et al.* (2013) suggested to average over the entire profile, especially when multi-frequency attenuation data is available. The strong advantage of this approach is the fact that the upper point of each range can be taken as a new reference measurement, so all signal losses above can be neglected.

2.3.4.4 Application notes

Turbidity currents can be detected and monitored with ADCP. Kostaschuk *et al.* (2005) detected a turbidity current in *Lillooet Lake* because of the strong reflectivity of suspended sediments. Xu *et al.* (2010) studied event-driven sediment fluxes in two canyons offshore California. Passing turbidity currents led to distinct changes in SNR and flow velocity patterns; even a passing solitary wave could be detected by ADCP. Menczel and Kostaschuk (2013) studied low-density hyperpycnal flows in *Lillooet Lake, British Columbia*. They used an ADCP working at 0.5 MHz. Xu *et al.* (2014) measured turbidity currents in *Monterey Canyon* (USA) with two ADCPs, amongst other measurement devices. Some selected applications of ADCP technology are presented in Table 6. Successful application of ADCP technology requires to take the following issues into account.

Table 6: Selected field applications of ADCP technology (f is the ADCP frequency; h is the sampling range; v_{max} is the maximum flow velocity; and SSC is the suspended sediment concentration)

authors	f [MHz]	h [m]	v_{max} [m/s]	SSC [mg/l]
Holdaway <i>et al.</i> (1999)	1.0	8.5–14.9	1.6	10–350
Alvarez and Jones (2002)	—	1.2–16.0	0.8	5–85
Kim and Voulgaris (2003)	1.2	<12	0.5	1–1000
Gartner (2004)	1.2 and 2.4	0.15–1.49	0.7	0–715
Kostaschuk <i>et al.</i> (2005)	0.5	0–60	0.6	0–1000
Xu <i>et al.</i> (2010)	0.3	>80	0.122	2–200
Moore <i>et al.</i> (2012)	0.3, 0.6 and 1.2	15–85	1.3	4.7–8300

Particle size distribution (PSD)

PSD is an important information for the interpretation of the backscattered signal. A change in the backscattered signal can arise from a change of SSC or PSD. Reichel and Nachtnebel (1994) presented measurements in the *Danube* river. PSD was wide-spread and only “a very small percentage” of the particles dominated the backscattered signal. The comparison of PSD from ADCP measurements and PSD measured with optical instruments might therefore be large, as Hawley (2004) reported. Guerrero *et al.* (2011) showed that, in the lower *Paraná* river, backscattering power and attenuation of sand is two orders of magnitude higher than those of wash load (silt and clay), although the wash load concentration was ten times higher. Compared to sand scattering, wash load has a small effect on sound propagation. The authors presented an approach using two different frequencies and combining the SONAR equations with a particle size model, which allows to circumvent the problems of sampling the largest grain sizes only. Gartner (2004) calibrated the coefficients ξ_1 and ξ_2 of Equation (18) for different SSC and PSD. Their results illustrate that ξ_1 and ξ_2 are dependent on PSD.

Multi-frequency ADCP

Multi-frequency ADCP measurements are being carried out to capture not only SSC, but also PSD. Topping *et al.* (2007) applied ADCPs working at 0.6, 1

and 2 MHz on the same sampling volume. They came up with a procedure to estimate SSC within a range of 10–3000 mg/l (for sand suspensions) or 20 mg/l (for silt suspensions), respectively. The computed values from ADCP measurements deviated less than 5% from the values derived with conventional sampling methods. d_{50} was computed with an accuracy of 10%. Hurther *et al.* (2011) derived an approach working with two frequencies that has two major advantages: First, no assumption on sediment attenuation is needed; and second, it avoids error propagation along the profile. Thorne and Hurther (2014) recommended using at least three different frequencies to obtain a more stable inversion. Jourdin *et al.* (2014) examined the capability of multi-frequency ADCPs to measure PSD. They stated that frequencies should differ by at least two octaves¹⁴. Coupling of 0.3 and 0.5 MHz was considered to be unsuitable for the determination of d_m ; Combination of 0.075, 0.3, 1.2 and 4.8 MHz (= 6.4 octaves) was considered to be suitable for measuring particle sizes in the range of 30–3000 μm .

Attenuation by sediment and air bubbles

Signal attenuation due to sediments must generally be taken into account. Nevertheless, several studies showed that it can be neglected if low SSC are present. Alvarez and Jones (2002) showed that at short ranges of up to 1.5 m (i.e. near-surface measurements) and low SSC of less than 1 g/l, the attenuation by suspended sediments is small. Holdaway *et al.* (1999) found that errors introduced by neglecting sediment attenuation at concentrations of 350 mg/l were up to 26%. Kim and Voulgaris (2003) showed that for SSC of up to 1.2 g/l, sediment attenuation coefficients were in the range of 10^{-3} – 10^{-4} dB/m, whereas the water attenuation coefficient was 0.48 dB/m. Therefore, sediment attenuation is two orders of magnitude smaller than water attenuation and thus can be neglected. Unfortunately, no information about PSD was provided in the paper mentioned. Moore *et al.* (2012) stated that, for SSC of lower than 10 mg/l and water temperatures of 10 °C, sediment attenuation is one order of magnitude smaller than water attenuation and thus can be neglected. Topping *et al.* (2007) suggested correcting the return signal (e.g. SNR for *SonTek* ADCPs) with beam spreading and water attenuation and to use a graphical method for the estimation of sediment attenuation. This was further illustrated in Wood and Teasdale (2013).

SSC can be estimated with ABS. The coefficients of Equation (18) were developed with SSC data in the range of 1–100 mg/l, having a coefficient of determination (R^2) of 0.8. Kim and Voulgaris (2003) reported an underestimation

¹⁴ an octave is defined by a frequency ratio of 1:2

of SSC by 11% with Equation (16) for SSC in the range of 1–1000 mg/l. They achieved $R^2 = 0.9$. Moore *et al.* (2013) claimed that SSC estimations based on attenuation, for example Equations (27) and (28) with (23), are less sensitive to changes in grain size than estimates based on backscattered intensities, for example Equation (16).

Guerrero *et al.* (2011) mentioned that not only suspended sediments affect attenuation, but also air bubbles, organic matter and dissolved solids. Air bubbles are of resonant nature (Thorne and Hanes 2002). Deane (1997) measured air bubble sizes: The smallest bubbles had diameters of 80–100 μm , 10% had diameters larger than 2 mm.

2.3.5 Comparison of measuring techniques

The presented measuring techniques have essentially different characteristics. A graphical overview and summary of the three main measuring techniques water sample analysis (Niskin bottle sampler), laser in-situ scattering and transmissometry (LISST) and acoustic Doppler current profiler (ADCP) is presented in Figure 13. Secchi disk measurements are auxiliary measurements for LISST and are not discussed further.

Acquisition and laboratory analysis of water samples with the Niskin bottle sampler is both time-consuming and work-intensive, but result quality is high, as the samples can be analysed with advanced laboratory techniques that best fit the sample properties. Reliable information on both PSD and SSC can be obtained. The water samples are always point measurements. Investment costs are low. No information about hydraulic conditions can be derived.

LISST has the advantage of simultaneous measurements of PSD and SSC, but the application range is limited. The effort in data acquisition and post-processing is much lower than for water sample analysis, because of post-processing delivered by the manufacturer. Profiles over the whole water column can be recorded, because this device can be applied to depths of up to 300 m and high sampling rates of 1 Hz can be set. It is still an intrusive technology and does not provide any information about hydraulic conditions, like water sample analysis.

ADCP technology has been designed to measure flow velocities; that is, this technique focusses on hydraulic conditions. A by-product of ADCP measurements are SNR values, which can be used as a proxy for SSC. No information about PSD can be gained. Advanced automations allow efficient data acquisition and post-processing. Measurements over the whole water column are taken at the same time, which speeds up the measurements, allowing transect measurements. ADCP is a non-intrusive technology, which is an advantage in turbulent flows (like for example in the inflow region of reservoirs) or for

monitoring of turbidity currents. LISST and ADCP devices are significantly more expensive than Niskin bottle samplers, but the laboratory analysis of water samples might be costly as well, depending on the properties to be examined.

2.4 Mathematical and numerical reservoir sedimentation models

2.4.1 Delta formation

2.4.1.1 Mathematical models

Kenyon and Turcotte (1985) presented a theoretical model for delta progradation for time-independent boundary and input conditions. Under the assumption of a constant delta shape and sediment transport being linearly proportional to delta slope, they found that the height of the delta front above the basin decreases exponentially with distance from shore and increases exponentially with time as the delta grows:

$$z_d = z_0 \exp \left[-\frac{v_d}{D_s} (x - v_d t) \right] \quad (29a)$$

$$v_d = \frac{q_s}{z_0} \quad (29b)$$

$$D_s = -v_d z_d \left(\frac{\partial z_d}{\partial x} \right)^{-1} \quad (29c)$$

where z_d is the height of the delta (subscript d) front [m]; z_0 is the height of the landward edge [m]; v_d is the progradation velocity [m/s]; D_s is a (diffusive) sediment transport coefficient [m²/s]; x is the distance [m]; t is the time [s]; q_s is the constant sediment supply [m²/s]; and $\partial z_d / \partial x$ is the sedimentation rate, which is equal to the delta slope [-]. The model was tested against surveyed delta evolutions of the *Fraser River* in the *Straight of Georgia* (Canada), the *Alpine Rhine* in *Lake Constance* (Switzerland) and the *Mississippi River* in the *Gulf of Mexiko* (USA).

Muto and Swenson (2005) derived an analytical 1D model that couples diffusive alluvial morphodynamics to a geometric treatment of an avalanching delta foreset. They claimed that delta formation will always lead to a disequilibrium state and that “grade is an intrinsically non-equilibrium state that requires a fall in relative sea level”. They developed equations for the position of delta

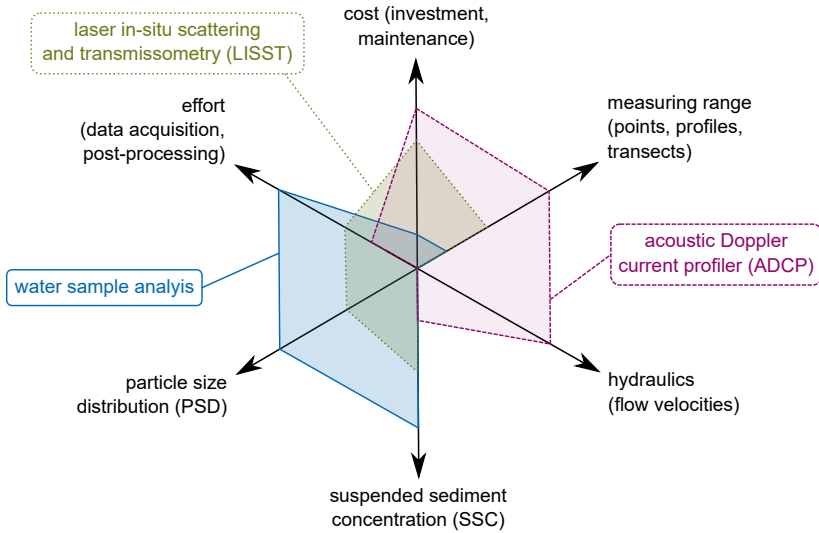


Figure 13: Comparison of the three main measuring techniques water sample analysis (Niskin bottle sampler), laser in-situ scattering and transmissometry (LISST) and acoustic Doppler current profiler (ADCP)

toe, Equation (30a), and shoreline, Equation (30b), as well as for the relative time-dependent water level, Equation (30c), required to maintain grade:

$$x_d = \frac{1}{J - S} (Jx_l + z_l) \quad (30a)$$

$$x_l = -\frac{D}{q_s} z_l \quad (30b)$$

$$z_l = -\sqrt{2q_s (J - S) \left(1 - S\frac{D}{q_s}\right)^{-1} \left(1 - J\frac{D}{q_s}\right)^{-1}} \sqrt{t} \quad (30c)$$

where x_d is the position of the delta toe [m]; J is the constant (delta) foreset slope [-]; S is the alluvial slope [-]; x_l is the position of the shoreline [m]; z_l is the relative water level [m]; D is the diffusivity [m^2/s]; q_s is the constant sediment discharge [m^2/s]; and t is the time [s]. According to Equation (30c) sustained grade for a uniform alluvial slope and a constant sediment discharge is only achieved if water level varies with the square root of time. If not, the

alluvial system is in an aggradation or degradation state. Equation (30c) can be derived for non-constant sediment discharge as well. For known relative water levels, the position of the shoreline and delta toe can be calculated using Equations (30a) and (30b). Flume experiments supported these findings.

Capart *et al.* (2007) derived the analytical solution for the 1D morphodynamic evolution of channel profiles governed by the diffusion equation. They worked with an idealized semi-infinite channel, where one boundary position is at an infinite distance, whereas the other is allowed to move. This requires that the length scale of the solution is short compared to the overall length and that the evolution of the solution is fast compared to the changes in the whole domain. Furthermore, the evolution should be driven by diffusion:

$$z_d = \Omega \cdot 2\sqrt{Dt} \quad (31a)$$

$$\Omega = -S_0\hat{x} + \eta [\exp(-\hat{x}^2) + \sqrt{\pi}\hat{x} [\operatorname{erf}(\hat{x}) + 1]] \quad (31b)$$

$$\hat{x} = \frac{x}{2\sqrt{Dt}} \quad (31c)$$

$$\eta = \frac{z_l + S_0\xi}{\exp(-\xi^2) + \sqrt{\pi}\xi [1 + \operatorname{erf}(\xi)]} \quad (31d)$$

$$\frac{\xi}{\xi + z_l/S_0} = 2 \frac{J/S_0}{J/S_0 - 1} \xi \left[\xi + \frac{z_l}{J} \right] + \frac{\sqrt{\pi}\xi [1 + \operatorname{erf}(\xi)]}{\exp(-\xi^2) + \sqrt{\pi}\xi [1 + \operatorname{erf}(\xi)]} \quad (31e)$$

where z_d is the channel bed elevation [m]; Ω is the shape function [-]; D is the diffusion coefficient [m^2/s]; t is the time [s]; x is the horizontal coordinate [m]; \hat{x} is the reduced horizontal coordinate [-]; S_0 is the initial channel slope [-]; η is an integration constant [-]; z_l is the water-level evolution parameter (negative values correspond to falling water levels, positive values correspond to rising levels, 0.0 is the special case of constant water level) [-]; ξ is a scaling constant [-]; and J is the foreset slope [-]. The analytical solutions were validated by Lai and Capart (2009) for a set of laboratory experiments, where effects of inflow density (homopycnal against hyperpycnal), inclination (moderate to steep) and sediment supply (high to low) on delta formation were examined.

2.4.1.2 Numerical models

Hotchkiss and Parker (1991) examined delta formation by bed load transport with a 1D numerical model. They showed that conservation of mass (continuity equation) and momentum (*Navier-Stokes equation*)—the *Saint-Venant equations* (Section 5.3.2.1)—combined with conservation of mass of bed sediment (*Exner*

equation, Section 5.3.3.1) capture the essentials of Gilbert-type delta formation. Additional closures for friction and for sediment transport are needed. They emphasised that a shock-fitting procedure is needed to model correct slopes at the delta front; without shock-fitting, these slopes are greatly reduced and spread over unrealistically long distances. The model was validated with flume experiments.

Seybold *et al.* (2007) proposed to use cellular automata to model river-, wave- and tide-dominated deltas over long time periods, because discrete models have the advantage of less computation time over continuum models (e.g. classical finite volume schemes). They used mass conservation of water and sediment and phenomenological sedimentation and erosion laws. The model was validated with geological records of the delta of the *Mississippi River*.

Viparelli *et al.* (2012) developed a 1D model for simulating bottom stratigraphy in Gilbert-type deltas. The governing equations are the *Saint-Venant equations* and the *Erner equation*, as well as shock and continuity equations for the movement of the topset-foreset break and the foreset-bottomset break. The model accounts for vertical sorting in the topset and on the delta front by applying a sorting function. It was tested against data from laboratory experiments.

Ridderinkhof *et al.* (2016) applied the 2D depth-averaged module of *Delft3D* for ebb-tidal deltas. The authors claimed that the 2D model reveals comparable results to a 3D model. They applied mass and momentum conservation for fluid (shallow water equations) and mass conservation for suspended load (convection-diffusion equation) and mass conservation for bed sediment (*Erner equation*). Empirical closures for bed drag coefficient and reference concentrations were used, combined with a spectral wave model (SWAN). Within the implicit scheme (timestep of 15 s), a morphological acceleration factor of 20 was applied to allow fast computations. The model was validated using a hypothetical test case, which is inspired by a real case in the *Wadden Sea* at the *Wichter Ee* inlet system with wave data from a station near the island *Schiermonnikoog*.

2.4.2 Turbidity currents

2.4.2.1 Mathematical models

One of the first theoretical approaches on turbidity currents was provided by Benjamin (1968). He was able to derive an equation for the steady-state head speed of the turbidity current at large depths:

$$v_t = F \sqrt{g \frac{\rho_t - \rho_l}{\rho_l} h_t} \quad (32)$$

where v_t is the head speed of the turbidity current [m/s]; F is the Froude number [-]; g is the gravitational acceleration [9.81 m/s²]; ρ_t is the density of the turbidity current [kg/m³]; ρ_l is the density of the ambient lake water [kg/m³]; and h_t is the height of the turbidity current [m]. Benjamin (1968) suggested to set $F = \sqrt{2}$ based on mathematical studies.

Huppert and Simpson (1980) later proposed an equation for small depths. They used Equation (32), but changed the value of F :

$$F = 1.19 \quad \text{for } \frac{h_t}{h_l} \leq 0.075 \quad (33a)$$

$$F = 0.5 \left(\frac{h_t}{h_l} \right)^{-1/3} \quad \text{for } 0.075 \leq \frac{h_t}{h_l} < 1.0 \quad (33b)$$

where h_l is the water depth [m].

Chu *et al.* (1979) developed an analytical 1D model. They identified four stages of turbidity currents: (a) flow establishment with increasing F and sediment entrainment from the bed into the turbidity current; (b) uniform flow with constant F and no sediment exchange; (c) a *hydraulic jump* at the abyssal plain where the slope is being significantly reduced and F changes from larger than 1.0 to lower than 1.0; and (d) flow decay where F vanishes and sediment detrainment (deposition) occurs. Flow dynamics were found to be determined mainly by sediment exchange with the bed, bottom resistance, slope of the bed and turbulent entrainment of water.

Muck and Underwood (1990) presented a conceptual 1D model. They focussed on maximum run-up elevation of subcritical turbidity currents. Based on field and laboratory observations, they derived an energy conservation equation that states that maximum run-up elevation is approximately equal to 1.53 times the thickness of the turbidity current.

A major advance in the understanding of the physics of turbidity currents is due to the outstanding work of Parker *et al.* (1986). They derived layer-averaged equations of motion for turbid underflows by neglecting lateral variations. It is a complete set of hyperbolic partial differential equations, similar to the shallow water equations. Indeed, the vertical structure of the turbidity current is averaged over depth; that is, flow velocity and concentration are vertically uniform and pressure is assumed to be hydrostatic within the current. They consider fluid mass conservation with Equation (34a), fluid momentum conservation with

Equation (34b), and sediment mass conservation with Equation (34c) for the turbid layer:

$$\frac{\partial h_t}{\partial t} + \frac{\partial v_t h_t}{\partial x} = e_w v_t \quad (34a)$$

$$\frac{\partial v_t h_t}{\partial t} + \frac{\partial v_t^2 h_t}{\partial x} = 0.5 \gamma g \frac{\partial C_t h_t^2}{\partial x} + \gamma g C_t h_t S - u_*^2 \quad (34b)$$

$$\frac{\partial C_t h_t}{\partial t} + \frac{\partial v_t C_t h_t}{\partial x} = w (e_s - C_b) \quad (34c)$$

where v_t is the flow velocity of the turbidity current [m]; h_t is the thickness of the turbidity current [m]; C_t is the volumetric concentration of suspended sediment in the turbidity current [-]; e_w is the coefficient of water entrainment from the quiescent fluid above [-]; γ is the submerged specific gravity [1.65]; g is the gravitational acceleration [9.81 m/s²]; S is the bottom slope [-]; u_* is the bed shear velocity [m/s]; w is the settling velocity of the particles [m/s]; e_s is the coefficient of sediment entrainment from the bed below [-]; and C_b is the near-bed volumetric sediment concentration [-], which can be approximated as 1.6 C_t . Apart from water entrainment, the fluid above the turbidity current is completely neglected in this set of equations.

This system of equations requires three closures, which were found in laboratory analyses by Parker *et al.* (1987):

$$e_w = \frac{0.00153}{0.0204 + \text{Ri}} \quad (35a)$$

$$e_s = \begin{cases} 0.3 & Z \geq 13.2 \\ \frac{3Z^{10}}{10^{12}} \left(1 - \frac{5.0}{Z}\right) & 5.0 < Z < 13.2 \\ 0.0 & Z \leq 5.0 \end{cases} \quad (35b)$$

$$u_*^2 = c_d v_t^2 \quad (35c)$$

where Ri is the Richardson number [-]; Z is a dimensionless coefficient [-]; and c_d is the bed drag coefficient [-]:

$$\text{Ri} = \frac{\gamma g C_t h_t}{v_t^2} \quad (36a)$$

$$Z = \sqrt{R} \frac{u_*}{w} \quad (36b)$$

$$R = \frac{\sqrt{\gamma g d d}}{\nu} \quad (36c)$$

where R is the particle Reynolds number [-]; d is the particle diameter [m]; and ν is the kinematic viscosity of water [m²/s]. A different formulation of the particle Reynolds number can be found in Equation (44). The model takes water and sediment entrainment into account. It allows self-iteration because of sediment entrainment. Energy balance may be included in the closure for bed shear velocity. This set of equations has been implemented in many numerical models, as it captures essential features of turbidity currents.

Wright *et al.* (2001) developed a simplified model for shelves, where the bed drag coefficient is not only controlled by the turbidity current itself, but also by tides, waves and wind-driven flows. They found an empirical relationship between the bed drag coefficient and Richardson number:

$$c_d = 0.01 - 0.028\text{Ri} \quad (37)$$

0.25 was identified as a critical Richardson number Ri_{cr} , because it damps bed drag significantly, but still allows enough turbulence to keep sediment in suspension. They proposed to compute v_t in the Richardson number, Equation (36a), with the maximum flow velocity:

$$v_{max} = \sqrt{v_{wave}^2 + v_{curr}^2 + v_{grav}^2} \quad (38)$$

where v_{wave} is the wave orbital velocity amplitude [m/s]; v_{curr} is the current magnitude [m/s]; and v_{grav} is the down-slope turbidity current speed [m/s]. Combined with the critical Richardson number of 0.25, the maximum sediment flux is

$$q_t = \frac{\sin(S)\text{Ri}_{\text{cr}}^2 v_{max}^3}{g\gamma c_d} \quad \text{with} \quad \text{Ri}_{\text{cr}} = 0.25 \quad (39)$$

where q_t is the specific volumetric transport capacity [m³/(s·m)]; S is the bottom slope [-]; and γ is the submerged weight of the sediment [kg/m³].

2.4.2.2 Numerical models

Meiburg and Kneller (2010) compiled a summary of theoretical models, field observations and numerical simulations of turbidity currents. Some selected models will be briefly presented herein. If not otherwise stated, all numerical models respect conservation of fluid mass (continuity equation, Equation (34a)) and

fluid momentum (*Reynolds-averaged Navier-Stokes equation*, Equation (34b)) as well as conservation of sediment mass (usually in form of a convection-diffusion equation, also known as advection-diffusion equation, Equation (34c)) according to Parker *et al.* (1986).

Zeng and Lowe (1997a) developed a 1D model. They implemented the closures of Parker *et al.* (1986) for the water (Equation (35a)) and sediment (Equation (35b)) entrainment coefficient and applied a Chézy relationship for bed shear velocity (i.e. $u_*^2 = c_f U^2$ in Equation (35c)). They validated their model with turbidity current events at *Bute Inlet* in *British Columbia* (Canada) (Zeng and Lowe 1997b).

Bradford and Katopodes (1999) developed another 1D model with the approach of Parker *et al.* (1986), but they applied different closures for sediment entrainment and modified the treatment of the near-bed concentration calculation. Additionally, they added the conservation of bed sediment mass (*Exner equation*). They emphasised on non-uniform sediment transport, growth and evolution and sediment entrainment and deposition for deep sea turbidity currents (where the thickness of the turbid layer is less than 7.5% of the ambient fluid). A finite volume-framework was applied. The model was validated with experimental data.

Mulder *et al.* (1998) applied *Newton's second law* to the fluid motion and derived a new model that uses a modified Chézy equation for the depth-integrated flow velocity of a dense gravity flow: moving force is the down-slope component of the flow weight, the resisting force is due to bed friction and internal friction. The model captures the essential behaviour of a riverine turbidity current in *Saguenay Fjord* (Canada); that is, the erosional phase, the subsequent transitional phase (without erosion and deposition of large particles only) and the depositional phase.

Scully *et al.* (2003) applied the simplified equations of Wright *et al.* (2001) to model deposition in a shelf. They validated the model with measurements from *Eel River* estuary in California (USA).

Choi and García (2002) presented a further development of 1D models, as they came up with a vertical structure model. In such a model, the variables like concentration or flow velocity are no longer uniform over the current height. They implemented a $k-\varepsilon$ turbulence closure. Comparison with results of the integral model of Parker *et al.* (1986) revealed that the tendencies of both models are similar and that the integral model is acceptable for field-scale turbidity currents.

Huang *et al.* (2005) came up with another vertical structure model with a $k-\varepsilon$ turbulence model included. Different closures for water and sediment entrainment and shear velocity calculation were implemented. The model works

with an implicit scheme within a finite volume framework. It was tested against laboratory results.

Kostic (2014) developed a model that captures all stages of interactions of a turbidity current with a dam. The model combines a quasi-steady river flow sub-model for the delta region with an unsteady underflow sub-model for the muddy pond in front of the dam. The four stages (i) progression towards the dam; (ii) runup against the face of the dam; (iii) formation of an upstream-migrating bore; and (iv) establishment of an internal hydraulic jump as the bore stabilizes can be simulated with this model.

Cao *et al.* (2015) presented a further developed model, as it incorporates a set of equations for the turbidity current and a set of equations for the upper clear-water flow layer. Both layers are depth-averaged. This model can resolve the formation process of the “transition from subaerial open-channel sediment-laden flow to subaqueous turbidity current” and the propagation and recession as well. Closures of Parker *et al.* (1986) and Manning’s formula for bed and interface shear stress were applied. A Riemann solver (HLLC) was used in a finite volume scheme. The model was validated and used for simulations of large-scale prototype turbidity currents in *Xiaolangdi Reservoir* in the *Yellow River* (China).

Increasing computational power has led to applications of 3D models in the last 20 years. A first milestone was the work of de Cesare *et al.* (2001). They used the commercial flow solver *CFX-4* with a $k-\varepsilon$ turbulence model and added algorithms that account for settling of particles as well as deposition and entrainment, which were modelled according to Parker *et al.* (1986). The model works on a staggered grid with the finite volume-approach. It was validated with laboratory data and a turbidity current event in *Luzzone Reservoir* (Switzerland). A comparable model was used by Oehy and Schleiss (2007). There, it was used to study interaction of solid obstacles (e.g. a dam) and permeable obstacles (e.g. a geotextile screen) on turbidity currents.

An *et al.* (2012) present another example of a 3D model. The commercial software *FLOW-3D* was used with two different turbulence closures: (a) the $k-\varepsilon$ turbulence model with *Reynolds-averaged Navier-Stokes equations*; and (b) the Smagorinsky closure with large-eddy simulation (LES) technique. The model captured both intrusive gravity currents (i.e. propagation of a fluid along an interface of two fluids with different densities) and particle-driven gravity currents (i.e. turbidity currents).

Scheu *et al.* (2015) used a 3D model with Mellor-Yamada turbulence closure for modelling river inflow intrusion in *Lake Maggiore* in *Pallanza Bay* at the mouth of the river *Toce* (Italy). The model included suspended sediment transport only. It was validated with ADCP measurements.

In recent years, new computational paradigms such as cellular automata, neuronal networks or genetic algorithms have become popular. Salles *et al.* (2008) used cellular automata and assumed turbidity currents to be a succession of quasi-steady states with permanent values for sediment transport. They used potential and kinetic energy of each automaton to compute water, sediment and energy fluxes. The model takes water entrainment, sediment deposition and erosion into account. It was tested with two field cases, the Indo-Pakistan *Pab Formation* and the Angolan deep offshore *Girassol Oil Field*.

2.4.3 Reservoir-scale sediment transport models

A summary of 1D, 2D and 3D models for reservoir sedimentation and flushing models has been compiled by Abood *et al.* (2009). Detailed literature reviews can be found in Sloff (1997), Ahn (2011) or Harb (2016). Some selected studies will be portrayed in this section. If not otherwise indicated, all models ensure mass and momentum conservation (continuity equation and *Reynolds-averaged Navier-Stokes equation*, respectively) for the fluid, mass conservation for suspended sediment (e.g. convection-diffusion equation) and the bed material (*Exner equation*).

2.4.3.1 1D models

Chang *et al.* (1996) presented *FLUVIAL-12*, a model for unsteady (non-stationary) flow, working with a stepwise steady-flow computation (based on backwater computation using the standard-step method). Finite difference approximations are used for mass and energy conservation. Non-equilibrium sediment transport includes sediment sorting and diffusion. *FLUVIAL-12* is suitable for water and sediment routing in river channels. The model was applied to study drawdown flushings during floods in three reservoirs (*Poe, Cresta* and *Rock Creek Dams*) in the *North Fork Feather River* in California (USA). The model was validated with surveyed reservoir geometries.

Nicklow and Mays (2000) developed *HEC-6*¹⁵, another model conserving mass and energy of the fluid. Again, the quasi-steady backwater equation is used to compute water-flow conditions uncoupled from sediment transport. Friction and form losses are incorporated. Sediment mass conservation is solved with an explicit finite difference scheme. The model claims to be capable to simulate formation of uniform delta deposits and the phenomena of coarser material being deposited further upstream in a reservoir. It was validated

¹⁵ HEC-6 has later been replaced by *HEC-RAS*

by application to a hypothetical three-reservoir network and the *Yazoo River* network in Mississippi (USA) with six rivers and four lakes.

Kostic and Parker (2003a,b) provided a well-documented and sophisticated model set-up with two linked sub-models: (a) a fluvial sub-model; and (b) a turbidity current sub-model. The fluvial sub-model captures the evolution of prograding delta topset and foresets. It uses closures of Chézy for shear velocity and the bed load transport equation of Engelund-Hansen for transport capacity. The turbidity current sub-model uses the layer-averaged equations (including closures) of Parker *et al.* (1986) including energy conservation. It captures the evolution of bottomset deposits. Equations are solved with the conservative difference scheme *ULTIMATE*. Model validation was carried out using laboratory experiment data. The co-evolution of sandy topset and foreset deposits with muddy bottomset deposits could be simulated.

González *et al.* (2006) developed a numerical model working with a finite volume scheme. Turbidity currents are implemented following the approach of Parker *et al.* (1986), with an additional closure for plunging of the turbidity current. The model was validated with simulation of sedimentation of the *Puntilla del Viento* reservoir on the *Aconcagua River* (Chile).

Mamede *et al.* (2006) derived a model with two sub-models: (a) a river sub-model; and (b) a reservoir sub-model. They applied the standard step method for a gradually varied flow in the river sub-model and the *GSTARS* approach in the reservoir sub-model. Different non-equilibrium transport equations can be applied. There is no sub-model for turbidity currents. The model was validated with measurements from the *Barasona Reservoir* on the river *Esera* (Spain). It was further developed and applied by Müller *et al.* (2010) as *WASA-SED* in the *Isábena River* catchment (Spain).

Toniolo *et al.* (2007) presented a model with two sub-models: (a) a sub-model for the fluvial topset region; and (b) a sub-model for the turbidity current (subaqueous) region. A *hydraulic jump* in the muddy pond can be taken into account. The model describes essential features of reservoir sedimentation, such as fluvial deposition of sand on the delta topset, progradation of the foreset due to sand deposition, plunging of muddy river water and formation of turbidity current, formation of internal *hydraulic jump* because of reflection at dam, deposition from turbidity current and formation of bottomset and detrainment of water at the settling interface of the muddy pond. It was validated with data from laboratory experiments.

Guertault *et al.* (2016) applied the codes *MAGE* and *ADIS-TS* for sediment flushing simulations. The shallow water equations are solved with a semi-implicit finite difference scheme. Exponential concentration profiles are computed in areas of large water depths where a vertical gradient is observed and depth-averaging is no long suitable. The model was validated with a flushing event in

the *Génissiat Reservoir* and *Seysse Reservoir* on the *Rhône* downstream of *Lake Geneva* (France).

2.4.3.2 2D models

Ziegler and Nisbet (1995) used the code *ECOM* for solving the depth-averaged shallow water equations. They added the bed load transport equation of Ackers and White, settling velocities accounting for flocculation and a relationship for re-suspension. The semi-implicit code was suitable to model long-term fine-grained sedimentation in *Watts Bar Lake* in Tennessee (USA) over 30 years (from 1961–1991).

Olsen (1999) developed a model for shallow water reservoirs, where no secondary currents are expected. It uses a zero-equation turbulence model and a total load concept, combined with an estimate for near-bed SSC. The model was validated with results from a physical model study of the flushing of the *Kali Gandaki Reservoir* in Nepal.

Scully *et al.* (2003) implemented the equations found by Wright *et al.* (2001) into a numerical model, where the turbulence was generated by waves and ambient currents and not internally, as in Parker *et al.* (1986) and others. The model focusses solely on turbidity currents. The simplified model has a strong dependency on the Richardson number, but with real and smoothed bathymetries it captured magnitude and location of deposition of turbidity currents in the continental shelf of *Eel River* in California (USA).

Souza *et al.* (2010) applied *MIKE21C* for modelling sediment transport in a shallow reservoir. An implicit scheme with different time steps for hydrodynamics and morphodynamics and a constant turbulent viscosity was used. The model was validated with experimental data.

2.4.3.3 3D models

Fang and Rodi (2003) applied the *FAST3D* and *SIMPLE* codes with a $k-\varepsilon$ turbulence model in a finite volume scheme with adaptive grid. Only suspended load transport was included into the model, because 98% of the sediments in the chosen case study of the *Three Gorges Reservoir* were smaller than 1 mm. 76 summer seasons (June–September) of operation could be simulated on a super computer facility. The model was validated with laboratory experiments.

Umeda *et al.* (2006) developed a semi-implicit model working with a finite volume scheme. Effects of buoyancy (caused by temperature only and not by SSC) are included by the *Boussinesq approximations*, turbulence is included with a $k-\varepsilon$ model. The model also takes heat transport into account (i.e. solar radiation, long-wave radiation and sensitive and latent heat transport). Sediment transport includes diffusion, deposition and re-suspension. It was

validated with prototype measurements (ADCP and sediment traps) in the *Shichikashuku Reservoir* (Japan) during a three week flooding event in 1996, when a turbidity current occurred.

Chung *et al.* (2009) applied *ELCOM* (Estuary Lake and Coastal Ocean Model) for hydrodynamics and *CAEDYM* (Computational Aquatic Ecosystem Dynamics Model) for morphodynamics in a semi-implicit finite volume framework. Both *Boussinesq* and hydrostatic pressure approximations can be applied. Energy conservation (long-wave radiation, short-wave radiation, sensible heat transfer, evaporative heat loss) is implemented again. Settling and re-suspension of sediments can be simulated. Density is a function of both temperature and SSC. The model was validated with field measurements of the mixing processes of turbidity currents in the morphologically complex, stratified *Daechong Reservoir* (Korea). The same model system *ELCOM-CAEDYM* was successfully applied by other researchers for simulation of turbidity currents, for example by Mirbach and Lang (2016) in *Lake Constance*.

Haun and Olsen (2012) developed *SSIIM 2*, an implicit, finite volume scheme working on unstructured, non-orthogonal and adaptive grids. It includes a $k-\varepsilon$ turbulence model and empirical bed load transport equations. It can be applied for reservoir flushing and reservoir sedimentation (Haun *et al.* 2013). The implicit scheme allows computation on desktop computers. It has been validated with results of physical models studies of the flushing of the *Kali Gandaki Reservoir* in Nepal (Haun and Olsen 2012) and field measurements of the sedimentation of *Angostura Reservoir* in Costa Rica (Haun *et al.* 2013).

3 Swiss periglacial hydropower potential

3.1 Introduction

Climate change leads to glacier retreat in the Swiss Alps. This has a twofold impact on hydropower in the periglacial environment: new potential locations for HPP reservoirs become ice-free and additional meltwater from glaciers may be available for production. The Swiss *Energy Strategy 2050* anticipates 37.4 TWh of annual electricity production from hydropower in 2035. In 2016, the annual production reached ca. 36.3 TWh. Therefore, a further annual net potential of ca. 1.1 TWh needs to be exploited until 2035. This potential can be found in the periglacial environment. In this chapter, it will be demonstrated that seven new HPPs are needed to meet the target imposed by the Swiss *Energy Strategy 2050*. A systematic analysis to evaluate the potential of new HPPs in the periglacial environment considering climate change scenarios is presented, starting from (1) evaluating glacier runoff projections for different global circulation models (GCM) and emission scenarios; (2) selecting sites with annual runoff volumes above a certain threshold; (3) subjecting all remaining sites to an evaluation matrix to rate them consistently; and (4) estimating the HPP potential of the best-rated sites. Furthermore, layouts of the HPPs are developed and main characteristics are calculated. Uncertainties and challenges will be discussed and reservoir sedimentation will be addressed.

3.1.1 Swiss Energy Strategy 2050

After the nuclear disaster of *Fukushima Daiichi* on 11 March 2011, the Federal Council and Parliament of Switzerland decided to withdraw from nuclear power. The five Swiss nuclear power stations shall be shut down once they reach their technically safe operation life and they are not to be replaced by new ones. This game-changing decision as well as the changes in the international electricity markets, combined with newly available technologies, require adaptations of the Swiss energy system. On 4 September 2013, the Federal Council submitted a set of measures to the Parliament. It consists of activities to increase energy efficiency, to further exploit the potential of hydropower and to extend renewable

electricity production. This set of measures was implemented into the Energy Act, which was finally approved by the Parliament on 30 September 2016.

On 21 May 2017, the Swiss voting population passed the new Energy Act. It contains three strategic objectives: (1) increase energy efficiency; (2) increase the use of renewable energy; and (3) withdraw from nuclear energy. Amongst others, the following targets are defined in the new Energy Act: (1) annual electricity production from hydropower shall increase to 37.4 TWh by 2035 (Art. 2-2); and (2) average annual electricity consumption per capita shall be reduced by 13% in 2035 compared to 2000 (Art. 3-2) (BBL 2017).

Currently, average annual electricity production from hydropower is ca. 36.3 TWh (BFE 2017). Large-scale hydropower development will benefit from three measures offered in the new Energy Act: (1) investment subsidies; (2) market premium; and (3) status of national interest. Investment subsidies will be available for new plants being built until 2030 (Art. 38-1b). For plants with an installed capacity of 1–10 MW, the subsidies may cover up to 60% of the investment costs; for plants with an installed capacity of more than 10 MW, the subsidies will be limited to 40% of the investment costs (Art. 26-1). The market premium aims to compensate a possible difference between production costs and a lower market price. It is capped by the total available financial resources and limited until 2023 (Art. 38-2). Furthermore, it is restricted to HPPs with more than 10 MW of installed capacity and cannot exceed 1 Cent/kWh, (Art. 30-1). The status of national interest improves the basis for weighing up interests (Art. 12); both “protection” and “use” are now of equal value.

3.1.2 Previous studies

Laufer *et al.* (2004) estimated the hydropower potential of Switzerland for different scenarios. They stated that a maximum additional annual potential of 1.761 TWh (worst-case scenario) up to 5.309 TWh (best-case scenario) is feasible in 2035 based on the 2004 values. Total annual electricity production from hydropower in 2035 was estimated between 35.747 TWh (worst-case scenario) and 39.295 TWh (best-case scenario), including environmental flow regulations. Furthermore, the authors calculated that new machines with improved efficiencies could lead to an annual production increase of 0.6–1.1 TWh. Another annual production increase of 0.24 TWh could be achieved by raising full supply levels by 2 m in ten large reservoirs. Finally, they estimated that new HPPs could provide an additional annual electricity production of 2.36 TWh.

Boes (2011) investigated the additional hydropower potential in Switzerland, focussing on the upgrading and optimization of existing HPPs. 4.2 TWh might be achieved under favourable political and legislative conditions by upgrading existing schemes and constructing new HPPs. The extension and upgrade of

existing schemes would allow for 1.3–1.7 TWh (30–40% of the total potential) of additional annual production; the pure exchange of hydraulic machinery with better efficiencies would allow for 0.7 TWh (17% of the total potential) of additional annual production. In these numbers, future production losses at existing schemes due to increased environmental flow prescriptions are taken into account (i.e. the numbers refer to the net increase.).

BFE (2012) examined the hydropower potential in Switzerland until 2050. If today's legal, economical and social condition were maintained, then an additional annual potential of 1.53 TWh seems realistic. If economical and social conditions were improved and legal restrictions maintained, then an additional annual potential of 3.16 TWh seemed feasible. Adapted environmental flow regulations were considered. Large HPPs might provide up to an additional 1.8 TWh in 2050.

Schleiss (2012) investigated the potential of dam heightenings in Switzerland. Many dams could be heightened by 10% of their original height because they have enough excess bearing capacity. Existing waterways could be used with minor adoptions. 19 dams could be heightened by 10% and this would lead to an additional 700 hm³ of storage volume and an additional annual winter production of 2 TWh. Dam heightening would be feasible in these cases, because the dams cannot store the entire inflow from summer. At these locations, winter electricity production could therefore be increased significantly. Examples of successful dam heightenings are, for example, *Lac de Mauvoisin* or *Luzzone*. The former was heightened by 13.5 m (from 236.5 m to 250 m), which led to an additional storage volume of 30 hm³ and an additional annual winter electricity production of 0.1 TWh. The latter was heightened by 17 m (from 208 m to 225 m), leading to an additional storage volume of 20 hm³ and an additional annual winter electricity production of 0.06 TWh.

Haeberli *et al.* (2013) investigated the potential of new HPPs in the periglacial Swiss Alps. By applying the model presented by Linsbauer *et al.* (2012), they identified 500–600 depressions below glaciers, which might eventually be filled with water and finally become new lakes. Most lakes would have maximum depths of 50 m. 40 lakes would have a volume of more than 10 hm³. Lakes with volumes of more than 50 hm³ might form at *Aletsch Glacier*, *Gorner Glacier*, *Otemma Glacier*, *Corbassière Glacier* and *Gauli Glacier*. Today, newly formed lakes at *Lower Grindelwald Glacier*, *Trift Glacier*, *Plaine Morte Glacier*, *Patü Glacier*, *Gauli Glacier* and *Rhône Glacier* might already be used for hydropower. The largest depression is located at *Konkordia Place* in the middle of *Aletsch Glacier* with a maximum depth of 300 m and a volume of 250 hm³, which equals the volume of *Lac d'Emosson* (Linsbauer *et al.* 2012). Except from a few case studies, Haeberli *et al.* (2013) did not present estimates of hydropower potential for electricity production, however.

3.2 Methods

3.2.1 Site selection

Site selection was based on expected glacier runoff volumes. The runoff volumes were computed based on data by Huss and Hock (2015) and Farinotti *et al.* (2016). Huss and Hock (2015) computed the mass changes of 197 654 glaciers worldwide during the 21st century, excluding the ice-sheets of Greenland and Antarctica. This *Global Glacier Evolution Model (GloGEM)* was driven by monthly near-surface air temperature and precipitation from 14 Global Circulation Models (GCM), forced by the emission scenarios RCP2.6, RCP4.5 and RCP8.5. From 2010 to 2100, the global glacier volume losses will be in the range of 25–48%.

Farinotti *et al.* (2016) analysed this data set and derived runoff projections for 1576 glaciers in Switzerland. Four GCM were skipped because they do not use RCP2.6, so there are only ten GCM remaining¹⁶. The runoff data is available as monthly averages for the area of the current glacier outline. Precipitation is included, but runoff from non-glaciated parts within the catchment is not considered.

In the present study, only RCP4.5 was considered (as it is the intermediate scenario between the extremes of RCP2.6 and RCP8.5) and all ten GCM were averaged. The average of the years 2017–2035 was taken, because this is the time frame for the first set of measures of the Swiss *Energy Strategy 2050*. Within this time frame, the differences between RCP4.5 and RCP8.5 are not distinct (Figure 2), so the approach of analysing RCP4.5 only is justifiable. For the time period 2017–2035, annual runoff volumes of RCP2.6 are only 2% lower on average (9% lower on maximum) compared to RCP4.5; annual runoff volumes of RCP8.5 are 1% higher on average (10% on maximum) for RCP8.5 compared to RCP4.5. By the end of the century, for the time period 2090–2100, annual runoff volumes of RCP2.6 are 9% lower on average (20% on maximum) or 2% higher on average (20% on maximum) for RCP8.5, both compared to RCP4.5. Ice-free sites were investigated further if the average annual runoff volume between 2017 and 2035 exceeded 10 hm³. HPPs with lower annual runoff volumes would require more than 1500 m head to be classified as large-scale hydropower¹⁷ assuming 3000 production hours and were therefore neglected. Nevertheless, runoff from these catchments can be used in combination with larger catchments with water transfer systems. With these simplifications, the

¹⁶ *CSIRO-Mk3-6-0, GFDL-CM3, GISS-E2-R, HadGEM2-ES, INMCM4, IPSL-CM5A-LR, MIROC-ESM, MPI-ESM-LR, MRI-CGCM3 and NorESM1-M*

¹⁷ in Switzerland, the differentiation between small-scale hydropower and large-scale hydro-power depends on installed capacity: HPPs with less than 10 MW are small-scale; HPPs with more than 10 MW are large-scale

data set was reduced to 62 glaciers. Runoff from non-glacierized parts of the catchments was not taken into account. An upgrade of existing HPPs was explicitly considered.

3.2.2 Site rating criteria

At this stage, all remaining sites are considered technically feasible. The feasibility is modulated, however, by economical, environmental and social feasibility. Therefore, all 62 sites were subjected to an evaluation matrix to rate them consistently, respecting the classical goals of sustainability. The 16 criteria (Table 7) were grouped into the domains economy, environment and society. Each criterion has a value of 1, 2, or 3, depending on target achievement. 1 is low target achievement, 2 is medium target achievement and 3 is high target achievement. Below, the criteria and rating are explained in detail.

The criteria and structure of the evaluation matrix was chosen to adequately rate HPPs in the Swiss periglacial environment. The criteria weights are generally subjective and are based on personal experience. They reflect the Swiss framework with its specific economical, environmental and social regulations and restrictions. The weights were varied during a sensitivity analysis (i.e. by setting all weights to an equal value of 6.25% or by choosing high weights for environmental criteria like degree of protection), but the order of best-rated sites did not significantly change. Hence, the ranking is quite robust. Furthermore, it has to be noted that some criteria can be assigned to other domains, for example “degree of protection”, which is both an environmental and social criterion.

Installed capacity

The installed capacity was calculated as:

$$W = \eta g \rho Q_d H \quad (40)$$

where W is the capacity [W]; η is the overall efficiency [-]; Q_d is the turbine design discharge [m^3/s]; and H is the gross head [m]. The overall efficiency was assumed to be 0.73. It includes 10% loss at the turbines and 5% friction loss (Laufer *et al.* 2004) as well as 15% loss due to year-to-year variability and uncertainty in runoff projections, which is the uncertainty in precipitation (CH2011 2011) and a good estimate for uncertainties in glacier runoff projections for the data set used (D. Farinotti / VAW ETH Zurich, pers. comm.). The design discharge for storage HPPs was set as the ratio of annual runoff volume (V_w) to production hours (t_p). The gross head was taken as the vertical distance between the center of mass of the reservoir and the reference level of the turbine.

Table 7: Evaluation matrix applied to rate potential HPPs with rating boundaries and corresponding weights

critierion	1 point if...	2 points if...	3 points if...	weight
economy				60%
installed capacity	< 10 MW	10–20 MW	> 20 MW	10%
annual electricity production	< 50 GWh	50–100 GWh	> 100 GWh	10%
investment costs	high	intermediate	low	11%
evolution of annual runoff	reduction > 25%	reduction < 25%	increase > 25%	3%
reservoir sedimentation	infill time < 100 years	infill time 100–1000 years	infill time > 1000 years	7%
earthquake vulnerability	Zone 3 (a and b)	Zone 2	Zone 1	3%
impulse wave vulnerability	most slopes 30–45°	few slopes 30–45°	no slopes 30–45°	3%
flood protection	daily storage	monthly storage	seasonal storage	3%
flexibility & storage capacity	run-of-river HPP	storage HPP	pumped storage HPP	10%
environment				25%
visibility from settlements	visible	not visible	no dam, natural lake	3%
environmental flow	natural river	impaired river	artificial river	7%
sediment continuity	trap efficiency > 90%	trap efficiency 50–90%	trap efficiency < 50%	10%
hydro- and thermopeaking	release into river	release into lake	pumped storage scheme	5%
society				15%
degree of protection	high (BLN areas)	low (UNESCO, Emerald a.o.)	no protected areas	7%
land use	settlement areas	agricultural area or forests	unproductive areas	5%
tourism	negative impacts	negligible impacts	positive impacts	3%

The center of mass was assumed to be 40% of the maximum reservoir depth below the full supply level. HPPs with an installed capacity of less than 10 MW were rated with 1 because they cannot benefit from the market premium (BBL 2017). HPPs with 10–20 MW were rated with 2 and HPPs with more than 20 MW with 3.

Annual electricity production

The annual electricity production is the product of installed capacity W and the annual production hours t_p :

$$G = W t_p \quad (41)$$

It was assumed that run-of-river power plants have 5000 full-load production hours per year (ca. 13.7 hours per day), whereas storage plants have 3000 full-load production hours per year (ca. 8.2 hours per day). Annual electricity production estimates were calculated based on natural runoff only; that is, pumping operations were not included. HPPs with an annual electricity production below 50 GWh were rated with 1, HPPs with 50–100 GWh with 2 and HPPs with more than 100 GWh with 3.

Investment costs

Investment costs cannot be calculated at this stage, therefore they were rated qualitatively. Six factors were defined that can either be positive or negative. A negative and a positive factor level out. If more positive than negative factors are obtained, then the HPP is rated with 3; if more negative factors are obtained, then the HPP is rated with 1. Neutral HPPs were rated with 2. The factor and corresponding thresholds were defined as follows:

- dam height: positive if less than 150 m. This threshold follows the ICOLD¹⁸ definition of a “major” dam (Fichtner 2015), and it is related to the fact that only 5% of all 168 large dams in Switzerland are higher than 150 m.
- tunnel lengths (water transfer and power tunnels): positive if less than 2 km. For tunnels longer than ca. 2 km, tunnel boring machines with high investment costs become economically feasible (Girmscheid 2003).
- HPP type: positive if run-of-river or storage HPP. Pumped storage HPP require pumps or pump-turbines which are expensive compared to pure turbines.

¹⁸ International Commission On Large Dams

- gross head: positive if the gross head is less than 500 m. HPPs with heads lower than ca. 500 m can operate with Francis or Pelton turbines, so there are more degrees in freedom regarding turbine selection and therefore the most economical solution can be chosen.
- surge shaft: positive if the ratio of power tunnel length to gross head is less than 4. A rule of thumb shows that no surge shaft is needed for such HPPs, which will likely result in reduced investment costs.
- distance to access road: positive if less than 2 km. Especially in high-Alpine environments, accessibility of the construction site is a major issue; and often a tunnel is required, so that the same threshold as for tunnel lengths applies.

Evolution of annual runoff

Average annual runoff volumes of the time periods 2017–2035 and 2090–2099 were compared. HPPs where a reduction of more than 25% (from 2017–2035 to 2090–2099) is expected were rated with 1 and HPPs where an increase is expected were rated with 3. HPPs with only a moderate reduction of less than 25% were rated with 2.

Reservoir sedimentation

Reservoir sedimentation was considered by computing infill times using the approach of Gurnell *et al.* (1996). HPPs with infill times below 100 years were rated with 1 because they will be significantly affected by reservoir sedimentation. HPPs with infill times above 1000 years were rated with 3 as the impacts of reservoir sedimentation are of inferior importance. HPPs with infill times in the range of 100–1000 years were rated with 2.

Earthquake vulnerability

Earthquake vulnerability of the dams was checked according to the classification of SNV (2003). Dams in zone 3 were rated with 1, dams in zone 2 with 2 and dams in zone 1 with 3.

Impulse wave vulnerability

Impulse waves, such as rock falls in summer or avalanches in winter, are expected mainly on slopes with angles of 30–45°. At higher angles, the inner friction angle is usually exceeded and unstable masses continuously slide off in small portions, but not as large volumes at once. At lower angles, friction forces are

usually high enough to prevent large mass movements. If the majority of the reservoir slopes are in the critical range of 30–45°, the site is rated with 1. If the minority of slopes in this critical range, it is rated with 2, and if no slopes are in the critical range, it is rated with 3.

Flood protection

The larger the reservoir volume compared to the annual runoff, the more storage volume may be used for flood protection. Therefore, daily storage reservoirs provide the lowest degree of protection and were rated with 1; monthly storage reservoirs were rated with 2 and seasonal storage reservoirs were rated with 3. All reservoirs that have a volume of at least 40% of the average annual runoff were considered as seasonal storage reservoirs. This ratio is also known as “hydrologic size”, “capacity-inflow-ratio” (CIR), or “turnover rate”.

Flexibility and storage capacity

Storage capacity and power system stability are important regarding future electricity demands. Therefore, run-of-river power plants were rated with 1 because they predominantly rely on natural discharge conditions and have limited options to quickly react to electricity market conditions. Storage power plants were rated with 2 because of their increased flexibility. Pumped storage plants were rated with 3 because they are the most flexible setup possible.

Visibility from settlement area

Visibility from settlement areas was considered as an environmental criterion. Dams visible from settlement area were rated with 1 because in public perception they significantly change the environment. Dams not visible from the settlement area were rated with 2 and reservoirs that can make use of natural lakes and do not require a dam were rated with 3.

Environmental flow

Minimum environmental flows are defined in Art. 31 of BBL (1991). These values must be increased if rare habitats and biocoenoses cannot be properly maintained (Art. 31c) or if there is a higher interest against water withdrawal than in favour (Art. 33); for example, the protection of a natural habitat (in particular the fish fauna) or the conservation of the diversity of fauna and flora. Natural rivers will require more restrictive environmental flow regulations and are therefore rated with 1. Purely artificial reaches may be less restrictive and are consequently rated with 3. Partly artificial and impaired reaches are rated with 2.

Sediment continuity

According to Art. 43a of BBL (1991), reservoirs may not interrupt bed load transport in a way that flora or fauna are seriously harmed. Therefore, reservoirs with a trap efficiency of more than 90% were rated with 1; sediment continuity is practically prevented. Reservoirs with a trap efficiency of less than 50% were rated with 3 because they still allow more than half of the sediment to pass through. Reservoirs with trap efficiencies in-between were rated with 2.

Hydro- and thermopeaking

Short-term, rapid artificial changes in discharge and water level in rivers (hydropeaking) must be prevented or eliminated, as Art. 39a of BBL (1991) states. There are not yet regulations regarding thermopeaking. The extent of the measures against hydropeaking depends, amongst others, on the ecological potential of the downstream water body. It is assumed that a release of turbinated water into a river is most problematic and therefore it was rated with 1. Vice versa, a pumped storage scheme was rated with 3 because no natural habitat is directly affected. Release into a lake was rated with 2 because the impact will likely be moderate.

Degree of protection

19% of the Swiss territory are protected by the *Federal Inventory of Landscapes and Natural Monuments of National Importance* (so-called BLN¹⁹ areas). These areas deserve a high degree of protection, because they are unique in Switzerland or representative for a characteristic type of landscape, or they are especially attractive because of their quietness, privacy, or beauty. HPPs located in BLN sites were rated with 1 because opposition will likely be high. A lower degree of protection applies for *UNESCO World Heritage* sites or the *Emerald Network*,²⁰ and others. These HPP sites were rated with 2. If no protected areas are affected, the HPP sites were rated with 3.

Land use

HPP and reservoir locations within settlement areas were rated with 1 because they will likely face the heaviest opposition. Vice versa, reservoir locations within unproductive areas (such as glacier forefields) will likely be accepted and

¹⁹ BLN = Bundesinventar der Landschaften und Naturdenkmäler

²⁰ Emerald Network is known as "Smaragd-Netzwerk" in Switzerland

are therefore rated with 3. Locations in agricultural areas or forests were rated with 2.

Tourism

New reservoirs may have positive or negative impacts on tourism. Positive impacts could be new recreational activities such as water sports or fishing. Negative impacts include, for example, loss of sights, hiking or skiing trails. Reservoirs with negative impacts on tourism were rated with 1, reservoirs with positive impacts were rated with 3. Reservoirs with negligible impacts on tourism were rated with 2.

3.2.3 Evaluation matrix

The criteria, rating boundaries and weights are summarized in Table 7. Economy was chosen as the most important domain with 60%, followed by environment with 25% and society with 15%. Each potential HPP was assessed by rating each criterion with 1, 2 or 3 and multiplying this value with the respective weight. Sites with the highest scores were then investigated further. The assessment of each individual site can be found in Gauye *et al.* (2017) and Helfenberger *et al.* (2017).

3.3 Results

3.3.1 Best-rated potential HPPs

Aletsch Glacier, *Gorner Glacier*, *Grindelwald Glacier*, *Hüfi Glacier*, *Rhône Glacier*, *Roseg Glacier* and *Trift Glacier* were rated best in the assessments for new HPPs. *Trift Glacier* was not investigated further, because the future operator *KWO* already computed the basic values. The characteristics of these seven new HPPs are summarised in Table 8 and are described more detailed below.

It has to be noted that these reservoirs achieve 192–213 points out of the maximum 300 points (and the minimum of 100 points). This shows that even the best-rated sites have significant drawbacks or, vice versa, the most feasible sites are already being exploited and only partially well-suited sites remain.

New pumped storage HPPs would be feasible at *Allalin Glacier* or *Schwarzberg Glacier* (both combined with *Mattmarksee*), *Oberaletsch Glacier* (combined with *Gebidem*), *Brunegg/Turtmann Glacier* (combined with *Turtmann reservoir*), *Corbassière Glacier* (combined with *Lac de Mauvoisin*), *Gauli Glacier* (combined with *Grimmsee*). These sites were not investigated further, as they strongly interact with existing HPPs.

Table 8: Best-scored potential future HPPs in the periglacial environment of Switzerland (V_w is the annual runoff volume; V_{min} is the minimum reservoir volume needed for all-year production; V_{max} is the maximum reservoir volume needed for winter production only; V_l is the reservoir volume achieved with bed rock topography of Farinotti *et al.* (2016), marked with * or *swissALTI3D*, marked with +; Q_d is the turbine design discharge; z_{max} is the full supply level; h_{max} is the maximum reservoir depth; z_{turb} is the turbine level; W is the installed capacity; G is the annual electricity production; z_{casc} is the elevation of the lowermost turbine in the whole cascade; and E is the energy equivalent, defined as the amount of energy that can be produced with the reservoir volume over the whole cascade) [N.B.: data for *Trift Glacier* was provided by *KWO* and includes values of the preliminary design study only (pers. comm.)]

reservoir location [glacier]	V_w [hm ³]	V_{min} [hm ³]	V_{max} [hm ³]	V_l [hm ³]	Q_d [m ³ /s]	z_{max} [m a.s.l.]	h_{max} [m]	z_{turb} [m a.s.l.]	W [MW]	G [GWh]	z_{casc} [m a.s.l.]	E [GWh]
Aletsch Glacier	309	170	291	181*	28.6	1880	200	1445	73	218	700	396
Gorner Glacier	199	108	186	168*	18.4	2300	140	1650	78	235	–	199
Grindelwald Glacier	94	48	86	71+	8.7	1520	160	950	28	85	–	64
Hüfi Glacier	44	23	41	36+	4.1	1780	140	520	35	105	–	86
Rhône Glacier	56	30	53	46*	5.2	2300	100	1750	19	57	1445	75
Roseng Glacier	96	53	92	78+	8.9	2260	120	1000	77	231	530	261
Trift Glacier	154	–	–	85	21.0	1776	167	1327	80	145	620	215
Total									390	1076		1296

3.3.1.1 Aletsch Glacier

The reservoir at *Aletsch Glacier* is mainly fed by *Aletsch Glacier* itself and its adjacent *Mittelaletsch Glacier*. 90% of the runoff originates from *Aletsch Glacier*, 10% originates from *Mittelaletsch Glacier*. Average annual runoff volumes in the time frame 2017–2035 are 283 hm³ (RCP4.5), 288 hm³ (RCP8.5) or 277 hm³ (RCP2.6) for *Aletsch Glacier* and 26 hm³ (RCP4.5), 26 hm³ (RCP8.5) or 25 hm³ (RCP2.6) for *Mittelaletsch Glacier*. As stated above, the difference between the different RCPs is negligible within the near future, given the overall uncertainties in such runoff projections. The catchment area is 144 km², of which 90 km² (63%) are currently covered by glaciers. 54 km² are non-glaciated. These areas are not considered in the annual runoff volumes, but they will lead to a significant contribution to the runoff, available for environmental flows.

Downstream of *Aletsch Glacier* is the reservoir *Gebidem* (Section 4.2.1.3). Full supply level is at 1436.5 m a.s.l. The reservoir has a volume of 9.2 hm³ and is small compared to the annual runoff volume of 430 hm³ (turnover rate 0.02). The water of *Gebidem* is turbined in the power station in *Bitsch*. This HPP of *Electra-Massa* has a design discharge of 55 m³/s, and the head is 750 m. The installed capacity is 340 MW, the annual electricity production is 564 GWh. Furthermore, there is the intake of the HPP *Aletsch-Mörel* at 1442 m a.s.l. in the *Massa* gorge, upstream of the reservoir. Design discharge of this HPP is 7 m³/s, which is relatively low compared to the natural discharge, and the head is 700 m. Installed capacity is 38 MW, annual electricity production is 138 GWh.

Given these boundary conditions, it was decided that a new HPP has to release the water into *Gebidem* reservoir or the *Massa* gorge at an elevation of 1442 m a.s.l. to ensure that the HPPs *Electra-Massa* and *Aletsch-Mörel* maintain production. Turbine axis of the new HPP was assumed at 1445 m a.s.l. A dam with a height of 200 m could be built at today's glacier terminus at 1680 m a.s.l., just upstream of the confluence of *Massa* and *Oberaletsch-/Driestbach*. Full supply level would be 1880 m a.s.l. The reservoir volume—computed with the topography provided by *swissALTI3D*²¹—would be 80 hm³ with *Aletsch Glacier* being partly inside the reservoir. If the reservoir volume is computed with the bed rock topography provided by Farinotti *et al.* (2016), a volume of 181 hm³ will be achieved. A minimum reservoir volume of 170 hm³ is required to ensure a production of 8.2 hours each day (i.e. 3000 production hours distributed equally over the whole year). A reservoir volume of 290 hm³ would be needed to produce during 16.4 hours each day in the winter season only (i.e. 3000

²¹ https://shop.swisstopo.admin.ch/de/products/height_models/alti3d

production hours distributed equally October–March). The reservoir is shown in Figure 14a.

3.3.1.2 Gorner Glacier

The reservoir at *Gorner Glacier* is essentially fed by the glacier itself. Average annual runoff volumes in the time frame 2017–2035 are 199 hm³ (RCP4.5), 201 hm³ (RCP8.5) or 191 HM (RCP2.6). Again, RCP4.5 and RCP8.5 are nearly identical, and RCP2.6 would lead to a reduction by 4% only. The catchment area is 76 km², of which 56 km² (74%) are covered by glaciers. 20 km² of the catchment are not considered in the annual runoff volumes.

Gorner Glacier is part of the highly complex HPP *Grande Dixence* (Figure 16). At an elevation of 2005 m a.s.l, water is taken from *Gornera* and conveyed into the reservoir *Z'Mutt*, from where it is pumped into *Lac des Dix*. The intake has a maximum discharge of 26 m³/s. Each year, ca. 140 hm³ are being pumped from *Z'Mutt* reservoir. Apart from water of *Gorner Glacier*, *Z'Mutt* reservoir is fed by runoff from *Bis Glacier* and *Schali Glacier*. Furthermore, the reservoir is located closely downstream of the pumping station *Stafel*, which is fed by *Zmutt Glacier*, *Findel Glacier*, *Mischabel Glaciers*, *Furgg Glacier*, *Upper Theodul Glacier* and various others. It can be assumed that the system would be able to compensate losses from *Gorner Glacier*: Westaway (2000) showed that in the future even a slight warming of 1.4 °C and an increase in annual precipitation of only 2.6% would lead to an increase in annual inflow of 26%. Therefore, existing infrastructure is not considered further.

The water of *Gorner Glacier* could be turbinated at *Zermatt* at an elevation of 1650 m a.s.l. In the narrow gorge of *Gagenhaupt*, at 2160 m a.s.l., a dam with a height of 140 m could be built. Full supply level would be at 2300 m a.s.l. The reservoir volume would be 34 hm³ with the current topography, but up to 168 hm³ if the bed rock topography is used. The minimum reservoir volume for an equally-distributed whole year production is 108 hm³; for equally distributed winter production it is 187 hm³. The reservoir is shown in Figure 14b.

3.3.1.3 Lower Grindelwald Glacier

The reservoir at *Lower Grindelwald Glacier* would receive water from both *Lower Grindelwald Glacier* and *Upper Grindelwald Glacier*. 70% of the runoff originates from *Lower Grindelwald Glacier*, 30% from *Upper Grindelwald Glacier*. Average annual runoff volumes in the time frame 2017–2035 are 67 hm³ (RCP4.5), 68 hm³ (RCP8.5) or 66 hm³ (RCP2.6) from *Lower Grindelwald Glacier*, and 27 hm³ (for all three RCPs) from *Upper Grindelwald Glacier*, respectively. The catchment area is 53 km², of which 23 km² (43%) are currently covered by glaciers. 30 km² of the catchment are non-glaciated, but nevertheless will contribute to runoff.

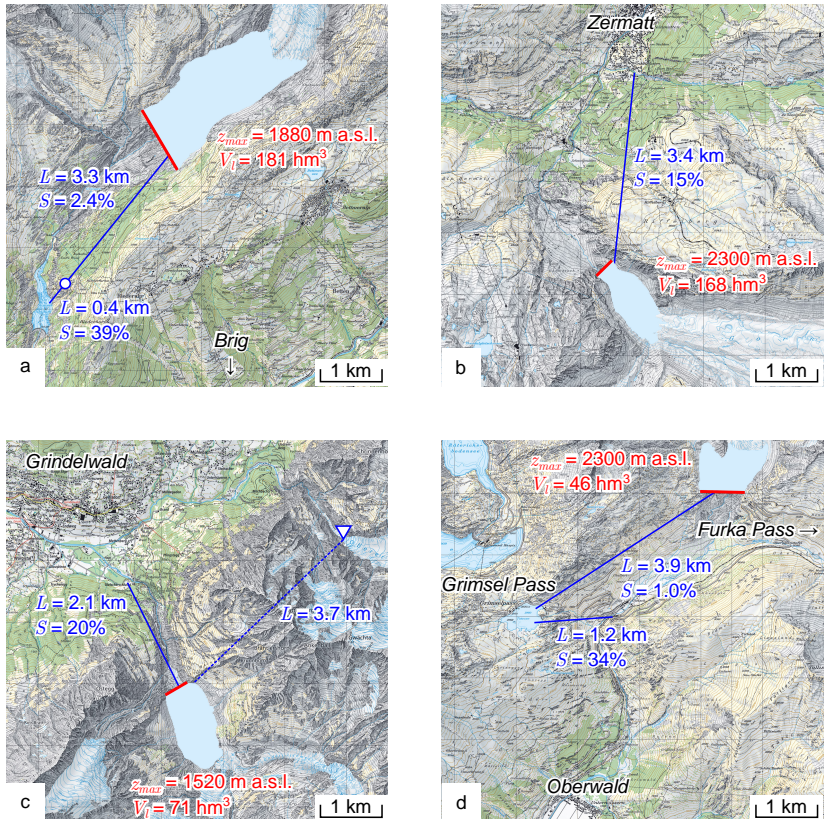


Figure 14: Possible layout of the HPPs at (a) *Aletsch Glacier*, (b) *Gorner Glacier*, (c) *Grindelwald Glacier* and (d) *Rhône Glacier*; z_{max} is the full supply level; V_l is the reservoir volume; L is the length; d the diameter; and S is the slope of a tunnel; the circle \circ marks the location of the surge shaft and therefore the change from pressure tunnel to pressure shaft; the triangle ∇ indicates intakes; and dashed lines are water transfer tunnels [topographical maps reproduced by permission of swisstopo (JA100120)]

In 2005, a lake started forming at the terminus of *Lower Grindelwald Glacier*. It grew larger each season. The volume was 0.8 hm^3 in 2008 and 2.6 hm^3 in 2009 (Germann 2012). From time to time it emptied rapidly, leading to flood events downstream. Therefore, a 2.13 km long tunnel was built in 2010 to control the lake level and prevent outburst floods. The intake is at 1373 m a.s.l. and maximum discharge capacity is $50 \text{ m}^3/\text{s}$. This system would become obsolete with a new reservoir. Turbine level of the new HPP was set at 950 m a.s.l. in *Grindelwald*. The dam could be built at *Bäregg* at 1360 m a.s.l. With a height of 160 m, full supply level would be at 1520 m a.s.l. The resulting reservoir would have a volume of 71 hm^3 with the current topography as well as with the bed rock topography. 48 hm^3 are required for all-year production and 85 hm^3 for winter production only. The reservoir is shown in Figure 14c.

3.3.1.4 Hüfi Glacier

An existing proglacial lake at the tongue of *Hüfi Glacier* could be enlarged further by runoff from the glacier. Average annual runoff volumes in the time frame 2017–2035 are 44 hm^3 (RCP4.5), 45 hm^3 (RCP8.5) or 44 HM (RCP2.6). The catchment area is 23 km^2 , of which 12 km^2 (53%) are covered by glaciers. 11 km^2 of the catchment are not considered in the annual runoff volumes.

Water is currently taken from *Chärstelenbach* in *Bristen* at 824 m a.s.l. and is used for the HPP *Amsteg*. This HPP is mainly operating with water from the *Reuss* valley. It is the lowermost HPP of the *Reuss* cascade *Göschenen-Wassen-Amsteg*. Minor water contributions originate from the *Maderan valley*, *Brunni valley*, *Etzli valley* and *Felli valley*. These minor contributions would be reduced by ca. 20% if the new HPP at *Hüfi Glacier* would be built. It was assumed that this missing water can be compensated and that no further restrictions are needed.

The lake at the tongue of *Hüfi Glacier* at 1640 m a.s.l. could be impounded by a 140 m high dam. Full supply level would be at 1780 m a.s.l. The corresponding lake volume is 36 hm^3 . A minimum volume of 23 hm^3 is required for all-year production and 40 hm^3 are needed for winter production. The water would be turbined at *Amsteg* at 520 m a.s.l. The reservoir is shown in Figure 15a.

3.3.1.5 Rhône Glacier

A natural lake has already formed at the terminus of *Rhône Glacier*. It has a volume of ca. 6 hm^3 and the lake level is at 2200 m a.s.l. Average annual runoff volumes in the time frame 2017–2035 are 56 hm^3 (RCP4.5), 57 hm^3 (RCP8.5) or 54 hm^3 (RCP2.6). The catchment area is 26 km^2 , of which 16 km^2 (62%) are covered by glaciers. 10 km^2 are not considered in annual runoff volumes.

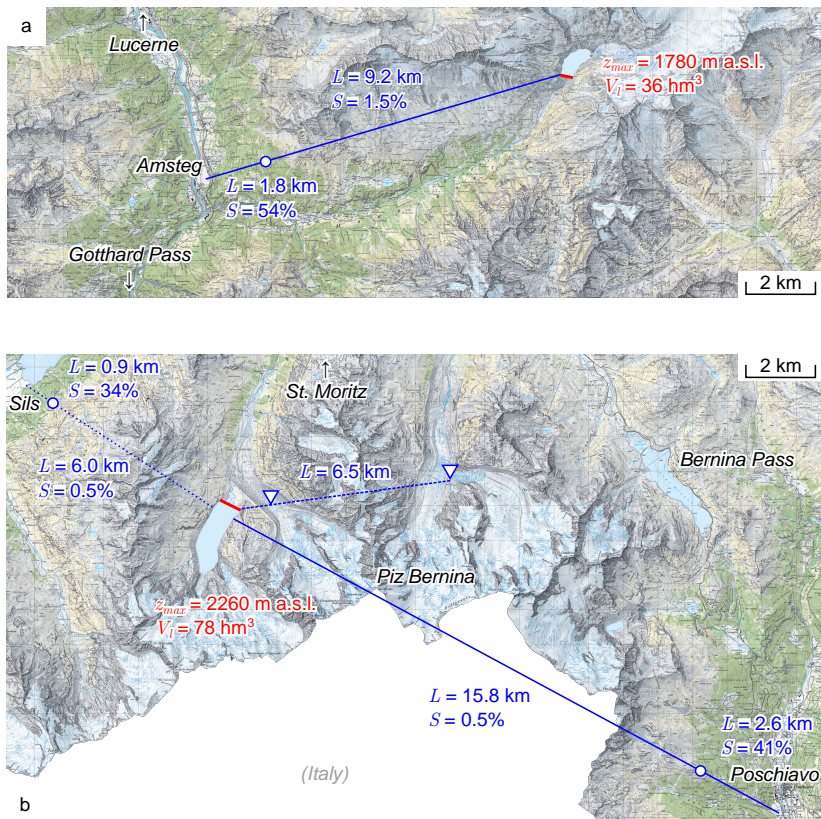


Figure 15: Possible layout of the HPPs at (a) *Hüfi Glacier* and (b) *Roseg Glacier*; z_{max} is the full supply level; V_I is the reservoir volume; L is the length; d the diameter; and S is the slope of a tunnel; the circle \circ marks the location of the surge shaft and therefore the change from pressure tunnel to pressure shaft; the triangles ∇ indicate intakes; dashed lines are water transfer tunnels; and dotted lines are alternative waterways (here: a power station at *Sils* instead of *Poschiavo*) [topographical maps reproduced by permission of swisstopo (JA100120)]

The HPP *Gletsch-Oberwald* was commissioned in 2017. The intake is in *Gletsch* at 1750 m a.s.l. The design discharge is 5.7 m³/s and the head is 300 m. The installed capacity is 14 MW and the estimated annual electricity production is 41 GWh. It was decided that the new HPP has to release the water immediately upstream of the intake of the HPP *Gletsch-Oberwald* to ensure that this HPP can maintain its production.

The natural rock barrier at the terminus of *Rhône Glacier* could be heightened with a dam by 100 m. This would result in a full supply level at 2300 m a.s.l., which equals a reservoir volume of 29 hm³ with the actual topography, where the glacier is part of the reservoir. With the bed rock topography, a reservoir volume of 46 hm³ is computed. 30 hm³ reservoir volume are required to ensure all-year production. 52 hm³ are needed if production shall be restricted to winter. The reservoir is shown in Figure 14d.

3.3.1.6 Roseg Glacier

The reservoir at *Roseg Glacier* would be fed by four glaciers: *Roseg Glacier*, *Tschierva Glacier*, *Morteratsch Glacier* and *Pers Glacier*. *Morteratsch Glacier* and *Pers Glacier* are located within the same catchment and are considered as one glacier. 55% of the runoff result from *Morteratsch/Pers Glacier*, 24% from *Roseg Glacier* and 21% from *Tschierva Glacier*. The average runoff volumes in the time frame 2017–2035 are 53 hm³ (RCP4.5), 55 hm³ (RCP8.5) or 53 hm³ (RCP2.6) from *Morteratsch/Pers Glacier*, 23 hm³ (for all RCPs) from *Roseg Glacier* and 20 hm³ (for all RCPs) from *Tschierva Glacier*. The total catchment area is 52 km², of which 30 km² (58%) are currently covered by glaciers. 22 km² of the catchment are neglected in annual runoff volumes.

The small HPP *Roseg* has its intake in *Roseg valley* at 1905 m a.s.l. The water is turbined in *Punt Muragl*. This HPP has a design discharge of 0.18 m³/s and the head is 180 m. The installed capacity is 0.31 MW, annual electricity production is 1.9 GWh. This HPP is small enough for not being affected by a new HPP. There are no other boundary conditions regarding existing HPPs.

The natural lake *Lej da Vadret* at 2140 m a.s.l. with a volume of 1.5 hm³ (Uehlinger *et al.* 2003) could be impounded by a dam of 120 m height. Full supply level would result at 2260 m a.s.l. The reservoir would have a volume of 78 hm³. A minimum reservoir volume of 53 hm³ would be necessary for all-year production and 89 hm³ are necessary for winter production. The water would be turbined in *Poschiavo* at 1000 m a.s.l. The reservoir is shown in Figure 15b.

3.3.2 Technical potential

The potential future HPPs presented in Table 8 could produce ca. 1.1 TWh electricity each year. This would be enough to achieve the intermediate 2035

goals of *Energy Strategy 2050* regarding electricity production from large hydropower. Storage energy equivalent would be ca. 1.2 TWh. It is computed similar to the annual electricity production, but with two main differences: (a) instead of the design discharge, the ratio of reservoir volume to full production hours is used; and (b) the lowermost turbine level of the whole cascade is used. This is important at *Aletsch Glacier* and *Trift Glacier*, where the water can be turbined further downstream of the power station within the same scheme. The storage energy equivalent is a measure for winter production which will gain importance with the increase of new renewables for electricity production.

3.3.3 Feasibility

Narrow gorges and steep rocky slopes provide favourable technical conditions, although natural hazards will have to be accounted for carefully. Nevertheless, construction site preparation will be costly, there will likely be societal controversy as some sites are located in protected areas and the integration into the existing dense hydropower network will be a major challenge. However, the present study gives an overview of possible future HPP sites in the periglacial environment.

3.4 Discussion

3.4.1 Upgrade projects

Large runoff volumes are in general favourable for HPPs, because they allow high capacities and large productions. Apart from the suggested new HPPs, large annual runoff volumes are expected at *Fiescher Glacier* (105 hm³/a for RCP4.5), *Unteraar Glacier* (97 hm³/a for RCP4.5), *Oberaletsch Glacier* (66 hm³/a for RCP4.5), *Corbassière Glacier* (57 hm³/a for RCP4.5), *Tiefmatten Glacier* (51 hm³/a for RCP4.5), *Findel Glacier* (50 hm³/a for RCP4.5) and *Zinal Glacier* (46 hm³/a for RCP4.5). Runoff from these glaciers is already used for existing HPPs; for example, at *Fieschertal* (*Fiescher Glacier*), *Grimseelsee* (*Unteraar Glacier*), *Gebidem* (*Oberaletsch Glacier*), *Lac de Mauvoisin* (*Corbassière Glacier*), *Lac des Dix* (*Tiefmatten Glacier* and *Findel Glacier*) or *Moiry* (*Zinal Glacier*). All these HPPs could benefit from additional meltwater in the next decades if they were upgraded; for example, with new turbines or dam heightening.

3.4.2 Uncertainties

It is in the nature of things that uncertainties in runoff projections are considerably high. Although RCP4.5 and RCP8.5 lead to similar results in the near future (2017–2035), the differences will become more pronounced in the far future (after 2035). Furthermore, the applied models are another important source of uncertainty. Additionally, only glaciated parts of the catchments were considered, so large parts of the catchments do not contribute to runoff. However, this implies that the given annual runoff volumes will likely be achieved, because the negligence of non-glaciated catchment parts provides large reserves.

The computed reservoir volumes are afflicted with uncertainties as well, as they are based on *swissALTI3D*. This data set has a spatial resolution of 2x2 m. Nevertheless, the reservoir volumes are likely conservative: The current glacier topography is included, but it is likely to decrease or even disappear until the time the reservoirs would be built. Bed rock topography from Farinotti *et al.* (2016) was used for an alternative computation of reservoir volumes. This data set has been derived from ground-penetrating radar measurements; it has a spatial resolution of 50x50 m (at *Aletsch Glacier* and *Gorner Glacier*) or 25x25 m (at *Grindelwald Glacier* and *Rhône Glacier*). This approach is likely on the unsafe side: The topography is far less accurate and debris cover on bed rock is completely neglected. Therefore, the data of *swissALTI3D* has been used in the potential estimates (e.g. in Table 8). At *Hüfi Glacier* and *Roseg Glacier*, the reservoir area is ice-free, so only *swissALTI3D* data set was applied.

The operation modes of the new HPPs depend on the evolution of new renewables as well as on political measures and market conditions. Here, it was assumed that all new HPPs operate as seasonal storages to reduce the winter season deficit imposed by the Swiss *Energy Strategy 2050*, where base load provided by nuclear power plants will be absent due to their phase-out. The need for multi-purpose reservoirs (e.g. for irrigation in dry and hot summers) and the demand for grid regulation and network stabilisation, which may increase significantly (e.g. when the share of volatile, weather-dependent new renewables increase), were neglected.

Assumptions of overall efficiency, full production hours, etc. may be inadequate, as they solely rely on empirical values. Although these uncertainties may significantly affect the estimated potentials (Table 8), the sites selected as best reservoir options are judged to remain among the most interesting of all 62 potential sites.

3.4.3 Challenges

All reservoirs would be located within BLN objects. These areas have a relatively high degree of protection. Although the new Energy Law concedes large-scale

hydropower status of national interest, the projects will definitely face social opposition. The affected BLN objects would be: “1603 Maderan valley – Felli valley” at *Hüfi Glacier*, “1706 Bernese High Alps and Aletsch-Bietschhorn region” at *Aletsch Glacier* and *Grindelwald Glacier*, “1707 Dent Blanche – Matterhorn – Monte Rosa” at *Gorner Glacier*, “1710 Rhône Glacier and forefield” at *Rhône Glacier* and “1908 Upper Engadine Lakes and Bernina massif” at *Roseg Glacier*. Furthermore, the reservoir at *Aletsch Glacier* would be built within the *UNESCO World Heritage* site “*Swiss Alps Jungfrau-Aletsch*”; and the *Roseg valley* is part of the *Emerald Network*. The chances of realization are therefore difficult to predict.

Water from *Roseg valley* naturally flows into the *Inn*, which is a tributary of the *Danube*, and finally into the *Black Sea*. If the proposed scheme was built, the water would be released into the *Poschiavino*, a tributary of the *Adda*. The *Adda* itself is a tributary of the *Po*, so the water would finally flow into the *Adriatic Sea*. The hydrological characteristics of the catchment would therefore be distorted significantly. This problem could be circumvented by turbinizing the water at *Sils* in the *Engadine*. Unfortunately, the elevation difference is distinctively smaller, as *Sils* is at 1800 m a.s.l. whereas *Poschiavo* is at 1000 m a.s.l. This would result in smaller installed capacity and production of 25 MW and 75 GWh, respectively. The corresponding reduction is 68%. Furthermore, a part of the headrace would be on Italian territory in the proposed layout.

Natural hazards might endanger some of the potential future HPPs. Especially the catchment area of *Lower Grindelwald Glacier* has large, steep, instable slopes and hanging glaciers, which increase impulse wave hazard. Instable slopes have been detected at *Aletsch Glacier* as well. Haeberli *et al.* (2012) expect at least two new lakes at *Aletsch Glacier* with surface areas of 2 km² to form in the middle of this century. Because of steep and potentially instable slopes, a dam might be needed to avoid impulse (flood) waves that could endanger the city of *Brig*.

Integration of the new HPPs into the dense Swiss hydropower network is an important issue. It might become a major challenge at *Gorner Glacier*, which interacts with the *Grande Dixence* scheme, and at *Hüfi Glacier*. The *Grande Dixence* scheme has 75 intakes and 5 pumping stations conveying water into *Lac des Dix*. The eastern part of the scheme is shown in Figure 16. Pumping station *Z'Mutt* is fed by *Bis Glacier*, *Schali Glacier* and *Gorner Glacier*. 140 hm³ of water are pumped each year. For RCP4.5, the average annual runoff volumes in the time frame 2017–2035 will be 12 hm³ from *Bis Glacier* and 4 hm³ from *Schali Glacier*. These two glaciers will be minor contributors and *Gorner Glacier* will remain the most important source of water. The missing water due to the new HPP will need to be compensated by other sources. A first option would be

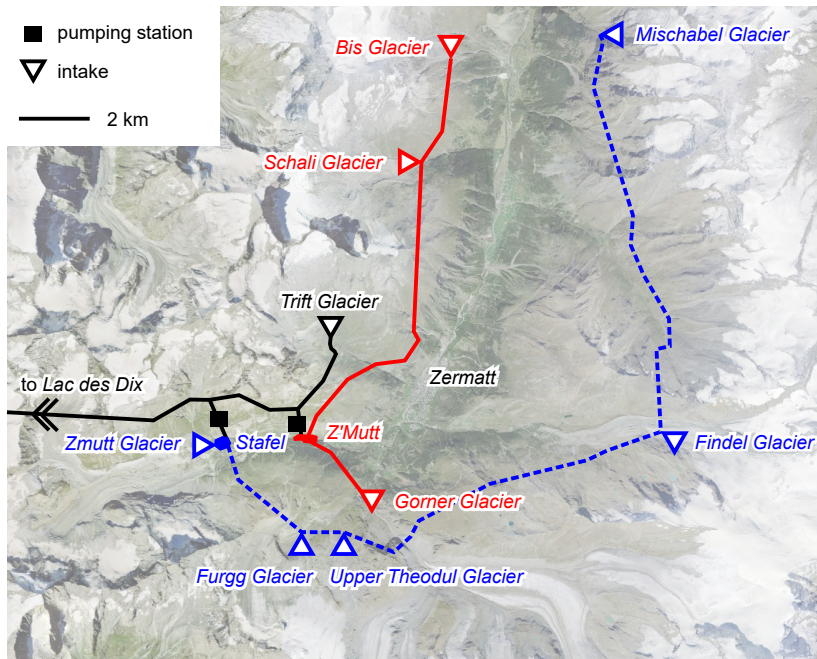


Figure 16: Simplified sketch of the intakes, water transfer tunnels, reservoirs and pumping stations of the eastern part of the *Grande Dixence* scheme [aerial picture reproduced by permission of swisstopo (JA100120)]

using excess water from the pumping station *Stafel*, which is located less than 3 km upstream. This station is fed by *Zmutt Glacier*, *Findel Glacier*, *Mischabel Glaciers*, *Furgg Glacier*, *Upper Theodul Glacier* and various others. 70 hm³ are pumped each year. For RCP4.5, expected average annual runoff volumes for the time frame 2017–2035 are 51 hm³ from *Zmutt Glacier*, 50 hm³ from *Findel Glacier*, 22 hm³ from the *Mischabel Glaciers*, and 23 hm³ from *Furgg Glacier* and *Upper Theodul Glacier*. This is approximately two times the annual pumping volume, so there would be the option to compensate some of the losses at the pumping station *Z'Mutt*. As shown above, a significant increase in inflow can be expected at *Grande Dixence*: Westaway (2000) predicted an increase of at least 26%, which equals 130 hm³ and corresponds to 65% of the deficit imposed by a new reservoir at *Gorner Glacier*. Impacts of a new reservoir at *Hüfi Glacier* on the HPP *Amsteg* cannot be assessed with the data available.

It is important to point out that existing HPPs do not solely rely on runoff from glaciers. In fact, non-glaciated areas contribute higher runoff volumes in most cases. Potential production losses due to new HPPs cannot be estimated without detailed hydrological models of the whole catchment.

3.4.4 Reservoir sedimentation

Control of reservoir sedimentation is a prerequisite to ensure a sustainable use of reservoirs. Annual suspended sediment input into the reservoirs can be estimated using the approach of Gurnell *et al.* (1996), shown in Equation (2). For the proposed new HPP reservoirs, the annual sedimentation input and infill times (neglecting potential wash load, see below) of Table 9 would result. It can be seen that the reservoir at *Gorner Glacier* is probably prone to rapid sedimentation.

Alternatively, the approach of Schlunegger and Hinderer (2003), shown in Equation (1), can be used to estimate annual sediment input. The calculated sediment volumes for the investigated new HPPs are shown in Table 9. In all cases, the upper limit of the ranges given by Schlunegger and Hinderer (2003) has been used. Again, *Gorner Glacier* is the reservoir with the fastest infill time.

Although the approach of Schlunegger and Hinderer (2003) has the advantage of underlying field measurements, it inherently neglects effects of climate change, as it is solely based on a constant annual denudation rate and a constant catchment area. The approach of Gurnell *et al.* (1996) has the advantage that changing runoff volumes as a consequence of climate change have a direct impact on sediment input. The former approach gives an estimate of suspended sediment conveyance and neglects bed load conveyance; the latter does not distinguish between different transport modes, it incorporates both modes inherently.

It is important to note that sediment conveyance is not necessarily equal to the sedimentation volume. A part of the sediment will likely be transported through the reservoir as wash load. Sediment volumes are an upper limit of sedimentation volumes and, vice versa, infill times are a lower limit of the expected infill times. Furthermore, all infill times refer to reservoir volumes achieved in the current topography with *swissALTI3D*; for the reservoirs at *Aletsch Glacier*, *Gorner Glacier* and *Rhône Glacier*, these volumes are significantly lower than reservoir volumes achieved with bed rock topography of Farinotti *et al.* (2016). Numerical models are suitable tools to investigate reservoir sedimentation processes in detail and to identify potential risk as well as to derive countermeasures. This will be shown in Section 5.5.2 for the potential reservoir at *Gorner Glacier*, which has the lowest infill time.

Table 9: Annual sedimentation volumes and estimated infill times for the proposed new HPPs (V_w is the annual runoff volume; V_s is the annual sediment volume; t is the infill time; F is the catchment area; and j is the annual denudation rate)

reservoir location [glacier]	Gurnell <i>et al.</i> (1996)			Schlunegger and Hinderer (2003)			
	V_w [hm ³]	V_s [hm ³]	t [a]	F [km ²]	j [mm]	V_s [hm ³]	t [a]
Aletsch Glacier	309	0.1053	760	144	0.50	0.0720	1111
Gorner Glacier	199	0.0630	539	76	0.50	0.0380	895
Grindelwald Glacier	94	0.0263	2703	53	0.30	0.0159	4465
Hüfi Glacier	44	0.0108	3324	23	0.20	0.0046	7826
Rhône Glacier	56	0.0144	2021	26	0.50	0.0130	2231
Roseg Glacier	96	0.0269	2898	52	0.15	0.0078	10 000
Trift Glacier	154	0.0467	1819	49	0.30	0.0147	5782

3.4.5 Layout of the HPP schemes

Proposed layouts of the new HPPs are shown in Figures 14 and 15. The underlying assumptions were:

- roughness of the power waterways was set to a constant value of $85 \text{ m}^{1/3}/\text{s} = 0.6 \text{ mm}$, which is valid for both steel- and concrete-lined tunnels and penstocks;
- a surge shaft is needed whenever the total start-up time exceeds 2.5 s and it should be located close to the surface;
- pressure shaft length should be minimised, while pressure tunnel length should be maximised;
- optimum flow velocities are 3–4 m/s in the pressure tunnel and 5–7 m/s in the pressure shaft;
- at *Aletsch Glacier*, the water shall be released into *Gebidem* reservoir, from which the total runoff is turbinised;
- at *Grindelwald Glacier*, it should be checked if the existing tunnel could be integrated into the new HPP; at this stage, this option was not examined further;

- at *Rhône Glacier*, a surge shaft could be omitted if the existing reservoir *Totensee* was used; furthermore, it was decided to release the water in *Gletsch* upstream of the intake of the newly built HPP *Gletsch-Oberwald*.

All proposed schemes are at the stage of feasibility studies; in the next step, preliminary design studies should examine the sites individually.

3.4.6 Comparison with previous studies

3.4.6.1 HPP potential analysis

Haerberli *et al.* (2013) examined locations where large depressions could become ice-free and consequently be used for new reservoirs. Amongst identifying potential sites, they examined two sites in detail and provided some estimates of installed capacity and electricity production (Table 10).

Fallegger (2014) and Iten (2014) systematically examined HPP potential in Switzerland. They used runoff projections from Farinotti *et al.* (2012) which are based on the SRES-A1B scenario. This scenario can be interpreted as the intermediate scenario between RCP4.5 and RCP8.5, although it is almost identical with RCP8.5 until 2035. Fallegger (2014) used site-dependent production hours which vary between 1000 and 3000 production hours per year. Iten (2014) used 3000 production hours per year equal to the present study. Both Fallegger (2014) and Iten (2014) budgeted ca. 20% of the annual runoff volume for environmental flow. Fallegger (2014) used an overall efficiency of 0.8 and Iten (2014) used a value of 0.85, respectively. The results of these two studies are shown in Table 10 as well.

3.4.6.2 Preliminary design studies

Two case studies of Maurizio (2014) and Plozza (2014) examined hydropower potential at *Gorner Glacier*. Runoff projections from Farinotti *et al.* (2012) were used, in combination with the bedrock topography later published in Farinotti *et al.* (2016). In both case studies, six full production hours each day were assumed. Maurizio (2014) used an overall efficiency of 0.81 and planned a new HPP without taking the existing network of *Grande Dixence* into account. Vice versa, Plozza (2014) integrated a new HPP into this scheme, which limited the degrees of freedom significantly, as the water had to be released into the reservoir of *Z'Mutt*. He used an overall efficiency of 0.85. The estimated installed capacity and annual electricity production differ by one order of magnitude due to the strong reduction of the head in the study of Plozza (2014). The main characteristics of the two studies are shown in Table 10.

Another case study at *Oberaletsch Glacier* was carried out by Rulli (2017). Runoff projections from Farinotti *et al.* (2016) were used. Six production hours

Table 10: Characteristics of potential future HPPs as proposed in other studies (z_{max} is the full supply level; V_l is the reservoir volume; V_w is the total annual runoff volume; Q_d is the design discharge; H is the head; W is the installed capacity; and G is the annual electricity production)

reservoir location [glacier]	study [author]	z_{max} [m a.s.l.]	V_l [hm ³]	V_w [hm ³ /s]	Q_d [m ³ /s]	power station [city/reservoir]	H [m]	W [MW]	G [GWh]
Allalin Glacier	Fallegger (2014)	2710	5	30	5	Mattmark	510	21	28
Corbassière Glacier	Fallegger (2014)	2520	13.5	49	9	Mauvoisin	550	42	50
Ferpècle Glacier	Haerberli <i>et al.</i> (2013)	2510	52		100	Mauvoisin	530	500	1100
Fischer Glacier *	Fallegger (2014)	2160	2	45	8	Ferpècle	255	17	21
Gauli Glacier	Fallegger (2014)	1780	44	194	15	Fieschertal	645	17	77
Gorner Glacier	Haerberli <i>et al.</i> (2013)	2200	60	89	20	Räterichsbodensee	400	84	83
	Maurizio (2014)	2225	80	237	17.6	Stalden	1160	165	262
	Piozza (2014)	2214	74	74	12.1	Z'Mutt	225	25	40
Grindelwald Glacier	Iten (2014)	1520	72	110	10.4	Grindelwald	470	42	123
Hüfi Glacier	Iten (2014)	1850	56	95	8.5	Amsteg	1175	88	257
Oberaletsch Glacier	Fallegger (2014)	2180	55	96	20	Gebidem	740	124	130
	Rulli (2017)	2280	31	60	7.6	Gebidem	880	53	115
Rhône Glacier	Fallegger (2014)	2250	28	75	10	Oberwald	865	73	120
	Hutter (2017)	2160	11	50	5.5	Gletsch	490	12	50
Zinal Glacier	Fallegger (2014)	2050	13	129	15	Mottec	490	61	117

* Fiescher Glacier would be an upgrade of an existing scheme. Therefore, only new (additional) installed capacity and electricity production to the existing 64 MW and 140 GWh are given

per day and an overall efficiency of 0.8 were assumed. The reservoir volume would currently be 31 hm³, but achieve 88 hm³ once it is completely ice-free. The reservoir would release water into *Gebidem* and could be used as a pumped storage reservoir. Main characteristics are summarised in Table 10.

Hutter (2017) examined the hydropower potential at *Rhône Glacier* using the runoff projections from Farinotti *et al.* (2016). 2130 production hours and an overall efficiency of 0.92 were assumed. The environmental flow was set equal to the values of the HPP *Gletsch-Oberwald* located directly downstream (0.2 m³/s except for September with 0.75 m³/s). The reservoir volume would currently be 11 hm³, but increase to 45 hm³ once the glacier in the reservoir will have melted. The main characteristics are shown in Table 10.

3.5 Conclusions

The intermediate 2035 goals of the Swiss *Energy Strategy 2050* regarding electricity production from hydropower can be achieved by different means. Currently, there is an anticipated deficit in annual electricity production of ca. 1.1 TWh. A first contribution towards additional production arises from improved efficiency of existing schemes. Laufer *et al.* (2004) estimated that an additional annual electricity production of 0.6–1.1 TWh would be feasible. In the best case, the deficit would be fully compensated; In the worst case, about half of it could be covered. Combined with lifting the full supply level of existing reservoirs, the deficit could be completely eliminated. If the dam at *Grimmelsee* was heightened by 23 m, an additional water volume of 85 hm³ could be stored, which results in an additional annual electricity production of 0.24 TWh. This is more than 1/5 of the deficit. Although the upgrade of *Grimmelsee* faced large opposition, upgrade projects of existing infrastructure will likely be the easiest way to achieve the goals of the Swiss *Energy Strategy 2050*. Schleiss (2012) identified 19 dams that could be heightened by 10%, leading to an additional storage volume of 700 hm³ and an additional annual winter electricity production of 2 TWh, which would fulfill the demands of the Swiss *Energy Strategy 2050*.

Apart from upgrading existing HPPs, new reservoirs could be built in the periglacial environment. New lakes started forming at the tongues of *Lower Grindelwald Glacier*, *Hüfi Glacier*, *Rhône Glacier*, *Roseg Glacier* or *Trift Glacier*. These locations are favourable for new reservoirs. Together with new HPPs at *Aletsch Glacier* and *Gorner Glacier*, these seven new HPPs could also achieve the 2035 goals of the Swiss *Energy Strategy 2050* and increase annual electricity production from hydropower production by 1.1 TWh. Although this increase may seem small, it should be noted that the exploitable Swiss hydropower potential under today's severe environmental and economic restrictions is limited.

Additionally, new reservoirs could help to increase the production of existing HPPs. Examples are, amongst others, *Fiescher Glacier* or *Corbassière Glacier*, where the HPPs could be operated as pumped storage scheme, which would provide additional flexibility in electricity supply.

Potential estimates are subjected to considerable uncertainties. Case studies and preliminary design studies showed that estimates of installed capacity and annual electricity production might differ significantly. These differences are mainly due to the underlying climate change scenarios (e.g. RCP4.5 vs. SRES-A1B) and the resulting runoff volumes, estimates of environmental flows and overall efficiency. The estimate of production hours has a major impact on the required reservoir volume and the installed capacity, but only minor impact on annual electricity production (if the other parameters are kept). The estimate of production hours and reservoir volume are linked to the question whether a new HPP should cover all-year or winter production. This question cannot be answered without taking new renewables like wind turbines or solar panels into account. The future development of these energy suppliers is very uncertain, as it is strongly linked with political boundary conditions.

At *Aletsch Glacier*, *Gorner Glacier* and *Rhône Glacier*, the reservoir volumes were calculated using bed rock topography (Table 8) derived from ground-penetrating radar measurements, which have a resolution of $\pm 25\text{--}50$ m. Lapazaran *et al.* (2016) showed that these measurements are affected by various sources of errors, such as velocity of the measurement vehicle, bed slope, refreshing period of the global positioning system (GPS) and triggering interval of the radar. Bed rock elevation can generally be estimated with an accuracy of ± 10 m (D. Farinotti / VAW ETH Zurich, pers. comm.). Combined with the coarse resolution, uncertainties in the bed rock elevation model are relatively high.

The quantities in Table 8 may be significantly affected by these uncertainties. Nevertheless, the sites selected as best reservoir options are judged to remain among the most interesting of all 62 potential sites. Most criteria can be rated relatively precisely, but reservoir sedimentation and sediment continuity are affected with high uncertainties. They account for a weight of 17%, so that site rating significantly depends on the handling of the sediment fluxes. Empirical relationships are insufficient to assess reservoir sedimentation, because they usually miss site-specific configurations. Numerical models allow for a holistic assessment of reservoir sedimentation processes. This will be demonstrated in Section 5.5.2 for the potential future reservoir at *Gorner Glacier*. Such studies should be made for every potential future reservoir to ensure that reservoir use would not be compromised due to failed sediment management.

Some important aspects of HPPs were not considered in this study. These are: (a) runoff from non-glacierized parts of the catchments (which is $1/4$ to $1/2$

of the total area for the investigated HPPs); (b) environmental flow regulations; (c) water loss due to infiltration; and (d) costs. These are important factors that should be addressed in case studies or preliminary design studies. Furthermore, several cantons have their own strategies for the hydropower development, such as Valais²², or adopt overall energy strategies, such as Uri²³. These regional considerations were completely neglected, but are very important, because they define the frame of social and political acceptance. Additionally, atmospheric warming might lead to new claims. Dry seasons might require large reservoirs for drinking water or irrigation, so that water needs to be released in summer instead of winter. Although enough technical potential has been identified to reach the goals of the Swiss *Energy Strategy 2050*, social and political restrictions might endanger its implementation.

Climate change offers new perspectives for hydropower in the periglacial environment. Main findings are:

- (a) Hydropower potential can be enhanced by upgrading existing infrastructure or new HPPs; both upgrade projects and new HPPs would cover the deficit between actual electricity production from hydropower and the target production in 2035 defined by the *Swiss Energy Strategy 2050*.
- (b) 62 sites in the periglacial environment could be of interest for new HPPs, as they will have annual runoff volumes larger than 10 hm³; nevertheless, they can be ranked based on economical, environmental and social criteria and promising sites can be selected.
- (c) Seven new HPPs at *Aletsch Glacier*, *Gorner Glacier*, *Grindelwald Glacier*, *Hüfi Glacier*, *Rhône Glacier*, *Roseg Glacier* and *Trift Glacier* would provide ca. 1.1 TWh per year and thereby fulfil the 2035 goals of the *Swiss Energy Strategy 2050*.
- (d) All potential reservoirs are located within BLN objects, *UNESCO World Heritage* sites, or are part of the *Emerald Network* and will face severe social opposition; furthermore, natural hazards and integration into the existing network will be challenging.
- (e) Upgrade projects are probably the easier course of action; (small) heightening of 10–20 existing dams seems to be most promising approach for the time being, as only a deficit of 1.1 TWh per year has to be covered.

The last finding can be illustrated from an operator's perspective: *KWO* has planned a heightening of *Grimselfsee* and is currently planning a new dam at

²² <https://www.vs.ch/de/web/sefh/strategie-wasserkraft>

²³ https://www.ur.ch/_doc/50442

Trift Glacier. The heightening of the 114 m dam by 23 m (+20%) would lead to an additional annual electricity production of 240 GWh. The new reservoir at *Trift Glacier* with a dam of 167 m would lead to an additional annual production of 145 GWh (which is only 60% of the potential production increase at *Grimselsee*). Estimated costs are 306 Mio. CHF²⁴ for the heightening and 387 Mio. CHF²⁵ for the new reservoir.

Annandale (2015) demonstrated that storage HPPs with large capacity-inflow-ratio offer the greatest resilience to climate change. Nevertheless, reservoir sedimentation management is imperative to prevent storage loss and ensure sustainable use of the reservoirs. This requires a long-term perspective, taking effects of climate change into account. Numerical models allow to simulate reservoir sedimentation under different climate scenarios and variable boundary conditions, but they need to be calibrated and validated first. In Chapter 4, field measurements will be presented that provide the basis for the numerical modelling, which will be presented in Chapter 5.

²⁴ <http://www.grimselestrom.ch/ausbauvorhaben/vergroesserung-des-grimselees/>

²⁵ <http://www.grimselestrom.ch/ausbauvorhaben/speichersee-und-kraftwerk-trift/>

4 Field measurements

4.1 Introduction

Reservoir sedimentation is determined based on the sediment fluxes in the lake. Governing parameters include, amongst others, PSD, SSC and flow velocities. Recent innovations, such as LISST and ADCP, provide new measurement techniques for data acquisition. So far, only few applications of LISST and ADCP in glacier-fed mountain lakes are reported, for example in Kostaschuk *et al.* (2005) and Menczel and Kostaschuk (2013) or Hodder and Gilbert (2007) and Hodder (2009). One reason for that is the fact that these techniques require an accurate calibration and validation with water samples or the like.

In environments different to the periglacial one, LISST and ADCP has been applied in several studies: Haun and Lizano (2015) measured sediment fluxes in a tropical reservoir in Costa Rica and tracked density currents (Haun and Lizano 2016), Lee *et al.* (2016) studied a river plume in Taiwan, Duclos *et al.* (2013) examined dredging plumes in the *Bay of Seine*; Fettweis *et al.* (2006), Bartholomä *et al.* (2009), Santos *et al.* (2014) investigated sediment transport processes in the Belgian coastal zone, the *German Wadden Sea* and in an inner shelf of Portugal, respectively. Tidal currents and their impacts on sedimentation and resuspension were studied by Yuan *et al.* (2008) or Unverricht *et al.* (2014) in *Jiaozhou Bay* and *Mekong Delta*, respectively. Ha *et al.* (2015) measured suspended sediments under ice in the *Arctic Ocean*. These studies demonstrate the wide application range of LISST and ADCP.

In the scope of this project, suspended sediments in the three Swiss reservoirs *Lac de Mauvoisin*, *Griessee* and *Gebidem* were investigated. For the first time, the combination of Secchi disk measurements, water sample analysis, LISST and ADCP was applied systematically to gain profound insights into sediment fluxes in reservoirs in the periglacial environment. The field measurements have been documented in Ehrbar *et al.* (2016a,b, 2017); this chapter is almost identical to these publications.

4.2 Methods

4.2.1 Prototypes

Griessee, *Lac de Mauvoisin* and *Gebidem* were selected as prototypes for field measurements. Some information about these reservoirs are given in Section 2.2.4; basic characteristics are presented in Table 11. *Lac de Mauvoisin* is a large reservoir with a length of more than 5 km. *Griessee* is currently on second place regarding the altitude²⁶. Catchment and reservoir are both affected by climate change. *Gebidem* is a small reservoir, but it faces unique sedimentation rates: infill time is in the order of a few dozens of years.

4.2.1.1 Lac de Mauvoisin

Lac de Mauvoisin (LV03: 593 400 / 92 000²⁷) is situated in the *Pennine Alps* in south-western *Valais* (Switzerland). The reservoir has a total volume of 204 hm³ and a lake surface area of 2.26 km² (FMM 2001). The average annual inflow is 265 hm³; capacity-inflow ratio is 0.77. Full supply level is at 1975 m a.s.l., minimum operating level is at 1825 m a.s.l. (Schleiss *et al.* 1996). The catchment area is 150 km², of which 42% were covered by glaciers in 2009 (Gabbi *et al.* 2012). Main natural inflow rivers are *Dranse de Bagnes* at the southern end of the reservoir and *Cascade du Giétro* at the northern end of the reservoir. Figure 17 shows the inflow region of *Lac de Mauvoisin* near *Dranse de Bagnes*. A water transfer tunnel delivers additional water from the catchments *Corbassière* and *Séry* into the reservoir. The water of *Lac de Mauvoisin* scheme is turbined in four power stations at *Chanrion*, *Fionnay*, *Champsec* and *Riddes*. The installed power is 386 MW and annual production is roughly 900 GWh (FMM 2016), which equals ca. 2.4% of the total annual production of Swiss hydropower.

Lac de Mauvoisin was brought into service in 1956. A bathymetric measurement, taken before impounding, is available. In 1985, the reservoir had to be flushed. Prior (and after) flushing, bathymetry was measured. For these 29 years, a yearly sedimentation volume of 0.33 hm³ can be derived based on the bathymetry changes. Bathymetry measurements near the dam, the bottom outlet and water intake structures were carried out in 1995, 1997, 1998, 2000 and 2004. From 2001–2006, the water intake and bottom outlet were heightened by 38 m and 36 m, respectively, due to sedimentation (Jenzer Althaus 2011).

IGT (2014) examined two water samples taken from the turbine water at the power station in *Chanrion*. SSC was 1.7 and 2.3 g/l. Clay content was 3.3 and

²⁶ the reservoir with the highest altitude is *Muttsee* with full supply level at 2446 m a.s.l.

²⁷ LV03 (CH1903 / LV03) is the Swiss coordinate system, its EPSG code is 21781



Figure 17: *Lac de Mauvoisin* on 11 August 2015 near the inflow of *Dranse de Bagnes* (LV03: 593 500 / 89 390); view from south to north

0.2%, sand content was 5.4 and 0.1% and the rest of 91.3 and 99.7% was silt. d_{50} were 9.3 and 11.4 μm .

4.2.1.2 Griessee

Griessee (LV03: 671 600 / 145 600) is one of the highest located reservoirs in Switzerland. The reservoir has a total volume of 18.6 hm^3 and an active volume of 18 hm^3 . The average annual inflow is 20.7 hm^3 ; capacity-inflow ratio is 0.90. The lake has a surface area of 0.21 km^2 . Full supply level is at 2386.5 m a.s.l., minimum operating level is at 2350 m a.s.l. The catchment area is 10 km^2 , of which 48% are covered by glaciers (Farinotti *et al.* 2012). Main natural inflow is at the south-west end of the reservoir. *Gries Glacier* has been continuously monitored since 1847 (Bourban and Papilloud 2015). *Griessee* reservoir was brought into service in 1966. At that time, *Gries Glacier* occupied circa 0.3 hm^3 of the reservoir. Since then, the glacier has retreated: the tongue of *Gries Glacier* is currently ca. 800 m behind the reservoir outline. Maintenance works in 2011 required closing the spherical valve of the penstock upstream of the turbine. Subsequent resetting of energy production failed due to blockage of the penstock by sediments. This is remarkable, because the hydraulic head was more than 400 m at that time. As a consequence, the water intake was heightened from 2335 to 2344 m a.s.l. and the minimum operating level was heightened as well from 2340 to 2350 m a.s.l. in 2015. The annual bottom outlet test will be combined with flushing of deposited sediments. The water of *Griessee* is being turbinated at least four times (in *Altstafel*, *Bavona*, *Caveragno*

and *Verbano*) and it flows through two other reservoirs (*Robiei* and *Palagnedra*) until it reaches *Lago Maggiore*, thus constituting the cascade with the largest head in Switzerland. The first associated level until *Altstafel* has an installed power of 10 MW and an annual production of ca. 21 GWh, but the whole cascade reaches an annual production of 162 GWh (Albrecht 2016).

Beck and Baron (2011) report a deposition volume of 0.618 hm³ between 1976 and 30 August 2011. Since then, (bi-)annual deposition volumes were 0.13 hm³ (30 August 2011 to 21 September 2013), 0.008 hm³ (21 September 2013 to 21 October 2014), 0.064 hm³ (21 October 2014 to 1 October 2015) and 0.016 hm³ (1 October 2015 to 26 October 2016) (Beck and Baron 2013, 2014, 2015, 2016). The bathymetric measurements in 2011, 2013, 2014, 2015 and 2016 were realized with multi-beam echo-sounding, which is one of the most reliable technologies available for this purpose. It is important to note that in summer 2015, the construction works at the dam required lowering the reservoir to a level of 2341 m a.s.l. from mid-June to mid-July. The sedimentation volume between 21 October 2014 and 1 October 2015 might be distorted because the lowering implied a flushing of the reservoir and completely different sediment transport dynamics. Figure 18 shows the sedimentation patterns in *Griessee* on 2 July 2015, when the reservoir level was lowered to 2341 m a.s.l.

In July 2012, Bourban and Papilloud (2015) measured PSD and SSC in the inflowing river water and the reservoir with LISST and ADCP. Sediments in all six water samples of the tributaries had diameters in the range of 1–200 µm, circa 80% of the diameters were in the silt fraction. Sediments in five water samples had d_{50} between 7 and 9 µm; sediments in one water sample had d_{50} of 20 µm. SSC in the tributaries ranged from 0.10 to 1.54 ml/l, which equals 265 to 4081 mg/l, if a density of 2650 kg/m³ is assumed. SSC and water discharge could not be correlated. ADCP measurements showed evidence of a turbidity current reaching the dam.

Delaney *et al.* (2017) examined the origin of sediments deposited in *Griessee*. They found that 70–80% of the deposition originates from subglacial erosion or has at least been routed through the subglacial hydraulic system. Although the glacier forefield grows continuously, it is not the main source of sediment, as it can only be removed by fluvial transport which is limited to erosion gullies in the forefield. Furthermore, the forefield has begun to stabilise in recent years.

4.2.1.3 Gebidem

Gebidem (LV03: 643 400 / 135 900) is situated in the *Massa* gorge downstream of *Aletsch Glacier*, the largest glacier in Europe. Figure 19 shows the tongue of *Aletsch Glacier* and the adjacent *Massa* gorge, which leads to *Gebidem*. The distance between *Aletsch Glacier* and *Gebidem* is ca. 3 km. The reservoir has a total volume of 9.2 hm³ and an active volume of 5.8 hm³ (Meile *et al.* 2014).

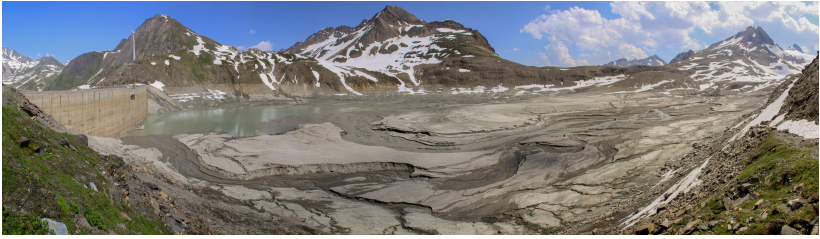


Figure 18: Sedimentation pattern in *Griessee* when reservoir level was at 2341 m a.s.l. during construction works at the dam on 2 July 2015 (LV03: 671 330 / 145 840); *Gries Glacier* and main inflow are on the right; view from north-west to south-east

The average annual inflow is 429 hm³ (Meile *et al.* 2014); capacity-inflow ratio is 0.02. The lake has a surface area of 0.21 km² (Alpiq 2016). Full supply level is at 1436.5 m a.s.l., minimum operating level is at 1400 m a.s.l. (Rechsteiner 1996). The catchment area is 198 km², of which 64% are covered by glaciers (Meile *et al.* 2014). The main natural inflow is the *Massa* at the northern end of the reservoir. *Gebidem* reservoir was brought into service in 1968. In 1996, the water intake was heightened from 1360 to 1396.65 m a.s.l. to reduce turbine abrasion (Rechsteiner 1996). The power station with an installed capacity of 340 MW and a maximum turbine discharge of 55 m³/s is situated in *Bitsch*. The annual electricity production is 555 GWh (Alpiq 2016), which is roughly 1.5% of the annual electricity production of hydropower in Switzerland.

Bathymetry measurements with single-beam echosounding were made each year in autumn from 1992 to 2012 (Meile *et al.* 2014). Multi-beam echosoundings are available since 2013 (i.e. 2013, 2014, 2015 and 2016). Additionally, a reference measurement of the empty reservoir with *LIDAR*²⁸ technology was conducted in 2010.

The first impoundment took place in 1969. Since then, annual flushings are carried out, except in 1978 and 2015. Flushings are usually realized when the inflow from the river *Massa* is 10–15 m³/s and river *Rhône* has a discharge of circa 100 m³/s (Giezendanner and Dawans 1981), which is usually given from May to June (Meile *et al.* 2014). To flush the reservoir, free flow through the bottom outlet is allowed for two to four days. A maximum sediment concentration of 4–6% (= 100–160 g/l, if a density of 2650 kg/m³ is assumed)

²⁸ *LIDAR* = light detection and ranging; a surveying method that measures distances with laser light



Figure 19: Catchment of *Gebidem* reservoir with *Aletsch Glacier* and *Massa* gorge on 13 August 2016 (LV03: 642 540 / 136 780); view from south-west to north-east

has to be satisfied (Meile *et al.* 2014). Annual flushings remove circa 0.3–0.4 hm³ of sediment and require less than 3 hm³ of water.

Giezendanner and Dawans (1981) reported annual sediment loads of 0.5 hm³, of which 0.13 hm³ (26%) are bed load and 0.37 hm³ (74%) are suspended load. Bed load transport sets in at approximately 20 m³/s and increases almost linearly with water discharge. Most of the sediment is fine sand with 0.1–1.0 mm grain diameter. 15% is silt, 20% is gravel and 65% is sand. d_{50} is slightly above 0.3 mm. Rechsteiner (1996) reported annual sediment loads of 0.35 hm³ for 1991 and 1993–1996. 20% of the sediments being conveyed into *Gebidem* reservoir do not settle inside the reservoir. These sediments origin from granite; they are very hard and sharp-edged. This leads to severe turbine abrasion. 0.095 hm³ of sand were sent to the turbine as wash load each year. Morris and Fan (2010) reported total sediment volumes of 0.4 hm³/a entering the reservoir, which corresponds to an annual denudation rate of 2.5 mm/a. 80% of the sediments have diameters below 1 mm, 20% have diameters between 1 and 100 mm. Meile *et al.* (2014) reported annual sediment loads of 0.43–0.47 hm³. In contrast to Rechsteiner (1996), they stated that 10% of the sediments cross *Gebidem* reservoir towards the dam, whereas 90% are retained and must be flushed. The sediments range is from blocs/gravel to clay with a mean grain size of 1–3 mm. Alpiq (2016) reported that SSC in the turbine water can reach 10–13 g/l in summer. This equals an annual sediment load of 0.18 hm³ impinging the turbines.

Table 11: Characteristics of investigated reservoirs (V_w is the annual inflow; V_l is the total reservoir volume; z_{max} is the full supply level; z_{min} is the minimum operating level; a is the lake surface area; F is the catchment area; and i is the glaciation of the catchment)

reservoir	V_w [hm ³]	V_l [hm ³]	z_{max} [m a.s.l.]	z_{min} [m a.s.l.]	a [km ²]	F [km ²]	i [%]
Lac de Mauvoisin	265	204	1975.0	1825.0	2.26	150	42
Griessee	20.7	18	2386.5	2350.0	0.60	10	48
Gebidem	430	9.2	1436.5	1400.0	0.21	198	64

4.2.2 Measurement techniques

4.2.2.1 Secchi disk measurements

A white-painted Secchi disk (Figure 7) of 0.2 m diameter with six holes of 0.055 m diameter was attached to a measuring tape. The disk fulfils the requirements of EN ISO 7027:1999. It was lowered until visibility depth was reached (i.e. the depth where the disk became invisible). It was then lowered another 0.5 m, before it was lifted until it could be seen again. The average of both depths was taken as the Secchi depth. Measurements were conducted at each water sampling location at the shady side of the boat. All measurements were taken around midday at calm water surface.

4.2.2.2 Water sample analysis

84 water samples were taken in the reservoirs and the inflowing rivers at different locations and depths. A Niskin bottle sampler (Figure 7) with an inner diameter of 0.1016 m (= 4 inches) and a sampling tube length of 0.254 m (= 10 inches) was applied. It had a sampling volume of roughly 2 litres. The general sampling procedure is described in Section 2.3.2. Sampling depths were limited to approximately 20 m due to technical constraints.

PSD was analysed using a *Horiba Partica LA-950* laser diffraction particle size distribution analyser. SSC was determined based on drying and weighing, using a *Mettler Toledo XPE205* high-precision balance. The analysis was done in the *Clay Lab* of the *Institute for Geotechnical Engineering (IGT)* of ETH Zurich.

PSD was measured using two procedures, depending on the SSC. High SSC (SSC > 1 g/l) made direct measurement of PSD from the water sample possible.

Low SSC ($SSC < 1 \text{ g/l}$) required that the suspension had to be concentrated first by evaporating the water sample at $65 \text{ }^\circ\text{C}$ in an oven. Long storage times in the climate chamber or the evaporating led to the formulation of flocs in a few cases. These flocs were destroyed with ultrasounding. The laser diffraction analyser has a dynamic range from 0.01 to $3000 \text{ }\mu\text{m}$. All samples showed PSD completely in this range.

SSC was measured with a basic weighing procedure. First, a cling film was weighed with the balance. Second, this cling film was put into a porcelain bowl, which was then filled with 1 liter of sample water. Third, this probe was dried in the oven at $65 \text{ }^\circ\text{C}$ for at least three days. Fourth, cling film and remaining sediments were weighed again and SSC was calculated. Usually, SSC weight was less than 10% of the weight of the cling film. Laboratory analysis of SSC depends on the accuracy of the weighing, as most of the weight is represented by the cling film and not the remaining sediment.

4.2.2.3 LISST measurements

In this study, a *LISST-100X Type C* (Figure 8) was applied. Operating principles, limitations, application examples and experiences are given in Section 2.3.3. It has a maximum operating depth of 300 m. The randomly shaped particle inversion method was used in the post-processing. Operating ranges are limited to particle sizes between 1.9 and $381 \text{ }\mu\text{m}$ and concentrations between 1 and 750 mg/l , approximately. A 90% path reduction module (PRM) allowed measuring higher concentrations. It was applied in 2015 and removed in 2016. Additional measurement parameters apart from PSD and SSC are, amongst others, optical transmission, beam attenuation, depth and temperature.

The LISST was operated at fixed sample rate, where ten measurements were taken each second and averaged to one measurement (i.e. nominal sampling rate was 1 Hz). The device was lowered and lifted slowly by hand with a speed of a few cm/s . All LISST measurements will be presented as “profiles”. Before starting a measurement profile, the device was kept in the water just below the water surface. This allowed the instrument to adjust for the temperature differences between air and water (sometimes more than $20 \text{ }^\circ\text{C}$), which should reduce noise in the measurements.

The uppermost measurements were skipped until the depth where the light intensity at the water surface I_0 is reduced to 10%. This depth z was calculated combining Equations (8) and (9):

$$z_{lim} = \frac{-\ln(0.1)}{1.1z_{Secchi}^{-0.73}} \quad (42)$$

where z_{lim} is the minimum depth were LISST measurements were processed [m]; and z_{Secchi} is the Secchi depth [m].

LISST measurements were converted from volume to mass concentration by assuming a constant sediment particle density of 2650 kg/m^3 . This does not imply the negation of flocculation, but it is the most reasonable first-order assumption, given the fact that no information about possible flocculation is available.

4.2.2.4 ADCP measurements

A *RiverSurveyor M9* (Figure 11) from *SonTek*²⁹ was used in this study. This 9 beam device operates with frequencies of 3 and 1 MHz, depending on water depth, and a vertical beam echo-sounder at 0.5 MHz used for bottom-tracking. The *RiverSurveyor M9* switches frequency independently and adjusts the cell size. The frequency of 3 MHz is used either if (a) flow depths are smaller than 1.5 m and flow velocities are lower than 0.4 m/s or (b) flow depths are smaller than 5 m and flow velocities are higher than 0.4 m/s (SonTek 2017). Otherwise, the frequency of 1 MHz is used. The device uses only one specific frequency for a specific profile (i.e. the two frequencies are never applied at the same time). The beams are inclined by 25° . The *RiverSurveyor M9* measures velocities of $\pm 20 \text{ m/s}$ with an accuracy of $\pm 0.25\%$ of the measured velocity or $\pm 2 \text{ mm/s}$ and a resolution of 0.001 m/s (SonTek 2016). The velocity profile distance is limited to 40 m. Bottom-tracking allows detecting the ground to 80 m depth with an accuracy of 1% of the measured value and a resolution of 0.001 m .

Main measurement parameters used in this study were: (i) flow velocities; (ii) Signal-to-Noise ratios (SNR) along the water column; and (iii) depth. Unfortunately, *SonTek* devices do not provide signal and noise separately. Only little information on signal processing is given. Not only frequency, but also cell sizes and blanking distances (see below) are being changed autonomously by the device. SonTek (2000) expects the noise floor of their ADCPs at 3 dB. Coupled to a differential global positioning system (D-GPS) with an accuracy of less than 1 m in a horizontal plane, the device was mounted on a hydro-board attached to a boat and operated in moving real-time mode. All ADCP measurements will be presented as “transects”.

According to Equation (11), an ADCP working with 3 MHz would be most sensitive to particles of $160 \text{ }\mu\text{m}$ diameter, an ADCP working with 1 MHz would be most sensitive to particles of $480 \text{ }\mu\text{m}$ diameter. Minimum detectable particle radii should be $8 \text{ }\mu\text{m}$ and $24 \text{ }\mu\text{m}$, respectively (Kostaschuk *et al.* 2005). The lower boundaries of detectable particle size are assumed to be in the range of

²⁹ <http://www.sontek.com>

medium and coarse silt, respectively, for the *RiverSurveyor M9*. It should react most sensitive on fine and medium sand.

ADCP was mainly used for measuring flow velocities. SSC in the near field of the ADCP was computed using Equation (18) of Thevenot *et al.* (1992) with the values for the coefficients ξ_1 and ξ_2 chosen according to Alvarez and Jones (2002). Because of low SSC in most parts of the reservoirs, SNR provided a qualitative view of changes in SSC, but did not allow for robust quantitative analysis over the whole flow depth.

Only measurements below the so-called blanking distance and above bottom estimate were evaluated. The blanking distance (sometimes also referred to as “top estimate”) is the distance between transducer and first measurement cell. It is determined by the time the transducer needs to stop from vibrating and to prepare for recording the returning signal (Mueller *et al.* 2007). The bottom estimate is usually the last cell above the bottom (i.e. the cell that is partially or fully touching the bottom) (SonTek 2015). Data within this layer are too close to the bottom and may be affected by erroneous interference with the bottom.

4.2.3 Field measurements

A set of five field measurements series was realised. The first series took place in *Lac de Mauvoisin* on 11 August 2015. It was a warm and nice day after some days of heavy rainfall and low temperatures. Inflow was 29.7 m³/s on average. The lake level was at 1966.85 m a.s.l. Water temperature³⁰ was 6.1–6.4 °C throughout the whole reservoir.

Three series were realised in *Griessee*. The measurements on 18 August 2015 and 08 August 2016 can be interpreted as “summer states”. 18 August was a cold and rainy day, the inflow was moderate with a peak of 1.5 m³/s. The lake level was at 2373.3 m a.s.l. Water temperature was 6.3–6.4 °C. Contrary, 08 August 2016 was a very warm and sunny day with a peak inflow of 5.6 m³/s, occurring early in the afternoon. The lake level was at 2379.0 m a.s.l. Water temperature was 6.0–6.4 °C. The measurements of 01 October 2015 correspond to a “winter state”. That day, it was cold and snowing. There was only negligible inflow. The lake level was at 2383.2 m a.s.l. Water temperature was 5.1–5.3 °C. *Griessee* measurements can be used to either compare summer and winter state in the same year or summer states of two subsequent years.

The fifth series in *Gebidem* was realised on 06 October 2015. It was a cold and rainy day, the average inflow was ca. 11 m³/s. The lake level was at 1431.5 m a.s.l. Water temperature was 1.4–2.0 °C.

³⁰ water temperatures were measured with the in-built thermometer of the LISST device

4.3 Results

4.3.1 Secchi disk measurements

Secchi depths between 0.2 and 1.5 m were measured. *Lac de Mauvoisin* and *Gebidem* had low values between 0.2 and 0.3 m, whereas Secchi depths in *Griessee* were higher with values from 0.5 to 1.5 m. The comparison of *Griessee* measurements shows that Secchi depths may differ at least by (a) a factor of 3 between summer and winter states and (b) a factor of 2 between two summer states. All values are given in Table 12. The minimum depth for starting with LISST measurements according to Equation (42), z_{lim} , is calculated as well and will be used later. Following Lewis (1970), the Secchi depth of 0.2 m corresponds to a SSC of 113 mg/l. The highest values of 1.5 m would equal to SSC of 0 mg/l.

4.3.2 Water sample analysis

Water samples were usually taken both from the inflowing rivers and within the reservoirs. A summary of the laboratory analysis is given in Tables 13 and 14. PSDs are shown in Figures 20–24. On 01 October 2015, the inflow into *Griessee* was negligible, so no water samples were taken from the inflowing river. Inflow water samples were obtained close to the reservoir outline.

4.3.3 LISST measurements

4.3.3.1 Lac de Mauvoisin

Four LISST profiles were recorded in *Lac de Mauvoisin*. Their location is shown in Figure 25. The maximum profile depth was 120 m. To reduce the influence of ambient light, the uppermost 0.9 m of the profiles were not analysed. Measurement of profile L2231628 was aborted at a depth of 85 m, because either the boat or the LISST began to drift apart from one another due to strong currents (Figure 26).

d_{50} of the recorded PSD were in the range of 4–67 μm (Figure 26) with high fluctuations. A weak trend towards larger d_{50} with increasing depth could be observed. In the uppermost 20 m of the profiles, d_{50} were more uniform in the order of 10 μm .

SSC measurements showed a distinct increase with depth (Figure 27). Measurements range from 39 to 2329 mg/l. In profile L2231419, the increase in SSC close to the ground is remarkably high. Either it might be because of a muddy pool or because the LISST hit ground and thereby swirled up deposited fine sediments. Due to operation in logging mode, such irregularities could not be

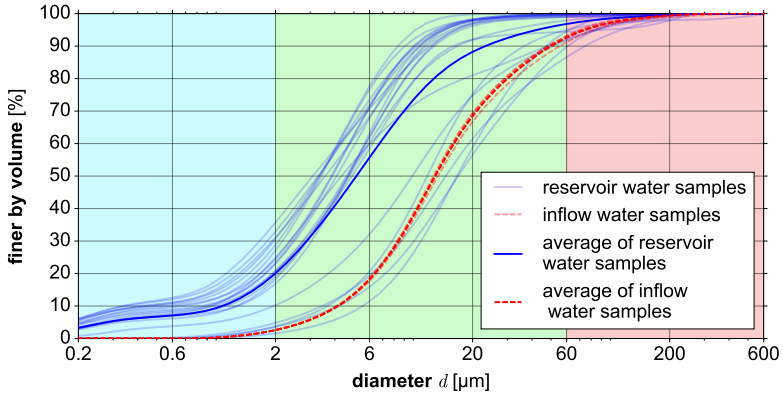


Figure 20: PSD in *Lac de Mauvoisin* obtained from water samples on 11 August 2015

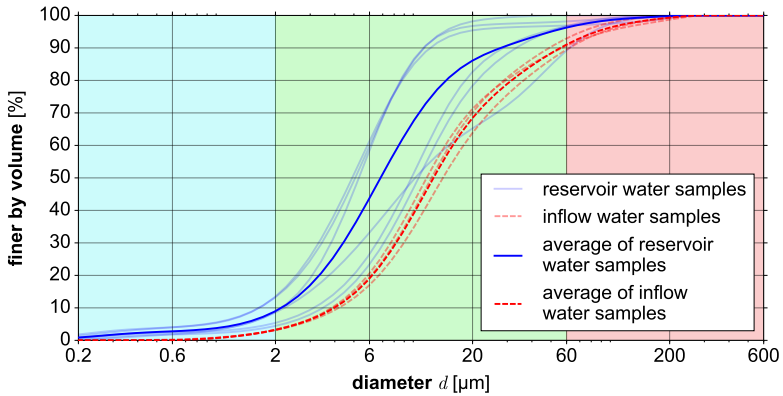


Figure 21: PSD in *Griessee* obtained from water samples on 18 August 2015

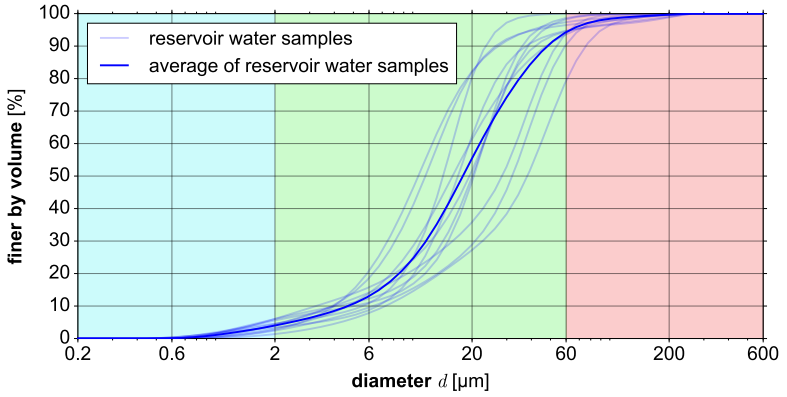


Figure 22: PSD in *Griessee* obtained from water samples on 01 October 2015

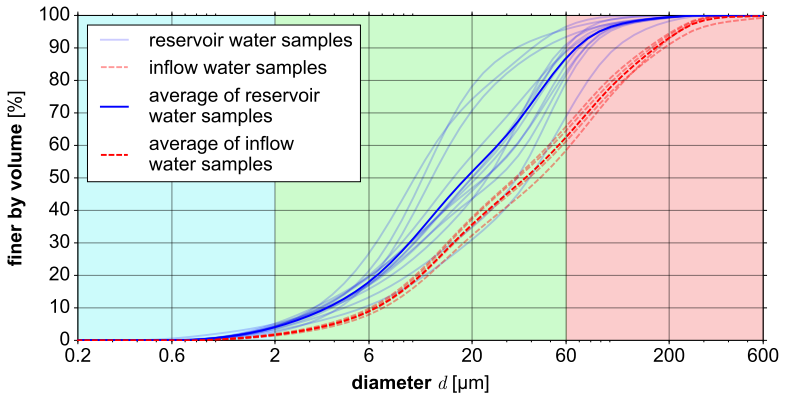


Figure 23: PSD in *Griessee* obtained from water samples on 08 August 2016

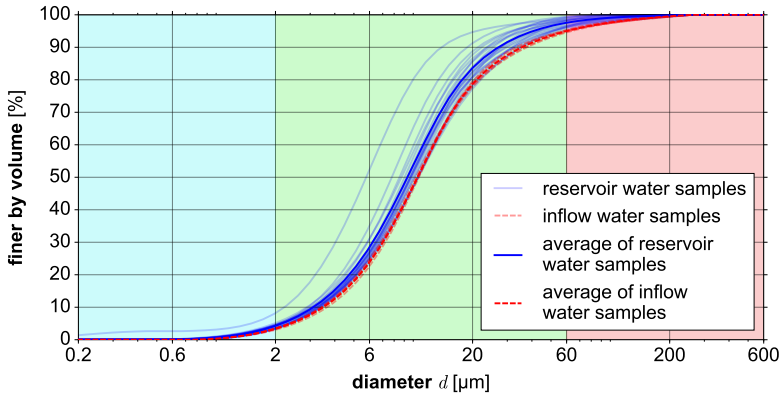


Figure 24: PSD in *Gebidem* obtained from water samples on 06 October 2015

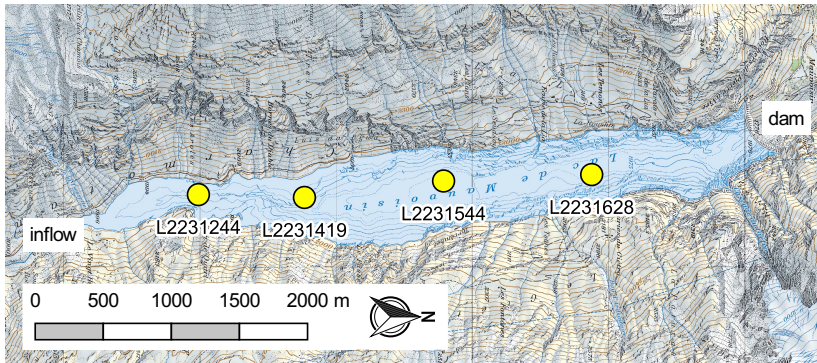


Figure 25: Location of LISST profiles in *Lac de Mauvoisin* [topographical map reproduced by permission of swisstopo (JA100120)]

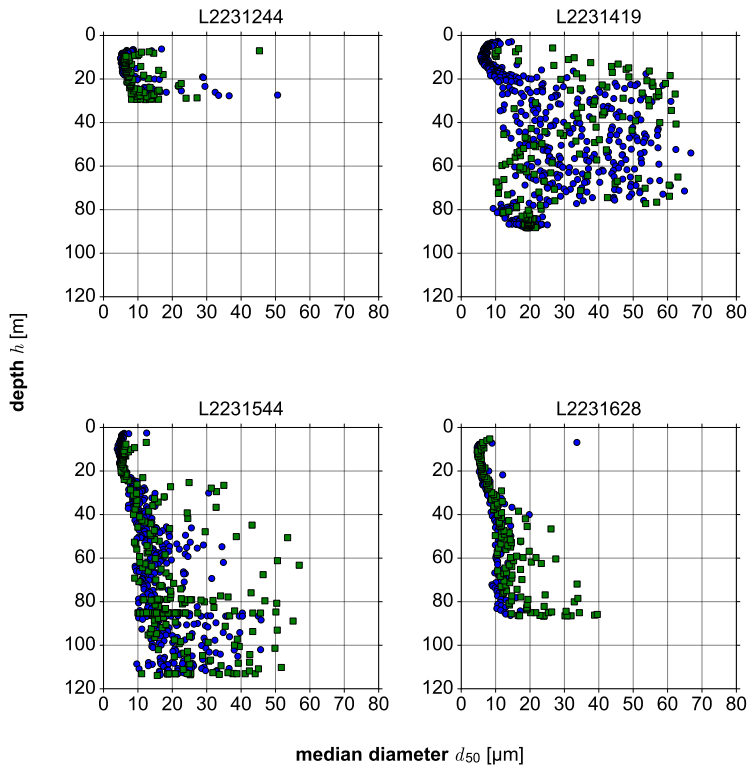


Figure 26: d_{50} in Lac de Mauvoisin measured with LISST on 11 August 2015; blue points indicate measurements recorded while lowering the instrument from the water surface to the reservoir bottom, green squares indicate measurements recorded while lifting the instrument up from the reservoir bottom to the water surface

Table 12: Secchi depths measured in three periglacial reservoirs (z_{Secchi} is the Secchi depth; and z_{lim} is the minimum depth for evaluating LISST measurements)

reservoir	Mauvoisin	Griessee		Gebidem	
date [dd/mm/yy]	11/08/15	18/08/15	01/10/15	08/08/16	06/10/15
z_{Secchi} [m]	0.20–0.30	0.50	1.50	0.80–0.90	0.25–0.30
SSC [mg/l] (Eq. 10)	113–59	22	— (0)	6–3	80–59
z_{lim} [m] (Eq. 42)	0.65–0.87	1.26	2.80	1.78–1.94	0.76–0.87

observed during the measurements and therefore no additional measurements were conducted to further examine this issue. At a depth of 80 m, transmission values of this profile decrease from 0.7 to 0.4. These values are still within the recommended application ranges, so a malfunction of the instrument is unlikely.

Figures 28 and 29 show PSD derived from the LISST measurements. PSD have been divided into measurements from the top 20 m of the water column and measurements at larger depths. This allows for an easier comparison with water samples, which were taken in the top 20 m only. In the top 20 m, d_{50} were in the range of 4 to 60 μm .

Some measurements in the top 20 m show a kind of “plateau” with relatively flat PSD curve before it increases again. The latter increase may be attributed to formation of flocs or influence of ambient light. As this plateau is only present in near-surface measurements, it is more likely linked to ambient light, as flocculation is expected to occur at larger depths as well. Most of the particle diameters are in the range of fine silt and sand and therefore within the measurement range of the applied LISST device.

Measurements at larger depths are shown in Figure 29. They had d_{50} of 4 to 67 μm .

4.3.3.2 Griessee

Data from 18 August 2015

Four LISST profiles were recorded in *Griessee* on 18 August 2015. Their location is shown in Figure 30. Maximum profile depth was 30 m. To reduce the influence of ambient light, the uppermost 1.3 m of the profiles were not analysed.

d_{50} were almost constant over the whole water depth, except for the profile L2301032 close to the dam (Figure 32). There were only a few isolated outliers.

Table 13: Summary of 15 water sample analyses from the inflowing rivers (n is the number of samples; d_{50} is the median diameter and values in square brackets are minimum and maximum values)

reservoir	n [-]	clay portion [%]	silt portion [%]	sand portion [%]	d_{50} [μm]	SSC [mg/l]
Lac de Mauvoisin	4	2.6	90.5 [89.3–91.1]	6.9 [6.3–8.2]	12.9 [12.7–13.4]	2182 [2051–2300]
Griessee 18 August 2015	3	3.2 [3.1–3.3]	88.4 [87.1–90.2]	8.4 [6.5–9.7]	12.7 [11.7–14.1]	1281 [1221–1330]
Griessee 08 August 2016	4	1.7 [1.4–2.0]	62.3 [58.6–65.3]	36.0 [32.7–40.0]	37.5 [33.0–44.3]	4278 [3846–4699]
Gebidem	4	3.4 [3.1–3.5]	91.9 [91.4–92.4]	4.7 [4.3–5.1]	10.5 [10.3–10.7]	85 [84–86]

Table 14: Summary of 69 water sample analyses from the reservoirs (n is the number of samples; d_{50} is the median diameter and values in square brackets are minimum and maximum values)

reservoir	n [-]	clay portion [%]	silt portion [%]	sand portion [%]	d_{50} [μm]	SSC [mg/l]
Lac de Mauvoisin	20	20.1 [1.6–35.8]	76.9 [64.1–93.6]	3.0 [0.1–12.6]	6.5 [3.1–16.9]	111 [85–194]
Griessee 18 August 2015	5	9.0 [4.5–13.5]	87.5 [81.7–92.6]	3.5 [0.0–9.7]	7.7 [4.9–10.6]	82 [75–86]
Griessee 01 October 2015	11	4.0 [1.4–6.1]	90.9 [80.4–95.4]	5.1 [0.0–18.2]	20.7 [10.7–38.1]	85 [77–109]
Griessee 08 August 2016	13	4.1 [2.5–5.2]	84.1 [68.1–91.4]	11.8 [3.0–28.9]	21.6 [10.2–39.2]	122 [113–139]
Gebidem	20	4.3 [3.3–8.2]	93.5 [90.5–96.1]	2.2 [0.5–4.4]	9.5 [5.8–10.6]	75 [64–103]

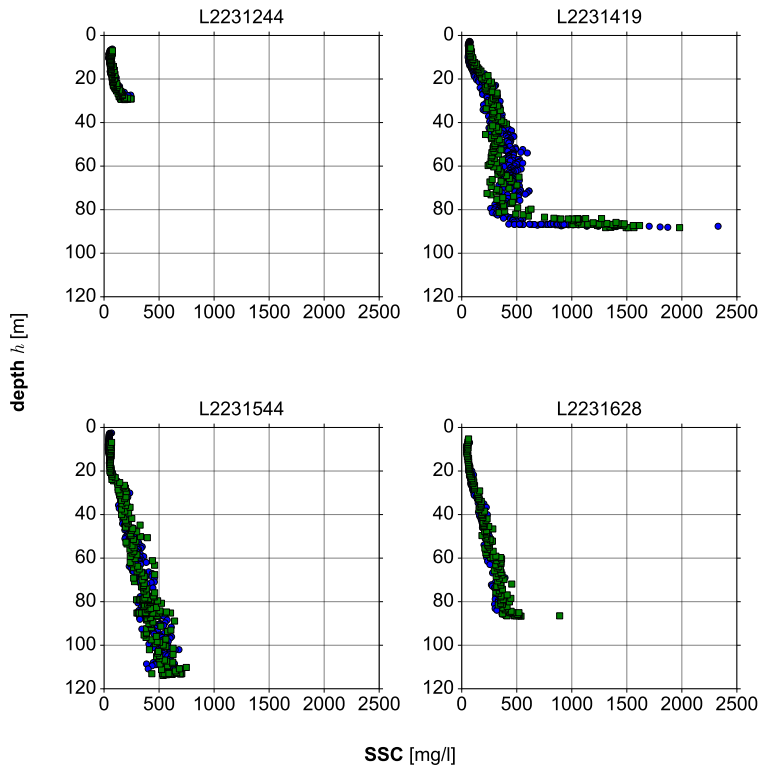


Figure 27: SSC in *Lac de Mauvoisin* measured with LISST on 11 August 2015; blue points indicate measurements recorded while lowering the instrument from the water surface to the reservoir bottom, green squares indicate measurements recorded while lifting the instrument up from the reservoir bottom to the water surface

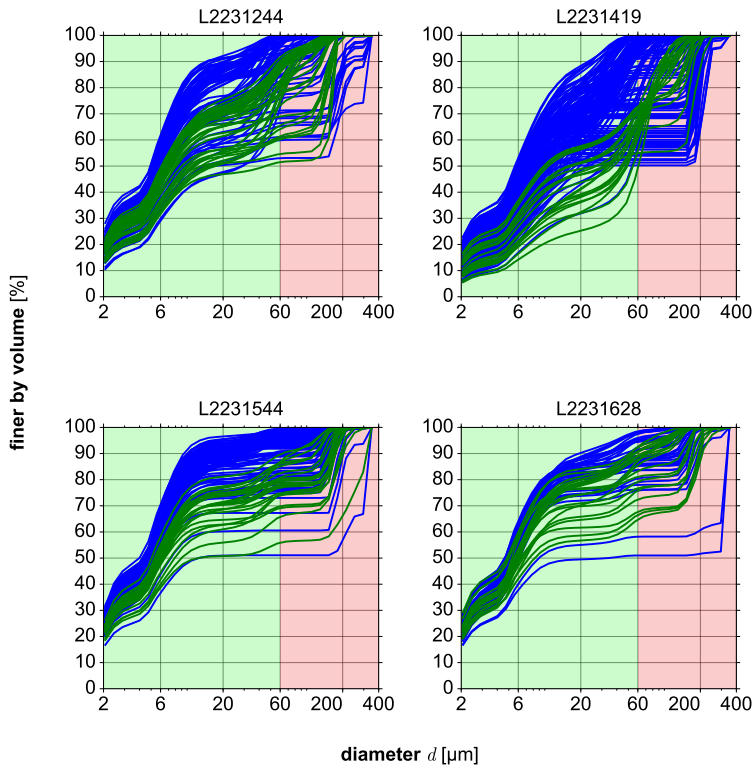


Figure 28: PSD in the top 20 m of the water column in *Lac de Mauvoisin* measured with LISST on 11 August 2015; blue lines indicate measurements taken while lowering the instrument, green lines indicate measurements taken while lifting the instrument

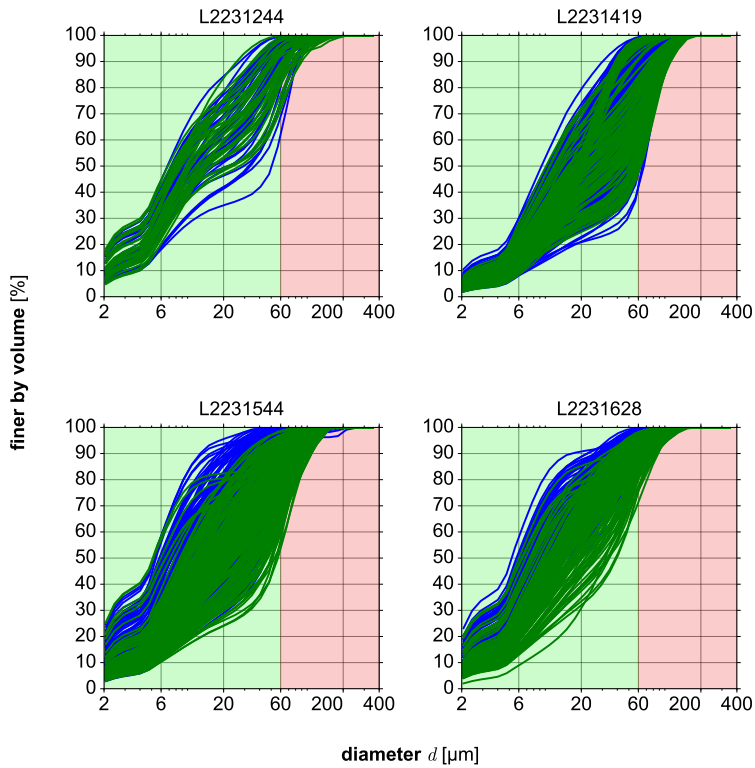


Figure 29: PSD at depths larger than 20 m in *Lac de Mauvoisin* measured with LISST on 11 August 2015; blue lines indicate measurements taken while lowering the instrument, green lines indicate measurements taken while lifting the instrument

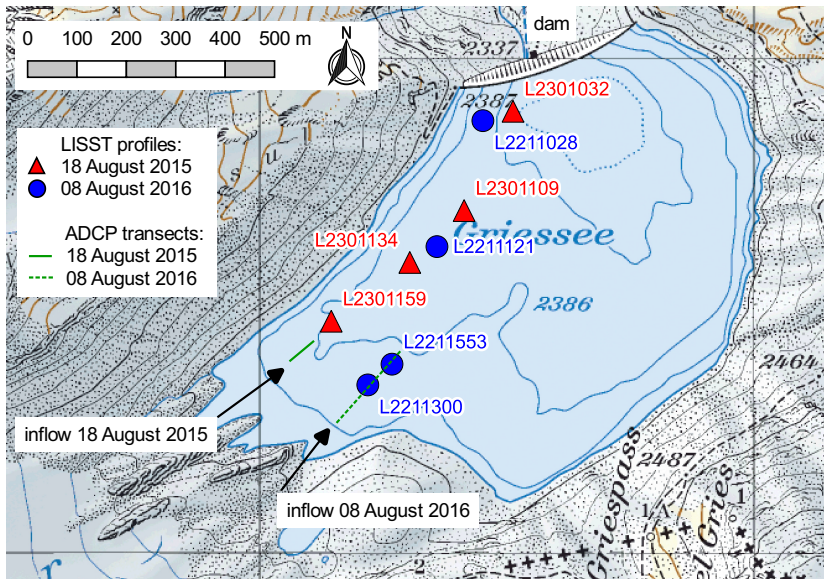


Figure 30: Location of LISST profiles and ADCP transects in *Griessee* [topographical map reproduced by permission of swisstopo (JA100120)]

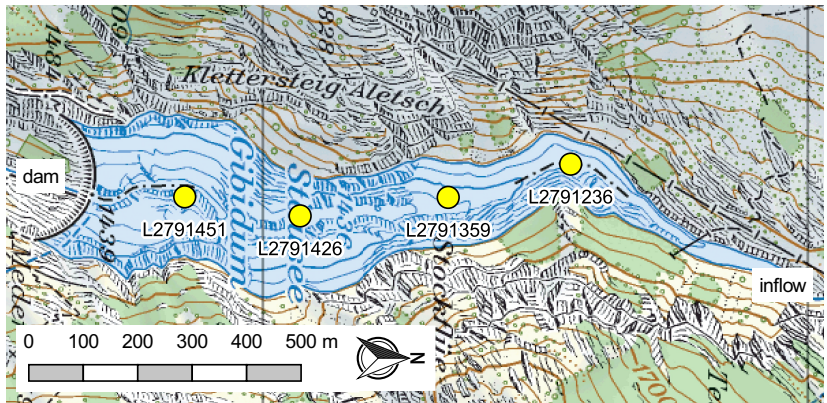


Figure 31: Location of LISST profiles in *Gebidem* [topographical map reproduced by permission of swisstopo (JA100120)]

Most sensed sediment particles had d_{50} of about 10 μm , but values from 7 to 64 μm were recorded.

SSC did not significantly increase over depth (Figure 33). All measured values were in the range of 60 to 248 mg/l. In the profile close to the dam, the SSC values were higher when lifting the instrument. This may be due to sediment that have been swirled up when the instrument hit the bottom of the reservoir and were clogging the sensors.

Figure 34 shows PSD derived from LISST measurements over the whole water column. Most of the particles are in the range of silt and fine sand and therefore in the measurement range of the applied LISST device.

Data from 01 October 2015

On 01 October 2015, several LISST profiles were recorded. Subsequent analysis revealed a malfunction of the instrument. No reliable data could be obtained.

Data from 08 August 2016

Four LISST profiles were recorded in *Griessee* on 08 August 2016. Their location is shown in Figure 30. Maximum profile depth was 30 m. To reduce the influence of ambient light, the uppermost 1.9 m of the profiles were not analysed.

d_{50} varied between 6 and 87 μm (Figure 35). There is a trend towards increasing d_{50} with depth. Some measurements were conducted in a stationary mode at a certain depth for at least 30 seconds. These measurements show the fluctuations of both d_{50} and SSC. For example, in profile L2211121 at 10 m depth, d_{50} varied within one order of magnitude from 8 to 67 μm .

The fluctuations of SSC at the same depths were high as well, they varied between 180 and 790 mg/l (Figure 36). Most SSC were in the range of 200–1000 mg/l. There was a general trend towards increasing SSC with depth, especially in profile L2211300, where SSC from 145 to 3008 mg/l were measured. This profile is close to the inflow, where ADCP measurements indicated evidence of a minor turbidity current. Water temperature was 6.2 °C at the water surface. It decreased linearly to 6.0 °C at a depth of 15 m. Optical transmission started to decrease at 10 m depth from an almost constant value of 0.7 to 0.4 at 15 m depth and decreased further to 0.2 at 17 m depth. Therefore, below a depth of 15 m, LISST reaches its recommended application range. The decrease of SSC in L2211121 and L2211028 at depths of ca. 20 m and 15 m, respectively, can currently not be explained.

PSD is shown in Figure 37 for measurements over the whole water column. Again, most particles are in the range of silt and fine sand. The plateau found in

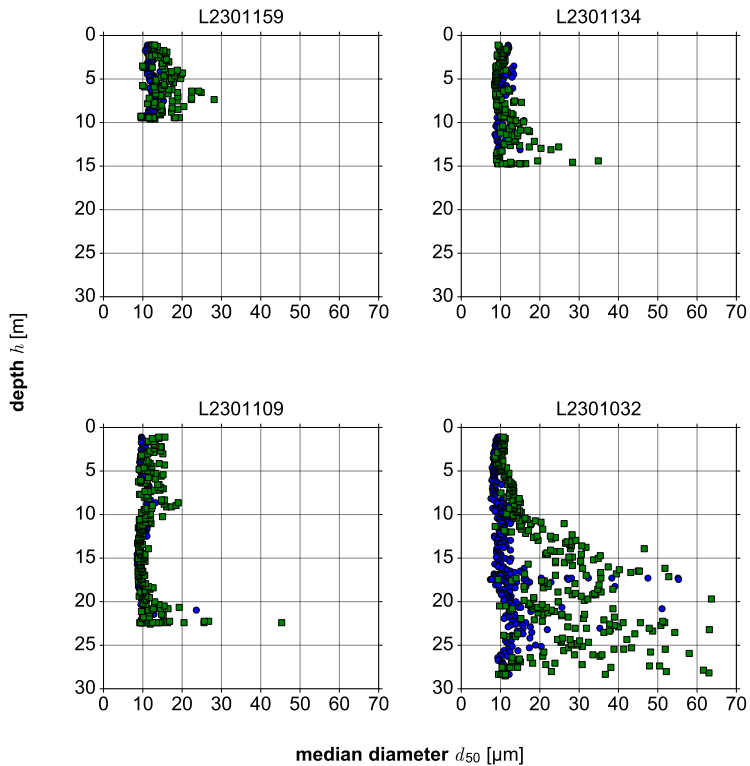


Figure 32: d_{50} in *Griessee* measured with LISST on 18 August 2015 (blue points indicate measurements recorded while lowering the instrument from the water surface to the reservoir bottom, green squares indicate measurements recorded while lifting the instrument up from the reservoir bottom to the water surface)

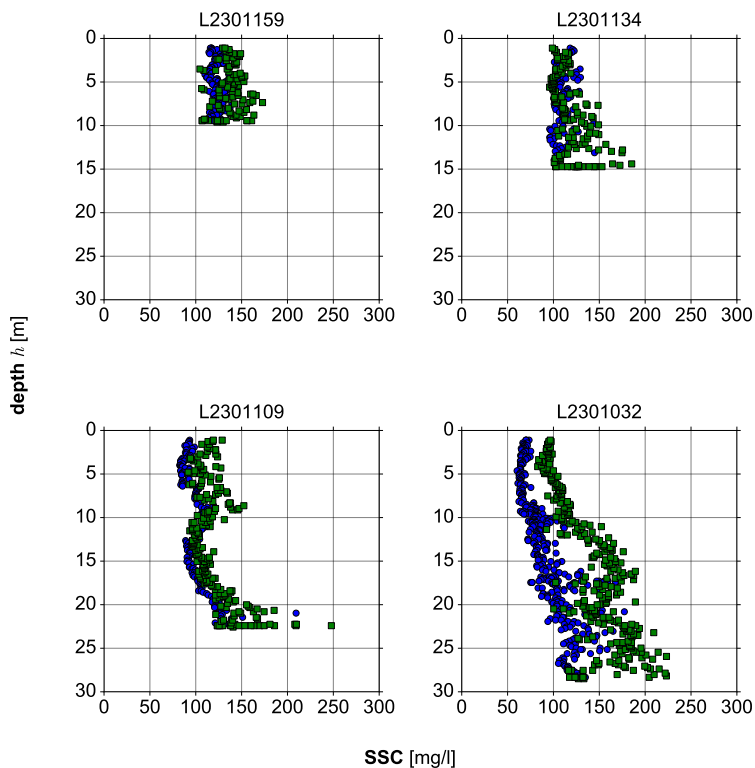


Figure 33: SSC in *Griessee* measured with LISST on 18 August 2015 (blue points indicate measurements recorded while lowering the instrument from the water surface to the reservoir bottom, green squares indicate measurements recorded while lifting the instrument up from the reservoir bottom to the water surface)

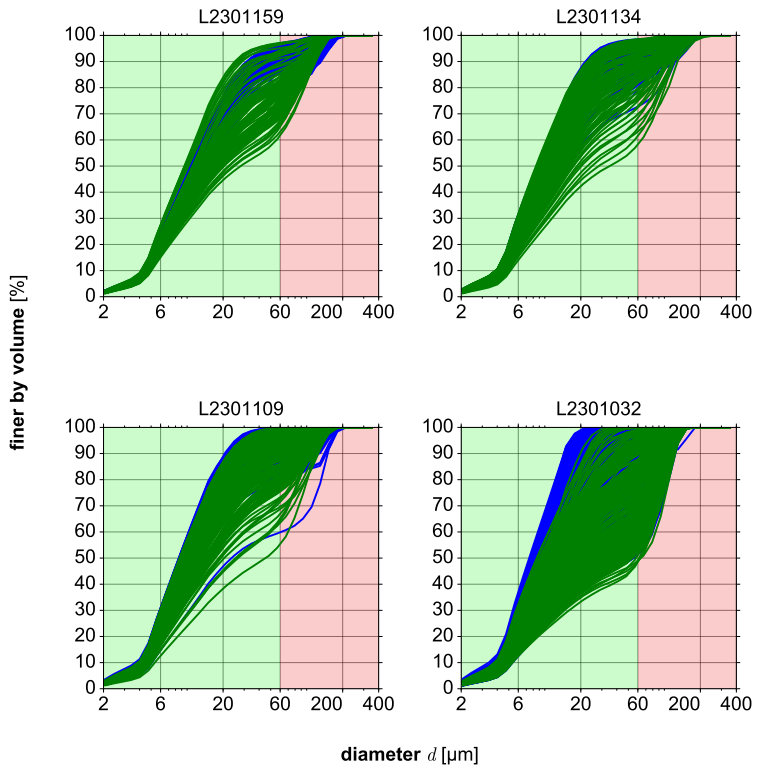


Figure 34: PSD in the top 20 m of the water column in *Griessee* measured with LISST on 18 August 2015; blue lines indicate measurements taken while lowering the instrument, green lines indicate measurements taken while lifting the instrument

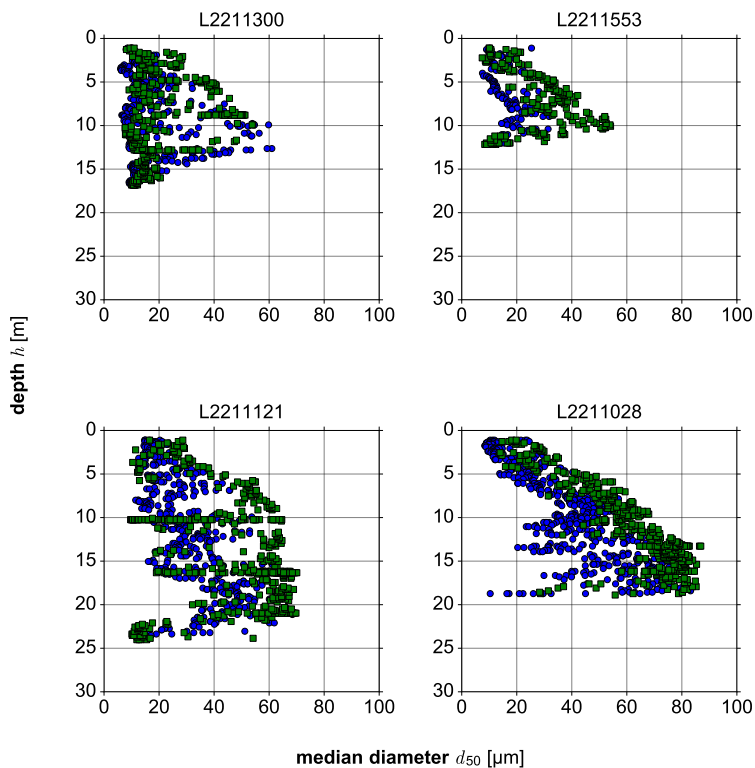


Figure 35: d_{50} in *Griessee* measured with LISST on 08 August 2016 (blue points indicate measurements recorded while lowering the instrument from the water surface to the reservoir bottom, green squares indicate measurements recorded while lifting the instrument up from the reservoir bottom to the water surface)

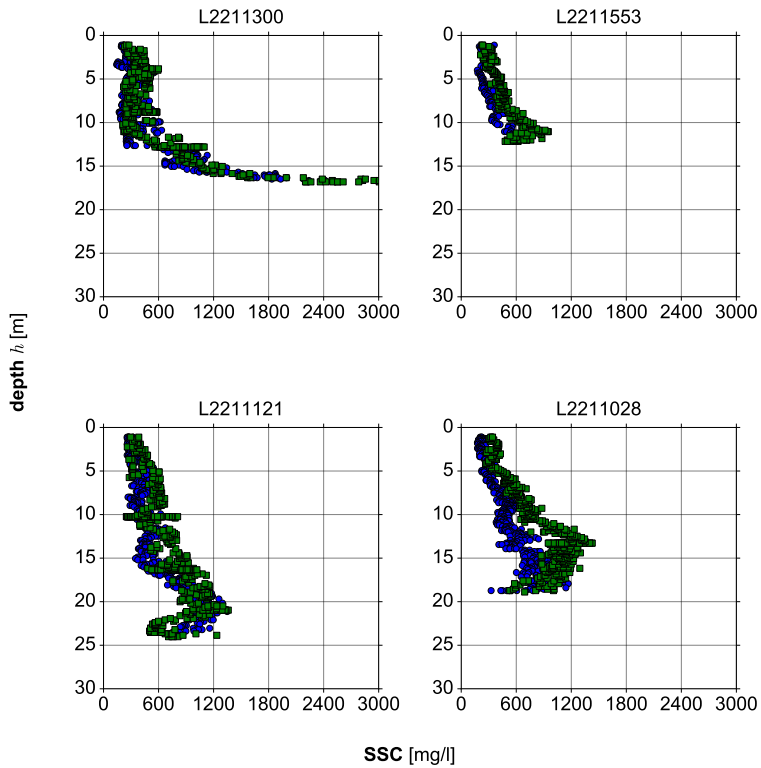


Figure 36: SSC in *Griessee* measured with LISST on 08 August 2016 (blue points indicate measurements recorded while lowering the instrument from the water surface to the reservoir bottom, green squares indicate measurements recorded while lifting the instrument up from the reservoir bottom to the water surface)

LISST measurements at *Lac de Mauvoisin* (Figure 28) can equally be observed in a few near-surface measurements at *Griessee*.

4.3.3.3 Gebidem

Four LISST profiles were recorded in *Gebidem* reservoir. Their location is shown in Figure 31. Maximum profile depth was 80 m. To reduce the influence of ambient light, the uppermost 0.9 m of the profiles were not analysed.

d_{50} in the range of 7–24 μm were recorded (Figure 38). The range of d_{50} is relatively narrow, apart from profile L2791236, which shows a high scatter. There is no significant change of d_{50} over depth. The measurements taken while lowering the instrument differ from those taken while lifting it up.

This issue appears more pronounced in the SSC records (Figure 39). Records in the “lowering” set indicate a slight increase in SSC with depth, but the records in the “lifting” set tend to a constant distribution of SSC. No satisfying answer could be found for this feature. SSC measurements are in the range of 122 to 1795 mg/l. There is a high scatter in the first profile L2791236, possibly because of the proximity to the inflow and its location in a curve. Both facts might lead to higher turbulent fluctuations than in the rest of the reservoir. Other reasons for the fluctuations could be organic content in the water or air bubbles, although neither organic material nor air bubbles were actually visible. Temperature in the first profile was 1.8 °C at the surface, increased to 1.95 °C in 5 m depth and remained constant with increasing depth. In all other profiles, water temperature in the top 20 m was constantly 1.95 °C. At a depth of 20 m, temperature started to decrease until a depth of 50 m, where it stayed constant again at 1.5 °C. *Gebidem* was the only reservoir in this set of field measurements where temperature changed over depth along the entire reservoir.

Figures 40 and 41 show PSD derived from LISST measurements. The range of diameters is narrow, as almost all particles are in the range of silt and fine sand. There is no significant difference between measurements in the top 20 m of the water column and the measurements at larger depths.

4.3.4 ADCP measurements

Various ADCP transects along and transversal to the main flow path were recorded in *Griessee*. Transects along the flow path from the inflow towards the dam provide insights into the damping of flow velocities and mixing of suspended sediments. Two distinct transects from summer 2015 and 2016 will be discussed below. Both were recorded along the flow path from the inflow to the dam (x). The goal was to track the distribution of the suspended sediments being conveyed into the reservoir. Flow velocities (v) will be shown as magnitudes,

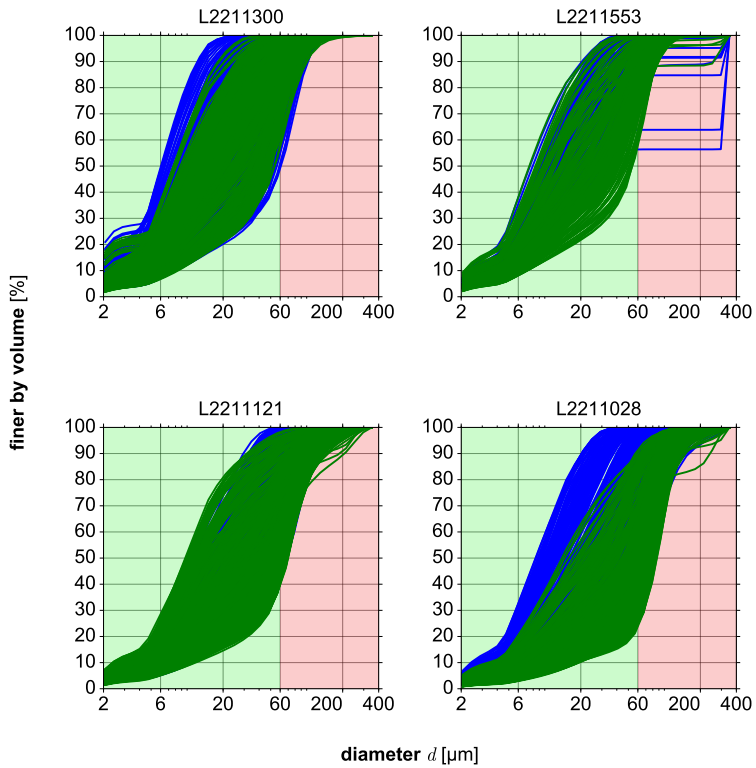


Figure 37: PSD in the top 20 m of the water column in *Griessee* measured with LISST on 08 August 2016; blue lines indicate measurements taken while lowering the instrument, green lines indicate measurements taken while lifting the instrument

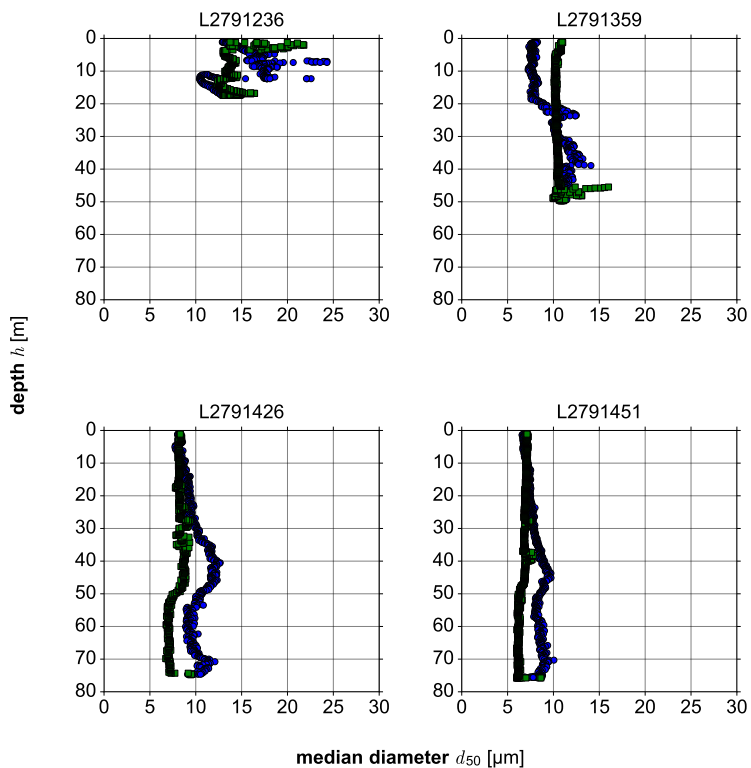


Figure 38: d_{50} in *Gebidem* measured with LISST on 06 October 2015 (blue points indicate measurements recorded while lowering the instrument from the water surface to the reservoir bottom, green squares indicate measurements recorded while lifting the instrument up from the reservoir bottom to the water surface)

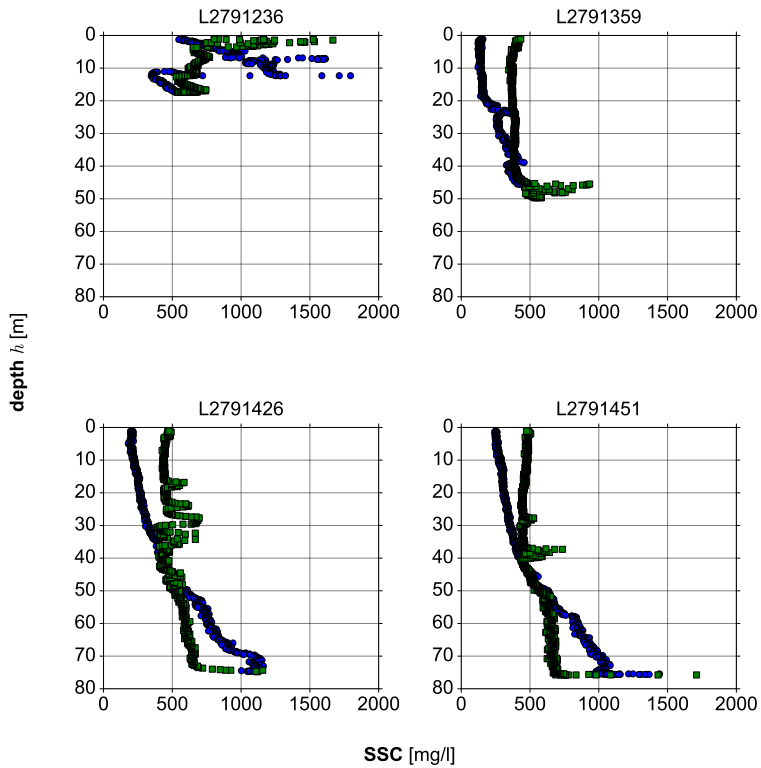


Figure 39: SSC in *Gebidem* measured with LISST on 06 October 2015 (blue points indicate measurements recorded while lowering the instrument from the water surface to the reservoir bottom, green squares indicate measurements recorded while lifting the instrument up from the reservoir bottom to the water surface)

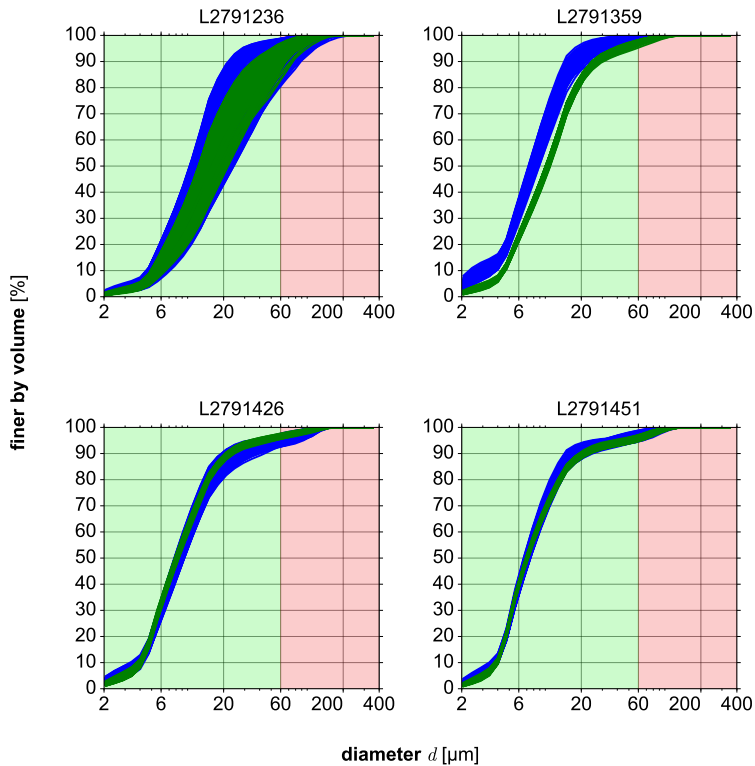


Figure 40: PSD in the top 20 m of the water column in *Gebidem* measured with LISST on 06 October 2015; blue lines indicate measurements taken while lowering the instrument, green lines indicate measurements taken while lifting the instrument

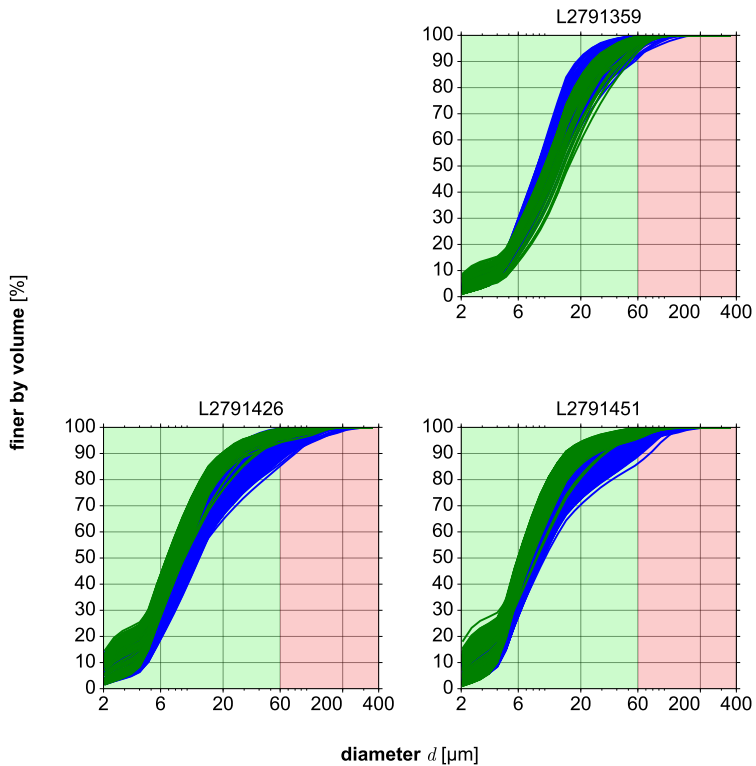


Figure 41: PSD at depths larger than 20 m in *Gebidem* measured with LISST on 06 October 2015; blue lines indicate measurements taken while lowering the instrument, green lines indicate measurements taken while lifting the instrument

the horizontal and upward (vertical) flow velocities will be given in the text. SNR (Δ) are averages of the SNR values measured by each individual beam.

4.3.4.1 Data from 18 August 2015

A 60 m long transect was recorded on 18 August 2015 (Figures 42 and 43). It can be divided into two parts: the “inflow regime” on the left and the “reservoir regime” on the right. In the first part, higher SNR values close to the ground can be observed. The transition of both parts can be set at ca. 25 m distance from the inflow. The average bottom slope of the transect is 5.5%.

In the inflow regime, horizontal flow velocities ranged from 12.04 to 1147 mm/s with a median horizontal flow velocity of 213 mm/s. Vertical (upward) flow velocities covered a range from -218 to $+284$ mm/s; the median vertical flow velocity was -8 mm/s. In the reservoir regime, the horizontal flow velocities were significantly lower: they ranged from 3.61 to 383 mm/s with a median horizontal flow velocity of 102 mm/s. Vertical flow velocities varied between -146 and $+141$ mm/s; the median vertical flow velocity was 11 mm/s.

In the inflow regime, SNR were in the range of 22.1–70.0 dB with a median value of 42.2 dB (Figure 43). SNR decreases with depth, but close to the reservoir bottom, it increases again. In the reservoir regime, average SNR values varied between 1.1 and 54.3 dB, the median SNR value was 19.3 dB. SNR is strictly decreasing with depth. Uppermost SNR values in the reservoir regime were between 39.6 and 48.3 dB with a mean value of 54.3 dB. No information about SNR in the bottom estimate can be given.

All over the lake, near-surface SNR values ranged from 17.9 to 82.3 dB. The mean near-surface SNR value was 37.7 dB.

4.3.4.2 Data from 08 August 2016

A 200 m long transect was recorded on 08 August 2016 (Figures 44 and 45). Again, two parts can be distinguished with a transition at ca. 75 m. The average bottom slope of the transect is 6%.

In the inflow regime, horizontal flow velocities ranged from 7.81 to 881 mm/s with a median horizontal flow velocity of 192 mm/s. Vertical flow velocities covered a range from -211 to $+153$ mm/s; the median vertical flow velocity was -1 mm/s. In the reservoir regime, the horizontal flow velocities ranged from 3.61 to 464 mm/s with a median horizontal flow velocity of 101 mm/s. Vertical flow velocities varied from -86 to $+92$ mm/s; the median vertical flow velocity was 5 mm/s.

In the inflow regime, SNR values ranged from 6.8 to 53.8 dB. The median SNR value was 25.4 dB (Figure 45). SNR generally decreases with depth, but increases again close to the reservoir bottom. In the reservoir regime, SNR

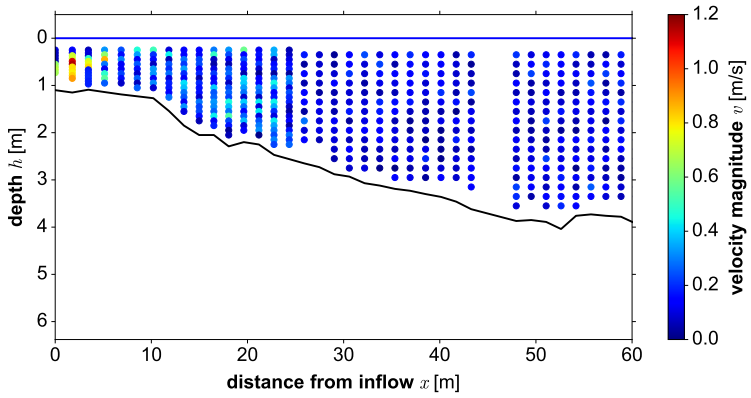


Figure 42: Flow velocities in *Griessee* along the flow path measured with ADCP on 18 August 2015

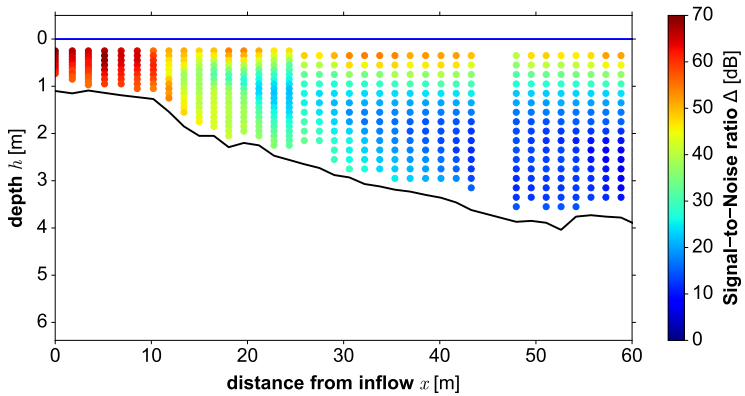


Figure 43: SNR in *Griessee* along the flow path measured with ADCP on 18 August 2015

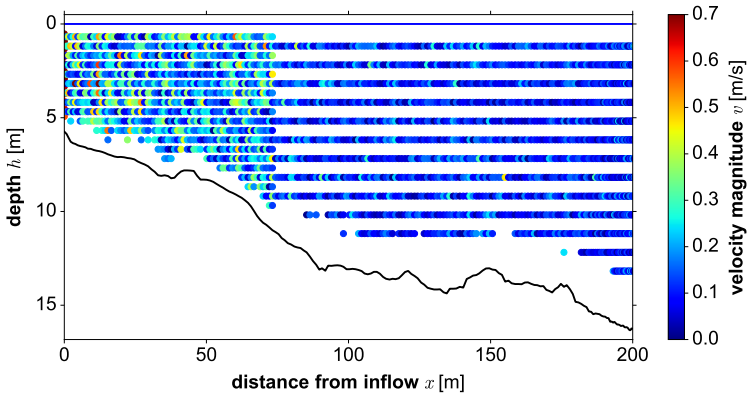


Figure 44: Horizontal flow velocities in *Griessee* along the flow path measured with ADCP on 08 August 2016

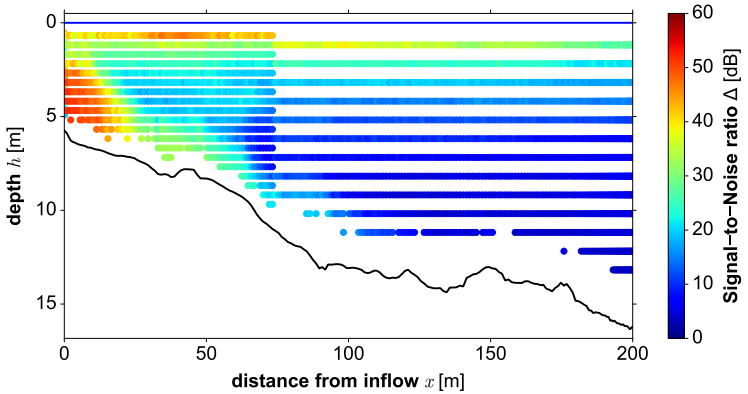


Figure 45: SNR in *Griessee* along the flow path measured with ADCP on 08 August 2016

values were measured between 3.1 and 39.6 dB. The median SNR value was 10.7 dB. SNR values decrease with increasing depth. Uppermost SNR values in the reservoir regime were between 24.6 and 39.6 dB with a mean value of 33.2 dB.

All over the lake, near-surface SNR values ranged from 21.6 to 85.7 dB. The mean near-surface SNR value was 38.8 dB.

4.4 Discussion

4.4.1 Secchi disk measurements

Secchi disk measurements showed that near-surface turbidity differs by roughly one order of magnitude for the investigated reservoirs. Given that mean SSC was comparable in all field measurements (74–111 mg/l), this large range cannot be explained by differences in SSC alone. The relationship of Lewis (1970) leads to reasonable results in the case of *Lac de Mauvoisin* and *Gebidem*, but it fails in all three measurement campaigns at *Griessee*. Secchi depths are likely strongly influenced by ambient light conditions, particle characteristics, organic suspended particles and other factors. A relation between Secchi depths and SSC should therefore be site-specific and account for environmental conditions. To the author's knowledge, there are no studies available addressing these issues.

4.4.2 Water sample analysis

85 water samples were analysed, of which 15 samples were taken from inflowing rivers and 70 from the reservoir. In the inflowing river water samples, 59–92% of the suspended particle diameters were in the silt fraction. d_{50} covered the range of 10–44 μm . In the reservoir water samples, 64–96% of the grain diameters were in the silt fraction. d_{50} were 3–39 μm in all reservoirs. Suspended sediments were primarily silt with d_{50} in the medium silt fraction. There was no significant change (e.g. fining) between inflowing river water samples and reservoir water samples. IGT (2014) confirms these findings, as their water sample analysis of turbine water from *Lac de Mauvoisin* revealed silt proportions of 92–100% and d_{50} in the range of 9.3–11.4 μm . Bourban and Papilloud (2015) measured almost identical values of d_{50} between 7 and 9 μm in water samples from *Griessee* tributaries. Sparse data from water sample analysis of other periglacial lakes in Switzerland correspond well with the findings of this study: Bezinge (1987) reported d_{50} in the range of 20–40 μm in *Z'Mutt* lake (a small reservoir downstream of *Zmuttgletscher*). Bühler *et al.* (2004) measured d_{50} of 2–4 μm in deep water of *Grimselsee*. The range of diameters was 0.2–40 μm . Water sample

analysis of Bonalumi *et al.* (2011) revealed d_{50} of 3.2–4.2 μm in *Grimselee* and *Oberaarsee*.

The largest particle diameters in suspension were in the order of 100 μm . According to Stoke's law, the laminar settling velocity of such particles is (Wu 2008):

$$w = \frac{1}{18} \frac{\rho_s - \rho_w}{\mu} g d^2 \quad (43)$$

where w is the settling velocity of a single particle [m/s]; ρ_s is the density of the particle [2650 kg/m^3]; ρ_w is the density of the fluid [1000 kg/m^3]; μ is the dynamic viscosity of the fluid [0.0014 $\text{kg}/(\text{m}\cdot\text{s})$ at 6 °C]; g is the gravitational acceleration [9.81 m/s^2]; and d is the particle diameter [m]. A particle with a diameter of 100 μm has a settling velocity of 6.4 mm/s. Stoke's law can be applied, as these particles are still in the laminar settling region, when the particle Reynolds number is smaller than unity. Here, the particle Reynolds number R can be defined as (Wu 2008):

$$R = \frac{w d \rho_w}{\mu} \quad (44)$$

where d is the particle diameter [m]. For a particle with a diameter of 100 μm and a settling velocity of 6.4 mm/s, R is 0.46. Particles of that size were found close to the dams, near the water surface. They stayed in suspension because turbulence counter-acted the gravitation-driven settling process. Therefore, the effects of turbulence could be estimated: average vertical (upward) flow velocity fluctuations are expected to have been in the range of some mm/s. This agrees well with ADCP measurements in *Griessee* (11 mm/s on 18 August 2015 and 4 mm/s on 08 August 2016) and with observations reported by Hutter *et al.* (2011) for lakes and by Ortmanns (2006) and Paschmann *et al.* (2017) for desanding facilities.

SSC in the inflowing river waters of *Lac de Mauvoisin* and *Griessee* on 18 August 2015 amounted up to a few g/l. In the reservoirs, SSC was relatively constant in the range of 74 to 111 mg/l. Many studies (Section 2.2.1) have shown that periglacial meltwater streams may have SSC of more than 10 g/l, so the results seem plausible. Measurements of this study are located within the SSC range of 265 and 4081 mg/l given by Bourban and Papilloud (2015) for tributaries of *Griessee*. Alpiq (2016) reported SSC of 180–240 mg/l in the turbine water of *Gebidem*, which is basically reservoir water and has therefore similar SSC. As the measurements at *Gebidem* were conducted in October, lower SSC of 74 mg/l seem to be plausible, too, because highest SSC is expected in summer when inflow is high and turbid. Bonalumi *et al.* (2011) proved that such seasonal changes may exist: in *Oberaarsee*, SSC was 40–45 mg/l in winter

and 40–180 mg/l in summer; in *Grimseelsee*, SSC was 35–40 mg/l in winter and 130–180 mg/l in summer. These values agree well with SSC found in *Lac de Mauvoisin*, *Griessee* and *Gebidem*. Another measurement series of Oehy and Schleiss (2002) revealed SSC of 60–90 mg/l in *Grimseelsee*, which is as well in the same order of magnitude. Müller *et al.* (2014) measured SSC downstream of the surge tank of *Oberaarsee*: monthly means of 55–60 mg/l (February–April 2011) to 80 mg/l (November–December 2010, May–June 2011) may be representative values for wash load in the *Oberaarsee*.

4.4.3 LISST measurements

Out-of-range particles and multiple scattering affect the signals in the outermost ring detectors. If significant out-of-range particles are present or SSC is high and multiple scattering occurs, these detectors are often omitted in the post-processing. However, herein no significant difference was observed if the first lower and upper three ring detectors were excluded. This is an indication that there were only little out-of-range particles and SSC was low enough so that multiple scattering had only minor influence on LISST measurements.

Different definitions of the mean diameter are available; for example, arithmetic mean, volume-to-surface mean (Sauter mean), mean diameter over volume (de Broukere mean) and others (Horiba 2012). All of them are being used in laser diffraction analysis, but comparison is difficult, as the mean diameter over volume is typically 50–100% larger than the arithmetic mean. The definition of median diameter (d_{50}) was used to circumvent these problems. It is clearly defined and has a distinct meaning. PSD were derived to compare LISST results with water sample analysis.

d_{50} measured with LISST were in good agreement with water sample analysis: in the uppermost 20 m, LISST measurements at *Lac de Mauvoisin*, *Griessee* (on 18 August 2015) and *Gebidem* indicated d_{50} in the order of 10 μm similar to the water samples. SSC in the uppermost 20 m measured with LISST corresponded well with data from water sample analysis. SSC recorded with LISST were in the same order of magnitude as the water samples with 64 (minimum measured SSC) and 194 mg/l (maximum measured SSC).

Some LISST records close to the surface at *Lac de Mauvoisin* (Figure 28) and *Griessee* on 8 August 2016 (Figure 37) indicate a kind of “plateau” in the range of ca. 20 and 200 μm . This might either be due to ambient light or due to flocculation. As this feature is hardly observed at larger depths (Figure 29), it is more likely linked to ambient light. Both measurement series were recorded at days with clear sky, whereas the other series (*Griessee* on 18 August 2015, Figure 34; and *Gebidem* on 6 October 2015, Figure 40) were recorded when

it was cloudy. This supports the hypothesis that the ambient light had an influence on these records.

In general, fluctuations in d_{50} records were larger than in SSC records. This is especially pronounced in *Lac de Mauvoisin* (Figures 26 and 27), but it can be observed in other reservoirs as well. Most profiles showed constant SSC or slightly increasing SSC over depth. In *Griessee*, a strong increase in SSC close to the bottom in profile L2211300 in Figure 36 is likely linked with a turbidity current. In *Gebidem*, the relatively large scatter in profile L2791236 in Figures 38 and 39 might have occurred because of the proximity to the inflow and its location in a curve. Both facts might lead to higher turbulent fluctuations than in the rest of the reservoirs.

The path reduction module (PRM) was applied in all measurements in 2015. Because of the combination of the 90%-PRM and the relatively low SSC, optical transmission values were generally high (i.e. above 0.8). Nevertheless, the results are in good agreement with water sample analysis. No negative effect of the PRM could be observed in the measurement data. Measurements in 2016 were taken without PRM. They showed lower transmission values between 0.4 and 0.7. Apart from that, the record did not show qualitative differences. Therefore, it can be concluded that the PRM did not have an influence on the derivation of d_{50} .

Haun *et al.* (2015) compared results gained with *LISST-SL* and *LISST-STX* in stationary³¹ mode to those from moving (where the device was kept at a pre-defined depth and moved horizontally) operation mode and measured distinct differences in SSC (up to 9%) and in d_{50} (up to 19%). Therefore, the operation mode may affect the measurement results. In *Griessee* on 8 August 2016, both stationary and moving measurements were recorded. Here, moving mode refers to lowering and lifting the instrument at a fixed location. Furthermore, a slightly different type of device was applied, so the results are not directly comparable. d_{50} varied by a factor of 10, SSC varied by a factor of 5. It is impossible to distinguish between the influence of the operating mode (stationary/moving) and natural fluctuations possibly caused by turbulence. The average of each stationary measurement is in line with the value measured in moving operation mode (e.g. Figures 35 and 36, profile L2211121). Felix *et al.* (2013) reported the ratio of instantaneous SSC to time-averaged SSC in a laboratory analysis. The ratio was generally between 1.5 and 0.5, that is, much lower than the fluctuations observed herein. It can consequently be assumed that the fluctuations are mainly caused by natural variability and not by the operation mode.

³¹ in stationary operation mode, the device is kept at a fixed depth at a certain location; in moving operation mode, depth or location change

Bonalumi *et al.* (2011) measured SSC in *Oberaarsee* and *Grimselsee* over a depth of 43 m and 28 m in March and July 2009. SSC was between 35 and 180 mg/l, which is the same order of magnitude as the present measurement series. In March, SSC was constant over depth; in July, SSC increased with depth in *Oberaarsee*, but it remained constant in *Grimselsee*. This is in good agreement with the LISST measurements: *Lac de Mauvoisin* and *Griessee* on 08 August 2016 showed an increase of SSC as well, but there was no increase in SSC in *Griessee* on 18 August 2015 and in *Gebidem*. It has not been examined in the scope of this project why SSC might increase with depth or why it might be constant over depth. A decrease of SSC with depth was never observed.

4.4.4 ADCP measurements

ADCP measurements provided flow velocities in both horizontal and vertical direction. Rapid data acquisition and the non-intrusive technology are advantageous, especially in the highly turbulent inflow region, where flow velocity magnitudes were as high as 3.7 m/s.

SSC can be derived from ADCP data based on SNR. From various approaches provided in literature (Section 2.3.4), two relations were selected for further analysis. The formula of Thevenot *et al.* (1992) (Equation 18) links SNR directly with SSC; it does not account for transmission losses. It can be applied in the near-field of the ADCP, as Alvarez and Jones (2002) showed. The constants ξ_1 and ξ_2 in this formula were replaced with values of $\xi_1 = 1.1186$ and $\xi_2 = 0.0245$ as suggested by Alvarez and Jones (2002). Due to short signal propagation distance, it was assumed that acoustic backscatter (ABS) equals SNR; that is, $\Gamma = \Delta$. In the *Griessee* reservoir, near surface had a mean value of 37.7 dB and 33.2 dB on 18 August 2015 and 08 August 2016, respectively. These values correspond to 110 mg/l and 86 mg/l. This is only slightly higher than the estimates gained from water sample analysis. The maximum values of 70 dB and 53.8 dB close to the inflow correspond to 682 and 273 mg/l, which is lower than SSC measured in the inflowing river water. These values are plausible as well, so no attempt was made to carry out a new regression analysis.

In general, SNR obtained at larger depths can be used to determine SSC as well. Here, low SSC and fairly small particle diameters found in the reservoir prohibit a quantitative analysis of the ADCP data regarding SSC. This is illustrated by means of Figure 46. It shows the two-way-transmission losses for two different cases. The panel on the left shows transmission losses for a particle diameter of 10 μm (fine silt) and SSC of 100 mg/l. These are typical values for the three reservoirs that were examined. Transmission losses are governed by beam spreading, absorption by water is one order of magnitude lower and absorption by sediment is another order of magnitude lower. Correction of the

SNR signal due to absorption by sediment has a vanishing influence. Because of this, it is difficult to derive quantitative information on SSC from SNR. Furthermore, adjustments due to transmission losses should exceed the noise level, which is not necessarily the case for absorption by sediment. Nevertheless, qualitative interpretation of the data is possible, so the mixing of suspended sediments in the inflow region can be observed and increasing SSC close to the bottom can be detected. The panel on the right shows transmission losses for a particle diameter of 1 mm (medium sand) and SCC of 1 g/l. Such values can be found in rivers at high discharges. Here, absorption by sediment is almost as important as beam spreading. Absorption by water is one order of magnitude lower, which is favourable, as water properties (temperature, salinity and others) are usually not in the focus of such measurement campaigns. Correction of the SNR signal due to absorption by sediment has a strong influence in this case, and therefore reliable information about SSC can be gained.

On 18 August 2015, increasing SNR towards the reservoir bottom of *Griessee* could be detected up to a distance of ca. 30 m from the inflow (Figure 43). On 08 August 2016, increasing SNR were detected up to a distance of ca. 70 m (Figure 45). These increases can be interpreted as minor turbidity currents. The propagation distance is small and the turbidity currents decay within some dozens of meters from the inflow because the density difference between inflowing river water and reservoir water is no longer large enough to maintain these density-driven currents. The turbidity currents were not distinct; there was no clear boundary between plunging inflowing river water and ambient reservoir water. Decaying turbidity currents deposit sediments. Indeed, bathymetry measurements of Beck and Baron (2015, 2016) showed that pronounced deposition patterns occur close to the inflow³² and reach up to 200 m into the lake. LISST profile L2211300 (Figure 36) implied the existence of a turbidity current, as SSC of up to 2500 mg/l were recorded close to the ground. This is additional evidence of an existing turbidity current. The moderate increase of water temperature further indicates the existence of such a current. A strong increase of water temperature cannot be expected, because there is hardly any temperature difference between inflowing river water and the reservoir water. Bourban and Papilloud (2015) measured turbidity currents in *Griessee* that reached the dam even at dry weather conditions.

On 18 August 2015, there was evidence of a stratified flow in terms of SSC up to a distance of ca. 30 m from the inflow at *Griessee*. On 8 August 2016, the stratified flow reached a distance of ca. 70 m from the inflow. The stratification was most likely due to the evolution of minor turbidity currents, as inflowing

³² reported deposition patterns in front of the dam were due to construction works and the corresponding drawdown of the water table

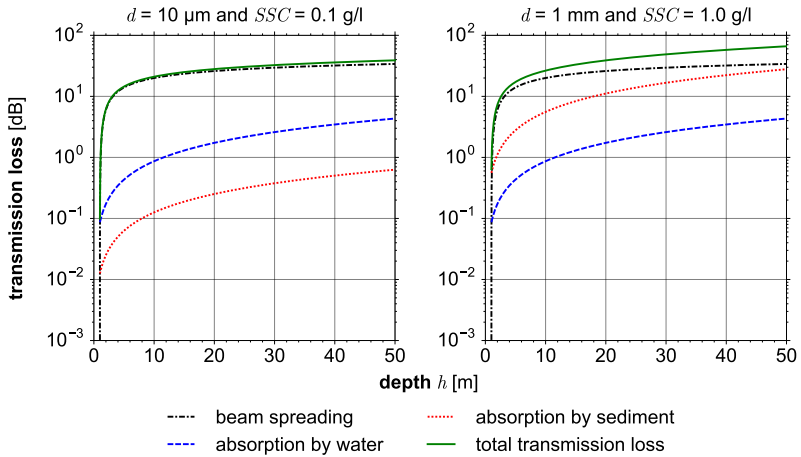


Figure 46: Two-way-transmission losses according to the procedure presented in Moore (2011): The calculations were done for a frequency of 1 MHz, a water temperature of 6 °C, speed of sound in water of 1500 m/s, kinematic viscosity of water of $1.5 \cdot 10^{-6} \text{ m}^2/\text{s}$ (at 6 °C), water and sediment densities of 1000 and 2650 kg/m^3 , respectively, a particle diameter of 10 μm and SSC of 0.1 g/l (left) or a particle diameter of 1 mm and SSC of 1.0 g/l (right)

river water had SSC of 1281 mg/l and 4278 mg/l, whereas average SSC in the reservoir was 82 mg/l and 122 mg/l, respectively. The higher SSC on 8 August 2016 led to a stronger turbidity current with longer propagation distance and increased thickness (Figures 43 and 45). Nevertheless, the density difference and the bottom slope were not high enough for the evolution of a distinct turbidity current (i.e. the upper boundary of the turbid layer is not distinct and the turbidity current decays rapidly). After a few tens of meters, the turbidity current is being mixed with ambient reservoir water and the hyperpycnal conditions change to homopycnal conditions.

It is not possible to derive PSD from a single-frequency ADCP. Guerrero *et al.* (2011) showed that the combination of at least two ADCPs working on different frequencies is needed to derive PSD information.

4.5 Conclusions

4.5.1 Summary

PSD and SSC were measured in three periglacial reservoirs, namely *Lac de Mauvoisin*, *Griessee* and *Gebidem*. The four different measurement techniques Secchi disk measurements, water sample analysis, laser in-situ scattering and transmissometry (LISST) and acoustic Doppler current profiler (ADCP) were applied.

The field measurements have been conducted in five different campaigns. Extreme events (e.g. floods) as well as continuous measurements (e.g. over the whole deposition season from early summer to late autumn) are missing. Stationary (bottom-mounted or moored) ADCP could be applied to measure both during extreme events and over a long time period. This would provide additional insights, like for example on return period, vertical thickness or propagation distance of turbidity current events, which are still major unknowns of periglacial reservoirs. Automatic bottle samplers or LISST measurements could be used to assess SSC and PSD dynamics in the inflowing river water over a long time period. Apart from a better process understanding, this would improve the data basis for subsequent numerical modelling significantly.

Secchi depths were 0.2–1.5 m. According to the laboratory analysis of 85 water samples, 77–93% of the suspended sediments from the three reservoirs were in the silt fraction. Clay portions were between 4 and 20%, sand portions were between 2 and 13%. d_{50} were 5–19 μm . Average SSC in the reservoir was 74–122 mg/l. Both PSD and SSC did not show significant spatial variations in the three reservoirs.

In the inflowing rivers, 60 to 92% of the suspended sediments were silt. Clay and sand portions ranged from 2 to 3% and 5 to 38%, respectively. d_{50} were between 11 and 37 μm . Average SSC was measured from 85 to 4278 mg/l. Water sample analysis did not show evidence of significant flocculation, as probes before and after ultra-sounding did not reveal different PSD. Nevertheless, long storage times or drying procedures can result in cluster formation, which should not be misinterpreted as flocculation. Due to technical limitations, water sampling was restricted to the uppermost 20 m.

The 16 measurements with LISST were in good agreement with the water sample analysis. The LISST device was able to reproduce the whole range of PSD and characteristic diameters such as the d_{50} could be derived. At *Lac de Mauvoisin*, where large depths of more than 100 m were reached, a slight increase in d_{50} (Figure 26) and a pronounced increase in SSC (Figure 27) were observed. The trend of increasing SSC with depth was likewise observed in *Griessee* (Figures 33 and 36), where depths were less than 30 m. A distinct trend of increasing d_{50} could not be detected (Figures 32 and 35), however. In

Gebidem, a deep reservoir similar to *Lac de Mauvoisin*, the trend of increasing SSC was only weak (Figure 39), which may be linked to the fact that these measurements were taken late in the season and correspond to a “winter state” rather than to a “summer state” as for example in *Lac de Mauvoisin*. d_{50} were constant over the whole flow depth (Figure 38).

PSD from LISST measurements (Figures 28, 29, 34, 37, 40 and 41) could be computed using all bin sizes, as hardly any out-of-range particles were present and multiple scattering was not an important factor, given the low SSC. Flocculation and the effects of mica or organic content were neglected. Flocculation could not be detected by means of LISST measurements, as the floc sizes would be in the same range as the grain sizes in suspension. Measuring flocs combined with single particles would hinder conversion from volume to mass concentration, as the density would be strongly reduced because of the flocs present. Some near-surface measurements were possibly affected by ambient light, so that all measurements at depths smaller than 1 m to the surface were neglected.

An unsolved issue is the fact that measurements from moving operation mode (i.e. lowering and lifting the instrument at constant speed of 0.1 m/s at a given location) and stationary operation mode (i.e. keeping the instrument at a certain depth and location) deviate (e.g. Figure 35). Stationary measurements showed variations of up to a factor of 10 for d_{50} and fluctuations of up to a factor of 5 for SSC. It is assumed that the stationary measurements reveal natural fluctuations, but this needs to be proven with further field measurements.

ADCP measurements in *Griessee* provided not only flow velocities, but also SNR that could be used to estimate SSC. Because of relatively low SSC, the influence of SSC on SNR values was hardly detectable. Beam spreading and attenuation by water determined signal losses and therefore the SNR values. This is supported by findings of Guerrero *et al.* (2014). ADCP measurements could not be used for reliable quantitative SSC estimates. Nevertheless, the measurements provided a qualitative view of SSC in the inflow region, as the mixing of inflowing river water with lake water can be studied.

4.5.2 Main findings

Water samples provide the most robust data set. Due to their time-consuming and work-intensive acquisition, their number should be kept small. LISST provides the unique opportunity to measure both PSD and SSC at the same time, but the application range is limited. In most parts of the lake, PSD and SSC are within this range. Easy handling and straightforward data processing are advantages of this technique. LISST can be operated in real-time mode, which allows identifying irregularities in the water body where water samples

should be taken. The effort of data acquisition with LISST is between water sample analysis and ADCP measurements. ADCP measurements provide unique advantages: they are non-intrusive, have a high degree of spatial and temporal resolution and allow profile measurement, where flow velocities at different depths are measured simultaneously. Flow velocities can be measured within the accuracy range guaranteed by the manufacturer.

SNR, a by-product of ADCP measurements, can be used for SSC estimations. The translation from SNR to SSC remains a major issue, as the actual PSD and SSC are necessary for adjusting SNR for transmission losses. Iterative calibration techniques are available, but their application range is limited. Transmission losses can be neglected for SSC close to the ADCP. SSC estimations at larger distances from the ADCP depend on both SSC and particle diameters; high values are in general favourable and lead to more reliable estimates. In the present case, both SSC and particle diameters were too low for a robust quantitative analysis, so ADCP measurements were restricted to a qualitative analysis of SSC profiles over depth, for example, the mixing of inflowing river water and the evolution of turbidity currents. For the given situation, low ADCP frequencies would be preferable as they (a) reduce backscatter from large particles; (b) increase attenuation of clay and silt; and (c) reach larger depths (Guerrero *et al.* 2016). Feasible first-order estimates of near-surface SSC could be made, as these did not have to account for transmission losses. It is not clear how flocs would affect ADCP measurements (Moate and Thorne 2009). Water samples are the best way to calibrate ADCP data, as they provide SSC and particle diameters that can be used for the derivation of transmission losses due to attenuation by sediment. Taking calibration samples simultaneously to ADCP measurements is hardly possible, however. PSD cannot be derived from a single-frequency ADCP.

The set of the four measurement techniques Secchi disk measurements, water sample analysis, LISST and ADCP was applied successfully to study PSD and SSC in periglacial reservoirs. The main findings are:

- (a) Most of the suspended sediments in the reservoir are in the range of silt and clay. Sand and gravel present in the inflow is likely being transported as bed-load in the inflow region and being deposited nearby the inflow.
- (b) d_{50} does only weakly increase with depth (if at all).
- (c) The increase of SSC with depth is more pronounced if depth ranges are large.
- (d) There is no evidence of significant changes of PSD and SSC on the horizontal plane within the reservoir.

- (e) Sediment-laden inflowing river water may lead to turbidity currents, but these stratified flows were restricted close to the inflow zones for the given reservoirs.
- (f) In most parts of the reservoirs, homopycnal conditions seem to be dominant.
- (g) LISST-100X is the most suitable device to examine PSD and SSC over the whole reservoir depth in periglacial reservoirs because it covers the entire ranges of present PSD and SSC.
- (h) Water sample analyses are crucial to check the plausibility of the LISST records.
- (i) There is no evidence that flocculation or the influence of mica or organic content significantly influenced the LISST measurements; ambient light has to be taken into account, however.

Based on the experience made during the field work, the combination of the four different techniques for the present situation at periglacial reservoirs is recommended. The statements of Section 2.3.5 and Figure 13 are confirmed. Nevertheless, it has to be added that the application limits of LISST may be problematic in inflow regions where either PSD consists of a significant amount of medium and coarse sand or large SSC is present. Large amounts of clay particles may lead to flocculation, which is problematic for LISST as well, but this was not an issue in the investigated reservoirs. ADCP measurements could be used for qualitative assessment of SSC only, because concentrations were too low for quantitative assessment inside the reservoir.

The field measurements showed that both a width- and a depth-averaged model should be able to capture the essential long-term and large-scale reservoir sedimentation processes. Such a 1D model will be presented in Section 5.3 and it will be verified in Section 5.4 for the well-documented *Gebidem* reservoir. “1D” implies that longitudinal (stream-wise) transport processes are dominant and that cross-sectional changes (e.g. of PSD, SSC or flow velocities) are neglected. 1D models are no longer appropriate when (a) the ratio of width to length of the reservoir is less than ca. 3³³ or (b) flow or sediment transport characteristics are no longer dominated by longitudinal processes, but also significantly affected by depth- or width-dependent processes. Many periglacial reservoirs impound narrow gorges that have been formed due to strong erosional activity of the

³³ there is no distinct threshold, so the value recommended by HEC-RAS developers <http://hecramodel.blogspot.com/2016/03/1d-2d-or-1d2d-how-should-i-build-my.html> is used

stream or glacier ice; their topography is usually of 1D nature, as these reservoirs are significantly longer than wide. *Griessee*, however, is an example where a 1D model is likely not appropriate, as the reservoir has a circular shape (i.e. it is as long as wide). *Grimseelsee* is another example where a 1D model is likely insufficient, because turbidity currents play an important role in this reservoir. A series of coarse-grained turbidites³⁴ larger than ca. 200 μm (medium sand or larger) have been observed close to many dams of periglacial reservoirs, for example by Anselmetti *et al.* (2007). The causing turbidity currents have seldom been recorded; that is why the return period and prerequisites of these events (e.g. minimum SSC in the tributary) are usually not known. Future measurement campaigns in periglacial reservoirs should therefore focus on these events and provide both long-term measurements to quantify the frequency as well as the importance regarding deposition volumes.

³⁴ deposits of turbidity currents

5 Numerical modelling

5.1 Introduction

As shown in Section 3.5, reservoir sedimentation threatens the sustainable use of reservoirs by reducing storage capacity or endangering safe operation. The former results in a loss of energy production, the latter usually requires costly counter-measures to guarantee operating safety. Observed infill times of reservoirs in the Swiss periglacial environment (Figure 4) differ by several orders of magnitude, which cannot be fully explained by empirical relationships, such as the approach of Gurnell *et al.* (1996) for sediment input and the approach of Brune (1953) for trap efficiency. More sophisticated tools are required to account for site-specific conditions like sediment input, PSD, SSC-Q relationships or hydraulic conditions. In this Chapter, a simple, robust and stable numerical 1D model is presented that allows to quickly tackle problems of reservoir sedimentation on both the large-scale and long-term. It is applied to an existing reservoir to show its applicability. Afterwards, the main drivers of sedimentation in periglacial reservoirs for different climate scenarios are identified, before the model is finally applied to a potential future reservoir, where the full prediction potential for early planning stages will be demonstrated.

5.2 Scope of application

The model presented herein closes a relevant gap in a sequence of sediment transport models in the periglacial environment. Upstream of reservoirs (or lakes in general), morphodynamic models show how sediments are evacuated from underneath glaciers (e.g. Delaney *et al.* (2018b)) and transported through steep glacier valleys (e.g. Kammerer *et al.* (2016)) until they are being conveyed into the reservoir or withdrawn into desanding facilities (e.g. Paschmann (2018)). Downstream of the reservoir, models for turbine abrasion (e.g. Felix (2017)) or operation of sediment bypass tunnels (Facchini (2018)) are available. The only missing link is the reservoir itself.

A selection of numerical models related to reservoir sedimentation is presented in Section 2.4.3. These models are suitable within their application range, but

they may be challenged by conditions found in periglacial reservoirs. The numerical model presented herein must master:

- flow transition: Many periglacial reservoirs have steep inflow channels where supercritical flow conditions (i.e. Froude number $F > 1$) are present. Once the lake level is reached, the flow is abruptly decelerated, and subcritical flow conditions (i.e. Froude number $F < 1$) establish. The *hydraulic jump* at the location of the transition often triggers instabilities of numerical models, especially when combined with sediment transport.
- highly unsteady boundary conditions: Some periglacial reservoirs are exposed to rapid lake level changes in the order of 10% of the maximum flow depth or more per day. In addition, inflow is strongly linked to subglacial drainage and extreme weather conditions, and therefore inflow can increase by orders of magnitude within a few hours.
- large range of PSD: Glacial streams usually cover a wide range of grain fractions from clay to gravel. This implies that both suspended sediment transport and bed load transport occur at the same time. Furthermore, the interaction of both transport processes must be taken into account.
- two deposition modes: As a consequence of the broad PSD, two deposition modes occur in the reservoir. Coarse sediment will lead to Gilbert-type delta formation in the inflow region, whereas fine sediment will lead to sedimentation from homopycnal (non-stratified) flows along the reservoir.
- strongly varying geometry: Periglacial reservoirs have been built in high-alpine rugged post-glacial valleys. Strong variations in width and bed level are commonly found.
- long simulation periods: Simulations of sedimentation on time scales from seasons to decades require models that allow for efficient computation. A trade-off between simplified mathematical models and accuracy of process description as well as computational stability is crucial.

Studies (Section 4.5 or Ehrbar *et al.* (2017)) show that there is no evidence of significant changes of neither PSD nor SSC in the horizontal plane and that homopycnal conditions are dominant in most parts of the investigated periglacial reservoirs. Therefore, a 1D model (i.e. a both depth- and width-averaged model) is capable to capture long-term sedimentation processes on reservoir scale. In general, 1D models are computationally less expensive than 2D or 3D models and, correspondingly, more efficient. Large problem domains and long simulation periods as well as a large amount of simulation runs can usually be handled easier with 1D models than with 2D or 3D models.

The numerical model developed in the scope of this project fulfils these requirements. It will be introduced by (1) presenting the mathematical and numerical model; (2) verifying it with the test case of *Gebidem* reservoir; (3) forcing it with changing boundary conditions to mimic potential impacts of climate change; and (4) applying it to a potential future reservoir to demonstrate its usability in prediction and highlighting the importance of taking reservoir sedimentation into account to ensure the sustainable use of the reservoir.

5.3 Mathematical and numerical model

5.3.1 Introduction

The numerical model is included into the software *BASEMENT*³⁵ which has been developed at the *Laboratory of Hydraulics, Hydrology and Glaciology at ETH Zürich*. This tool was improved to meet the requirements of this study. *BASEMENT* applies the finite volume method. An elaborate documentation of the software is given in Vetsch *et al.* (2017), so only a brief summary is presented below. In the numerical 1D model, a water reach is discretised by cross sections with control volumes from midpoint to midpoint in between (Figure 47). Cross sections provide geometry information, which is reduced to width and bed level here. The interfaces between control volumes are called edges and are purely virtual. Cross sections have states, such as flow area or discharge, whereas edges contain fluxes of mass or momentum. Each cross section covers a length Δx [m], which is defined by the extent of the control volume. Conservative variables are flow area, discharge, and suspended sediment volume concentration. Other variables, such as flow depth or velocity, are secondary variables that can be derived from the conservative variables.

5.3.2 Governing flow equations

5.3.2.1 Saint-Venant equations and closure

Governing flow equations of the numerical 1D model are the *Saint-Venant equations*. They consist of (a) mass conservation (Equation 45a), also referred to as the “continuity equation”; and (b) momentum conservation (Equation 45b), which are a 1D derivation of the *Navier-Stokes equations*. Underlying assumptions of these two equations are: (i) hydrostatic pressure distribution; (ii) uniform flow velocity over the whole cross section and horizontal water surface; (iii) small channel slope, so that its cosine can be assumed to be 1.0; and (iv) a

³⁵ <http://www.basement.ethz.ch>

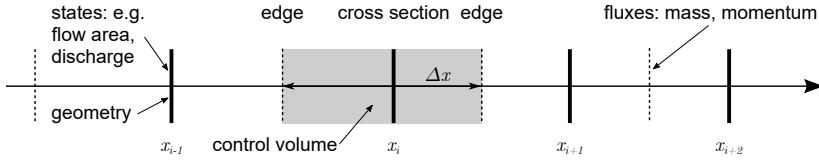


Figure 47: Nomenclature in the numerical 1D model: cross sections provide geometry information and have states; virtual edges are located at the midpoints between cross sections and contain fluxes

steady-state resistance law can be applied (Chaudhry 2008). The *Saint-Venant equations* can be written in the following conservation form (Vetsch *et al.* 2017):

$$\frac{\partial A}{\partial t} + \frac{\partial Q}{\partial x} = 0 \quad (45a)$$

$$\frac{\partial Q}{\partial t} + \frac{\partial}{\partial x} \left(\frac{Q^2}{A} \right) + gAS + gAJ = 0 \quad (45b)$$

where A is the flow area [m²]; Q is the discharge [m³/s]; t is the time [s]; x is the longitudinal coordinate (in flow direction) [m]; g is the gravitational acceleration [m/s²]; S is the bed slope [-]; and J is the friction slope [-]. These equations hold even in cases of *hydraulic jumps*, since mass and momentum flux are continuous across flow transitions.

Flow area (A) and discharge (Q) are the conservative variables, which are computed at a distinct space (x) and time (t). The bed slope (S) is given by the geometry of the cross sections. To close this system of equations, an empirical relationship for the friction slope (J) is used. Here, a *Manning-Strickler* equation was applied, which is:

$$J = \frac{Q^2}{A^2 k^2 l^{4/3}} \quad (46)$$

where k is the Strickler coefficient which describes the channel roughness [m^{1/3}/s]; and l is the hydraulic radius [m].

5.3.2.2 Numerical scheme and discretisation

The conservative variables A and Q are computed with an explicit scheme; thus, new values at a certain time step depend solely on old values from the previous time step:

$$A^{new} = A^{old} - \frac{\Delta t}{\Delta x} (\phi_r - \phi_l) \quad (47a)$$

$$Q^{new} = Q^{old} - \frac{\Delta t}{\Delta x} (\Phi_r - \Phi_l) + \sum Sources \quad (47b)$$

where Δt is the time step [s]; $\phi_{r/l}$ are the continuity fluxes over the right and left edge, calculated by the *Riemann solver* [m^3/s]; $\Phi_{r/l}$ are the momentum fluxes over the right and left edge, calculated by the *Riemann solver* [m^4/s^2]; and $\sum Sources$ is the sum of the bed slope source term and the friction source term [m^3/s].

The continuity and momentum fluxes are computed by the approximate *Riemann solver* of Roe (1981). Beffa (1994) presented the following solution for the computation of the fluxes over the edges:

$$\phi = \frac{Q_r + Q_l}{2} - \frac{1}{4c} (\chi_1 |\chi_2| - \chi_2 |\chi_1|) A + \frac{1}{4c} (|\chi_1| - |\chi_2|) (Q_r - Q_l) \quad (48a)$$

$$\Phi = \frac{U_r + U_l}{2} - \frac{1}{4c} (\chi_1 \chi_2 [|\chi_2| - |\chi_1|]) A - \frac{1}{4c} (|\chi_1| \chi_1 - |\chi_2| \chi_2) (Q_r - Q_l) \quad (48b)$$

where $U = Q^2/A$ [m^4/s^2]; and $\chi_{1/2}$ are eigenvalues of the *Roe matrix* defined as:

$$\chi_{1/2} = \frac{v_l + v_r}{2} \pm \beta \quad (49a)$$

$$\beta = \sqrt{g \frac{h_l + h_r}{2}} \quad (49b)$$

where $v_{l/r}$ are the flow velocities [m/s]; $h_{l/r}$ are the flow depths in the left and right element of the edge [m]; and β is the wave celerity [m/s]. Both flow velocity and flow depth are derived variables; they are calculated as:

$$v = \frac{Q}{A} \quad (50a)$$

$$h = \frac{A}{y_b} \quad (50b)$$

where y_b is the width of the cross section [m].

The source terms include bed slope and friction. The former is discretised explicitly, the latter is discretised with a semi-implicit approach to prevent numerical instabilities. Details are provided in Vetsch *et al.* (2017).

The time step is computed according to the *Courant–Friedrichs–Lewy condition*:

$$\Delta t = CFL \cdot \frac{\Delta x}{v + \sqrt{gh}} \quad (51)$$

where CFL is a the dimensionless Courant number [-], which must be lower than or equal to 1.0.

5.3.3 Governing sediment transport equations

Fluvial sediment transport is determined by hydraulic flow conditions. It can be splitted into bed load transport and suspended load. The former transport mode describes the movement of coarse grain particles near the bed, whereas the latter describes the movement of fine particles in suspension distributed over the whole water column.

5.3.3.1 Bed material mass conservation

Bed material mass is conserved by the so-called *Exner equation* (Exner 1925). It states:

$$(1 - p) \frac{\partial z_b}{\partial t} + \sum \left[\frac{\partial q_b}{\partial x} + b \right]_i = 0 \quad (52)$$

where p is the porosity of the bed material [-]; z_b is the bed elevation [m]; q_b is the specific volumetric bed load transport rate [m³/(s·m)]; and b is the exchange rate between suspension and bed [m/s]. b is positive for net entrainment and negative for net deposition. The sum sign indicates that the contribution

from each grain fraction i has to be taken into account in case of multi-grain simulations.

Equation (52) is discretised in explicit form as:

$$A_{sed}^{new} = A_{sed}^{old} + \frac{\Delta t}{\Delta x} \sum [Q_{b,l} - Q_{b,r} - b]_i \quad (53)$$

where A_{sed} is the sediment area in the control volume [m^2]; and $Q_{b,r/l}$ are the volumetric bed load fluxes [m^3/s] over the right and left edge. Again, i denotes that every single grain fraction has to be taken into account in case of multi-grain simulations. Here, bed load fluxes were not interpolated over the edges; the bed load fluxes over the edges were set equal to the bed load fluxes of the upstream cross section. For rectangular cross sections, A_{sed} in Equation (53) can be replaced as $A_{sed} = z_b \cdot y_b$.

5.3.3.2 Bed load transport

Bed load transport can be modelled with different semi-empirical formulas. Here, the approach of Meyer-Peter and Müller (1948) is applied in the following form:

$$q_{b,i} = (1 - \Theta_i) \xi_1 \sqrt{\gamma g d_i^3} (\theta_i - \theta_{cr,i})^{\xi_2} \quad (54)$$

where $q_{b,i}$ is the specific volumetric bed load transport capacity [$\text{m}^3/(\text{s}\cdot\text{m})$]; Θ_i is the transport mode selector [-]; ξ_1 is the bed load factor [-]; γ is the submerged specific density [-]; g is the gravitational acceleration [m/s^2]; d_i is the characteristic grain diameter [m]; θ_i is the dimensionless bed shear stress [-]; $\theta_{cr,i}$ is the critical dimensionless shear stress [-]; and ξ_2 is the bed load exponent [-]. i denote variables that depend on the grain fraction in case of multi-grain simulations. The authors proposed values of $\xi_1 = 8$ and $\xi_2 = 1.5$, which will be used here.

The critical shear stress $\theta_{cr,i}$, above which bed load transport occurs, is determined according to Yalin and da Silva (2001):

$$\theta_{cr,i} = \xi_3 \left\{ 0.13 D_i^{-0.392} \exp[-0.015 D_i^2] + 0.045 (1 - \exp[-0.068 D_i]) \right\} \quad (55)$$

where ξ_3 is the the hiding function proposed by Ashida and Michiue (1971) [-]; and D_i is the dimensionless grain diameter [-]. The hiding function of Ashida and Michiue (1971) is defined in Wu (2008) as:

$$\xi_3 = \begin{cases} \left[\frac{\log(19)}{\log(19d_i/d_m)} \right]^2 & \frac{d_i}{d_m} \geq 0.4 \\ \frac{d_m}{d_i} & \frac{d_i}{d_m} < 0.4 \end{cases} \quad (56a)$$

$$\quad \quad \quad (56b)$$

where d_m is the mean diameter of the grain mixture (i.e. the sum of all grain fractions i) [m]; and d_i is the characteristic grain diameter of fraction i [m]. This hiding function increases the critical shear stress for grains with a diameter of less than 40% of the mean diameter of the mixture, because these relatively small grains “hide” behind the large grains and are less exposed to bed load transport. In contrast, the critical shear stress for larger grains is decreased, because these grains are more exposed to bed load.

The dimensionless grain diameter is defined as:

$$D_i = \left(\frac{\gamma g}{\nu^2} \right)^{1/3} d_i \quad (57)$$

where ν is the kinematic viscosity of water [m²/s].

The submerged specific density is defined as:

$$\gamma = \frac{\rho_s - \rho_w}{\rho_w} \quad (58)$$

where ρ_s is the density of sediment [kg/m³]; and ρ_w is the density of water [kg/m³].

The dimensionless bed shear stress (θ_i) is derived from the bed shear stress (τ) as:

$$\tau = \rho_w g \frac{v^2}{k^2 l^{1/3}} \quad (59a)$$

$$\theta_i = \frac{\tau}{\rho_w g \gamma d_i} \quad (59b)$$

where τ is the bed shear stress [N/m²].

5.3.3.3 Suspended load transport

Suspended load transport is modelled with a convection-diffusion equation:

$$A \frac{\partial C_i}{\partial t} + Q \frac{\partial C_i}{\partial x} - \frac{\partial}{\partial x} \left(AD \frac{\partial C_i}{\partial x} \right) - B_i = 0 \quad (60)$$

where C is the volumetric SSC [-]; D is the diffusion coefficient [m^2/s]; and B is the exchange rate between suspension and bed [m^2/s]. This equation has to be solved for each grain fraction i . Considering convection as the dominant form of transport, diffusion will be neglected from here on. Thus, Equation (60) reads in discretised form:

$$C_i^{new} = C_i^{old} - \frac{\Delta t}{\Delta x A} [\psi_r - \psi_l]_i \quad (61)$$

where $\psi_{r/l}$ are the advective fluxes over the edges between the cross sections of each grain fraction i [m^3/s].

Both stability and accuracy of the results of the advection equation are determined by the scheme applied to compute the advective fluxes. Here, the *QUICKEST* scheme of Leonard (1979) was used with a limiter to avoid negative SSC in order to ensure mass conservation. The advective fluxes for each grain fraction i ³⁶ are computed with the following equations, using the nomenclature defined in Figure 48:

$$\psi = C_u + \eta_2 (C_d - C_u) + \eta_3 (C_u - C_{uu}) - \eta_1 \frac{C_d - C_u}{2} + \eta_1 \frac{C_d - 2C_u + C_{uu}}{8} \quad (62a)$$

$$\eta_1 = \frac{(v_u + v_d) \Delta t}{2(x_d - x_u)} \quad (62b)$$

$$\eta_2 = \frac{(x_{edge} - x_u)(x_{edge} - x_{uu})}{(x_d - x_u)(x_d - x_{uu})} \quad (62c)$$

$$\eta_3 = \frac{(x_{edge} - x_u)(x_d - x_{edge})}{(x_u - x_{uu})(x_d - x_{uu})} \quad (62d)$$

5.3.3.4 Exchange rate

Xu (1998) presented an approach to compute the exchange rate between suspension and bed. He determined two components: (1) entrainment of bed material; and (2) deposition of suspended sediments. The exchange rate is defined as:

$$b_i = \Theta_i b_{e,i} - b_{d,i} = \frac{B_i}{y_b} \quad (63)$$

³⁶ for better readability, the indices i are omitted here

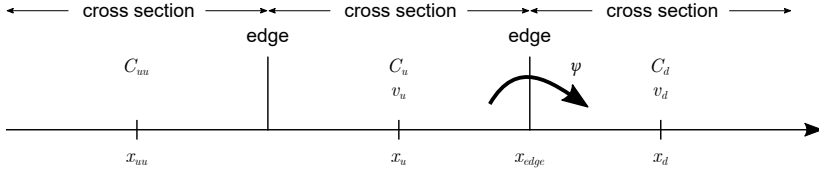


Figure 48: Nomenclature for the *QUICKEST* scheme (C is the volumetric SSC; v is the flow velocity; x is the longitudinal distance; indices u and d stand for “upstream” and “downstream”, respectively)

where b_i is the exchange rate between suspension and bed [m/s]; $b_{e,i}$ is the entrainment rate [m/s]; and $b_{d,i}$ is the deposition rate [m/s]. The entrainment rate is computed using the following relationship:

$$b_{e,i} = \begin{cases} \frac{\xi_1}{\rho_s} \left(\frac{\tau}{\tau_{cr,e,i}} - 1 \right)^{\xi_2} & \tau > \tau_{cr,e,i} \\ 0 & \tau \leq \tau_{cr,e,i} \end{cases} \quad (64a)$$

$$\tau \leq \tau_{cr,e,i} \quad (64b)$$

where ξ_1 is a calibration parameter (“erosion coefficient”) [kg/(m²·s)]; $\tau_{cr,e,i}$ is the critical bed shear stress for entrainment [N/m²]; and ξ_2 is another calibration parameter [–], accounting for non-linear erosion rates. Xu (1998) recommends values of ξ_1 in the range of $1.6 \cdot 10^{-5}$ to $1.38 \cdot 10^{-3}$ kg/(m²·s) and ξ_2 in the range of 1 to 4. Here, linear erosion was assumed (i.e. $\xi_2 = 1.0$). For a model application in the *Lauffen* reservoir (Germany), Xu (1998) calibrated $\xi_1 = 7.5 \cdot 10^{-4}$ kg/(m²·s), which will be used from here on. The critical bed shear stress is computed using the following approach:

$$\tau_{cr,e,i} = \rho_w u_*^2 = \theta_{cr,i} g \rho_w \gamma d_i \quad (65)$$

where u_* is the bed shear velocity [m/s]. The deposition rate is usually related to a reference concentration at a certain distance above bed level. As no significant changes in SSC over depth were observed during the measurement campaign, the depth-averaged SSC was used. The deposition rate is then modelled as:

$$b_{d,i} = \begin{cases} w_i C_i \left(1 - \frac{\tau}{\tau_{cr,d,i}} \right) & \tau < \tau_{cr,d,i} \\ 0 & \tau \geq \tau_{cr,d,i} \end{cases} \quad (66a)$$

$$\tau \geq \tau_{cr,d,i} \quad (66b)$$

where w_i is the particle settling velocity [m/s]; and $\tau_{cr,d}$ is the critical bed shear stress for deposition [N/m^2]. It is determined as:

$$\tau_{cr,d,i} = (\rho_s - \rho_w) \frac{ghw_i C_i}{\xi_3 v} \quad (67)$$

where ξ_3 is a calibration parameter (“sedimentation coefficient”) [-]. The calibration of the *Lauffen* reservoir test case led to $\xi_3 = 0.005$, which will be used from here on.

The particle settling velocity w_i is computed following the approach provided by Wu and Wang (2006):

$$w_i = \frac{\eta_1 \nu}{\eta_2 d_i} \left[\sqrt{\frac{1}{4} + \left(\frac{4\eta_2}{3\eta_1^2} D_i^3 \right)^{1/\eta_3}} - \frac{1}{2} \right]^{\eta_3} \quad (68a)$$

$$\eta_1 = 53.5 \exp[-0.65S] \quad (68b)$$

$$\eta_2 = 5.65 \exp[-2.5S] \quad (68c)$$

$$\eta_3 = 0.7 + 0.9S \quad (68d)$$

where S is the Corey shape factor of the particles [-]. It is usually in the range of 0.3–0.9 for naturally worn particles; for perfectly spherical particles, S is 1.0.

5.3.3.5 Transport mode selector

The same particle can be transported either as suspended load or bed load. Spasojevic and Holly (1990) stated that the ratio of bed shear velocity (u_*) to settling velocity (w) is the decisive factor for the transport mode: for $u_*/w > 10$, a grain is transported as suspended load only, whereas for $u_*/w < 0.4$, a grain is transported solely as bed load. Between these thresholds, both transport modes can occur at the same time. Thus, the transport mode selector in *BASEMENT* is implemented according to Gessler *et al.* (1999):

$$\Theta_i = \begin{cases} 0 & \frac{u_*}{w_i} < 0.4 \end{cases} \quad (69a)$$

$$\Theta_i = \begin{cases} 0.25 + 0.325 \ln \left[\frac{u_*}{w_i} \right] & 0.4 \leq \frac{u_*}{w_i} \leq 10 \end{cases} \quad (69b)$$

$$\Theta_i = \begin{cases} 1.0 & \frac{u_*}{w_i} > 10 \end{cases} \quad (69c)$$

The transport mode selector acts on the bed load transport rate (Equation 54) and the exchange rate (Equation 63).

5.4 Model verification

5.4.1 Test case selection

Gebidem reservoir was selected as test case for the model verification. Information about reservoir sedimentation is given in Section 2.2.4.3, general information about the reservoir is provided in Section 4.2.1.3. *Gebidem* is a unique test case: it combines delta formation and deposition from homopycnal flows, and these processes happen fast, as the infill time is as low as 20–30 years. Furthermore, multi-beam echo-soundings provide high-quality bathymetry data of recent years. A gauging station³⁷ in *Massa* river 400 m upstream of the inflow provides discharge measurements. According to *FOEN* statistics, the mean annual inflow is 13.4 m³/s, HQ₂ is 82–89 m³/s, HQ₃₀ is 114–142 m³/s, and HQ₃₀₀ is 120–200 m³/s. The reservoir has a gross capacity of 9.2 hm³, of which 5.8 hm³ constitute the active storage between full supply level at 1436.5 m a.s.l. and minimum operating level at 1400 m a.s.l. The capacity-inflow-ratio amounts to 0.02. The owner of the reservoir (*Alpiq*) records lake levels daily. Apart from that, *Gebidem* is located immediately downstream of *Aletsch Glacier*, the largest glacier of the Alps, which is of particular interest for studies dealing with impacts of climate change. Runoff projections for *Aletsch Glacier* are available for different climate change scenarios and models (Section 3.2.1).

5.4.2 Test case set-up

5.4.2.1 Geometry

Cross sections of the reservoir were taken every 20 m, resulting in 81 cross sections. Measured bathymetry data was converted into rectangular cross sections by meeting two constraints: (a) minimum bed elevation (often referred to as “thalweg”) must be maintained; and (b) flow area at full supply level must be equal in the rectangular cross section and in the measured (natural) cross section. The former constraint defines the bed level, the latter the width of each cross sections. This approach is simple, but it is capable of reproducing the delta with its mild topset slope and steep foreset slope, and the flattening reservoir bed towards the dam. Rectangular cross sections instead of “arbitrary” cross

³⁷ *FOEN* (Federal Office for the Environment) station 2161, available online at <https://www.hydrodaten.admin.ch/en/2161.html>

sections³⁸ increase the stability of the numerical model and save computation time. Figure 49 shows the reservoir geometry obtained with this conversion. No bathymetry data is available in *Massa* gorge upstream of the reservoir. Therefore, artificial data was used on the uppermost 200 m long stretch: following Morris and Fan (2010), a bed slope of 6% was taken and a mean width of 10 m was assumed. A sketch of the test case is shown in Figure 50.

5.4.2.2 Boundary conditions

Both water inflow and lake level are being measured at a temporal resolution of 1 day (i.e. daily averages). At the upstream boundary, water inflow was set according to the measurements of the gauging station. At the downstream boundary, measured lake levels were imposed by a weir with variable crest level. Lake levels can vary between 1436.5 m a.s.l. (full supply level) and 1400 m a.s.l. (minimum operating level).

Annual sediment conveyance into *Gebidem* has recently been estimated in the range of 0.43–0.47 hm³ by Meile *et al.* (2014), which is in good agreement with earlier studies (Giezendanner and Dawans 1981; Rechsteiner 1996; Beyer Portner 1998; Morris and Fan 2010). These estimates rely on single-beam echo-soundings, which are likely over-estimating the deposition volumes and therefore the sediment input (G. Bourban / *HYDRO Exploitation*, pers. comm.). Hence, this range is an upper limit for sediment input. Sediment inflow was back-calculated using the relationship between SSC and water inflow of Müller and Förstner (1968) (Equation 3). For a given hydrograph and target sediment volume, for each pre-factor ξ_1 a corresponding exponent ξ_2 can be found vice versa. Therefore, a second constraint was found in the fact that SSC has been measured in the precedent field measurement campaign, which leads to a single pair of pre-factor and exponent. At this stage, no distinction between suspended sediment and bed load was made.

Average PSD of the bed load entering *Gebidem* is given in Giezendanner and Dawans (1981). The authors state that on average 26% of the total sediment input is bed load. This information was combined with measured PSD from the measurement campaign of 6 October 2015 shown in Figure 24. A composite PSD was derived by combining and weighting the PSD of Giezendanner and Dawans (1981) with 26% and the PSD of Figure 24 by 74%. The result is shown in Figure 51. An idealised and discretised overall PSD is shown as well. Bed load sets in at ca. 20 m³/s (Giezendanner and Dawans 1981), suspended sediment transport is likely to occur whenever inflow takes place.

³⁸ arbitrary cross sections could be used as well in the software *BASEMENT*

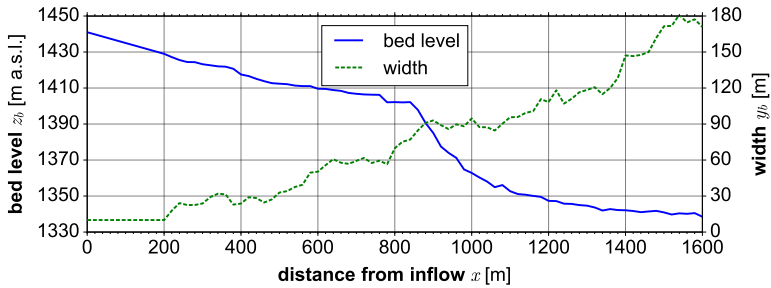


Figure 49: Geometry of *Gebidem* reservoir after conversion of the measured (natural) cross sections into rectangular cross sections

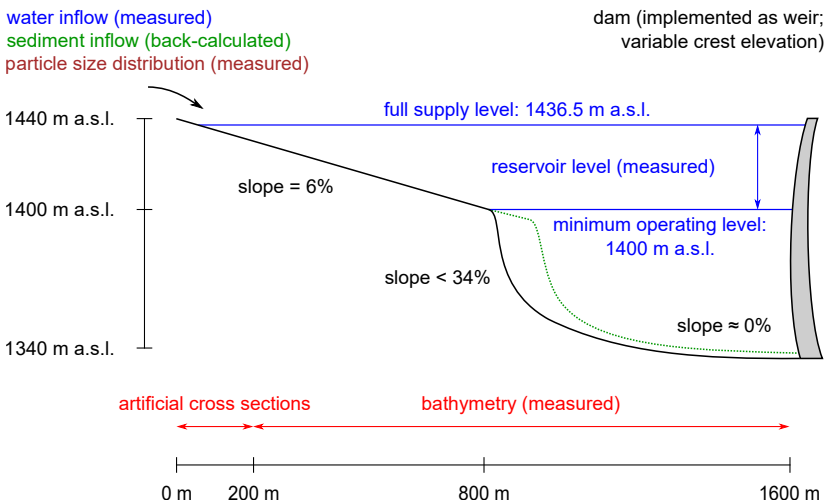


Figure 50: Sketch of the *Gebidem* test case (not to scale): rectangular cross sections are derived from bathymetry measurements (inside the reservoir) or are artificially constructed (within the *Massa* gorge where no measurements are available); water inflow measurements and lake level are based on measured daily averages, sediment inflow is back-calculated from measured deposition volumes; initial slope values are given

5.4.3 Calibration

5.4.3.1 Event

The numerical model was calibrated based on the 2015 season, because this is the most recent deposition season without interjacent reservoir flushing. Prior bathymetry measurements were made on 30 September 2014, posterior bathymetry measurements on 6 October 2015. Both data sets were acquired with multi-beam echo-sounding. In order to reduce computation time, only the time period from 1 June to 1 October was simulated. In the winter season, there is hardly any inflow into the reservoir and, hence, hardly any deposition. In spring, inflow is generally low due to the high altitude and no significant deposition is expected. The measured inflow and lake level of the calibration time period are shown in Figure 52. In 2015, annual inflow volume was 536 hm^3 , of which 479 hm^3 (89%) occurred in the calibration period between 1 June and 1 October. Peak discharge was in the range of HQ_{10} .

5.4.3.2 Targets

Only one measured bathymetry data set is available for calibration, and important boundary conditions such as sediment input are unknown, apart from vague estimates. Calibration targets were: (a) deposition volume; (b) SSC at the inflow; and (c) qualitative deposition patterns at the end of the time period.

Multi-beam echo-sounding revealed a deposition volume of 0.18 hm^3 between 30 September 2014 and 6 October 2015, with an estimated accuracy of $\pm 3\%$ (G. Bourban / *HYDRO Exploitation*, pers. comm.). This value includes an unknown porosity. The deposition pattern is shown in Figure 5. The first calibration target was to minimise the difference between measured and simulated deposition volume.

The measurement campaign on 6 October 2015 revealed average SSC in the inflowing river (*Massa*) of 85 mg/l at a discharge of $11 \text{ m}^3/\text{s}$ (Table 14). Inflow conditions on 1 and 6 October are almost identical. The second calibration target was to minimise the difference between measured and simulated SSC for a discharge of $11 \text{ m}^3/\text{s}$.

The third calibration target was to qualitatively reproduce delta formation and sedimentation from homopycnal flows.

5.4.3.3 Parameters

The numerical model as described in Section 5.3 was used with all parameters as reported. Remaining calibration parameters were: (a) pre-factor ξ_1 and exponent ξ_2 in Equation 3; (b) the discretisation of the PSD; and (c) the porosity.

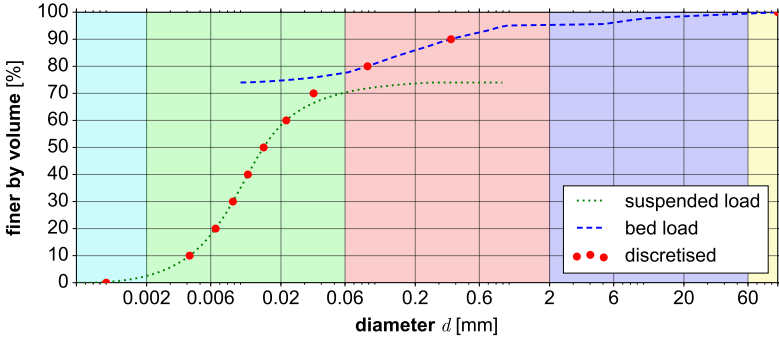


Figure 51: Composite PSD of the sediment discharge into *Gebidem*, combining bed load data from Giezendanner and Dawans (1981) and own measurements of suspended sediment transport as shown in Figure 24

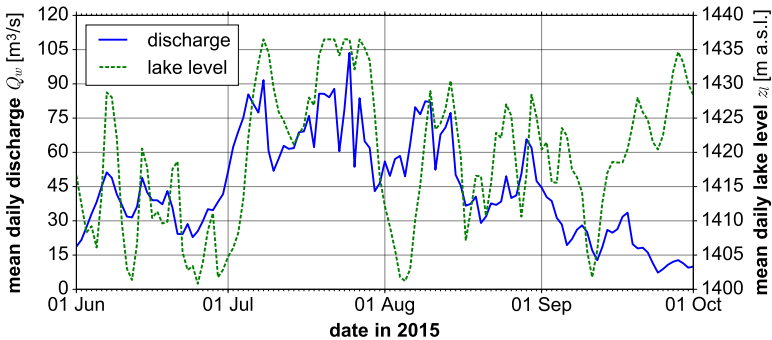


Figure 52: Measured inflow of water into *Gebidem* reservoir (upstream boundary) and lake level (downstream boundary) for the calibration period of 1 June 2015 until 1 October 2015

If Equation 3 is applied to a given *hydrograph*, a specific sediment volume can be obtained for each pre-factor ξ_1 by adjusting exponent ξ_2 , and vice versa. A second constraint is needed to select one pair of pre-factor and exponent. Here, the measured SSC of 85 mg/l at a discharge of 11 m³/s was used to select the best combination of pre-factor and exponent. A pre-factor ξ_1 of 0.001 and an exponent ξ_2 of 1.8 lead to a total sediment input of 0.28 hm³ in the chosen period from 1 June to 1 October 2015. This fits well with the value of 0.275 hm³ measured by Stutenbecker *et al.* (2017), and will lead to the best fit regarding deposition volumes, as it will be shown below. For a discharge of 11 m³/s, SSC is 75 mg/l, which is again closest to the target value of 85 mg/l (deviation of -12%). Maximum SSC is 4.2 g/l, which is in good agreement with maximum measured SSC in the inflow of *Griessee* (Table 13) and in the same range as maximum SSC of other studies presented in Section 2.2.1.2.

PSD was discretised into ten grain fractions, each accounting for 10% of the overall PSD. For each fraction, the median diameter was taken to represent the characteristic diameter of the corresponding fraction. The numerical model revealed that the first six grain fractions ($0.001 \leq d \leq 0.021$) exhibit almost identical transport characteristics for the situation at hand: these grain diameters are small enough to be transported through the reservoir as wash load. Therefore, these six grain fractions were summed up in single fraction accounting for 60% of the overall PSD. The final discretisation of the PSD is given in Table 15.

In order to compare measured and modelled deposition volumes, porosity must be taken into account. Wu and Wang (2006) provided a formula for estimating the average initial porosity of sediment mixtures:

$$p = 0.13 + \frac{0.21}{(d_{50} + 0.002)^{0.21}} \quad (70)$$

where p is the porosity [-]; and d_{50} is the median diameter of the mixture [mm]. Deposits consist primarily of large grains of 62 μm , 229 μm , and 50 mm. Corresponding porosities would be 0.50 (62 μm), 0.42 (229 μm), and 0.22 (50 mm). An average value of 0.37 was taken.

5.4.3.4 Results

The results of the calibration are shown in Figure 53. 0.11 hm³ of the 0.28 hm³ of sediment conveyed into the reservoir are maintained. This equals a trap efficiency of 40%. Including a porosity of 37%, this leads to a deposition volume of 0.18 hm³, which equals the measured deposition volume. The theoretical trap efficiency of *Gebidem* is 49% according to Brune's Equation 4a.

Table 15: Discretisation of the composite PSD (Figure 51) into five grain fractions (m is the per cent finer by mass; d is the range of diameters; and d_i is the mean diameter of this fraction when the PSD is linearly discretised, which is used as the characteristic diameter for the respective grain fraction)

m [%]	0–60	60–70	70–80	80–90	90–100
d [mm]	0.001–0.021	0.021–0.035	0.035–0.088	0.088–0.369	0.369–100
d_i [mm]	0.011	0.028	0.062	0.229	50

Delta propagation in the numerical model is ca. 60 m for the calibration season 2015 (Figure 53), which is in good agreement with measurements (Figure 5). The simulated maximum deposition at the delta front amounts to 18 m (Figure 53), which is in good agreement with the measured maximum deposition of 22 m (G. Bourban / *HYDRO Exploitation*, pers. comm.). Homopycnal sedimentation in the vicinity of the dam is 0.5 m in the numerical model, whereas the maximum measured deposition is 5.5 m. These depositions cannot be compared directly, because the deposition is equally distributed over the whole width of the rectangular profile of the numerical model, whereas it is allocated in the bottom range of the real reservoir. The numerical 1D model reaches its application limits here, because bed level changes are ofte distributed over the whole cross section due to the missing information in transversal direction. Nevertheless, deposition volumes can be compared. As soon as local deposition processes are of interest, a more detailed 2D or 3D model should be applied.

SSC is shown in Figure 54. A decrease of SSC throughout the reservoir can be observed. On 1 October 2015, SSC is ca. 75 mg/l on average in the reservoir, which is nearly identical to the measured value of 85 mg/l. Therefore, the first and second calibration targets are fulfilled.

The two deposition modes, delta formation and sedimentation from homopycnal flows, are captured. Figure 53 shows that small grains (here: 11 μm) are being transported through the reservoir as wash load, medium grains (here: 28 μm and 62 μm) contribute to sedimentation from homopycnal flow, and that coarse grains (here: 229 μm and 50 mm) lead to delta formation. This is in good agreement with the field measurements, where diameters of the suspended sediments were less than 200 μm , confirmed both by water sample analysis (Table 14) and LISST measurements (Figures 40–41). Coarse grains settle on the delta topset (grey area in Figure 53) in the backwater zone induced by the reservoir. Bed load transport is determined by bed shear stress, which is basically a function of the hydraulic radius (l) and flow velocity (v) (Equation 59a).

Although the hydraulic radius is large in the backwater zone, the flow velocity is close to zero, so that no bed load transport occurs. Whenever the lake level is lowered towards the brink point (Figure 3), the flow regime changes from backwater towards fluvial; despite lower flow depths, the significantly higher flow velocities allow bed load transport now. The relocation of sediment from the delta topset towards the delta front and the corresponding delta prolongation is due to bed load transport, not to suspended load transport. Sedimentation from homopycnal flow is purely determined by suspended load transport. From a purely qualitative view, the third calibration target is fulfilled.

The model has a real time speed in the order of ca. 450; that is, the calculation time is 450 times smaller than the simulation time, if the model is run in parallel on two cores of a 3.5 GHz CPU. This demonstrates the efficiency of the 1D model, as this real time speed is achieved for a model with five grain fractions, simulating both bed load and suspended load transport and their interaction throughout the whole reservoir. The Courant number (CFL) was taken equal to 0.5 to avoid instabilities due to *hydraulic jumps* and consequently rapid bed level changes. The proper choice of the Courant number is essential for model stability and mass conservation. Error in mass conservation is less than 0.1% in this model.

5.4.4 Validation

5.4.4.1 Event

The numerical model was validated using the deposition season 2014. From 4 to 10 June 2014, the reservoir was flushed completely. Multi-beam echo-soundings were carried out on 30 September 2014. They reveal that 0.11 hm^3 of sediment were deposited in the reservoir within the four months after the reservoir had been emptied by the flushing operation. The validation time period was set from 14 June to 1 October 2014 to ensure that previous flushing does not affect the simulation. The measured inflow and lake levels of the validation period are shown in Figure 55. Annual inflow volume in 2014 was 435 hm^3 , of which 312 hm^3 (72%) occurred in the validation period. Peak discharge is less than HQ_2 , lake level does not reach full supply level. For the given hydrograph and lake level measurements, all parameters from the calibration were used without modification: The same pre-factor ξ_1 and exponent ξ_2 , the same PSD, and the same porosity are applied.

5.4.4.2 Results

The results of the validation are shown in Figure 56. 0.037 hm^3 of the 0.082 hm^3 of sediment conveyed into the reservoir are maintained. This equals a trap

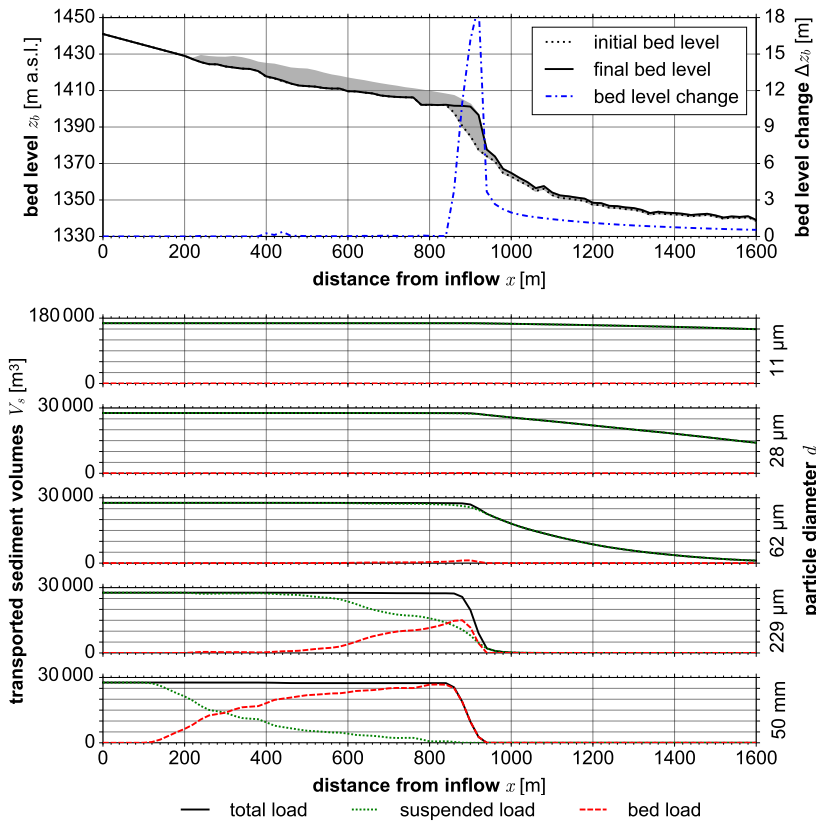


Figure 53: Simulation results of *Gebidem* test case for the calibration (2015) with daily-averaged boundary conditions: initial and final bed level as well as bed level changes are related to mass fluxes of sediment, which are broken down into single grain fractions (the grey area indicates maximum bed levels that evolved throughout the simulation)

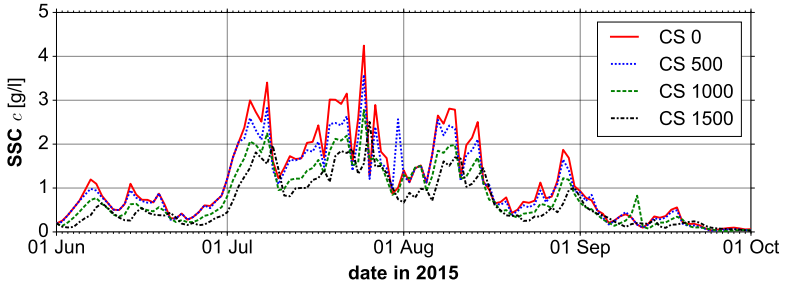


Figure 54: SSC in *Gebidem* in the calibration period from 1 June to 1 October 2015 (CS stands for cross sections, the value indicates the distance of the cross section from the upstream boundary in meters)

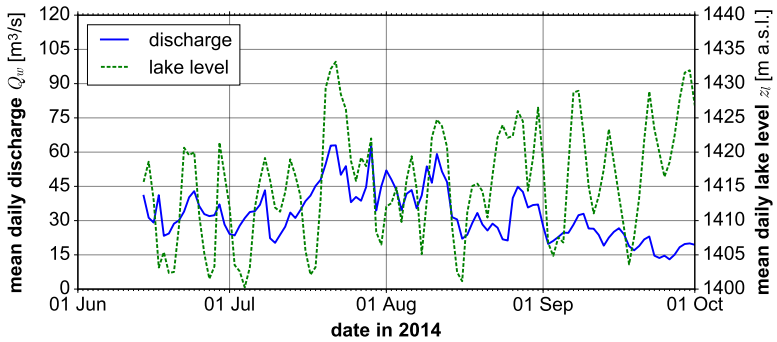


Figure 55: Measured inflow of water into *Gebidem* reservoir (upstream boundary) and lake level (downstream boundary) for the validation period from 14 June 2014 until 1 October 2014

efficiency of 46%. Including a porosity of 37% leads to a deposition volume of 0.059 hm^3 , which is half of the measured value of 0.11 hm^3 . The result is shown in Figure 56.

Various reasons for this discrepancy can be identified. The main drivers of reservoir sedimentation are amount and PSD of sediment input. Here, an SSC-Q relationship was used, which takes discharge non-linearly into account. The relation has been calibrated for a time period with high discharge and validated for a time period with moderate discharge. The corresponding sediment inputs differ significantly from 0.28 hm^3 (calibration) to 0.082 hm^3 (validation). Nevertheless, trap efficiencies of 40% (calibration) and 46% (validation) are comparable. It is a fact that such a general SSC-Q relationship may be valid for a large set of events, but not necessarily for single events. Indeed, the years 2015 and 2014 are special with regards to climate. Bader and Schlegel (2016) report that 2015 was the warmest year in Switzerland (surplus of $1.29 \text{ }^\circ\text{C}$); the summer 2015 was the second-warmest (after 2003) since observations started in 1864. According to Bader and Schlegel (2015), frequent rains (precipitation 200–300% above long-term norm) as well as the record deficit of sunshine hours (28% below long-term norm) in July and August 2014 resulted in the dullest midsummer since measurements started. Nevertheless, 2014 was the second warmest year in Switzerland (surplus of $1.25 \text{ }^\circ\text{C}$). It is expected that these anomalies have an impact on runoff evolution in the periglacial environment and corresponding fluvial sediment transport, respectively. General SSC-Q relationships cannot capture such “outliers”. Costa *et al.* (2018a) compared the performance of “traditional” SSC-Q relationships and non-linear multi-variate rating curves (hydro-climate multi-variate rating curves) for the *Rhône* catchment, which is superordinate to the catchment of *Gebidem* reservoir. Whereas the SSC-Q relationship depends on discharge alone, the non-linear multi-variate rating curve is a function of mean daily erosive rainfall, icemelt, snowmelt over unregulated areas and daily release of water from hydropower reservoirs. They demonstrated that the former cannot reproduce the probability distribution of SSC, whereas the latter reproduces seasonal patterns (although it does not use discharge at all) and captures seasonality and daily fluctuations better, especially in summer.

PSD is another main driver of the sedimentation volume. There is no evidence that PSD could have been significantly different in 2014 than in 2015. Nevertheless, PSD is not constant. As it is strongly linked to sub- and pro-glacial transport processes, it is not yet possible to account for such changes without field measurements.

Correct deposition volumes and SSC would be achieved by setting the pre-factor ξ_1 to 0.00057 and exponent ξ_2 to 2.1. The exponent is close to the value of 2.2 proposed by Müller and Förstner (1968) and Swift *et al.* (2005). Annual runoff of 435 hm^3 in 2014 is close to the long-term average (for the years

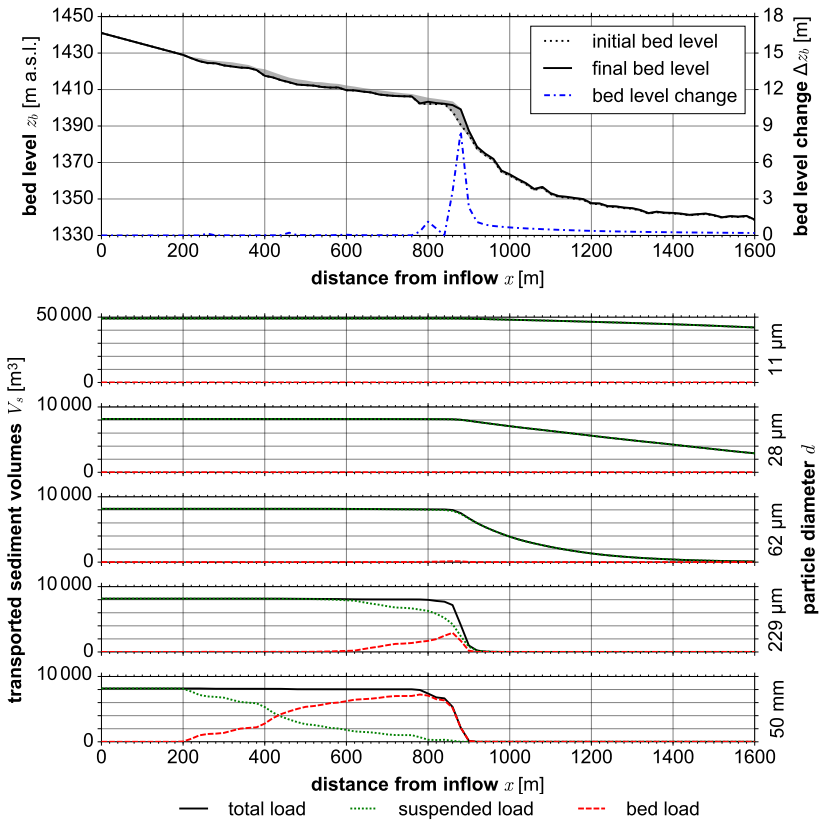


Figure 56: Simulation results of *Gebidem* test case for the validation (2014) with daily-averaged boundary conditions: initial and final bed level as well as bed level changes are related to mass fluxes of sediment, which are broken down into single grain fractions (the grey area indicates maximum bed levels that evolved throughout the simulation)

1931–2015) of 423 hm^3 , which leads to the conclusion that the exponent $\xi_2 = 2.1$ is a good approximation for years with discharge characteristics close to average values. If the combination of $\xi_1 = 0.00057$ and $\xi_2 = 2.1$ was applied in the calibration, then a sediment input of 0.488 hm^3 would result. Trap efficiency would be 40%, but the absolute deposition volume would be 0.311 hm^3 with porosity included.

5.5 Scenario simulations

5.5.1 Sensitivity of boundary conditions at Gebidem

5.5.1.1 Simulation time period

The calibration was done within a 122 day long time frame from 1 June to 1 October 2015. A simulation of the whole year without the winter season (when inflow is close to 0), led to almost identical results: Trap efficiency remained constant at 40%, the deposition pattern is almost the same. Thus, the reduction to the short time frame of four months is therefore justified if this SSC-Q relationship is applied.

5.5.1.2 SSC-Q relationship

The SSC-Q relationship has little impact on the trap efficiency. Exponents ξ_2 were varied between 0.7 and 2.2, and the pre-factors ξ_1 were adjusted between 0.1 and 0.0003 to ensure that all models were forced with the same sediment input. Trap efficiency remained at 40–42% for each model. SSC in the reservoir is significantly affected (maximum SSC at peak discharge of $104 \text{ m}^3/\text{s}$ between 2.6 and 8.2 g/l , dependent on the combination of ξ_1 and ξ_2). Nevertheless, the deposition pattern is nearly identical. This leads to the hypothesis, that the coefficients of the SSC-Q relationship have low sensitivity if their combination leads to correct sediment input into the reservoir with regard to volume.

5.5.1.3 Particle Size Distribution

Correct PSD is essential; if all diameters are multiplied with a factor of 2, then the trap efficiency will increase to 59%, and the deposition pattern will change. Delta formation is not affected, but sedimentation from homopycnal flows changes significantly, because larger parts of the fractions represented by 11 and $28 \text{ }\mu\text{m}$ will settle now. If no reliable information about PSD is available, then no resilient predictions about trap efficiency and sedimentation patterns can be made.

5.5.1.4 Temporal resolution

Inflow data (discharge and SSC) do not need a high temporal resolution. If monthly averages were used, a trap efficiency of 41% would result, and the sedimentation pattern would look similar. This is particularly important for modelling impacts of climate change, because runoff projections are usually not available at high temporal resolution (e.g. daily-averaged) but at rather low resolution (e.g. monthly-averaged).

Lake level data need a daily resolution when large fluctuations are present as observed in the *Gebidem* test case. If monthly averages of the lake level are used, then the sedimentation pattern will look completely different, as all deposits on the delta topset will no longer be transported towards the brink point due to the lack of significant drawdowns. In case of small reservoirs with high fluctuations in lake level, operation plays an important role in the relocation of sediments and must be taken into account. If the fluctuations, especially the drawdowns towards minimum operating level, were neglected, most coarse sediments would be deposited on the topset, thereby reducing the active storage. The results for the calibration (2015) using monthly-averaged lake levels is shown in Figure 58, the corresponding boundary conditions are shown in Figure 57. Although the deposition pattern has significantly changed compared to Figure 53, the trap efficiency is not affected.

5.5.2 Potential future reservoir at Gorner Glacier

5.5.2.1 Model set-up

In Chapter 3, it has been shown that a reservoir at *Gorner Glacier* would be feasible from a technical point of view. This potential reservoir would have the fastest infill time among the selected reservoirs, as estimates in Section 3.4.4 show. According to Table 9, an annual sediment input of 0.063 hm^3 must be expected following the approach of Gurnell *et al.* (1996), resulting in an infill time of 539 years. Although reservoir sedimentation is likely not an urgent issue at *Gorner Glacier* regarding loss of (active) volume, it is important to know the sedimentation patterns to ascertain that no outlet structures are endangered.

The potential future reservoir at *Gorner Glacier* would be at least four times larger than *Gebidem*: A gross volume of ca. 33 hm^3 can be derived from the actual topography and a full supply level at 2300 m a.s.l., where major parts of the future reservoir are still covered by glacier ice. The capacity-inflow ratio is 0.2, which is ten times larger than for *Gebidem* reservoir. Like for *Gebidem* reservoir, the inflow region is steep (up to 18%) and a large range of PSD is expected due to the proximity of the glacier forefield and the high transport capacity of the steep glacier stream. Both bed load and suspended

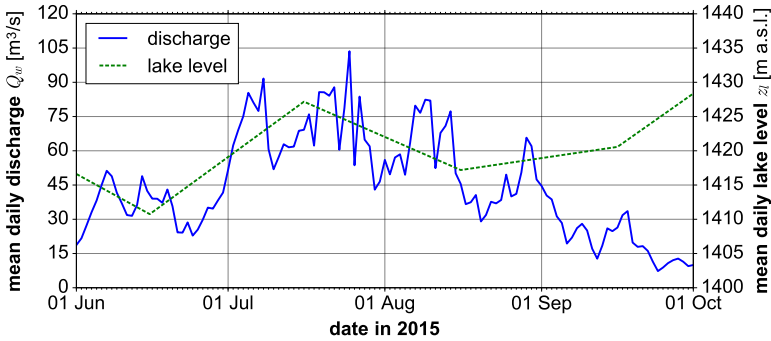


Figure 57: Boundary conditions of *Gebidem* test case for the calibration (2015) with daily-averaged inflow of water (upstream boundary) and monthly-averaged lake levels (downstream boundary)

load transport will occur. The ratio of width to length of the reservoir is $1/6$, so that a 1D model is assumed to be applicable. The reservoir volume with bed rock topography from Farinotti *et al.* (2016) is 168 hm^3 , but this volume cannot be achieved unless all ice in the future reservoir has melted. Therefore, the most critical phase regarding reservoir sedimentation is the actual state, with a relatively low reservoir volume and high discharge and sediment input due to glacier melt.

The most recent topography provided by *swissALTI3D* was used to extract cross sections and convert them into rectangular cross sections as described in Section 5.4.2.1. The 1400 m long basin between the glacier snout and *Gornera gorge* was divided into 71 cross sections with an equal spacing of 20 m. The widths and bed levels are shown in Figure 59. This leads to a minimum reservoir volume present today; the volume will eventually increase due to melting glaciers.

Monthly-averaged discharge projections for RCP4.5 were withdrawn from Farinotti *et al.* (2016). Each month was averaged over the time period 2030–2039 to achieve an average monthly discharge for this decade. Lake level was assumed to rise linearly from minimum operating level at 2160 m a.s.l. to full supply level at 2300 m a.s.l. The intake level was assumed at 2180 m a.s.l. Random lake level fluctuations were imposed, which are limited by the level change that could result after one day of turbine operation at design discharge of $18.4 \text{ m}^3/\text{s}$. Maximum lake level fluctuations at minimum operating and full supply levels are 18 m/d and 3 m/d, respectively. Design discharge is comparable to the

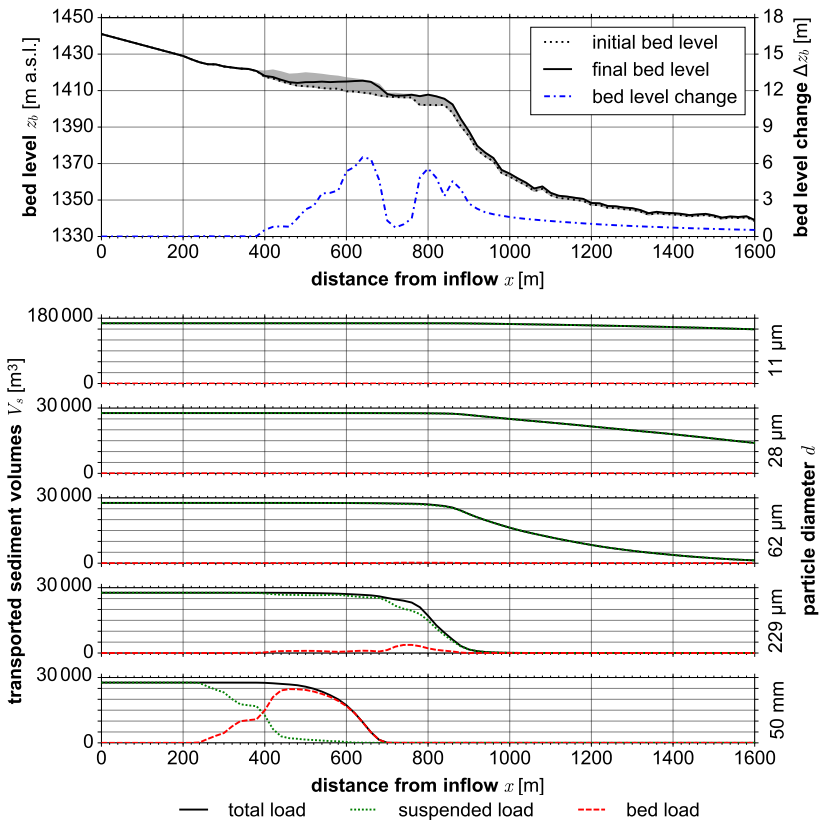


Figure 58: Simulation results of *Gebidem* test case for the calibration (2015) with monthly-averaged lake levels and daily-averaged discharge and sediment input: initial and final bed level as well as bed level changes are related to mass fluxes of sediment, which are broken down into single grain fractions (the grey area indicates maximum bed levels that evolved throughout the simulation)

inflow, so the fluctuations can be positive or negative. The boundary conditions are shown in Figure 60. PSD and sediment input are unknowns to be varied.

Long-term simulations over the 30-year-period 2020–2050 were carried out for RCP2.6, RCP4.5, and RCP8.5. For each year, the monthly-averaged inflow rates of Farinotti *et al.* (2016) from June–September were used. Within these four months, the lake level rose linearly from 2200 m a.s.l. to 2300 m a.s.l. The minimum operating level had to be raised from 2160 m a.s.l. to 2200 m a.s.l. to provide enough dead storage for 30 years of sedimentation and to ensure that sedimentation processes are not affected by the downstream boundary (which is implemented as a weir in the numerical model). The winter season was shortened to one month, where lake level was linearly reduced from 2300 m a.s.l. to 2200 m a.s.l. again. During this stage, a base flow of $1 \text{ m}^3/\text{s}$ was applied to prevent numerical instabilities due to wetting-drying processes. A short winter season of one month leads to nearly identical results as a significantly longer winter season of six months.

5.5.2.2 Results

In a first model series, annual sediment input was set at 0.063 hm^3 and different PSD were applied. Here, two PSD will be discussed: (a) the PSD of *Gebidem* reservoir to allow for a direct comparison of the two reservoirs; and (b) an “artificial” PSD consisting of 40% silt, 40% sand, and 20% gravel. Silt and sand were further subdivided into two classes, each accounting for 20%. Diameters are the averages of the corresponding classes; that is, $8 \text{ }\mu\text{m}$ (fine silt), $37 \text{ }\mu\text{m}$ (coarse silt), $230 \text{ }\mu\text{m}$ (fine sand), 1.2 mm (coarse sand) and 31 mm (gravel). For the PSD of *Gebidem* reservoir, a trap efficiency of 74% will result; for the artificial PSD, a trap efficiency of 87% is achieved. This confirms the findings of Section 5.5.1.3: PSD is the main determinant of trap efficiency. The deposition pattern and sediment fluxes of the model using the PSD of *Gebidem* are shown in Figure 61. Contrary to *Gebidem* reservoir (Figure 53), the grain fraction of $11 \text{ }\mu\text{m}$ is no longer wash load and the grain fractions of $28 \text{ }\mu\text{m}$ and $52 \text{ }\mu\text{m}$ contribute much more to homopycnal sedimentation. This diverging behaviour is due to the different hydraulic conditions. Delta formation of the coarse grain fractions of $229 \text{ }\mu\text{m}$ and 50 mm remains unchanged, as it does not depend on hydraulic conditions. The SSC-Q relationship was set up with $\xi_1 = 0.0041$ and $\xi_2 = 1.8$.

In a second model series, the PSD of *Gebidem* was kept fixed, and sediment input was varied. It turned out that the volume of sediment input has no significant impact on trap efficiency; even doubled sediment input would result in a trap efficiency of 75% for the PSD of *Gebidem*.

It can be observed that bed load transport is negligible in *Gorner Glacier* reservoir, as long the lake level is generally rising and has only minor fluctuations

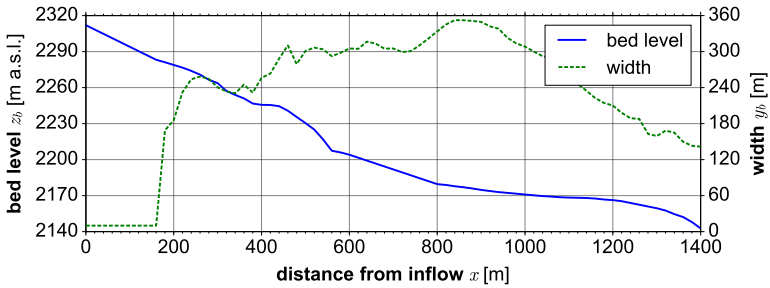


Figure 59: Geometry of potential future *Gorner Glacier* reservoir after conversion of measured into rectangular cross sections

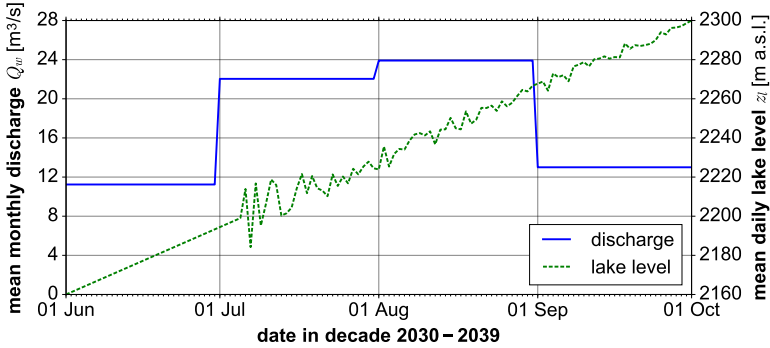


Figure 60: Monthly-averaged inflow into potential future *Gorner Glacier* reservoir for RCP4.5 scenario for 2030–2039 using data of Farinotti *et al.* (2016); combined with a linear rise of the lake level, superimposed by random lake level fluctuations induced by hypothetical turbine operations (N.B.: fluctuations are higher at low lake levels compared to fluctuations at high lake levels because of the topography of the reservoir)

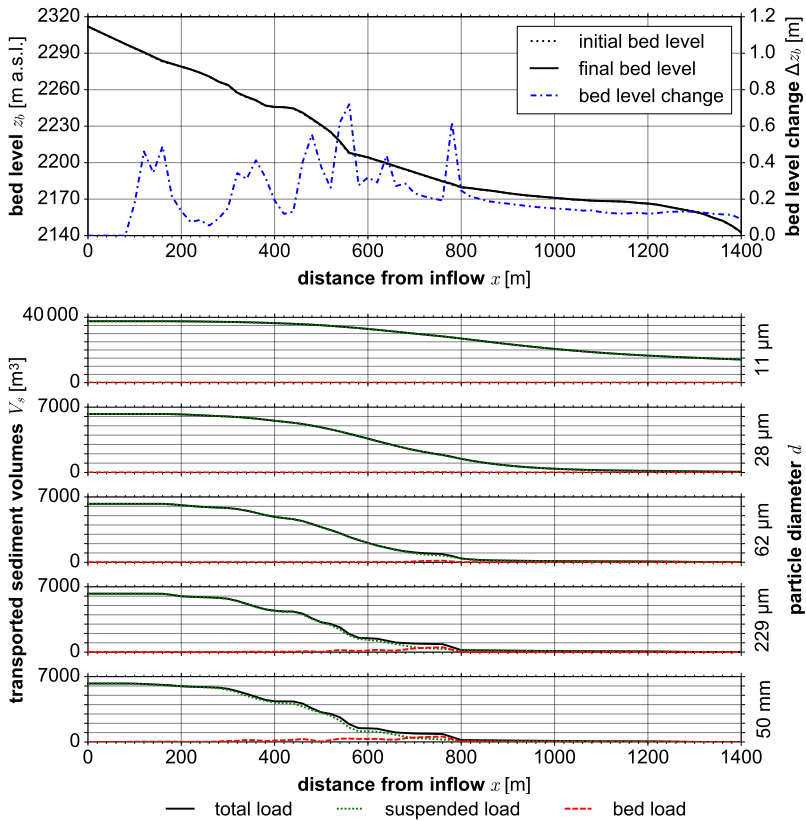


Figure 61: Simulation results of potential future *Gorner Glacier* reservoir for boundary conditions corresponding to Figure 60 and using the PSD of *Gebidem* test case: initial and final bed level as well as bed level changes are related to mass fluxes of sediment, which are broken down into single grain fractions (the grey area indicates maximum bed levels that evolved throughout the simulation); note that initial and final bed level collapse for this resolution due to the small bed level changes

(Figure 61). This is again in agreement with findings from Section 5.5.1.4: Bed load transport is restricted to the fluvial regime, as it needs a large hydraulic radius and high flow velocities compared to suspended load transport. These conditions are given only in non-impounded parts of the reservoir. Here, lake level changes are small, and so all cross sections of the reservoir usually stay impounded once they have been reached by the rising lake level. Bed load transport is important whenever lake level is lowered towards minimum operating level: This is the case during winter time in the long-term simulations and bed load is the dominant transport process for the relocation of sediments from the active into the inactive storage during drawdown to the minimum operating level (Figure 62).

The result of the long-term simulation over 30 years with RCP4.5 is shown in Figure 62. The results of RCP2.6 and RCP8.5 are similar; trap efficiency varies between 75% (RCP2.6) and 70% (RCP8.5), because the PSD is the same for all three RCPs. Absolute deposition volumes range from 1.8 hm^3 to 2.0 hm^3 . This small difference is due to the fact that the water volumes are similar: For RCP2.6, the total inflow volume is 6141 hm^3 ; for RCP8.5, the total inflow volume is 6628 hm^3 (i.e. only 8% higher). Sediment input was estimated using the same coefficients of the SSC-Q relationship as in the first model series (i.e. $\xi_1 = 0.0041$ and $\xi_2 = 1.8$). Total sediment input over 30 years is 1.7 hm^3 , of which 1.2 hm^3 (71%) are retained. Although the estimated infill time of more than 500 years is not yet a critical value, this simulation shows that the deposition thickness is ca. 4 m (increase of ca. 10 cm/a) close to the dam, which might endanger operating safety due to blocking of outlet structures. Furthermore, it can be observed that the delta front has propagated ca. 200 m within only 30 years (propagation speed of ca. 7 m/a); it might reach outlet structures considerably earlier than the 500 years infill time. The lowering of the lake level from full supply level at 2300 m a.s.l. to the adapted minimum operating level of 2200 m a.s.l. during winter leads to a relocation of all sediments into the dead storage.

The model performance is comparable to the *Gebidem* model regarding the error in mass conservation. Stable models were achieved with a Courant number (*CFL*) of 0.5.

5.6 Discussion

5.6.1 Numerical and mathematical model

Both models of *Gebidem* and *Gorner Glacier* show that 1D models are a suitable tool for the modelling of long-term sedimentation processes on large scales. The combination of the *Saint-Venant equations* with an explicit scheme

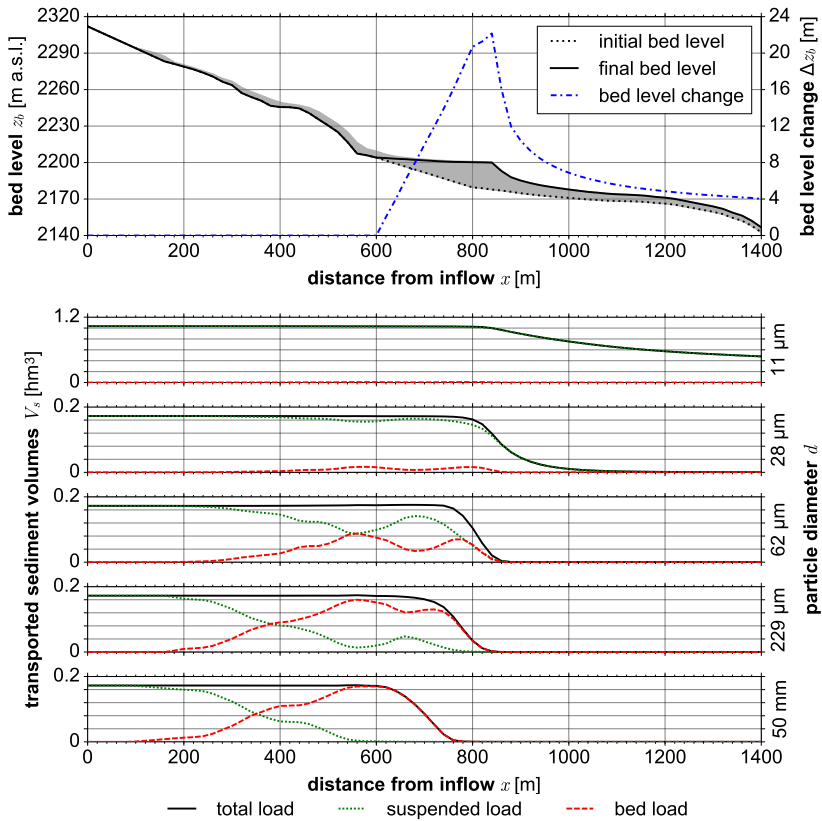


Figure 62: Long-term simulation results of potential future *Gorner Glacier* reservoir for RCP4.5 from 2020–2050 and using the PSD of *Gebidem* test case: initial and final bed level as well as bed level changes are related to mass fluxes of sediment, which are broken down into single grain fractions (the grey area indicates maximum bed levels that evolved throughout the simulation)

and the approximate *Riemann solver* of *Roe* guarantee the necessary stability and robustness of the model, although flow transitions occur and large gradients in the boundary conditions are present. Sediment transport is captured by a semi-empirical bed load transport formula and a modified version of the *QUICKEST* scheme for suspended sediment transport. The stability of the model is determined by an appropriate choice of the Courant number (*CFL*) and the threshold for minimum water depth. Wetting and drying of cross sections is still challenging; best results were achieved if all cross sections are wetted throughout the simulation. As all cross sections were rectangular, the minimum water depth must be set to a relatively low value (0.05–0.1 m).

5.6.2 Governing processes

The numerical models revealed the main drivers of trap efficiency, SSC, and deposition patterns. For a given reservoir, trap efficiency is mainly governed by PSD. This was already suggested by Brune (1953) and other researchers who recognized that trap efficiency for a reservoir with a given hydrologic size depends on PSD only (Equations 4a–4c).

SSC inside the reservoir depends on the chosen SSC-Q relationship. As such relations are calculated based on discharge, the temporal resolution of these data is crucial. High resolutions capture extreme values, whereas low resolutions or averaging of the data over longer time periods results in a low-pass filtering, where peak discharges disappear. SSC has not only impacts on the settling of suspended sediments, but also on SSC in waters being turbined or released. The former is an important driver in turbine abrasion, the latter is crucial for eco-hydraulics in downstream reaches. If correct SSC are of interest, then high-resolution inflow data is needed. If only trap efficiency is of interest, then low resolution data will be sufficient. In any case, the SSC-Q relationship needs a site- and time-dependent calibration and validation. It has been shown even for the same reservoir that two consecutive years cannot be modelled with the same SSC-Q relationship. Again, this finding has been confirmed by recent research; for example, by Swift *et al.* (2005), Riihimaki *et al.* (2005) or Delaney *et al.* (2018a).

Gebidem is a reservoir with strong fluctuations in lake level. These fluctuations are the origin of sediment relocation. Sediment deposits from homopycnal flow on the topset of the delta can be moved to the foreset when the lake level is lowered and the lacustrine (impounded) regime changes towards a fluvial regime. This regime is characterised by relatively high flow velocities and low hydraulic radii, enabling bed load transport. Without such fluctuations, the deposits remain on the topset, and bed load is negligible within the impounded part of the reservoir. This has been observed by operation of sediment bypass tunnels

(Müller-Hagmann 2017). Lake level fluctuations are more pronounced in small, weekly or daily storage reservoirs like *Gebidem*. In large seasonal reservoirs like the potential future reservoir at *Gorner Glacier*, they can be neglected, as they are too small compared to the overall flow depth.

Long-term simulations at the potential future reservoir at *Gorner Glacier* highlight the need to account for reservoir sedimentation due to climate change to ensure sustainable use of reservoirs. Large infill times do not necessarily imply that reservoir sedimentation can be neglected: Within a few decades, deposition layers can grow several meters and block bottom outlets or intake structures, as exemplified by the existing *Lac de Mauvoisin*. Delta evolution will mainly affect dead storage, but deltas may propagate several meters each year even in reservoirs with high infill times. This affects the definition of the minimum operating level: low minimum operating levels result in high active storage volumes, but reduce dead storage, which leads to faster delta propagation. Thus, the delta front will reach critical structures earlier. An analysis of reservoir sedimentation based on infill times only may fail because it may exclude crucial operational aspects.

5.6.3 Boundary conditions

Usually, forecasts or projections of reservoir sedimentation are of particular interest of operators. The controlling boundary conditions PSD and SSC-Q relationship are usually not known. Sensitivity analysis highlighted that these parameters are highly sensitive; hence, approximations and estimates based on literature might lead to diverging or even wrong results. Furthermore, impacts of climate change on PSD and SSC are not yet unravelled. Therefore, from a research point of view, the main field of action should be the generation of a more reliable data basis regarding input and boundary conditions. Without sound boundary conditions, no numerical model can reliably predict reservoir sedimentation processes, regardless of dimensions and processes. Recent innovations allow insights into the evolution of PSD and SSC at comparably low costs; even the “classic” analysis of water samples could contribute to substantial improvements of the boundary conditions.

Future hydrological conditions are further developed, as for ca. 200 000 glaciers worldwide runoff projections have been made available for different climate scenarios by Huss and Hock (2015) and Farinotti *et al.* (2016). Temporal resolution of these data sets is usually one month, so higher fluctuations are not present, and extreme floods are completely missing. Although SSC-Q relationships can be derived from such data sets and correct trap efficiencies result, the dynamics of the transport processes are most likely missed. Turbidity

currents, for example, cannot be implemented into such models, as they are bound to peak discharges with high SSC.

Inflow and lake level are usually recorded in Swiss reservoirs. This reduces the uncertainty in calibration and validation of reservoir sedimentation models. The future operation of the reservoirs (i.e. the evolution of lake level changes), is difficult to predict, as it depends not only on climate evolution, but also on market conditions. On the one hand, grid stability and control gain importance and would lead to stronger fluctuations of the lake level; on the other hand, winter energy will be required as well, which would lead to less fluctuations.

5.7 Conclusions

A simplified numerical 1D model was developed to simulate long-term and large-scale reservoir sedimentation processes. Its capacities include flow transition (*hydraulic jumps*), highly unsteady boundary conditions, large range of PSD, two transport modes, simulations of strongly varying geometries, and long time frames. The strictly 1D model approach with rectangular cross sections and purely cross section-averaged states (i.e. both depth- and width-averaged variables) provides useful insights into different processes and reveals first-order forcings of reservoir sedimentation. The model can be used for projections of reservoir sedimentation under future boundary and operating conditions, taking climate change into account.

The model concept was successfully tested for the *Gebidem* reservoir. This Swiss reservoir is a demanding test case, as its sediment input is high, resulting in an exceptionally low infill time of 20–30 years. Both formation of a Gilbert-type delta and sedimentation from homopycnal (non-stratified) flows can be observed. Multi-beam echo-soundings from the recent years provide sedimentation volumes, discharge into the reservoir and lake levels that are both recorded with a temporal resolution of 15 min and 1 day, respectively. A straightforward SSC-Q relationship was calibrated to estimate the unknown sediment input. Sensitivity of different boundary conditions were assessed. A similar set-up was applied for a potential future reservoir at *Gorner Glacier*, using runoff projections from a glacio-hydrological model.

Unfortunately, PSD of deposited sediments in the reservoir are missing for both *Gebidem* and *Gorner Glacier*. Hence, the longitudinal (stream-wise) fining of deposit composition cannot be validated. This information would be valuable to assess whether the dynamics of the homopycnal sedimentation is correctly modelled. The shapes of the transport diagrams of the fine sediments are either convex or concave, for example for particles of 28 μm or 62 μm in Figure 53. No clear trend could be observed in the PSD of the suspended sediments along

the reservoir axis, but PSD of deposited sediments could probably verify the accuracy of the chosen approach for homopycnal sedimentation.

The main findings of the short- and long-term simulations are summarised in Figure 63:

- Sediment transport is a function of discharge, as hydraulic conditions limit transport rates, given sufficient sediment availability. Raymond Pralong *et al.* (2015) argued that this will be the case for mountain streams which are currently limited by transport capacity (and not by sediment availability). Stott and Mount (2007) claimed that a warmer climate will likely result in increased suspended sediment transport. The relationship between sediment and water depends on climate change scenarios, which lead to different runoff evolutions in the periglacial environment. SSC-Q relationships, as for example presented in Equation 3, are not only site-specific, but also time-dependent. Most commonly applied SSC-Q relationships correlate SSC and discharge positively, so additional runoff from melting glaciers will increase sediment input into periglacial reservoirs. This will accentuate sedimentation problems. Beneficial additional discharge for production is weakened by increased sedimentation and, vice versa, disadvantageous discharge reductions might decrease sedimentation. These approaches are rather crude and not capable of capturing seasons variations, as they do not account for governing processes of sediment input like erosive rainfall or snow- and icemelt. Such well-developed relationships as for example presented by Costa *et al.* (2018a) would allow to study impacts of climate change in much more detail.
- PSD may change as well with climate change, as modified runoff regimes will lead to larger or lower peak flows and thereby affect the range of particle diameters that can be transported. This interaction of climate change and PSD is still a missing link.
- PSD is paramount for the estimation of trap efficiency, as it defines the amount of wash load. Only wash load will not settle within the reservoir, the rest of the sediment input will be trapped somewhere in the reservoir. Wash load does not cause reservoir sedimentation, but it can still be problematic when it is discharged via the power waterway. It causes turbine abrasion, which may result in large financial losses. Details can be found in Felix (2017). PSD determines which grain sizes can pass through the reservoir and reach the downstream river reach. Vice versa, missing grain sizes in environmental flows (or overflow) are determined by PSD as well.

- The sedimentation volume is related to the trap efficiency; the former is the quantitative amount of sediments retained in the reservoir, the latter the relative amount. Despite high infill times, reservoir sedimentation can be problematic if the sedimentation volume fills the dead storage too fast and endangers outlet structures. In most reservoirs, major sedimentation problems will arise because of disadvantageous sedimentation patterns and not because of fast infill times. Empirical models of trap efficiency like Brune (1953) or of sediment distribution like Annandale (1987) are not detailed enough to tackle these problems; numerical models are most valuable tools to investigate sediment transport in reservoirs and identify critical situations early, when efficient counter-measures can still be implemented. Moreover, homopycnal sedimentation requires sophisticated monitoring and might remain undetected over a long period of time because these depositions usually cannot be observed visually.
- The sedimentation volume is a function of the sediment-water discharge relationship, given a certain trap efficiency: The higher the sediment input is, the higher are the deposition volumes. This highlights the overarching importance of correct sediment input at the upstream boundary. Unfortunately, hardly any field records are available for most periglacial reservoirs in Switzerland to derive reliable SSC-Q relationships. Therefore, large uncertainties in estimates of sediment input are reflected in high uncertainties in reservoir sedimentation. Uncertainties in runoff projections amplify this problem even further.
- Sedimentation patterns are determined by PSD and reservoir operation. PSD defines the amount of coarse particles leading to delta formation and the amount of fine particles leading to homopycnal sedimentation. Hydraulic conditions along with grain characteristics (size, weight and shape) determine whether a specific grain fraction has to be considered as “coarse” or “fine” in a specific reservoir. This partitioning cannot be made with empirical relationships only, but numerical models provide these insights and allow to account for different sedimentation patterns, even in early planning stages of a project. Furthermore, changing climate manifests in modified runoff regimes; these impacts can be studied with numerical models as well.
- Delta formation is controlled by drawdowns of the reservoir, as brink point and minimum operating level coincide. Hence, delta dimensions and shape can be controlled by reservoir operation. Drawdowns to minimum operating level can be interpreted as partial flushings which lead to relocation of sediments inside the reservoir: The active storage is emptied

and full capacity for production is restored. Reservoir operation should not only be determined by market conditions and production considerations, but also by sediment handling. Additional discharge due to melting glaciers may provide additional degrees of freedom in reservoir operation. Delta formation affects active storage, but the temporarily deposited sediment on the topset slope is transported to the inactive storage below the brink point whenever a drawdown to the minimum operating level is carried out (Figure 3). Delta propagation can be monitored relatively easy, as the brink point can be located visually at minimum operating level. Critical propagation rates can be detected before security issues arise.

- Furthermore, reservoir size has impacts on trap efficiency as well: Large reservoirs usually have higher trap efficiencies because of longer travelling times of suspended sediments and related higher homopycnal sedimentation rates. Reservoir size has hardly any impact on coarse sediments, as they contribute to delta formation, which sets in whenever the regime changes from fluvial to lacustrine, regardless the size of the reservoir. Trap efficiency of bed load sediments is therefore usually close to 100%. Thus, it is important to know the partitioning of the total sediment load into bed load and suspended load. This topic has been addressed by Schlunegger and Hinderer (2003) and Turowski *et al.* (2010).

Efficient 1D models may miss important aspects, for example turbidity currents that cannot be reproduced with depth-averaged models. It has been shown by various researchers that turbid underflows occur occasionally in several Swiss reservoirs and lakes (Section 2.2.7.2). They might deposit a large sediment volume in the reservoir. Turbidity currents may be episodic events; nevertheless, they can be important because they relocate sediments inside the reservoir. Turbidity currents can lead to sedimentation at critical locations, for example, at the bottom outlet, and thereby endanger the safe reservoir operation. To account for these processes, the 1D model could be enhanced by a turbidity current model. A sophisticated model as suggested by Parker *et al.* (1986) seems to overpass the scope of the model, so a simplified model as presented by Wright *et al.* (2001) could be satisfactory. Furthermore, 1D models reach their application range when the bed level changes in transversal direction are of interest. In such cases, 1D models must be developed further to allocate bed level changes in transversal direction by taking the measured geometry of the cross section into account, or 2D or 3D models are required if the transport processes need to be resolved in 2D or 3D. In general, 2D and 3D models resolve processes with less simplifications and are therefore more accurate. As increasing

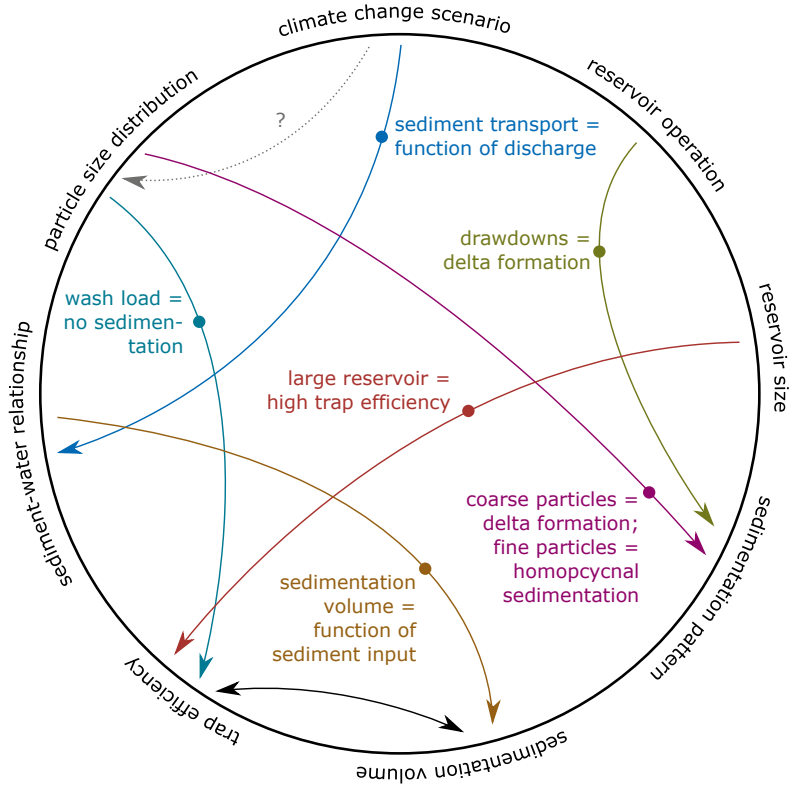


Figure 63: Links between climate change scenarios, reservoir characteristics, boundary conditions and processes within the periglacial environment

accuracy is at the expense of computational effort, a trade-off between accuracy and effort has to be made.

Different counter-measures against reservoir sedimentation are described in Sumi (2005); Schleiss *et al.* (2010); Boes and Hagmann (2015); Felix *et al.* (2017a,b) and others. At *Gebidem* reservoir, annual flushing operations have been carried out until 2015 and bi-annual flushing operations since then. Given the low capacity-inflow-ratio of 0.02, sediment sluicing or bypassing would be viable options, too. At the potential future reservoir at *Gorner Glacier*, the capacity-inflow-ratio is 0.2 and reservoir life is estimated to be at least 500 years. A check dam upstream of the reservoir or upstream of the dam within the reservoir or keeping fines in suspension by introducing extra turbulence and turbining these in the sediment season (Felix *et al.* 2017b) could be alternatives. Storage operation is another counter-measure: Lifting minimum operating level provides more inactive storage available for sedimentation resulting in slower delta propagation. Sedimentation close to the dam remains a critical factor, however. A higher minimum operating level reduces active storage, which has impacts on the economical use of the reservoir. Furthermore, ecological needs must be taken into account as well, because reservoirs with high trap efficiencies interrupt sediment continuity and lead to sediment deficits downstream. In such cases, sediment bypass tunnels, flushing or creating artificial floods combined with sediment replenishment downstream of dams can be suitable solutions. Although these measures are not always the most economic options, they are technically feasible and ecologically desirable to mimic natural floods of the pre-dam era.

6 Conclusions

6.1 Summary

Climate change is an important factor of influence on the Swiss *Energy Strategy 2050*. It leads to glacier retreat in the Swiss Alps, which has a twofold impact on hydropower in the periglacial hydropower: new potential locations for HPP reservoirs become ice-free, and additional meltwater may be available for production. Existing HPPs will be affected by changing reservoir sedimentation processes, as they are closely linked to hydrological and climate conditions. The impacts of climate change on periglacial hydropower were studied in this research project.

In 2016, annual electricity production from hydropower in Switzerland reached ca. 36.3 TWh. For 2035, the Swiss *Energy Strategy 2050* anticipates an annual production of 37.4 TWh. Therefore, a further annual net potential of ca. 1.1 TWh needs to be exploited until then. This potential can be found in the periglacial environment. Studies of Laufer *et al.* (2004), Boes (2011), BFE (2012) and Schleiss (2012) showed that upgrading existing HPPs (e.g. by means of dam heightenings, raising full supply level, or improving efficiency of electrical and mechanical components), could cover this deficit. In this study, new potential HPP sites were identified and pre-feasibility studies were carried out. Based on the glacier runoff projections from Farinotti *et al.* (2016), suitable reservoir sites were selected and compared to each other by applying an evaluation matrix. 62 sites were considered and new HPPs at the best-rated seven sites *Aletsch Glacier*, *Gorner Glacier*, *Grindelwald Glacier*, *Hüfi Glacier*, *Rhône Glacier*, *Roseg Glacier*, and *Trift Glacier* could cover the deficit as well. The total installed capacity would be ca. 400 MW, the total annual electricity production ca. 1.1 TWh, and the energy equivalent of the reservoirs would reach ca. 1.2 TWh. These numbers are affected with significant uncertainties, as the projections of water resources strongly depend on climate conditions. Furthermore, the topography is often not fully known as the dam locations are located in the vicinity of the glacier mouth; therefore, parts of the reservoir are still underneath glacier ice today. Sediment yield is not known and can only be estimated within orders of magnitude based on statistical relationships. Geological conditions are of crucial importance, but remain unknown in most places. Site access, interaction with other HPPs, grid connection, as well as social and environmental issues

will be major challenges. For the time being, the upgrade of existing HPPs seems to be an easier course of action, at least until 2035, because only a small deficit has to be covered, and market conditions are difficult for investments in new HPPs. Nevertheless, at specific sites like *Trift Glacier*, new HPPs may already be a valuable solution, even under today's market conditions. Control of reservoir sedimentation and support of sediment continuity are prerequisites to ensure the sustainable use of these reservoirs. Empirical relationships are not sufficiently detailed to account for all the processes that govern sediment transport in periglacial reservoirs; numerical models, however, are most suitable tools to study sediment fluxes in periglacial reservoirs.

Governing parameters of sediment transport in periglacial reservoirs include, amongst others, PSD, SSC, discharge, and flow velocities. In the scope of this project, suspended sediments in the three Swiss reservoirs *Griessee*, *Lac de Mauvoisin*, and *Gebidem* were investigated. For the first time, the combination of water sample analysis, LISST, and ADCP was applied systematically and successfully to gain profound insights into sediment fluxes in periglacial reservoirs. It was found that in general 80–100% of the sediments in the reservoirs were in the range of silt and clay and sand portions are usually less than 10%. d_{50} are usually between 10 and 100 μm , maximum grain diameters found in suspension were 200 μm . There was no evidence of significant changes of PSD and SSC on the horizontal plane within the reservoirs. Sediment-laden inflowing river water may lead to turbidity currents, but these hyperpycnal (stratified) flows were restricted close to the inflow zones for the given reservoirs. In most parts of the investigated reservoirs, homopycnal (non-stratified) conditions were dominant. The set of measurement techniques was proven to be suitable for studying sediment fluxes in periglacial reservoirs. Despite the limited sampling range, LISST provides the unique opportunity of simultaneously sampling PSD and SSC. ADCP provides valuable insights into flow fields and allows a qualitative view at SSC profiles, but due to low SSC and diameters, SNR of the ADCP records could not be used for SSC computations. Both techniques were referenced with 84 water samples that were analysed in the laboratory regarding PSD and SSC. The field measurements were documented and published in Ehrbar *et al.* (2017). They provided the basis for the development of a numerical model to examine sediment transport within periglacial reservoirs.

The numerical model has been optimised to allow simple, robust, stable and fast simulations. It masters several challenges, such as flow transitions (*hydraulic jumps*), highly unsteady boundary conditions, large ranges of PSD, two transport and corresponding deposition modes (Gilbert-type delta formation of coarse sediments and sedimentation from homopycnal flows of fine sediments), strongly varying geometries and long time frames. A 1D model is favourable to simulate long-term sedimentation processes on the reservoir scale due to relatively low

computation time. This allows to investigate the evolution of the sedimentation pattern and to identify critical locations, where deposition could endanger outlet structures. Furthermore, inactive storage and operation can be optimised, so that sedimentation does not compromise the sustainable use of the reservoirs. The model might be improved by including sediment transport induced by turbidity currents, which can lead to occasionally significant relocation of sediments inside the reservoirs. There is evidence of coarse-grained turbidites (sand or even clay) in proximity of the dam in many periglacial reservoirs, which can be explained by transport by turbidity currents only. The implementation of turbidity currents could answer under which conditions such events can be triggered (e.g. minimum SSC of the inflow river) and how much deposition they cause. This would allow to quantify the frequency (return period) and the significance (in terms of deposition volumes and PSD of the deposits) of turbidity currents.

The findings and tools presented in this thesis provide information for strategic decisions in the hydropower sector at the mid- to long-term and help to adapt the existing infrastructure to changing climate conditions. Thereby, they help to reach the goals of the Swiss *Energy Strategy 2050* regarding electricity production from hydropower.

6.2 Recommendations for future research

Runoff projections until 2100 are available for different climate change scenarios. Although future climate is afflicted with high uncertainties, the quality of these projections is high, and therefore likely evolutions of runoff can be drawn. Unfortunately, projections for sediment discharge are hardly available. Relations between water and sediment discharge are inconsistent and they do depend on time- and space-specific characteristics, so that the application range of such empirical models is very limited. Strong emphasis should be put on the understanding of the sediment delivery of glaciated catchments, as this is by far the most important boundary condition of periglacial reservoir sedimentation. Without sound boundary conditions, no numerical model will ever reliably predict reservoir sedimentation processes. Apart from that, the field measurements conducted in the scope of this thesis should be repeated in other reservoirs and under different weather and climate conditions (e.g. in winter or spring or when turbidity currents are present) to widen the range of available field data for the calibration and validation of models. Furthermore, the measurements presented herein could be proven. Recent innovations in measurement techniques allow for insights into the evolution of PSD and SSC at comparably low costs. Many numerical models from 1D to 3D are capable to simulate reservoir sedimentation processes on different scales regarding space

and time. Some of them, like the model presented herein, have low computation costs and could be applied in a model chain, allowing an integral view at the dynamics of the whole catchment.

Nomenclature

Abbreviations

ABS	Acoustic BackScatter
ADCP	Acoustic Doppler Current Profiler
D-GPS	Differential Global Positioning System
HPP	Hydropower Plant
LISST	Laser In-Situ Scattering and Transmissometry
PSD	Particle Size Distribution
RCP	Representative Concentration Pathway
SNR	Signal-to-Noise Ratio
SONAR	SOund NAVigation and Ranging
SRES	Special Report on Emission Scenarios
SSC	Suspended Sediment Concentration

Dimensionless Numbers

D	dimensionless grain diameter	[-]
F	Froude number	[-]
Ri	Richardson number	[-]
R	Reynolds number	[-]
S	Corey shape factor	[-]

Greek Symbols

α	attenuation coefficient of sound in water	[dB/m]
β	wave celerity	[m/s]
χ	eigenvalues of Roe matrix	[m/s]

Δ	Signal-to-Noise Ratio (SNR)	[dB]
δ	density excess (difference)	[kg/m ³]
ϵ	absorption coefficient of light in water	[1/m]
η	auxiliary variable	case-dependent
Γ	acoustic backscatter (ABS)	[dB]
γ	submerged specific gravity	[-]
λ	wave length (ADCP)	[m]
μ	dynamic viscosity of water	[Pa·s] = [kg/(m·s)]
ν	kinematic viscosity (“momentum diffusivity”) of water	[m ² /s]
ω	wave number	[1/m]
Φ	momentum flux	[m ⁴ /s ²]
ϕ	continuity flux	[m ³ /s]
ψ	advective suspended sediment flux	[m ³ /s]
ρ	density	[kg/m ³]
σ	sound speed in water	[m/s]
τ	bed shear stress	[Pa] = [N/m ²] = [kg/(m·s ²)]
Θ	transport mode selector	[-]
θ	dimensionless bed shear stress (Shields parameter)	[-]
ξ	calibration coefficient	[-]
ζ	attenuation constant	[m ² /kg]

Roman Symbols

A	flow area	[m ²]
a	lake surface area	[km ²]
B	exchange rate between suspension and bed	[m ² /s]
b	specific exchange rate between suspension and bed	[m/s]
C	sediment volume concentration	[-]
C_b	near-bed volumetric sediment concentration	[-]
c_d	bed drag coefficient	[-]
c_f	dimensionless bed friction coefficient	[-]
D	diffusion coefficient	[m ² /s]

d	particle diameter; tunnel diameter	$[\mu\text{m}]$ or $[\text{mm}]$ or $[\text{m}]$
d_{50}	median particle diameter	$[\text{m}]$
d_m	mean particle diameter	$[\text{m}]$
E	received echo strength	$[\text{counts}]$
e	coefficient of entrainment (water or sediment)	$[\text{m}^2/\text{s}]$
F	catchment area	$[\text{km}^2]$
f	ADCP frequency	$[\text{Hz}] = [1/\text{s}]$
G	(annual) electricity production	$[\text{GWh}] = [3.6 \cdot 10^{12} \cdot \text{kg} \cdot \text{m}^2/\text{s}^2]$
g	gravitational acceleration	$[\text{m}/\text{s}^2]$
H	hydraulic head	$[\text{m}]$
h	flow depth (or sampling range of ADCP) from water surface	$[\text{m}]$
I	light intensity	$[\text{W}/\text{m}^2] = [\text{kg}/\text{s}^3]$
i	glaciation of the catchment	$[\%]$
I_0	light intensity at the water surface	$[\text{W}/\text{m}^2] = [\text{kg}/\text{s}^3]$
J	friction slope	$[-]$
j	mean annual denudation rate	$[\text{mm}]$
K	factor to convert counts into decibel	$[\text{dB}/\text{count}]$
k	Strickler coefficient	$[\text{m}^{1/3}/\text{s}]$
L	tunnel length	$[\text{km}]$
l	hydraulic radius	$[\text{m}]$
N	received noise strength	$[\text{counts}]$
n	number of samples / amount of	$[-]$
P	received signal intensities	$[\text{dB}]$
p	porosity of the bed material	$[\%]$ or $[-]$
Q	discharge / conveyance / input	$[\text{m}^3/\text{s}]$
q	specific discharge	$[\text{m}^3/(\text{s} \cdot \text{m})] = [\text{m}^2/\text{s}]$
q_b	specific bed load transport rate	$[\text{m}^3/(\text{s} \cdot \text{m})] = [\text{m}^2/\text{s}]$
r	particle radius	$[\text{m}]$
R^2	coefficient of determination	$[-]$
S	bed (alluvial) slope; tunnel slope	$[-]$ or $[\%]$
SSC	sediment mass concentration	$[\text{kg}/\text{m}^3]$ or $[\text{mg}/\text{l}]$

T	temperature	[°C]
t	time	[s]
u_*	bed shear velocity	[m/s]
V	(runoff, reservoir or sediment) volume	[hm ³] = [10 ⁶ ·m ³]
v	flow velocity	[m/s]
W	(installed) capacity	[MW] = [10 ⁶ ·kg·m ² /s ³]
w	settling velocity of particles	[m/s]
x	longitudinal coordinate (distance along flow direction)	[m]
y	transverse coordinate (distance cross to flow direction)	[m]
y_b	width of cross section	[m]
z	vertical coordinate (elevation)	[m]
z_b	bed elevation	[m]
z_{max}	full supply level	[m a.s.l.]
z_{min}	minimum operating level	[m a.s.l.]
z_{Secchi}	Secchi depth	[m]

Indices

bl	bed load
cr	critical (value)
d	deposition
e	erosion or entrainment
i	grain fraction
l	lake (reservoir)
r	river
s	sediment
sl	suspended load
t	turbidity current
w	(pure) water

Bibliography

- Abood, M. M.; Mohammed, T. A.; Ghazali, A. H.; Mahmud, A. R.; Sidek, L. M. (2009). Review study and assessment for sedimentation models applied to impounding reservoirs. *Journal of Engineering & Applied Sciences*, 4(2): 152–160. <http://medwelljournals.com/abstract/?doi=jeasci.2009.152.160>.
- Addor, N.; Rössler, O.; Köplin, N.; Huss, M.; Weingartner, R.; Seibert, J. (2014). Robust changes and sources of uncertainty in the projected hydrological regimes of Swiss catchments. *Water Resources Research*, 50(10): 7541–7562. <http://dx.doi.org/10.1002/2014wr015549>.
- Agrawal, Y. C.; Pottsmith, H. C. (1994). Laser diffraction particle sizing in STRESS. *Continental Shelf Research*, 14(10): 1101–1121. [http://dx.doi.org/10.1016/0278-4343\(94\)90030-2](http://dx.doi.org/10.1016/0278-4343(94)90030-2).
- Agrawal, Y. C.; Pottsmith, H. C. (2000). Instruments for particle size and settling velocity observations in sediment transport. *Marine Geology*, 168(1): 89–114. [http://dx.doi.org/10.1016/s0025-3227\(00\)00044-x](http://dx.doi.org/10.1016/s0025-3227(00)00044-x).
- Agrawal, Y. C.; Whitmire, A.; Mikkelsen, O. A.; Pottsmith, H. C. (2008). Light scattering by random shaped particles and consequences on measuring suspended sediments by laser diffraction. *Journal of Geophysical Research: Oceans*, 113(C4). <http://dx.doi.org/10.1029/2007jc004403>.
- Ahn, J. (2011). Numerical modeling of reservoir sedimentation and flushing processes. *PhD Thesis*, Colorado State University. https://dspace.library.colostate.edu/bitstream/handle/10217/70431/Ahn_colostate_0053A_10781.pdf?sequence=1 [accessed: 20/04/2018].
- Albrecht, R. (2016). KW Aegina AG: Bauliche Massnahmen am Beispiel des Stausee Gries ('Hydropower Plant Aegina plc: Building activities in the case study of Gries reservoir'). Talk at Swiss Water Association Conference (1 September 2016) [in German, unpublished].
- Alley, R. B.; Cuffey, K. M.; Evenson, E. B.; Strasser, J. C.; Lawson, D. E.; Larson, G. J. (1997). How glaciers entrain and transport basal sediment: Physical constraints. *Quaternary Science Reviews*, 16(9): 1017–1038. [http://dx.doi.org/10.1016/s0277-3791\(97\)00034-6](http://dx.doi.org/10.1016/s0277-3791(97)00034-6).

- Alpiq (2016). Gebidem — Ausflüge rund um die Wasserkraft ('Gebidem — Excursions about hydro-power'). *Brochure*, Alpiq. http://www.alpiq.com/images/alpiq_gebidem_brochure_balade_hydroelectrique_de_tcm95-54921.pdf [in German, accessed: 20/04/2018].
- Alvarez, L. G.; Jones, S. E. (2002). Factors influencing suspended sediment flux in the upper Gulf of California. *Estuarine, Coastal and Shelf Science*, 54(4): 747–759. <http://dx.doi.org/10.1006/ecss.2001.0873>.
- Ambrosetti, W.; Barbanti, L.; Sala, N. (2003). Residence time and physical processes in lakes. *Journal of Limnology*, 62(1): 1–15. <http://dx.doi.org/10.4081/jlimnol.2003.s1.1>.
- An, S.; Julien, P. Y.; Venayagamoorthy, S. K. (2012). Numerical simulation of particle-driven gravity currents. *Environmental fluid mechanics*, 12(6): 495–513. <http://dx.doi.org/10.1007/s10652-012-9251-6>.
- Andrews, S. W.; Nover, D. M.; Reardon, K. E.; Reuter, J. E.; Schladow, S. G. (2011a). The influence of ambient light intensity on in situ laser diffractometers. *Water Resources Research*, 47(6): 1–10. <http://dx.doi.org/10.1029/2010wr009841>.
- Andrews, S. W.; Nover, D. M.; Reuter, J. E.; Schladow, S. G. (2011b). Limitations of laser diffraction for measuring fine particles in oligotrophic systems: Pitfalls and potential solutions. *Water Resources Research*, 47(5): 1–12. <http://dx.doi.org/10.1029/2010wr009837>.
- Annandale, G. W. (1987). Reservoir Sedimentation. ISBN 0-444-42729-5. Elsevier, Amsterdam, The Netherlands.
- Annandale, G. W. (2015). Policy considerations for sustainable hydropower: Reliability, climate change and sedimentation. *Proc. HYDRO 2015. International Hydropower Association (IHA)*.
- Anselmetti, F. S.; Bühler, R.; Finger, D.; Girardclos, S.; Lancini, A.; Rellstab, C.; Sturm, M. (2007). Effects of Alpine hydropower dams on particle transport and lacustrine sedimentation. *Aquatic sciences*, 69(2): 179–198. <http://dx.doi.org/10.1007/s00027-007-0875-4>.
- Ashida, K.; Michiue, M. (1971). An investigation of river bed degradation downstream of a dam. *Proc. Fourteenth Congress of the International Association for Hydraulic Research*. Paris, France: 247–255.

- Ashley, G. M. (2002). Chap. 11 — Glaciolacustrine environments: 335–359. In: J. Menzies (ed.) *Modern and Past Glacial Environments*. ISBN 978-0-7506-4226-2. *Butterworth-Heinemann*, Oxford, England. <http://dx.doi.org/10.1016/B978-075064226-2/50014-3>.
- Auel, C.; Boes, R. M. (2012). Sustainable reservoir management using sediment bypass tunnels. *Proc. 24th ICOLD Congress. International Commission on Large Dams (ICOLD)*, Kyoto, Japan. Q.92, R.16: 224–241. <https://bit.ly/203ykby> [accessed: 20/04/2018].
- Bader, S.; Schlegel, T. (2015). Klimareport 2014 (‘Climate Report 2014’). *Technical Report 313.001.d*, Federal Office of Meteorology and Climatology MeteoSwiss. http://www.meteoswiss.admin.ch/content/dam/meteoswiss/de/service-und-publikationen/Publikationen/doc/klimareport.2014.DE_web.pdf [in German, accessed: 20/04/2018].
- Bader, S.; Schlegel, T. (2016). Klimareport 2015 (‘Climate Report 2015’). *Technical Report 313.001.d*, Federal Office of Meteorology and Climatology MeteoSwiss. <http://www.meteoswiss.admin.ch/content/dam/meteoswiss/de/service-und-publikationen/Publikationen/doc/klimareport.2015.pdf> [in German, accessed: 20/04/2018].
- BAFU (2012). Effects of climate change on water resources and waters. Synthesis report on “Climate Change and Hydrology in Switzerland” (CCHydro) project. *Umwelt-Wissen 1217*, Bundesamt für Umwelt BAFU (‘Federal Office for the Environment FOEN’). <http://www.naturalsciences.ch/download/b9972880-cf98-55a0-a2ff-770f2a9738ee/4513> [accessed: 20/04/2018].
- Bale, A. J.; Morris, A. W. (1987). In situ measurement of particle size in estuarine waters. *Estuarine, Coastal and Shelf Science*, 24(2): 253–263. [http://dx.doi.org/10.1016/0272-7714\(87\)90068-0](http://dx.doi.org/10.1016/0272-7714(87)90068-0).
- Bartholomä, A.; Kubicki, A.; Badewien, T. H.; Flemming, B. W. (2009). Suspended sediment transport in the German Wadden Sea — seasonal variations and extreme events. *Ocean Dynamics*, 59(2): 213–225. <http://dx.doi.org/10.1007/s10236-009-0193-6>.
- BBL (1991). Bundesgesetz über den Schutz der Gewässer (‘Federal Act on the Protection of Waters’). Federal Law. <https://www.admin.ch/opc/de/classified-compilation/19910022/201701010000/814.20.pdf> [in German, accessed: 20/04/2018].
- BBL (2017). Energiegesetz (‘Energy Act’). Federal Law. <http://www.admin.ch/opc/de/federal-gazette/2016/7683.pdf> [in German, accessed: 20/04/2018].

- Beck, M.; Baron, L. (2011). Bathymetrie Gries — Rapport Technique ('Bathymetry Gries — Technical Report'). *Technical Report*, R.B.R. Geophysics GmbH [in French, unpublished].
- Beck, M.; Baron, L. (2013). Bathymetrie Gries 2013 — Rapport Technique ('Bathymetry Gries — Technical Report'). *Technical Report*, R.B.R. Geophysics GmbH [in French, unpublished].
- Beck, M.; Baron, L. (2014). Reconnaissances bathymétrique — Barrage de Gries (VS) ('Bathymetry measurements — Gries reservoir (VS)'). *Technical Report*, R.B.R. Geophysics GmbH [in French, unpublished].
- Beck, M.; Baron, L. (2015). Bathymetrie Gries — Rapport Technique ('Bathymetry Gries — Technical Report'). *Technical Report*, R.B.R. Geophysics GmbH [in French, unpublished].
- Beck, M.; Baron, L. (2016). Bathymetrie Gries — Rapport Technique ('Bathymetry Gries — Technical Report'). *Technical Report*, R.B.R. Geophysics GmbH [in French, unpublished].
- Beffa, C. J. (1994). Praktische Lösung der tiefengemittelten Flachwasser-gleichungen ('Solutions of the depth-averaged shallow water equations'). *VAW-Mitteilung 133* (D. Vischer, ed.). Laboratory of Hydraulics, Hydrology and Glaciology (VAW), ETH Zurich, Zurich, Switzerland. <https://www.ethz.ch/content/dam/ethz/special-interest/baug/vaw/vaw-dam/documents/das-institut/mitteilungen/1990-1999/133.pdf> [in German, accessed: 20/04/2018].
- Benjamin, T. B. (1968). Gravity currents and related phenomena. *Journal of Fluid Mechanics*, 31(2): 209–248. <http://dx.doi.org/10.1017/s0022112068000133>.
- Beyer Portner, N. (1998). Érosion des bassins versant alpins suisses par ruissellement de surface ('Erosion of alpine catchments in Switzerland by overland flow'). *PhD Thesis*, École Polytechnique Fédérale de Lausanne (EPFL). https://infoscience.epfl.ch/record/116153/files/Comm_LCH_6.pdf?version=1 [in French, accessed: 20/04/2018].
- Bezinge, A. (1987). Chap. 17 — Glacial meltwater streams, hydrology and sediment transport: The case of the Grande Dixence hydroelectricity scheme: 473–498. In: A. M. Gurnell; M. J. Clark (eds.) *Glacio-Fluvial Sediment Transfer — An Alpine Perspective*. ISBN 0-471-90929-7. *John Wiley & Sons, Ltd*, Chichester, England.

- Bezinge, A.; Aeschlimann, R. (1989). Eaux glaciaires, transports solides et décantation en hydro-électricité ('Glacial waters, carriage of solid materials and decantation in hydro-electricity'). *La Houille Blanche*, (3/4): 247–256. <http://dx.doi.org/10.1051/lhb/1989024> [in French].
- BFE (2012). Wasserkraftpotential der Schweiz. Abschätzung des Ausbaupotenzials der Wasserkraftnutzung im Rahmen der Energiestrategie 2050 ('Hydropower potential in Switzerland. Estimation of upgrade potential of hydropower in the framework of Energy Strategy 2050'). *Public Report*, Swiss Federal Office of Energy (SFOE). <http://www.news.admin.ch/NSBSubscriber/message/attachments/27057.pdf> [in German, accessed: 20/04/2018].
- BFE (2017). Wasserkraft Schweiz: Statistik 2016 und interaktive Karte ('Hydropower in Switzerland: Statistics 2016 and interactive map'). Press Release. <http://www.bfe.admin.ch/energie/00588/00589/00644/index.html?lang=de&msg-id=66533> [in German, accessed: 20/04/2018].
- Boes, R. M. (2011). Potenziale und Grenzen der Wasserkraft — Was bringen Anlagenoptimierungen? ('Potential and limits of hydropower — what can be gained from optimization of schemes?'). *Natur und Mensch, Sonderheft Quo Vadis Wasserkraft?*, 53(4): 24–28. <https://www.aquaviva.ch/images/Zeitschrift/ganze%20Ausgaben/NM04.2011.pdf> [in German, accessed: 20/04/2018].
- Boes, R. M.; Hagmann, M. (2015). Sedimentation countermeasures — examples from Switzerland. *Proc. First International Workshop on Sediment Bypass Tunnels*, R. M. Boes (ed.). *Laboratory of Hydraulics, Hydrology and Glaciology (VAW), ETH Zurich*, Zurich, Switzerland: 193–210. ISBN 0374-0056. <https://www.ethz.ch/content/dam/ethz/special-interest/baug/vaw/vaw-dam/documents/das-institut/mitteilungen/2010-2019/232.pdf> [accessed: 20/04/2018].
- Bogen, J. (1989). Glacial sediment production and development of hydroelectric power in glacierized areas. *Annals of Glaciology*, 13: 6–11. <http://dx.doi.org/10.3189/S0260305500007539>.
- Bonalumi, M.; Anselmetti, F. S.; Kaegi, R.; Wüest, A. (2011). Particle dynamics in high-Alpine proglacial reservoirs modified by pumped-storage operation. *Water Resources Research*, 47(9): 1–15. <http://dx.doi.org/10.1029/2010wr010262>.
- Bondurant, D. C. (1975). Chap. V — Sediment control methods: [E] Reservoirs. In: V.A. Vanoni (ed.) *Sedimentation Engineering*. ISBN 0-7844-0823-8.

- American Society of Civil Engineers (ASCE)*, Reston, Virginia (USA). <http://dx.doi.org/10.1061/9780784408230>.
- Borland, W. M.; Miller, C. R. (1958). Distribution of sediment in large reservoirs. *Journal of the Hydraulics Division*, 84(HY 2): 1–18. <http://cedb.asce.org/CEDBsearch/record.jsp?dockkey=0011217>.
- Bornhold, B. D.; Prior, D. B. (1990). Chap. 9 — Morphology and sedimentary processes on the subaqueous Noeick River delta, British Columbia, Canada: 169–181. In: A. Colella; D.B. Prior (eds.) *Coarse-Grained Deltas* (Special Publication Number 10 of the International Association of Sedimentologists). ISBN 0-632-02894-7. *Blackwell Scientific Publications*, Oxford, England. <http://dx.doi.org/10.1002/9781444303858>.
- Bourban, G.; Papilloud, E. (2015). Gries: a global approach example for hydropower reservoir sedimentation management. *Proc. HYDRO 2015. International Hydropower Association (IHA)*, Bordeaux, France: 1–6.
- Bradford, S. F.; Katopodes, N. D. (1999). Hydrodynamics of turbid underflows. I: Formulation and numerical analysis. *Journal of Hydraulic Engineering*, 125(10): 1006–1015. [http://dx.doi.org/10.1061/\(asce\)0733-9429\(1999\)125:10\(1006\)](http://dx.doi.org/10.1061/(asce)0733-9429(1999)125:10(1006)).
- Brune, G. M. (1953). Trap efficiency of reservoirs. *Transactions American Geophysical Union*, 34(3): 407–418. <http://dx.doi.org/10.1029/tr034i003p00407>.
- Bühler, J.; Siegenthaler, C.; Simitovic, R.; Wüest, A.; Zeh, M. (2004). Trübe- ströme im Grimsensee (‘Turbidity currents in Grimsensee’). *Wasser Energie Luft*, 96(5/6): 129–135 [in German].
- Bühler, J.; Siegenthaler, C.; Wüest, A. (2005). Turbidity currents in an Alpine pumped-storage reservoir. *Proc. Environmental Hydraulics and Sustainable Water Management*, J. H. W. Lee; K. M. Lam (eds.). *Taylor & Francis*, London, England: 239–244. ISBN 978-0-415-36546-8.
- Cao, Z.; Li, J.; Pender, G.; Liu, Q. (2015). Whole-process modeling of reservoir turbidity currents by a double layer-averaged model. *Journal of Hydraulic Engineering*, 141(2): 04014069. [http://dx.doi.org/10.1061/\(asce\)hy.1943-7900.0000951](http://dx.doi.org/10.1061/(asce)hy.1943-7900.0000951).
- Capart, H.; Bellal, M.; Young, D.-L. (2007). Self-similar evolution of semi-infinite alluvial channels with moving boundaries. *Journal of Sedimentary Research*, 77(1): 13–22. <http://dx.doi.org/10.2110/jsr.2007.009>.

- CH2011 (2011). Swiss Climate Change Scenarios 2011. *Technical Report*, C2SM, MeteoSwiss, ETH, NCCR Climate and OcCC, Zürich. <http://www.ch2011.ch/pdf/CH2011reportHIGH.pdf> [accessed: 20/04/2018].
- Chang, H. H.; Harrison, L. L.; Lee, W.; Tu, S. (1996). Numerical modeling for sediment-pass-through reservoirs. *Journal of Hydraulic Engineering*, 122(7): 381–388. [http://dx.doi.org/10.1061/\(asce\)0733-9429\(1996\)122:7\(381\)](http://dx.doi.org/10.1061/(asce)0733-9429(1996)122:7(381)).
- Chapron, E.; Juvigné, E.; Mulsow, S.; Ariztegui, D.; Magand, O.; Bertrand, S.; Pino, M.; Chapron, O. (2007). Recent elastic sedimentation processes in Lake Puyehue (Chilean Lake District, 40.5°S). *Sedimentary Geology*, 201(3-4): 365–385. <http://dx.doi.org/10.1016/j.sedgeo.2007.07.006>.
- Chaudhry, M. H. (2008). Open-Channel Flow. ISBN 978-0-387-30174-7. Springer, New York, USA.
- Chikita, K. A. (2007). Topographic effects on the thermal structure of Himalayan glacial lakes: Observations and numerical simulation of wind. *Journal of Asian Earth Sciences*, 30(2): 344–352. <http://dx.doi.org/10.1016/j.jseaes.2006.10.005>.
- Choi, S.-U.; García, M. H. (2002). $k-\varepsilon$ turbulence modeling of density currents developing two dimensionally on a slope. *Journal of Hydraulic Engineering*, 128(1): 55–63. [http://dx.doi.org/10.1061/\(asce\)0733-9429\(2002\)128:1\(55\)](http://dx.doi.org/10.1061/(asce)0733-9429(2002)128:1(55)).
- Chu, F. H.; Pilkey, W. D.; Pilkey, O. H. (1979). An analytical study of turbidity current steady flow. *Marine Geology*, 33(3-4): 205–220. [http://dx.doi.org/10.1016/0025-3227\(79\)90081-1](http://dx.doi.org/10.1016/0025-3227(79)90081-1).
- Chung, S. W.; Hipsey, M. R.; Imberger, J. (2009). Modelling the propagation of turbid density inflows into a stratified lake: Daecheong Reservoir, Korea. *Environmental Modelling & Software*, 24(12): 1467–1482. <http://dx.doi.org/10.1016/j.envsoft.2009.05.016>.
- Clifford, N. J.; Richards, K. S.; Brown, R. A.; Lane, S. N. (1995). Scales of variation of suspended sediment concentration and turbidity in a glacial melt-water stream. *Geografiska Annaler. Series A. Physical Geography*, 77A(1/2): 45–65. <http://dx.doi.org/10.2307/521277>.
- Collins, D. N. (1989). Seasonal development of subglacial drainage and suspended sediment delivery to melt waters beneath an Alpine glacier. *Annals of Glaciology*, 13: 45–50. <http://dx.doi.org/10.3189/S026030550000762X>.

- Costa, A.; Anghileri, D.; Molnar, P. (2018a). Hydroclimatic control on suspended sediment dynamics of a regulated Alpine catchment: a conceptual approach. *Hydrology and Earth System Sciences Discussions*: 1–23. <http://dx.doi.org/10.5194/hess-2018-5>.
- Costa, A.; Molnar, P.; Stutenbecker, L.; Bakker, M.; Silva, T. A.; Schlunegger, F.; Lane, S. N.; Loizeau, J.-L.; Girardclos, S. (2018b). Temperature signal in suspended sediment export from an Alpine catchment. *Hydrology and Earth System Sciences*, 22(1): 509–528. <http://dx.doi.org/10.5194/hess-22-509-2018>.
- Curran, K. J.; Hill, P. S.; Milligan, T. G.; Mikkelsen, O. A.; Law, B. A.; De Madron, X. D.; Bourrin, F. (2007). Settling velocity, effective density, and mass composition of suspended sediment in a coastal bottom boundary layer, Gulf of Lions, France. *Continental Shelf Research*, 27(10): 1408–1421. <http://dx.doi.org/10.1016/j.csr.2007.01.014>.
- Czuba, J. A.; Straub, T. D.; Curran, C. A.; Landers, M. N.; Domanski, M. M. (2015). Comparison of fluvial suspended-sediment concentrations and particle-size distributions measured with in-stream laser diffraction and in physical samples. *Water Resources Research*, 51(1): 320–340. <http://dx.doi.org/10.1002/2014wr015697>.
- de Cesare, G.; Boillat, J.-L.; Schleiss, A. (2006). Circulation in stratified lakes due to flood-induced turbidity currents. *Journal of Environmental Engineering*, 132(11): 1508–1517. [http://dx.doi.org/10.1061/\(asce\)0733-9372\(2006\)132:11\(1508\)](http://dx.doi.org/10.1061/(asce)0733-9372(2006)132:11(1508)).
- de Cesare, G.; Schleiss, A.; Hermann, F. (2001). Impact of turbidity currents on reservoir sedimentation. *Journal of Hydraulic Engineering*, 127(1): 6–16. [http://dx.doi.org/10.1061/\(asce\)0733-9429\(2001\)127:1\(6\)](http://dx.doi.org/10.1061/(asce)0733-9429(2001)127:1(6)).
- Deane, G. B. (1997). Sound generation and air entrainment by breaking waves in the surf zone. *The journal of the acoustical society of America*, 102(5): 2671–2689. <http://dx.doi.org/10.1121/1.420321>.
- Deines, K. L. (1999). Backscatter estimation using broadband acoustic Doppler current profilers. *Proc. IEEE 6th Working Conference on Current Measurement*, S.P. Anderson; E.A. Terray; J.A.R. White; A.J. Williams (eds.). San Diego, USA: 249–253. <http://dx.doi.org/10.1109/ccm.1999.755249>.
- Delaney, I.; Bauder, A.; Huss, M.; Weidmann, Y. (2017). Proglacial erosion reates and processes in a glacierized catchment in the Swiss Alps. *Earth Surface Processes and Landforms*. <http://dx.doi.org/10.1002/esp.4239>.

- Delaney, I.; Bauder, A.; Werder, M. A.; Farinotti, D. (2018a). Regional and annual variability in subglacial sediment transport by water for two glaciers in the Swiss Alps. *Frontiers in Cryosphere* [submitted].
- Delaney, I.; Werder, M. A.; Farinotti, D. (2018b). Physical modeling of subglacial sediment transport in 1 dimension: comparison with measurements and implications for glacier retreat. *Journal of Glaciology* [in preparation].
- Droppo, I. G.; Ongley, E. D. (1992). The state of suspended sediment in the freshwater fluvial environment: a method of analysis. *Water Research*, 26(1): 65–72. [http://dx.doi.org/10.1016/0043-1354\(92\)90112-h](http://dx.doi.org/10.1016/0043-1354(92)90112-h).
- Droppo, I. G.; Ongley, E. D. (1994). Flocculation of suspended sediment in rivers of southeastern Canada. *Water Research*, 28(8): 1799–1809. [http://dx.doi.org/10.1016/0043-1354\(94\)90253-4](http://dx.doi.org/10.1016/0043-1354(94)90253-4).
- Duclos, P.-A.; Lafite, R.; Le Bot, S.; Rivoalen, E.; Cuvilliez, A. (2013). Dynamics of turbid plumes generated by marine aggregate dredging: An example of a macrotidal environment (the Bay of Seine, France). *Journal of Coastal Research*, 29(1): 25–37. <http://dx.doi.org/10.2112/jcoastres-d-12-00148.1>.
- Dwinovantyo, A.; Manik, H. M.; Prartono, T.; Susilohadi, S. (2017). Quantification and analysis of suspended sediments concentration using mobile and static acoustic Doppler current profiler instruments. *Advances in Acoustics and Vibrations*, 2017: 1–14. <http://dx.doi.org/10.1155/2017/4890421>.
- Eder, M.; Wessels, M.; Dare, J. (2014). Underflows in Lake Constance — Numerical modeling, instrumental observations and sediment data. *Proc. EGU General Assembly Conference — Geophysical Research Abstracts. European Geosciences Union (EGU)*, Vienna, Austria: 10709. http://adsabs.harvard.edu/cgi-bin/nph-data_query?bibcode=2014EGUGA..1610709E&link_type=ARTICLE&db_key=PHY&high= [accessed: 20/04/2018].
- Ehrbar, D.; Schmocker, L.; Vetsch, D. F.; Boes, R. M.; Doering, M. (2016a). Messung von Sedimentflüssen in periglazialen Stauseen mit Wasserproben, LISST und ADCP. *Proc. 18. Wasserbau-Symposium 2016 “Wasserbau — mehr als Bauen im Wasser (18th Symposium on Hydraulic Engineering 2016 “Hydraulic Engineering — more than building in water”)*, P. Rutschmann (ed.). *Lehrstuhl und der Versuchsanstalt für Wasserbau und Wasserwirtschaft, Technische Universität München (‘Chair of Hydraulic Engineering and Water Resources Management, Technical University of Munich’)*, Munich, Germany: 215–226. ISBN 978-3-940476-10-3. <https://www.wb.bgu.tum.de/fileadmin/>

w00boi/www/Publikationen/Berichtshefte/Band134.pdf [in German, accessed: 20/04/2018].

- Ehrbar, D.; Schmocker, L.; Vetsch, D. F.; Boes, R. M.; Doering, M. (2016b). Measuring sediment fluxes in periglacial reservoirs using water samples, LISST and ADCP. *Proc. River Sedimentation*, S. Wieprecht; S. Haun; K. Weber; M. Noack; K. Terheiden (eds.). *CRC Press Taylor & Francis Group*, London, England: 1118–1125. ISBN 978-1-138-02945-3.
- Ehrbar, D.; Schmocker, L.; Vetsch, D. F.; Boes, R. M.; Doering, M. (2017). Measuring suspended sediments in periglacial reservoirs using water samples, laser in-situ scattering and transmissometry and acoustic Doppler current profiler. *International Journal of River Basin Management*, 15(4): 413–431. <http://dx.doi.org/10.1080/15715124.2017.1327866>.
- Elçi, Ş; Aydın, R.; Work, P. A. (2008). Estimation of suspended sediment concentration in rivers using acoustic methods. *Environmental Monitoring and Assessment*, 159(1-4): 255–265. <http://dx.doi.org/10.1007/s10661-008-0627-5>.
- Exner, F. M. (1925). Über die Wechselwirkung zwischen Wasser und Geschiebe ('On the interaction between water and gravel deposits in rivers'). *Sitzungsberichte Wiener Akademie der Wissenschaften* 134. 165–203.
- Facchini, M. (2018). Downstream morphological effects of Sediment Bypass Tunnels. *VAW-Mitteilung 243* (R. M. Boes, ed.). Laboratory of Hydraulics, Hydrology and Glaciology (VAW), ETH Zurich, Zurich, Switzerland. <https://www.ethz.ch/content/dam/ethz/special-interest/baug/vaw/vaw-dam/documents/das-institut/mitteilungen/2010-2019/243.pdf> [accessed: 20/04/2018].
- Fallegger, S. (2014). Wasserkraft bei Gletscherrückzug im Kanton Wallis ('Hydropower and glacier retreat in canton Wallis'). *Master Thesis*, Laboratory of Hydraulics, Hydrology and Glaciology (VAW), ETH Zurich [in German, unpublished].
- Fang, H.-W.; Rodi, W. (2003). Three-dimensional calculations of flow and suspended sediment transport in the neighborhood of the dam for the Three Gorges Project (TGP) reservoir in the Yangtze River. *Journal of Hydraulic Research*, 41(4): 379–394. <http://dx.doi.org/10.1080/00221680309499983>.
- Farinotti, D.; Pistocchi, A.; Huss, M. (2016). From dwindling ice to headwater lakes: could dams replace glaciers in the European Alps? *Environmental Research Letters*, 11(5): 054022. <http://dx.doi.org/10.1088/1748-9326/11/5/054022>.

- Farinotti, D.; Usselmann, S.; Huss, M.; Bauder, A.; Funk, M. (2012). Runoff evolution in the Swiss Alps: projections for selected high-alpine catchments based on ENSEMBLES scenarios. *Hydrological Processes*, 26(13): 1909–1924. <http://dx.doi.org/10.1002/hyp.8276>.
- Felix, D. (2017). Experimental investigation on suspended sediment, hydro-abrasive erosion and efficiency reductions of coated Pelton turbines. *VAW-Mitteilung 238* (R. M. Boes, ed.). Laboratory of Hydraulics, Hydrology and Glaciology (VAW), ETH Zurich, Zurich, Switzerland. <https://www.ethz.ch/content/dam/ethz/special-interest/baug/vaw/vaw-dam/documents/das-institut/mitteilungen/2010-2019/238.pdf> [accessed: 20/04/2018].
- Felix, D.; Albayrak, I.; Boes, R. M. (2013). Laboratory investigation on measuring suspended sediment by portable laser diffractometer (LISST) focusing on particle shape. *Geo-Marine Letters*, 33(6): 485–498. <http://dx.doi.org/s00367-013-0343-1>.
- Felix, D.; Albayrak, I.; Boes, R. M. (2017a). Weiterleitung von Feinsedimenten via Triebwasser als Massnahme gegen die Stauraumverlandung (‘Conveyance of fine sediments via power waterways as a mean to counter reservoir sedimentation’). *Wasser Energie Luft*, 109(2): 85–90 [in German].
- Felix, D.; Albayrak, I.; Boes, R. M. (2018). In-situ investigation on real-time suspended sediment measurement techniques: Turbidimetry, acoustic attenuation, laser diffraction (LISST) and vibrating tube densimetry. *International Journal of Sediment Research*, 33(1): 3–17. <http://dx.doi.org/10.1016/j.ijsrc.2017.11.003>.
- Felix, D.; Albayrak, I.; Boes, R. M.; Abgottspon, A. (2017b). Sediment transport through the power waterway and hydro-abrasive erosion on turbines. *Proc. HYDRO 2017. International Hydropower Association (IHA)*, Sevilla, Spain: 1–8.
- Fenn, C. R.; Gomez, B. (1989). Particle size analysis of the sediment suspended in a proglacial stream: Glacier De Tsidjiore Nouve, Switzerland. *Hydrological Processes*, 3(2): 123–135. <http://dx.doi.org/10.1002/hyp.3360030203>.
- Ferrer-Boix, C.; Martín-Vide, J. P.; Parker, G. (2015). Sorting of a sand-gravel mixture in a Gilbert-type delta. *Sedimentology*, 62(5): 1446–1465. <http://dx.doi.org/10.1111/sed.12189>.
- Fettweis, M. (2008). Uncertainty of excess density and settling velocity of mud flocs derived from in situ measurements. *Estuarine, Coastal and Shelf Science*, 78(2): 426–436. <http://dx.doi.org/10.1016/j.ecss.2008.01.007>.

- Fettweis, M.; Francken, F.; Pison, V.; Van den Eynde, D. (2006). Suspended particulate matter dynamics and aggregate sizes in a high turbidity area. *Marine Geology*, 235(1-4): 63–74. <http://dx.doi.org/10.1016/j.margeo.2006.10.005>.
- Fichtner (2015). Hydroelectric power — A guide for developers and investors. *Technical Report*, International Finance Corporation (IFC) — World Bank Group. http://www.ifc.org/wps/wcm/connect/06b2df8047420bb4a4f7ec57143498e5/Hydropower_Report.pdf?MOD=AJPERES [accessed; 20/04/2018].
- Fiedler, K. (2008). Erfassung hydromorphologischer Vorgänge bei Hochwasser mit Hilfe von ADCP-Messungen ('Detection of hydromorphological processes at flood water with ADCP'). *PhD Thesis*, Chair of Hydraulic Engineering and Water Resources Management, Technical University of Munich. <http://www.wb.bv.tum.de/fileadmin/w00boi/www/Publikationen/Berichtshefte/Band120.pdf> [in German, accessed: 20/04/2018].
- FMM (2001). Retenue de Mauvoisin — Rehaussement de la prise d'eau et de la vidange de fond 2001–2006 ('Reservoir of Mauvoisin — Heightening of the water intake and bottom outlet 2001–2006'). *Project description brochure*, Forces Motrices de Mauvoisin S.A. [in French].
- FMM (2016). Forces Motrices de Mauvoisin S.A. *Company documentation*, Forces Motrices de Mauvoisin S.A. [in French].
- Forel, F.-A. (1887/1888). Le ravin sous-lacustre du Rhône dans le Lac Léman ('The lacustrine ravine of the Rhone river in Lake Geneva'). *Bulletin de la Société Vaudoise des Sciences Naturelles*, 23(96): 85–107. <http://dx.doi.org/10.5169/seals-261388> [in French].
- Gabbi, J.; Farinotti, D.; Bauder, A.; Maurer, H. (2012). Ice volume distribution and implications on runoff projections in a glacierized catchment. *Hydrology and Earth System Sciences*, 16(12): 4543–4556. <http://dx.doi.org/10.5194/hess-16-4543-2012>.
- Gartner, J. W. (2004). Estimating suspended solids concentrations from backscatter intensity measured by acoustic Doppler current profiler in San Francisco Bay, California. *Marine Geology*, 211(3): 169–187. <http://dx.doi.org/10.1016/j.margeo.2004.07.001>.
- Gauye, F.; Sartori, F.; Wydler, J. (2017). Wasserkraftpotential in der Schweiz aufgrund des Gletscherrückzugs ('Hydropower potential in Switzerland due to glacier retreat'). *Project Thesis*, Laboratory of Hydraulics, Hydrology and Glaciology (VAW), ETH Zurich [in German, unpublished].

- Geilhausen, M.; Morche, D.; Otto, J.-C.; Schrott, L. (2013). Sediment discharge from the proglacial zone of a retreating Alpine glacier. *Zeitschrift für Geomorphologie, Supplementary Issues*, 57(2): 29–53. <http://dx.doi.org/10.1127/0372-8854/2012/s-00122>.
- Germann, J. (2012). Impulswellen — Natur und Modell (‘Impulse waves — nature and modell’). *Master Thesis*, Laboratory of Hydraulics, Hydrology and Glaciology (VAW), ETH Zurich [in German, unpublished].
- Gessler, D.; Hall, B.; Spasojevic, M.; Holly, F. M.; Pourtaheri, H.; Raphelt, N. (1999). Application of 3D mobile bed, hydrodynamic model. *Journal of Hydraulic Engineering*, 125(7): 737–749. [http://dx.doi.org/10.1061/\(ASCE\)0733-9429\(1999\)125:7\(737\)](http://dx.doi.org/10.1061/(ASCE)0733-9429(1999)125:7(737)).
- Giezendanner, W.; Dawans, P. (1981). Die Freihaltung des Stauraumes von Gebidem (‘Keeping Gebidem reservoir clear of sedimentation’). *Proc. Internationale Fachtagung über Verlandung von Flussstauhaltungen und Speicherseen im Alpenraum (‘International Symposium on Sedimentation of Run-of-River Plants and Alpine Reservoirs’)*, D. Vischer (ed.). *Laboratory of Hydraulics, Hydrology and Glaciology (VAW), ETH Zurich*, Zurich, Switzerland: 197–205. <https://www.ethz.ch/content/dam/ethz/special-interest/baug/vaw/vaw-dam/documents/das-institut/mitteilungen/1980-1989/053.pdf> [in German, accessed: 20/04/2018].
- Gilbert, G. K. (1890). Lake Bonneville. *Technical Report*, United States Geological Survey. <http://dx.doi.org/10.5962/bhl.title.45656>.
- Girmscheid, G. (2003). Bauprozesse und Bauverfahren des Tunnelbaus (‘Construction processes and methods in tunneling’). ISBN 978-3-433-03047-9. *Ernst W. + Sohn Verlag*, Berlin, Germany. <http://dx.doi.org/10.1002/9783433603123> [in German].
- González, J.; Tamburrino, A.; Niño, Y. (2006). Reservoir sedimentation: 1D model of turbidity currents and delta deposits. *Proc. River Flow 2006*, R. M. L. Ferreira; E. C. T. L. Alves; J. G. A. B. Leal; A. H. Cardoso (eds.). *Taylor & Francis Group*, Lisbon, Portugal: 1607–1616.
- Gostiaux, L.; Van Haren, H. (2010). Extracting meaningful information from uncalibrated backscattered echo intensity data. *Journal of Atmospheric and Oceanic Technology*, 27(5): 943–949. <http://dx.doi.org/10.1175/2009jtecho704.1>.
- Grande Dixence (2010). Grande Dixence — ein Mythos im Herzen der Alpen (‘Grande Dixence — a myth in the heart of the Alps’). *Brochure*,

- Grande Dixence S.A. <http://www.grande-dixence.ch/docs/default-source/documentation/grande-dixence/Grande-Dixence-Ein-Mythos-im-Herzen-der-Alpen.pdf?sfvrsn=12> [in German, accessed: 20/04/2018].
- Guerrero, M.; R  ther, N.; Archetti, R. (2014). Comparison under controlled conditions between multi-frequency ADCPs and LISST-SL for investigating suspended sand in rivers. *Flow Measurement and Instrumentation*, 37: 73–82. <http://dx.doi.org/10.1016/j.flowmeasinst.2014.03.007>.
- Guerrero, M.; R  ther, N.; Szupiany, R.; Haun, S.; Baranya, S.; Latosinski, F. (2016). The acoustic properties of suspended sediment in large rivers: Consequences on ADCP methods applicability. *Water-MDPI*, 8(13): 1–22. <http://dx.doi.org/10.3390/w8010013>.
- Guerrero, M.; R  ther, N.; Szupiany, R. N. (2012). Laboratory validation of acoustic Doppler current profiler (ADCP) techniques for suspended sediment investigations. *Flow Measurement and Instrumentation*, 23(1): 40–48. <http://dx.doi.org/10.1016/j.flowmeasinst.2011.10.003>.
- Guerrero, M.; Szupiany, R. N.; Amsler, M. (2011). Comparison of acoustic backscattering techniques for suspended sediments investigation. *Flow measurement and Instrumentation*, 22(5): 392–401. <http://dx.doi.org/10.1016/j.flowmeasinst.2011.06.003>.
- Guerrero, M.; Szupiany, R. N.; Latosinski, F. (2013). Multi-frequency acoustics for suspended sediment studies: an application in the Parana River. *Journal of Hydraulic Research*, 51(6): 696–707. <http://dx.doi.org/10.1080/00221686.2013.849296>.
- Guertault, L.; Camenen, B.; Peteuil, C.; Paquier, A.; Faure, J. B. (2016). One-dimensional modeling of suspended sediment dynamics in dam reservoirs. *Journal of Hydraulic Engineering*, 142(10): 04016033. [http://dx.doi.org/10.1061/\(asce\)hy.1943-7900.0001157](http://dx.doi.org/10.1061/(asce)hy.1943-7900.0001157).
- Guillon, H. (2016). Origine et transport des s  diments dans un bassin versant alpin englac   (Glacier des Bossons, France) ('Origin and transport of sediments in a glaciated alpine drainage basin (Glacier des Bossons, France)'). *PhD Thesis*, Universit   Grenoble Alpes. <https://tel.archives-ouvertes.fr/tel-01461481v2/document> [partially in French, accessed: 20/04/2018].
- Guillon, H.; Mugnier, J.-L.; Buoncristiani, J.-F.; Carcaillet, J.; Godon, C.; Prud'Homme, C.; Beek, P.; Vassallo, R. (2015). Improved discrimination of subglacial and periglacial erosion using ¹⁰Be concentration measurements in subglacial and supraglacial sediment load of the Bossons glacier (Mont Blanc

- massif, France). *Earth Surface Processes and Landforms*, 40(9): 1202–1215. <http://dx.doi.org/10.1002/esp.3713>.
- Guo, L.; He, Q. (2011). Freshwater flocculation of suspended sediments in the Yangtze River, China. *Ocean Dynamics*, 61(2/3): 371–386. <http://dx.doi.org/10.1007/s10236-011-0391-x>.
- Gurnell, A.; Hannah, D.; Lawler, D. (1996). Suspended sediment yield from glacier basins. *Proc. Erosion and Sediment Yield: Global and Regional Perspectives*, D. E. Walling; B. Webb (eds.). *International Association of Hydrological Sciences (IAHS)*, Exeter, England: 97–104. ISBN 978-0-947571-89-4.
- Gurnell, A. M. (1995). Chap. 22 — Sediment yield from Alpine glacier basins: 407–435. In: I. D. L. Foster; A. M. Gurnell; B. W. Webb (eds.) *Sediment and Water Quality in River Catchments*. ISBN 0-471-95728-3. *John Wiley & Sons, Ltd.*, Chichester, England.
- Ha, H. K.; Kim, Y. H.; Lee, H. J.; Hwang, B.; Joo, H. M. (2015). Under-ice measurements of suspended particulate matters using ADCP and LISST-Holo. *Ocean Science Journal*, 50(1): 97–108. <http://dx.doi.org/10.1007/s12601-015-0008-2>.
- Haerberli, W.; Bütler, M.; Huggel, C.; Schleiss, A. (2013). Neue Seen als Folge des Gletscherschwundes im Hochgebirge: Chancen und Risiken – Formation de nouveaux lacs suite au recul des glaciers en haute montagne: chances et risques (‘New lakes as a consequence of glacier retreat in high mountains: Chances and risks’). *Technical Report*, Nationales Forschungsprogramm NFP 61 “Nachhaltige Wassernutzung” (‘National Research Programme NRP 61 “Sustainable Water Management”’). https://infoscience.epfl.ch/record/197261/files/2013-911_Haerberli_Butler_Huggel_Muller_Schleiss_3534_Neue-Seen-als-Folge-des-Gletscherschwundes-im-Hochgebirge_0A.pdf [in German and French, accessed: 20/04/2018].
- Haerberli, W.; Schleiss, A.; Linsbauer, A.; Künzler, M.; Bütler, M. (2012). Gletscherschwund und neue Seen in den Schweizer Alpen (‘Glacier retreat and new lakes in the Swiss Alps’). *Wasser Energie Luft*, 104(2): 93–102. https://infoscience.epfl.ch/record/178376/files/2012-846_Haerberli_Schleiss_Linsbauer_K%C3%BCnzler_B%C3%BCTler_Gletscherschwund_und_neue_Seen_in.de_Schweizer_Alpen.pdf [in German, accessed: 20/04/2018].
- Hallet, B.; Hunter, L.; Bogen, J. (1996). Rates of erosion and sediment evacuation by glaciers: A review of field data and their implications. *Global*

- and *Planetary Change*, 12(1-4): 213–235. [http://dx.doi.org/10.1016/0921-8181\(95\)00021-6](http://dx.doi.org/10.1016/0921-8181(95)00021-6).
- Harb, G. (2016). Numerical modeling of sediment transport processes in Alpine reservoirs. *PhD Thesis*, Technische Universität Graz. <http://dx.doi.org/10.3217/978-3-85125-451-8>.
- Haun, S.; Kjærås, H.; Løvfall, S.; Olsen, N.R.B. (2013). Three-dimensional measurements and numerical modelling of suspended sediments in a hydro-power reservoir. *Journal of Hydrology*, 479: 180–188. <http://dx.doi.org/10.1016/j.jhydro1.2012.11.060>.
- Haun, S.; Lizano, L. (2015). Sensitivity analysis of sediment fluxes derived by using acoustic backscatter. *Proc. 36th IAHR World Congress*, A. Mynett (ed.). *International Association for Hydro-Environment Engineering and Research (IAHR)*, The Hague, The Netherlands: 1660–1664. ISBN 978-90-824846-0-1.
- Haun, S.; Lizano, L. (2016). Evaluation of a density current from ADCP backscatter data and LISST measurements. *Proc. Riverflow 2016, 8th International Conference on Fluvial Hydraulics*, G. Constantinescu; M. García; D. Hanes (eds.). *CRC Press Taylor & Francis Group*, Boca Raton, Florida: 875–881. ISBN 978-1-138-02913-2.
- Haun, S.; Olsen, N. R. B. (2012). Three-dimensional numerical modelling of the flushing process of the Kali Gandaki hydropower reservoir. *Lakes & Reservoirs: Research & Management*, 17(1): 25–33. <http://dx.doi.org/10.1111/j.1440-1770.2012.00491.x>.
- Haun, S.; Rütther, N.; Baranya, S.; Guerrero, M. (2015). Comparison of real time suspended sediment transport measurements in river environment by LISST measurements in stationary and moving operation mode. *Flow Measurement and Instrumentation*, 41: 10–17. <http://dx.doi.org/dx.doi.org/10.1016/j.flowmeasinst.2014.10.009>.
- Hawley, N. (2004). A comparison of suspended sediment concentrations measured by acoustic and optical sensors. *Journal of Great Lakes Research*, 30(2): 301–309. [http://dx.doi.org/10.1016/s0380-1330\(04\)70348-2](http://dx.doi.org/10.1016/s0380-1330(04)70348-2).
- Helfenberger, M.; Kannanmannil, R.; Klar, S. (2017). Wasserkraftpotential im Kanton Wallis aufgrund des Gletscherrückzugs ('Hydropower potential in the canton of Valais due to glacier retreat'). *Project Thesis*, Laboratory of Hydraulics, Hydrology and Glaciology (VAW), ETH Zurich [in German, unpublished].

- Hodder, K. R. (2009). Flocculation: a key process in the sediment flux of a large, glacier-fed lake. *Earth Surface Processes and Landforms*, 34(8): 1151–1163. <http://dx.doi.org/10.1002/esp.1807>.
- Hodder, K. R.; Gilbert, R. (2007). Evidence for flocculation in glacier-fed Lillooet Lake, British Columbia. *Water research*, 41(12): 2748–2762. <http://dx.doi.org/10.1016/j.watres.2007.02.058>.
- Hoitink, A. J. F.; Hoekstra, P. (2005). Observations of suspended sediment from ADCP and OBS measurements in a mud-dominated environment. *Coastal Engineering*, 52(2): 103–118. <http://dx.doi.org/10.1016/j.coastaleng.2004.09.005>.
- Holdaway, G. P.; Thorne, P. D.; Flatt, D.; Jones, S. E.; Prandle, D. (1999). Comparison between ADCP and transmissometer measurements of suspended sediment concentration. *Continental shelf research*, 19(3): 421–441. [http://dx.doi.org/10.1016/s0278-4343\(98\)00097-1](http://dx.doi.org/10.1016/s0278-4343(98)00097-1).
- Horiba (2012). A Guidebook to Particle Size Analysis. *Technical Documentation*, Horiba Instruments, Inc. https://www.horiba.com/fileadmin/uploads/Scientific/Documents/PSA/PSA_Guidebook.pdf [accessed: 20/04/2018].
- Hotchkiss, R. H.; Parker, G. (1991). Shock fitting of aggradational profiles due to backwater. *Journal of Hydraulic Engineering*, 117(9): 1129–1144. [http://dx.doi.org/10.1061/\(asce\)0733-9429\(1991\)117:9\(1129\)](http://dx.doi.org/10.1061/(asce)0733-9429(1991)117:9(1129)).
- Huang, H.; Imran, J.; Pirmez, C. (2005). Numerical model of turbidity currents with a deforming bottom boundary. *Journal of Hydraulic Engineering*, 131(4): 283–293. [http://dx.doi.org/10.1061/\(asce\)0733-9429\(2005\)131:4\(283\)](http://dx.doi.org/10.1061/(asce)0733-9429(2005)131:4(283)).
- Hubbart, J. A.; Kellner, E.; Freeman, G. (2014). A case study considering the comparability of mass and volumetric suspended sediment data. *Environmental Earth Sciences*, 71(9): 4051–4060. <http://dx.doi.org/10.1007/s12665-013-2788-y>.
- Hunter, R. E. (1985). Subaqueous sand-flow cross-strata. *Journal of Sedimentary Petrology*, 55(6): 886–894. <http://dx.doi.org/10.1306/212f8832-2b24-11d7-8648000102c1865d>.
- Huppert, H. E.; Simpson, J. E. (1980). The slumping of gravity currents. *Journal of Fluid Mechanics*, 99(04): 785–799. <http://dx.doi.org/10.1017/s0022112080000894>.

- Hurther, D.; Thorne, P. D.; Bricault, M.; Lemmin, U.; Barnoud, J.-M. (2011). A multi-frequency Acoustic Concentration and Velocity Profiler (ACVP) for boundary layer measurements of fine-scale flow and sediment transport processes. *Coastal Engineering*, 58(7): 594–605. <http://dx.doi.org/10.1016/j.coastaleng.2011.01.006>.
- Huss, M.; Bauder, A.; Funk, M.; Hock, R. (2008a). Determination of the seasonal mass balance of four Alpine glaciers since 1865. *Journal of Geophysical Research: Earth Surface*, 113(F1): 1–11. <http://dx.doi.org/10.1029/2007jf000803>.
- Huss, M.; Farinotti, D.; Bauder, A.; Funk, M. (2008b). Modelling runoff from highly glacierized alpine drainage basins in a changing climate. *Hydrological processes*, 22(19): 3888–3902. <http://dx.doi.org/10.1002/hyp.7055>.
- Huss, M.; Hock, R. (2015). A new model for global glacier change and sea-level rise. *Frontiers in Earth Science*, 3: 1–22. <http://dx.doi.org/10.3389/feart.2015.00054>.
- Huss, M.; Zemp, M.; Joerg, P. C.; Salzmann, N. (2014). High uncertainty in 21st century runoff projections from glacierized basins. *Journal of Hydrology*, 510: 35–48. <http://dx.doi.org/10.1016/j.jhydrol.2013.12.017>.
- Hutter, K.; Wang, Y.; Chubarenko, I. P. (2011). Physics of Lakes — Volume 3: Methods of Understanding Lakes as Components of the Geophysical Environment. ISBN 978-3-319-00473-0. *Springer*, Zürich, Switzerland.
- Hutter, V. (2017). Wasserkraft infolge Gletscherrückzug am Fallbeispiel Rhonegletscher (‘Hydropower due to glacier retreat in the case study of Rhône Glacier’). *Master Thesis*, Laboratory of Hydraulics, Hydrology and Glaciology (VAW), ETH Zurich [in German, unpublished].
- IGT (2014). Feststoffanalyse von Wasserproben. Kraftwerk Chanrion. (‘Sediment analysis of water samples. Power station Chanrion’). *Technical Report CL1048-1*, Institut für Geotechnik (‘Institute for Geotechnical Engineering’), ETH Zurich [in German, unpublished].
- IPCC (2007). Climate Change 2007 — Synthesis Report. *Technical Report*, Intergovernmental Panel on Climate Change (IPCC). https://www.ipcc.ch/pdf/assessment-report/ar4/syr/ar4_syr_full_report.pdf [accessed: 20/04/2018].
- IPCC (2013). Climate Change 2013 — The Physical Science Basis. *Technical Report*, Intergovernmental Panel on Climate Change (IPCC). <http://www.ipcc.ch>

//www.climatechange2013.org/images/report/WG1AR5_ALL_FINAL.pdf [accessed: 20/04/2018].

- Iten, A. (2014). Wasserkraft bei Gletscherrückzug ('Hydropower and glacier retreat'). *Master Thesis*, VAW ETH Zürich [in German, unpublished].
- Jay, D. A.; Orton, P.; Kay, D. J.; Fain, A.; Baptista, A. M. (1999). Acoustic determination of sediment concentrations, settling velocities, horizontal transports and vertical fluxes in estuaries. *Proc. IEEE 6th Working Conference on Current Measurement*, S.P. Anderson; E.A. Terray; J.A.R. White; A.J. Williams (eds.). San Diego, USA: 258–263. <http://dx.doi.org/10.1109/ccm.1999.755251>.
- Jenzer Althaus, J. M. I. (2011). Sediment evacuation from reservoirs through intakes by jet induced flow. *PhD Thesis*, École Polytechnique Fédérale de Lausanne (EPFL). https://infoscience.epfl.ch/record/154766/files/EPFL_TH4927.pdf [accessed: 20/04/2018].
- Jourdin, F.; Tessier, C.; Le Hir, P.; Verney, R.; Lunven, M.; Loyer, S.; Lusven, A.; Filipot, J.-F.; Lepesqueur, J. (2014). Dual-frequency ADCPs measuring turbidity. *Geo-Marine Letters*, 34(4): 381–397. <http://dx.doi.org/10.1007/s00367-014-0366-2>.
- Jouvet, G.; Huss, M.; Funk, M.; Blatter, H. (2011). Modelling the retreat of Grosser Aletschgletscher, Switzerland, in a changing climate. *Journal of Glaciology*, 57(206): 1033–1045. <http://dx.doi.org/10.3189/002214311798843359>.
- Kammerer, S.; Vonwiller, L.; Ehrbar, D.; Vetsch, D. F.; Boes, R. M. (2016). Numerische 1D Modellierung des Geschiebehaushaltes an der Ötztaler Ache ('Numerical 1D modelling of the bed load budget in Ötztaler Ache'). *Proc. 18. Wasserbau-Symposium 2016 "Wasserbau — mehr als Bauen im Wasser" ('18th Symposium on Hydraulic Engineering 2016 "Hydraulic Engineering — more than building in water")*, P. Rutschmann (ed.). *Lehrstuhl und der Versuchsanstalt für Wasserbau und Wasserwirtschaft, Technische Universität München ('Chair of Hydraulic Engineering and Water Resources Management, Technical University of Munich')*: 737–746. ISBN 978-3-940476-10-3. https://www.freunde.wb.bgu.tum.de/fileadmin/w00bo1/www/Symposium_2016/Beitraege_Wallgau2016/71.-_Kammerer.pdf [in German, accessed: 20/04/2018].
- Kammerlander, J.; Achleitner, S.; Schöber, J.; Hofer, B. (2017). Geschiebehaushalt in kleinen Hochgebirgsbächen der Nordtiroler Zentralalpen ('Bed load budget in small high-alpine streams in the North-Tirolean Central Alps').

- Österreichische Wasser- und Abfallwirtschaft ('Austrian Water and Waste Management'), 69: 114–124. <http://dx.doi.org/10.1007/s00506-017-0378-z> [in German].
- Kenyon, P. M.; Turcotte, D. L. (1985). Morphology of a delta prograding by bulk sediment transport. *Geological Society of America Bulletin*, 96(11): 1457–1465. [http://dx.doi.org/10.1130/0016-7606\(1985\)96<1457:MOADPB>2.0.CO;2](http://dx.doi.org/10.1130/0016-7606(1985)96<1457:MOADPB>2.0.CO;2).
- Kim, Y. H.; Voulgaris, G. (2003). Estimation of suspended sediment concentration in estuarine environments using acoustic backscatter from ADCP. *Proc. 5th International Conference on Coastal Sediments*, R.A. Davis; A. Sallenger; P. Howd (eds.). Clearwater Beach, USA.
- Kobierska-Baffie, F. A. (2014). Hydrological modelling of a glacierized catchment across spatial and temporal scales. *PhD Thesis*, ETH Zurich. <http://dx.doi.org/10.3929/ethz-a-010264039> [accessed: 20/04/2018].
- Kostaschuk, R.; Best, J.; Villard, P.; Peakall, J.; Franklin, M. (2005). Measuring flow velocity and sediment transport with an acoustic Doppler current profiler. *Geomorphology*, 68(1): 25–37. <http://dx.doi.org/10.1016/j.geomorph.2004.07.012>.
- Kostic, S. (2014). Chap. 6 — Advances in numerical modeling of reservoir sedimentation: 45–52. In: A. Schleiss; G. de Cesare; M.J. Franca; M. Pfister (eds.) *Reservoir Sedimentation*. ISBN 9781138026759. *Taylor & Francis Group*, London, England.
- Kostic, S.; Parker, G. (2003a). Progradational sand-mud deltas in lakes and reservoirs. Part 1. Theory and numerical modeling. *Journal of Hydraulic Research*, 41(2): 127–140. <http://dx.doi.org/10.1080/00221680309499956>.
- Kostic, S.; Parker, G. (2003b). Progradational sand-mud deltas in lakes and reservoirs. Part 2. Experiment and numerical simulation. *Journal of Hydraulic Research*, 41(2): 141–152. <http://dx.doi.org/10.1080/00221680309499957>.
- KWM (2003). Kraftwerk Mattmark AG ('Power plant Mattmark AG'). *Brochure*, Kraftwerk Mattmark AG. www.kwm.ch/content/kwm/leistungen/Mattmark_Infotafel.pdf [in German, accessed: 20/04/2018].
- Lai, S. Y. J.; Capart, H. (2009). Reservoir infill by hyperpycnal deltas over bedrock. *Geophysical Research Letters*, 36(8). <http://dx.doi.org/10.1029/2008gl1037139>.
- Lambert, A. (1979). Starke Bodenströmungen im Walensee ('Strong currents near the lake bottom in Walensee'). *Wasser Energie Luft*, 71(3): 50–53 [in German].

- Lambert, A. (1982). Trübestrome des Rheins am Grund des Bodensees ('Turbidity currents from the Rhine river on the bottom of Lake Constance'). *Wasserwirtschaft*, 72(4): 169–172 [in German].
- Lambert, A.; Giovanoli, F. (1988). Records of riverborne turbidity currents and indications of slope failures in the Rhone delta of Lake Geneva. *Limnology and Oceanography*, 33(3): 458–468. <http://dx.doi.org/10.4319/lo.1988.33.3.0458>.
- Lambert, A.M.; Kelts, K.R.; Marshall, N.F. (1976). Measurements of density underflows from Walensee, Switzerland. *Sedimentology*, 23(1): 87–105. <http://dx.doi.org/10.1111/j.1365-3091.1976.tb00040.x>.
- Lapazaran, J. J.; Otero, J.; Martín-Español, A.; Navarro, F. J. (2016). On the errors involved in ice-thickness estimates I: Ground-penetrating radar measurement errors. *Journal of Glaciology*, 62(236): 1008–1020. <http://dx.doi.org/10.1017/jog.2016.93>.
- Latosinski, F. G.; Szupiany, R. N.; García, C. M.; Guerrero, M.; Amsler, M. L. (2014). Estimation of concentration and load of suspended bed sediment in a large river by means of acoustic Doppler technology. *Journal of Hydraulic Engineering*, 140(7): 04014023. [http://dx.doi.org/10.1061/\(asce\)hy.1943-7900.0000859](http://dx.doi.org/10.1061/(asce)hy.1943-7900.0000859).
- Laufer, F.; Grötzing, S.; Peter, M.; Schmutz, A. (2004). Ausbaupotential der Wasserkraft ('Development potential of hydropower'). *Technical Report*, Swiss Federal Office of Energy (SFOE). <https://www.news.admin.ch/news/message/attachments/2663.pdf> [in German, accessed: 20/04/2018].
- Lee, J.; Liu, J. T.; Hung, C.-C.; Lin, S.; Du, X. (2016). River plume induced variability of suspended particle characteristics. *Marine Geology*, 380: 219–230. <http://dx.doi.org/10.1016/j.margeo.2016.04.014>.
- Leonard, B. P. (1979). A stable and accurate convective modelling procedure based on quadratic upstream interpolation. *Computer Methods in Applied Mechanics and Engineering*, 19(1): 59–98. [http://dx.doi.org/10.1016/0045-7825\(79\)90034-3](http://dx.doi.org/10.1016/0045-7825(79)90034-3).
- Lewis, C. P. (1970). Estimation of suspended sediment concentrations in natural water bodies from Secchi disk measurements. *PhD Thesis*, University of British Columbia. <http://dx.doi.org/10.14288/1.0104100>.
- Linsbauer, A.; Paul, F.; Haeberli, W. (2012). Modeling glacier thickness distribution and bed topography over entire mountain ranges with GlabTop:

- Application of a fast and robust approach. *Journal of Geophysical Research: Earth Surface*, 117(F3): 1–17. <http://dx.doi.org/10.1029/2011JF002313>.
- Lynch, J. F.; Irish, J. D.; Sherwood, C. R.; Agrawal, Y. C. (1994). Determining suspended sediment particle size information from acoustical and optical backscatter measurements. *Continental Shelf Research*, 14(10): 1139–1165. [http://dx.doi.org/10.1016/0278-4343\(94\)90032-9](http://dx.doi.org/10.1016/0278-4343(94)90032-9).
- Mamede, G. L.; Bronstert, A.; Francke, T.; Müller, E. N.; de Araujo, J. C.; Batalla, R. J.; Güntner, A. (2006). 1D Process-based modelling of reservoir sedimentation: A case study for the Barasona reservoir in Spain. *Proc. River Flow 2006*, R. M. L. Ferreira; E. C. T.L. Alves; J. G. A. B. Leal; A. H. Cardoso (eds.). *Taylor & Francis Group*, Lisbon, Portugal: 1585–1594.
- Maurizio, P. (2014). Wasserkraft am Gornergletscher ('Hydropower at Gorner Glacier'). *Master Thesis*, Laboratory of Hydraulics, Hydrology and Glaciology (VAW), ETH Zurich [in German, unpublished].
- Meiburg, E.; Kneller, B. (2010). Turbidity currents and their deposits. *Annual Review of Fluid Mechanics*, 42(1): 135–156. <http://dx.doi.org/10.1146/annurev-fluid-121108-145618>.
- Meile, T.; Bretz, N.-V.; Imboden, B.; Boillat, J.-L. (2014). Chap. 29 — Reservoir sedimentation management at Gebidem dam (Switzerland): 245–255. In: A. Schleiss; G. de Cesare; M.J. Franca; M. Pfister (eds.) *Reservoir Sedimentation*. ISBN 9781138026759. *Taylor & Francis Group*, London, England.
- Menczel, A.; Kostaschuk, R. (2013). Chap. 24 — Interfacial waves as coherent flow structures associated with continuous turbidity currents: Lillooet Lake, Canada: 371–383. In: J.G. Venditti; J.L. Best; M. Church; R.J. Hardy (eds.) ISBN 978-1-119-96277-9. *John Wiley & Sons, Ltd*, Burnaby, Canada.
- Meyer-Peter, E.; Müller, R. (1948). Formulas for bed-load transport. *Proc. IAHSR 2nd meeting. International Association for Hydraulic Structures Research (IAHSR)*: 39–64. <https://repository.tudelft.nl/islandora/object/uuid:4fda9b61-be28-4703-ab06-43cdc2a21bd7/datastream/OBJ/download> [accessed: 20/04/2018].
- Michalec, B. (2015). Evaluation of an empirical reservoir shape function to define sediment distributions in small reservoirs. *Water*, 7(12): 4409–4426. <http://dx.doi.org/10.3390/w7084409>.

- Micheletti, N.; Lane, S. N. (2016). Water yield and sediment export in small, partially glaciated Alpine watersheds in a warming climate. *Water Resources Research*, 52(6): 4924–4943. <http://dx.doi.org/10.1002/2016wr018774>.
- Middleton, G. V. (1993). Sediment deposition from turbidity currents. *Annual Review of Earth and Planetary Sciences*, 21: 89–114. <http://dx.doi.org/10.1146/annurev.earth.21.050193.000513>.
- Mikkelsen, O. A.; Hill, P. S.; Milligan, T. G.; Chant, R. J. (2005). In situ particle size distributions and volume concentrations from a LISST-100 laser particle sizer and a digital floc camera. *Continental Shelf Research*, 25(16): 1959–1978. <http://dx.doi.org/10.1016/j.csr.2005.07.001>.
- Mikkelsen, O. A.; Pejrup, M. (2000). In situ particle size spectra and density of particle aggregates in a dredging plume. *Marine Geology*, 170(3): 443–459. [http://dx.doi.org/10.1016/s0025-3227\(00\)00105-5](http://dx.doi.org/10.1016/s0025-3227(00)00105-5).
- Mirbach, S.; Lang, U. (2016). Density driven underflows with suspended solids in Lake Constance. *Proc. River Sedimentation*, S. Wieprecht; S. Haun; K. Weber; M. Noack; K. Terheiden (eds.). *CRC Press Taylor & Francis Group*, London, England: 1052–1056. ISBN 978-1-138-02945-3.
- Mirbach, S.; Lang, U. (2017). Density-driven underflows with suspended solids in Lake Constance. *Journal of Soils and Sediments*: 1–8. <http://dx.doi.org/10.1007/s11368-017-1753-x>.
- Müller-Hagmann, M. (2017). Hydroabrasion by high-speed sediment-laden flows in sediment bypass tunnels. *VAW-Mitteilung 239* (R. M. Boes, ed.). Laboratory of Hydraulics, Hydrology and Glaciology (VAW), ETH Zurich, Zurich, Switzerland.
- Moate, B. D.; Thorne, P. D. (2009). Measurements and inversion of acoustic scattering from suspensions having broad size distributions. *The Journal of the Acoustical Society of America*, 126(6): 2905–2917. <http://dx.doi.org/10.1121/1.3242374>.
- Möller, G.; Boes, R. M.; Theiner, D.; Fankhauser, A.; Daneshvari, M.; de Cesare, G.; Schleiss, A. (2011). Chap. B16 — Hybrid modeling of sediment management during drawdown of Räterichsboden reservoir: 421–428. In: A. Schleiss; R.M. Boes (eds.) *Dams and reservoirs under changing challenges*. ISBN 9780415682671. *CRC Press Taylor & Francis Group*, Boca Raton, USA.
- Moore, D. (1966). Deltaic sedimentation. *Earth-Science Reviews*, 1(2-3): 87–104. [http://dx.doi.org/10.1016/0012-8252\(66\)90001-8](http://dx.doi.org/10.1016/0012-8252(66)90001-8).

- Moore, S. A. (2011). Monitoring flow and fluxes of suspended sediment in rivers using side-looking acoustic Doppler current profilers. *PhD Thesis*, Université de Grenoble. <http://www.theses.fr/2011GRENU043.pdf> [accessed: 20/04/2018].
- Moore, S. A.; Le Coz, J.; Hurther, D.; Paquier, A. (2012). On the application of horizontal ADCPs to suspended sediment transport surveys in rivers. *Continental Shelf Research*, 46: 50–63. <http://dx.doi.org/10.1016/j.csr.2011.10.013>.
- Moore, S. A.; Le Coz, J.; Hurther, D.; Paquier, A. (2013). Using multi-frequency acoustic attenuation to monitor grain size and concentration of suspended sediment in rivers. *The Journal of the Acoustical Society of America*, 133(4): 1959–1970. <http://dx.doi.org/10.1121/1.4792645>.
- Morris, G. L.; Annandale, G.; Hotchkiss, R. (2008). Chap. 12 — Reservoir Sedimentation: 579–612. In: M.H. García (ed.) *Sedimentation Engineering: Processes, Measurements, Modeling, and Practice*. ISBN 978-0-7844-0814-8. *American Society of Civil Engineers (ASCE)*, Reston, Virginia (USA). <http://dx.doi.org/10.1061/9780784408148>.
- Morris, G. L.; Fan, J. (2010). Reservoir sedimentation handbook: Design and management of dams, reservoirs, and watersheds for sustainable use. ISBN 0-07-043302-X. *McGraw-Hill*, USA. https://www.engr.colostate.edu/~pierre/ce_old/classes/CE716/ResSedHandbook1_01.pdf [accessed: 20/04/2018].
- Muck, M. T.; Underwood, M. B. (1990). Upslope flow of turbidity currents: A comparison among field observations, theory, and laboratory models. *Geology*, 18(1): 54–57. [http://dx.doi.org/10.1130/0091-7613\(1990\)018<0054:UFOTCA>2.3.CO;2](http://dx.doi.org/10.1130/0091-7613(1990)018<0054:UFOTCA>2.3.CO;2).
- Mueller, D. S.; Abad, J. D.; García, C. M.; Gartner, J. W.; García, M. H.; Oberg, K. A. (2007). Errors in Acoustic Doppler Profiler Velocity Measurements Caused by Flow Disturbance. *Journal of Hydraulic Engineering*, 133(12): 1411–1420. [http://dx.doi.org/10.1061/\(asce\)0733-9429\(2007\)133:12\(1411\)](http://dx.doi.org/10.1061/(asce)0733-9429(2007)133:12(1411)).
- Mulder, T.; Syvitski, J. P. M.; Skene, K. I. (1998). Modeling of erosion and deposition by turbidity currents generated at river mouths. *Journal of Sedimentary Research*, 68(1): 124–137. <http://dx.doi.org/10.2110/jsr.68.124>.
- Müller, E. N.; Güntner, A.; Francke, T.; Mamede, G. (2010). Modelling sediment export, retention and reservoir sedimentation in drylands with the WASA-SED model. *Geoscientific Model Development*, 3(1): 275–291. <http://dx.doi.org/10.5194/gmd-3-275-2010>.

- Müller, G.; Förstner, U. (1968). General relationship between suspended sediment concentration and water discharge in the Alpenrhein and some other rivers. *Nature*, 217(5125): 244–245. <http://dx.doi.org/10.1038/217244a0>.
- Müller, M.; de Cesare, G.; Schleiss, A. (2014). Continuous long-term observation of suspended sediment transport between two pumped-storage reservoirs. *Journal of Hydraulic Engineering*, 140(5): 05014003. [http://dx.doi.org/10.1061/\(asce\)hy.1943-7900.0000866](http://dx.doi.org/10.1061/(asce)hy.1943-7900.0000866).
- Müller, P.; de Cesare, G. (2009). Sedimentation problems in the reservoirs of the Kraftwerke Sarganserland — venting of turbidity currents as the essential part of the solution. *Proc. 23th ICOLD Congress. International Commission on Large Dams (ICOLD)*, Brasilia, Brazil. Q.89, R.21: 1–13.
- Muto, T.; Swenson, J. B. (2005). Large-scale fluvial grade as a nonequilibrium state in linked depositional systems: Theory and experiment. *Journal of Geophysical Research: Earth Surface*, 110(F3). <http://dx.doi.org/10.1029/2005JF000284>.
- Nicklow, J. W.; Mays, L. W. (2000). Optimization of multiple reservoir networks for sedimentation control. *Journal of Hydraulic Engineering*, 126(4): 232–242. [http://dx.doi.org/10.1061/\(asce\)0733-9429\(2000\)126:4\(232\)](http://dx.doi.org/10.1061/(asce)0733-9429(2000)126:4(232)).
- Oehy, C.; de Cesare, G.; Schleiss, A. (2000). Einfluss von Trübeströmen auf die Verlandung von Staubecken (‘Impact of turbidity currents on the sedimentation of reservoirs’). *Proc. Symposium Betrieb und Überwachung wasserbaulicher Anlagen (‘Symposium on operation and monitoring of hydraulic structures’)*. *Mitteilung des Instituts für Wasserbau und Wasserwirtschaft Nr. 34*, Graz, Austria: 413–422.
- Oehy, C.; Schleiss, A. (2002). Einfluss von Hindernissen auf das Fließverhalten von Trübeströmen am Beispiel des Grimselsees (‘Impact of obstacles on flow of turbidity currents using the example of Grimsel reservoir’). *Proc. Moderne Methoden und Konzepte im Wasserbau (‘Modern methods and concepts in hydraulic engineering’)*, Minor, H.-E. (ed.). *Laboratory of Hydraulics, Hydrology and Glaciology (VAW), ETH Zurich*, Zurich, Switzerland: 51–60. <https://www.ethz.ch/content/dam/ethz/special-interest/baug/vaw/vaw-dam/documents/das-institut/mitteilungen/2000-2009/174.pdf> [in German, accessed: 20/04/2018].
- Oehy, C. D.; Schleiss, A. (2007). Control of turbidity currents in reservoirs by solid and permeable obstacles. *Journal of Hydraulic Engineering*, 133(6): 637–648. [http://dx.doi.org/10.1061/\(asce\)0733-9429\(2007\)133:6\(637\)](http://dx.doi.org/10.1061/(asce)0733-9429(2007)133:6(637)).

- Olsen, N. R. B. (1999). Two-dimensional numerical modelling of flushing processes in water reservoirs. *Journal of Hydraulic Research*, 37(1): 3–16. <http://dx.doi.org/10.1080/00221689909498529>.
- Ortmanns, C. (2006). Entsanter von Wasserkraftanlagen (‘Desanding facilities at hydroelectric power plants’). *VAW-Mitteilung 193* (H.-E. Minor, ed.). Laboratory of Hydraulics, Hydrology and Glaciology (VAW), ETH Zurich, Zurich, Switzerland. <https://www.ethz.ch/content/dam/ethz/special-interest/baug/vaw/vaw-dam/documents/das-institut/mitteilungen/2000-2009/193.pdf> [in German, accessed: 20/04/2018].
- Parker, G.; Fukushima, Y.; Pantin, H. M. (1986). Self-accelerating turbidity currents. *Journal of Fluid Mechanics*, 171: 145–181. <http://dx.doi.org/10.1017/s0022112086001404>.
- Parker, G.; Garcia, M.; Fukushima, Y.; Yu, W. (1987). Experiments on turbidity currents over an erodible bed. *Journal of Hydraulic Research*, 25(1): 123–147. <http://dx.doi.org/10.1080/00221688709499292>.
- Paschmann, C. (2018). Design optimization of alpine desanding facilities. *VAW-Mitteilung 247* (R. M. Boes, ed.). Laboratory of Hydraulics, Hydrology and Glaciology (VAW), ETH Zurich, Zurich, Switzerland.
- Paschmann, C.; Fernandes, J. N.; Vetsch, D. F.; Boes, R. M. (2017). Assessment of flow field and sediment flux at alpine desanding facilities. *International Journal of River Basin Management*, 15(3): 287–295. <http://dx.doi.org/10.1080/15715124.2017.1280814>.
- Pellicciotti, F.; Carenzo, M.; Bordoy, R.; Stoffel, M. (2014). Changes in glaciers in the Swiss Alps and impact on basin hydrology: current state of the art and future research. *Science of the Total Environment*, 493: 1152–1170. <http://dx.doi.org/10.1016/j.scitotenv.2014.04.022>.
- Plozza, V. (2014). Wasserkraft am Gornergletscher (‘Hydropower at Gorner Glacier’). *Master Thesis*, Laboratory of Hydraulics, Hydrology and Glaciology (VAW), ETH Zurich [in German, unpublished].
- Podolak, C. J. P.; Doyle, M. W. (2015). Reservoir sedimentation and storage capacity in the United States: Management needs for the 21st century. *Journal of Hydraulic Engineering*, 141(4): 02515001–1–02515001–5. [http://dx.doi.org/10.1061/\(asce\)hy.1943-7900.0000999](http://dx.doi.org/10.1061/(asce)hy.1943-7900.0000999).
- Rahmanian, M. R.; Banihashemi, M. A. (2011). Sediment distribution pattern in some Iranian dams based on a new empirical reservoir shape function. *Lake*

- and Reservoir Management*, 27(3): 245–255. <http://dx.doi.org/10.1080/07438141.2011.602510>.
- Rai, A. K.; Kumar, A. (2015). Continuous measurement of suspended sediment concentration: Technological advancement and future outlook. *Measurement*, 76: 209–227. <http://dx.doi.org/10.1016/j.measurement.2015.08.013>.
- Raymond Pralong, M.; Turowski, J. M.; Rickenmann, D.; Zappa, M. (2015). Climate change impacts on bedload transport in alpine drainage basins with hydropower exploitation. *Earth Surface Processes and Landforms*, 40(12): 1587–1599. <http://dx.doi.org/10.1002/esp.3737>.
- Rechsteiner, G. (1996). Ablagerungen im Stausee Gebidem und einige ihrer Folgen ('Sedimentation in Gebidem reservoir and some of its impacts'). *Proc. Verlandung von Stauseen und Stauhaltungen, Sedimentprobleme in Leitungen und Kanälen ('Sedimentation in reservoirs, pipes and conduits')*, D. Vischer (ed.). *Laboratory of Hydraulics, Hydrology and Glaciology (VAW), ETH Zurich, Zurich, Switzerland*: 137–148. <https://www.ethz.ch/content/dam/ethz/special-interest/baug/vaw/vaw-dam/documents/das-institut/mitteilungen/1990-1999/142.pdf> [in German, accessed: 20/04/2018].
- Reichel, G.; Nachtnebel, H. P. (1994). Suspended sediment monitoring in a fluvial environment: advantages and limitations applying an acoustic Doppler current profiler. *Water Research*, 28(4): 751–761. [http://dx.doi.org/10.1016/0043-1354\(94\)90083-3](http://dx.doi.org/10.1016/0043-1354(94)90083-3).
- Ridderinkhof, W.; Swart, H. E.; Vegt, M.; Hoekstra, P. (2016). Modeling the growth and migration of sandy shoals on ebb-tidal deltas. *Journal of Geophysical Research: Earth Surface*, 121(7): 1351–1372. <http://dx.doi.org/10.1002/2016JF003823>.
- Riihimäki, C. A.; MacGregor, K. R.; Anderson, R. S.; Anderson, S. P.; Loso, M. G. (2005). Sediment evacuation and glacial erosion rates at a small alpine glacier. *Journal of Geophysical Research*, 110(F3). <http://dx.doi.org/10.1029/2004jf000189>.
- Roe, P. L. (1981). Approximate Riemann solvers, parameter vectors, and difference schemes. *Journal of Computational Physics*, 43(2): 357–372. [http://dx.doi.org/10.1016/0021-9991\(81\)90128-5](http://dx.doi.org/10.1016/0021-9991(81)90128-5).
- Rössler, O.; Brönnimann, S. (2018). The effect of the Tambora eruption on Swiss flood generation in 1816/1817. *Science of The Total Environment*, 627: 1218–1227. <http://dx.doi.org/10.1016/j.scitotenv.2018.01.254>.

- Rulli, R. (2017). Wasserkraft infolge Gletscherrückzug am Fallbeispiel Oberaletschgletscher ('Hydropower due to glacier retreat in the case study of Oberaletsch Glacier'). *Master thesis*, VAW, ETH Zurich [in German, unpublished].
- Saito, Y. (2011). Delta-front morphodynamics of the Kurobe river fan-delta, central Japan. *Proc. River, Coastal and Estuarine Morphodynamics (RCEM) 2011*. Tsinghua University Press, Beijing, China: 592–601. https://www.researchgate.net/profile/Yoshiki_Saito/publication/234040046_Delta-front_morphodynamics_of_the_Kurobe_river_fan-delta_central_Japan/links/0fcfd50e78338dc29f000000/Delta-front-morphodynamics-of-the-Kurobe-river-fan-delta-central-Japan.pdf?origin=publication_detail [accessed on: 20/04/2018].
- Saito, Y.; Ikehara, K.; Tamura, T. (2016). Chap. 9 — Coastal geology and oceanography: 409–430. In: T. Moreno; S. Wallis; T. Kojima; W. Gibbons (eds.) *The Geology of Japan*. ISBN 978-1862397439. *The Geological Society of London*, London, England.
- Salles, T.; Lopez, S.; Eschard, R.; Lerat, O.; Mulder, T. ; Cacas, M. C. (2008). Turbidity current modelling on geological time scales. *Marine Geology*, 248(3): 127–150. <http://dx.doi.org/10.1016/j.margeo.2007.10.004>.
- Salzmann, N.; Machguth, H.; Linsbauer, A. (2012). The Swiss Alpine glaciers' response to the global '2°C air temperature target'. *Environmental Research Letters*, 7(4): 044001. <http://dx.doi.org/10.1088/1748-9326/7/4/044001>.
- Santos, A. I.; Oliveira, A.; Zacarias, N.; Pinto, J. P.; Ribeiro, M. (2014). Suspended sediment transport patterns in the inner shelf — S. Pedro de Moel (Portugal). *Journal of Sea Research*, 93: 47–56. <http://dx.doi.org/10.1016/j.seares.2014.04.009>.
- Sassi, M. G.; Hoitink, A.J.F.; Vermeulen, B. (2012). Impact of sound attenuation by suspended sediment on ADCP backscatter calibrations. *Water Resources Research*, 48(9). <http://dx.doi.org/10.1029/2012wr012008>.
- Schaefli, B.; Hingray, B.; Musy, A. (2007). Climate change and hydropower production in the Swiss Alps: quantification of potential impacts and related modelling uncertainties. *Hydrology and Earth System Sciences Discussions*, 11(3): 1191–1205. <http://dx.doi.org/10.5194/hess-11-1191-2007>.
- Scheu, K. R.; Fong, D. A.; Monismith, S. G.; Fringer, O. B. (2015). Sediment transport dynamics near a river inflow in a large alpine lake. *Limnology and Oceanography*, 60(4): 1195–1211. <http://dx.doi.org/10.1002/lno.10089>.

- Schleiss, A. (2012). Talsperreenerhöhungen in der Schweiz: energiewirtschaftliche Bedeutung und Randbedingungen ('Dam heightenings in Switzerland: economical importance and boundary conditions'). *Wasser Energie Luft*, 104(3): 199–203. https://infoscience.epfl.ch/record/181591/files/2012-881_Schleiss_Talsperreenerhohungen_in_der_Schweiz.pdf [in German, accessed: 20/04/2018].
- Schleiss, A.; de Cesare, G.; Jenzer Althaus, J. (2010). Verlandung der Stauseen gefährdet die nachhaltige Nutzung der Wasserkraft ('Reservoir sedimentation threatens the sustainable use of hydropower'). *Wasser Energie Luft*, 102(1): 31–40. https://infoscience.epfl.ch/record/147714/files/Schleiss_DeCesare_Jenzer_wel_2010_Verlandung.pdf [accessed: 20/04/2018].
- Schleiss, A.; Feuz, B.; Aemmer, M.; Zünd, B. (1996). Verlandungsprobleme im Stausee Mauvoisin ('Reservoir sedimentation problems in Lac de Mauvoisin'). *Proc. Verlandung von Stauseen und Stauhaltungen, Sedimentprobleme in Leitungen und Kanälen ('Sedimentation in reservoirs, pipes and conduits')*, D. Vischer (ed.). *Laboratory of Hydraulics, Hydrology and Glaciology (VAW), ETH Zurich*, Zurich, Switzerland: 37–58. <https://www.ethz.ch/content/dam/ethz/special-interest/baug/vaw/vaw-dam/documents/das-institut/mitteilungen/1990-1999/142.pdf> [in German, accessed: 20/04/2018].
- Schlunegger, F.; Hinderer, M. (2003). Pleistocene/Holocene climate change, re-establishment of fluvial drainage network and increase in relief in the Swiss Alps. *Terra Nova*, 15(2): 88–95. <http://dx.doi.org/10.1046/j.1365-3121.2003.00469.x>.
- Schulkin, M.; Marsh, H. W. (1962). Sound absorption in sea water. *The Journal of the Acoustical Society of America*, 34(6): 864–865. [http://dx.doi.org/10.1016/0041-624x\(63\)90210-5](http://dx.doi.org/10.1016/0041-624x(63)90210-5).
- SCNAT (2016). Brennpunkt Klima Schweiz. Grundlagen, Folgen und Perspektiven. ('Focus Climate Switzerland. Basics, Consequences and Perspectives'). *Swiss Academies Report 11 (5)*, Swiss Academy of Sciences. http://www.naturalsciences.ch/uuid/289496e5-c703-5917-ad42-1abd05b8fe36?r=20161005181841.1484061355_0d8762b6-48e9-5186-a15e-a89c7ed607ff [in German, accessed: 20/04/2018].
- Scully, M. E.; Friedrichs, C. T.; Wright, L. D. (2003). Numerical modeling of gravity-driven sediment transport and deposition on an energetic continental shelf: Eel River, northern California. *Journal of Geophysical Research*, 108(C4). <http://dx.doi.org/10.1029/2002jc001467>.

- Seiler, K.; Thomann, P. (2002). Höherlegung von Wasserfassung und Grundablass des Speichers Mauvoisin infolge Seeverlandung ('Heightening of intake and bottom outlet of Mauvoisin reservoir due to reservoir sedimentation'). *Proc. Moderne Methoden und Konzepte im Wasserbau ('Modern methods and concepts in hydraulic engineering')*, Minor, H.-E. (ed.). *Laboratory of Hydraulics, Hydrology and Glaciology (VAW), ETH Zurich, Zurich, Switzerland*: 13–25. <https://www.ethz.ch/content/dam/ethz/special-interest/baug/vaw/vaw-dam/documents/das-institut/mitteilungen/2000-2009/174.pdf>.
- Seybold, H.; Andrade, J. S.; Herrmann, H. J. (2007). Modeling river delta formation. *Proceedings of the National Academy of Sciences*, 104(43): 16804–16809. <http://dx.doi.org/10.1073/pnas.0705265104>.
- SGHL & CHy (2011). Auswirkungen der Klimaänderung auf die Wasserkraftnutzung — Synthesebericht ('Effects of climate change on hydropower use — synthesis report'). *Beiträge zur Hydrologie der Schweiz 38*, Schweizerische Gesellschaft für Hydrologie und Limnologie (SGHL) und Hydrologische Kommission (CHy). <http://www.hydrologie.unibe.ch/projekte/Synthesebericht.pdf> [in German, accessed: 20/04/2018].
- Sigl, M.; Winstrup, M.; McConnell, J. R.; Welten, K. C.; Plunkett, G.; Ludlow, F.; Büntgen, U.; Caffee, M.; Chellman, N.; Dahl-Jensen, D.; Fischer, H.; Kipfstuhl, S.; Kostick, C.; Maselli, O.J.; Mekhaldi, F.; Mulvaney, R.; Muscheler, R.; Pasteris, D. R.; Pilcher, J. R.; Salzer, M.; Schüpbach, S.; Steffensen, J. P.; Vinther, B. M.; Woodruff, T. E. (2015). Timing and climate forcing of volcanic eruptions for the past 2500 years. *Nature*, 523(7562): 543–549. <http://dx.doi.org/10.1038/nature14565>.
- Sloff, C. J. (1997). Sedimentation in reservoirs. *PhD Thesis*, Delft University of Technology. <http://repository.tudelft.nl/islandora/object/uuid:4d5cd422-931f-4e46-9730-d7c489ea87e4/datastream/OBJ/download> [accessed: 20/04/2018].
- SNV (2003). Schweizer Norm SN 505 261 — Einwirkungen auf Tragwerke ('Swiss Standard SN 505 261 — Actions on structures'). Swiss Association for Standardization (SNV).
- Sohn, Y. K.; Kim, S. B.; Hwang, I. G.; Bahk, J. J.; Choe, M. Y.; Chough, S. K. (1997). Characteristics and depositional processes of large-scale gravelly Gilbert-type foresets in the Miocene Doumsan Fan Delta, Pohang Basin, SE Korea. *Journal of Sedimentary Research*, 67(1): 130–141. <http://dx.doi.org/10.1306/d4268513-2b26-11d7-8648000102c1865d>.

- SonTek (2000). SonTek/YSI Acoustic Doppler Profiler. *Technical Documentation*, SonTek.
- SonTek (2015). SonTek RiverSurveyor S5/M9 System Manual. *Technical Documentation*, SonTek.
- SonTek (2016). SonTek RiverSurveyor S5/M9 Brochure. *Technical Documentation*, SonTek.
- SonTek (2017). RiverSurveyor S5/M9 SmartPulseHD®* Feature. *Technical Note*, SonTek.
- Souza, L. B. S.; Schulz, H. E.; Villela, S. M.; Gulliver, J. S. (2010). Experimental study and numerical simulation of sediment transport in a shallow reservoir. *Journal of Applied Fluid Mechanics*, 3(2): 9–21. http://jafmonline.net/JournalArchive/download?file_ID=15254&issue_ID=202 [accessed: 20/04/2018].
- Spasojevic, M.; Holly, F. M. (1990). 2-D bed evolution in natural watercourses — new simulation approach. *Journal of Waterway, Port, Coastal, and Ocean Engineering*, 116(4): 425–443. [http://dx.doi.org/10.1061/\(ASCE\)0733-950X\(1990\)116:4\(425\)](http://dx.doi.org/10.1061/(ASCE)0733-950X(1990)116:4(425)).
- Stott, T.; Mount, N. (2007). Alpine proglacial suspended sediment dynamics in warm and cool ablation seasons: implications for global warming. *Journal of Hydrology*, 332(3/4): 259–270. <http://dx.doi.org/10.1016/j.jhydrol.2006.07.001>.
- Strand, R. I.; Pemberton, E. L. (1987). Chap. A — Reservoir sedimentation. In: D. Webber; N. Parrett; H.K. Blair; T.N. McDaniel; R.D. Mohr (eds.) Design of Small Dams. *United States Department of the Interior, Bureau of Reclamation*, Washington, USA. <http://www.usbr.gov/tsc/techreferences/mands/mands-pdfs/SmallDams.pdf> [accessed: 20/04/2018].
- Sturm, M.; Matter, A. (1978). Chap. 8 — Turbidites and varves in Lake Brienz (Switzerland): Deposition of clastic detritus by density currents: 147–168. In: A. Matter; M. E. Tucker (eds.) Modern and Ancient Lake Sediments. ISBN 978-0-632-00234-4. *Blackwell Scientific Publications*, Oxford, England. <http://dx.doi.org/10.1002/9781444303698.ch8>.
- Stutenbecker, L. A.; Delunel, R.; Schlunegger, F.; Silva, T. A.; Šegvić, B.; Girardclos, S.; Bakker, M.; Costa, A.; Lane, S. N.; Loizeau, J-L.; Molnar, P.; Akçar, N.; Christl, M. (2017). Reduced sediment supply in a fast eroding landscape? A multi-proxy sediment budget of the upper Rhône basin, Central Alps. *Sedimentary Geology*, (10). <http://dx.doi.org/10.1016/j.sedgeo.2017.12.013>.

- Sumi, T. (2005). Sediment flushing efficiency and selection of environmentally compatible reservoir sediment management measures. *Proc. International Symposium on Sediment Management and Dams, 2nd EADC Symposium. East Asia of ICOLD*: 9–22.
- Swift, D. A.; Nienow, P. W.; Hoey, T. B. (2005). Basal sediment evacuation by subglacial meltwater: suspended sediment transport from Haut Glacier d’Arolla, Switzerland. *Earth Surface Processes and Landforms*, 30(7): 867–883. <http://dx.doi.org/10.1002/esp.1197>.
- Syvitski, J. P. M. (2003). Supply and flux of sediment along hydrological pathways: research for the 21st century. *Global and Planetary Change*, 39(1–2): 1–11. [http://dx.doi.org/10.1016/s0921-8181\(03\)00008-0](http://dx.doi.org/10.1016/s0921-8181(03)00008-0).
- Talling, P. J.; Paull, C. K.; Piper, D. J. W. (2013). How are subaqueous sediment density flows triggered, what is their internal structure and how does it evolve? Direct observations from monitoring of active flows. *Earth-Science Reviews*, 125: 244–287. <http://dx.doi.org/10.1016/j.earscirev.2013.07.005>.
- Tanaka, M.; Girard, G.; Davis, R.; Peuto, A.; Bignell, N. (2001). Recommended table for the density of water between 0°C and 40°C based on recent experimental reports. *Metrologia*, 38(4): 301–309. <http://dx.doi.org/10.1088/0026-1394/38/4/3>.
- Thevenot, M. M.; Prickett, T. L.; Kraus, N. C. (1992). Tylers Beach, Virginia, Dredged Material Plume Monitoring Project 27 September to 4 October 1991. *Technical Report DRP-92-7*, U.S. Army Corps of Engineers. <http://handle.dtic.mil/100.2/ADA261036> [accessed: 20/04/2018].
- Thorne, P. D.; Hanes, D. M. (2002). A review of acoustic measurement of small-scale sediment processes. *Continental Shelf Research*, 22(4): 603–632. [http://dx.doi.org/10.1016/s0278-4343\(01\)00101-7](http://dx.doi.org/10.1016/s0278-4343(01)00101-7).
- Thorne, P. D.; Hurther, D. (2014). An overview on the use of backscattered sound for measuring suspended particle size and concentration profiles in non-cohesive inorganic sediment transport studies. *Continental Shelf Research*, 73: 97–118. <http://dx.doi.org/10.1016/j.csr.2013.10.017>.
- Toniolo, H.; Parker, G.; Voller, V. (2007). Role of ponded turbidity currents in reservoir trap efficiency. *Journal of Hydraulic Engineering*, 133(6): 579–595. [http://dx.doi.org/10.1061/\(asce\)0733-9429\(2007\)133:6\(579\)](http://dx.doi.org/10.1061/(asce)0733-9429(2007)133:6(579)).
- Topping, D. J.; Wright, S. A.; Melis, T. S.; Rubin, D. M. (2007). High-resolution measurements of suspended-sediment concentration and grain size

- in the Colorado River in Grand Canyon using a multi-frequency acoustic system. *Proc. 10th International Symposium on River Sedimentation*: 470.
- Turowski, J. M.; Cook, K. L. (2017). Field techniques for measuring bedrock erosion and denudation. *Earth Surface Processes and Landforms*, 42(1): 109–127. <http://dx.doi.org/10.1002/esp.4007>.
- Turowski, J. M.; Rickenmann, D.; Dadson, S. J. (2010). The partitioning of the total sediment load of a river into suspended load and bedload: a review of empirical data. *Sedimentology*, 57(4): 1126–1146. <http://dx.doi.org/10.1111/j.1365-3091.2009.01140.x>.
- Uehlinger, U.; Malard, F.; Ward, J. V. (2003). Thermal patterns in the surface waters of a glacial river corridor (Val Roseg, Switzerland). *Freshwater Biology*, 48(2): 284–300. <http://dx.doi.org/10.1046/j.1365-2427.2003.01000.x>.
- Uhlmann, B.; Jordan, F.; Beniston, M. (2013). Modelling runoff in a Swiss glacierized catchment — Part II: daily discharge and glacier evolution in the Findelen basin in a progressively warmer climate. *International Journal of Climatology*, 33(5): 1301–1307. <http://dx.doi.org/10.1002/joc.3516>.
- Ulmann, M.; Wildi, W.; Lemmin, U. (2003). Sediment distribution on a current-dominated lake delta (Versoix delta, Lake Geneva, Switzerland). *Eclogae geologicae Helvetiae (Swiss Journal of Geosciences)*, 96: S91–S97. http://dx.doi.org/10.1007/978-3-0348-7992-7_11.
- Umeda, M.; Yokoyama, K.; Ishikawa, T. (2006). Observation and simulation of floodwater intrusion and sedimentation in the Shichikashuku reservoir. *Journal of Hydraulic Engineering*, 132(9): 881–891. [http://dx.doi.org/10.1061/\(asce\)0733-9429\(2006\)132:9\(881\)](http://dx.doi.org/10.1061/(asce)0733-9429(2006)132:9(881)).
- Unverricht, D.; Nguyen, T. C.; Heinrich, C.; Szczuciński, W.; Lahajnar, N.; Stattegger, K. (2014). Suspended sediment dynamics during the intermonsoon season in the subaqueous Mekong Delta and adjacent shelf, southern Vietnam. *Journal of Asian Earth Sciences*, 79: 509–519. <http://dx.doi.org/10.1016/j.jseaes.2012.10.008>.
- Urick, R. J. (1975). Principles of Underwater Sound. ISBN 978-0932146625. McGraw Hill, New York, USA.
- VAW (2011). Gletscher- und Abflussveränderungen im Zeitraum 1900–2100 in sieben Einzugsgebieten der Schweiz. VAW-Teilprojekt von CCHydro ('Glacier evolution and discharge changes from 1900–2100 in seven Swiss catchments. Sub-project of VAW for CCHydro'). *Technical Report*, Laboratory of Hydraulics, Hydrology and Glaciology (VAW), ETH Zurich.

<https://www.bafu.admin.ch/dam/bafu/de/dokumente/hydrologie/externe-studien-berichte/gletscher-und-abflussveraenderungen-im-zeitraum-1900-2100-in-sieben-einzugsgebieten-der-schweiz.pdf.download.pdf/gletscher-und-abflussveraenderungen-im-zeitraum-1900-2100-in-sieben-einzugsgebieten-der-schweiz.pdf> [in German, accessed: 20/04/2018].

- Vetsch, D. F.; Siviglia, A.; Caponi, F.; Ehrbar, D.; Facchini, M.; Gerke, E.; Kammerer, S.; Koch, A.; Peter, S.; Vonwiller, L. (2017). BASEMENT Version 2.7. *System Manuals*, Laboratory of Hydraulics, Hydrology and Glaciology, ETH Zurich. <http://people.ee.ethz.ch/~basement/baseweb/download/documentation/BMdoc-Reference-Manual-v2-7.pdf> [accessed: 20/04/2018].
- Viparelli, E.; Blom, A.; Parker, G. (2012). Modeling stratigraphy formed by prograding Gilbert deltas. *Proc. River Flow 2012*, R. Murillo (ed.). Taylor & Francis, London, England: 827–836. ISBN 9780415621298.
- Von Salis, A. (1884). Die Tiefenmessungen im Bodensee ('Depth measurements in Lake Constance'). *Schweizerische Bauzeitung*, 3/4(22): 127 [in German].
- Walling, D. E.; Webb, B. W. (1996). Erosion and sediment yield: a global overview. *Proc. Erosion and Sediment Yield: Global and Regional Perspectives*, D. E. Walling; B. Webb (eds.). *International Association of Hydrological Sciences (IAHS)*, Exeter, England: 3–19. ISBN 978-0-947571-89-4.
- Westaway, R. (2000). Modelling the potential effects of climate change on the Grande Dixence hydro-electricity scheme, Switzerland. *Water and Environment Journal*, 14(3): 179–185. <http://dx.doi.org/10.1111/j.1747-6593.2000.tb00247.x>.
- White, S. (2005). Sediment yield prediction and modelling. *Hydrological Processes*, 19(15): 3053–3057. <http://dx.doi.org/10.1002/hyp.6003>.
- Williams, N. D.; Walling, D. E.; Leeks, G. J. L. (2007). High temporal resolution in situ measurement of the effective particle size characteristics of fluvial suspended sediment. *Water research*, 41(5): 1081–1093. <http://dx.doi.org/10.1016/j.watres.2006.11.010>.
- Wisser, D.; Frohling, S.; Hagen, S.; Bierkens, M. F. P. (2013). Beyond peak reservoir storage? A global estimate of declining water storage capacity in large reservoirs. *Water Resources Research*, 49(9): 5732–5739. <http://dx.doi.org/10.1002/wrcr.20452>.

- Wittmann, H.; von Blanckenburg, F.; Kruesmann, T.; Norton, K. P.; Kubik, P. W. (2007). Relation between rock uplift and denudation from cosmogenic nuclides in river sediment in the Central Alps of Switzerland. *Journal of Geophysical Research*, 112(F4). <http://dx.doi.org/10.1029/2006JF000729>.
- Wood, M. S.; Teasdale, G. N. (2013). Use of surrogate technologies to estimate suspended sediment in the Clearwater River, Idaho, and Snake River, Washington, 2008–10. *Scientific Investigations Report 2013-5052*, U.S. Department of the Interior, U.S. Geological Survey. <https://pubs.usgs.gov/sir/2013/5052/pdf/sir20135052.pdf> [accessed: 20/04/2018].
- Wood, T. M.; Gartner, J. W. (2010). Use of acoustic backscatter and vertical velocity to estimate concentration and dynamics of suspended solids in Upper Klamath Lake, South-Central Oregon: Implications for *Aphanizomenon flos-aquae*. *Scientific Investigations Report 2010-5203*, U. S. Geological Survey. <https://pubs.usgs.gov/sir/2010/5203/pdf/sir20105203.pdf> [accessed: 20/04/2018].
- Woodward, J. C.; Porter, P. R.; Lowe, A. T.; Walling, D. E.; Evans, A. J. (2002). Composite suspended sediment particles and flocculation in glacial meltwaters: preliminary evidence from Alpine and Himalayan basins. *Hydrological Processes*, 16(9): 1735–1744. <http://dx.doi.org/10.1002/hyp.361>.
- Wren, D. G.; Barkdoll, B. D.; Kuhnle, R. A.; Derrow, R. W. (2000). Field techniques for suspended-sediment measurement. *Journal of Hydraulic Engineering*, 126(2): 97–104. [http://dx.doi.org/10.1061/\(asce\)0733-9429\(2000\)126:2\(97\)](http://dx.doi.org/10.1061/(asce)0733-9429(2000)126:2(97)).
- Wright, L. D. (1977). Sediment transport and deposition at river mouths: A synthesis. *GSA Bulletin*, 88(6): 857–868. [http://dx.doi.org/10.1130/0016-7606\(1977\)88<857:STADAR>2.0.CO;2](http://dx.doi.org/10.1130/0016-7606(1977)88<857:STADAR>2.0.CO;2).
- Wright, L. D. (1985). Chap. 1 — River deltas: 1–76. In: R. A. Jr. Davis (ed.) Coastal Sedimentary Environments. ISBN 978-1-4612-9554-9. *Springer-Verlag*, New York, USA. <http://dx.doi.org/10.1007/978-1-4612-5078-4>.
- Wright, L. D.; Friedrichs, C. T.; Kim, S. C.; Scully, M. E. (2001). Effects of ambient currents and waves on gravity-driven sediment transport on continental shelves. *Marine Geology*, 175(1-4): 25–45. [http://dx.doi.org/10.1016/s0025-3227\(01\)00140-2](http://dx.doi.org/10.1016/s0025-3227(01)00140-2).
- Wu, W. (2008). Computational River Dynamics. ISBN 978-0-415-44960-1. *Taylor & Francis*, London, England. <http://dx.doi.org/10.4324/9780203938485>.

- Wu, W.; Wang, S. S. Y. (2006). Formulas for sediment porosity and settling velocity. *Journal of Hydraulic Engineering*, 132(8): 858–862. [http://dx.doi.org/10.1061/\(ASCE\)0733-9429\(2006\)132:8\(858\)](http://dx.doi.org/10.1061/(ASCE)0733-9429(2006)132:8(858)).
- Xu, J. (1998). Numerical modeling of suspended sediment transport in rivers. *PhD Thesis*, Institute for Modelling Hydraulic and Environmental Systems, University of Stuttgart. http://www.iws.uni-stuttgart.de/institut/wasserbau/publikationen/098_Xu_Yichun.pdf [accessed: 20/04/2018].
- Xu, J. P. (2011). Measuring currents in submarine canyons: Technological and scientific progress in the past 30 years. *Geosphere*, 7(4): 868–876. <http://dx.doi.org/10.1130/ges00640.1>.
- Xu, J. P.; Sequeiros, O. E.; Noble, M. A. (2014). Sediment concentrations, flow conditions, and downstream evolution of two turbidity currents, Monterey Canyon, USA. *Deep Sea Research Part I: Oceanographic Research Papers*, 89: 11–34. <http://dx.doi.org/10.1016/j.dsr.2014.04.001>.
- Xu, J. P.; Swarzenski, P. W.; Noble, M.; Li, A.-C. (2010). Event-driven sediment flux in Hueneme and Mugu submarine canyons, southern California. *Marine Geology*, 269(1): 74–88. <http://dx.doi.org/10.1016/j.margeo.2009.12.007>.
- Yalin, M. E.; da Silva, A. M. F. (2001). Fluvial Processes. ISBN 90-805649-2-3. *International Association of Hydraulic Engineering and Research (IAHR)*, Delft, The Netherlands.
- Yuan, Y.; Wei, H.; Zhao, L.; Jiang, W. (2008). Observations of sediment resuspension and settling off the mouth of Jiaozhou Bay, Yellow Sea. *Continental Shelf Research*, 28(19): 2630–2643. <http://dx.doi.org/10.1016/j.csr.2008.08.005>.
- Zeng, J.; Lowe, D. R. (1997a). Numerical simulation of turbidity current flow and sedimentation: I. Theory. *Sedimentology*, 44(1): 67–84. <http://dx.doi.org/10.1111/j.1365-3091.1997.tb00424.x>.
- Zeng, J.; Lowe, D. R. (1997b). Numerical simulation of turbidity current flow and sedimentation: II. Results and geological applications. *Sedimentology*, 44(1): 85–104. <http://dx.doi.org/10.1111/j.1365-3091.1997.tb00425.x>.
- Ziegler, C. K.; Nisbet, B. S. (1995). Long-term simulation of fine-grained sediment transport in large reservoir. *Journal of Hydraulic Engineering*, 121(11): 773–781. [http://dx.doi.org/10.1061/\(asce\)0733-9429\(1995\)121:11\(773\)](http://dx.doi.org/10.1061/(asce)0733-9429(1995)121:11(773)).

Curriculum vitae

Daniel EHRBAR

Sonnenhalde 1
CH-8603 Schwerzenbach ZH
Switzerland

+41 (0)79 712 20 54
daniel.ehrbar@bluewin.ch

birth date: 31 August 1986
citizenship: Urnäsch, AR

Education

since 01/2015	PhD thesis at VAW, ETH Zurich
09/2010 - 06/2012	Master of Science ETH in Civil Engineering
09/2006 - 07/2009	Bachelor of Science ETH in Civil Engineering

Employments

11/2012 - 12/2014	Research engineer at VAW, ETH Zurich
09/2011 - 06/2012	Student assistant at VAW, ETH Zurich
09/2009 - 06/2010	Internship at Basler & Hofmann AG, Esslingen

VAW: Laboratory of Hydraulics, Hydrology and Glaciology
ETH: Swiss Federal Institute of Technology